Gradually detuned coupled waveguides for quantum-like robust light transfer and splitting

Hassan Oukraou

CentraleSupélec

N° d'ordre :2018-01-TH

École doctorale n° 409 : Énergie, Mécanique et Matériaux

Doctorat CentraleSupélec

THÈSE

pour obtenir le grade de docteur délivré par

l'École Supérieure CentraleSupélec

Spécialité doctorale "Photonique"

présentée et soutenue publiquement par

Hassan Oukraou

le 09 mai 2018

Gradually detuned coupled waveguides for quantum-like robust light transfer and splitting

---

Directeur de thèse : **Germano Montemezzani**
Co-directeur de thèse : **Virginie Coda**

Jury

Mr. H. R. Jauslin,	Prof., Univ. de Bourgogne, France	Rapporteur
Mr. E. Fazio,	Prof., Sapienza Università di Roma, Italie	Rapporteur
Mme. M. Jazbinsek,	Prof. ass., Zurich University of Applied Sciences, Suisse	Examinateur
Mr. J. F. Henninot,	Prof., Univ. d'Artois, France	Examinateur

CentraleSupélec
LMOPS, 2 rue Edouard Belin, 57070 Metz, France

THESIS

Acknowledgement

This work, funded by CentraleSupélec foundation and Région Lorraine has been performed in the Laboratoire Matériaux Optiques, Photonique et Systèmes (LMOPS), Metz, France. I would like to thank its director Jean Paul Salvestrini and Marc Fontana for having welcomed me in the laboratory.

I would like to express my sincere gratitude to my advisors Germano and Virginie for their continuous support during these years of research, for their patience, motivation, and immense knowledge. I thank them for the encouragement they gave me, during this adventure. Their constant feedback and their guidance helped me during all the time of research and the writing of this thesis. I could not have imagined having a better advisors for my Ph.D study.

Besides my advisors, I would like to thank my thesis jury members: Prof. Hans-Rudolf Jauslin, Prof. Eugenio Fazio, Ass. Prof. Mojca Jazbinsek and Prof. Jean-François Henninot for having accepted to evaluate this work and for their insightful comments and encouragements.

I greatly appreciate the support received through the collaborative work undertaken with the university of Sofia, Bulgaria, during my thesis work. I am especially grateful to Andon for his strong involvement in this work.

I also thank Laura from the university of Padova, Italy, for the help during my first steps in the experiments.

I am also grateful to Evelyne, Stéphanie, Fabienne, Sophie, Thérèse, Jean Claude, and Céline who were always helpful and provided me with their assistance throughout my dissertation.

Thanks go to the laboratory members with whom I shared lots of fruitful discussions, and with whom I shared mint tea from time to time, they like it. I especially thank Patrice for giving me access to teaching but also for his jokes.

I am indebted to all my friends and especially the Bouazama family in Dijon, France,

who opened its home to me during my studies at the university of Bourgogne and who were always so helpful in numerous ways.

Special thanks to Rawdha, Chérifa, Sara, Ahmed, Ivan, Wahab, Alban, Abdelhamid, Mohammed, Ines, Mohammadou, Stéphane, Joris, Hadrien, Marie, Elise, Imed, Rim, Thibault, Rana, Israa, Hicham, Amel,...

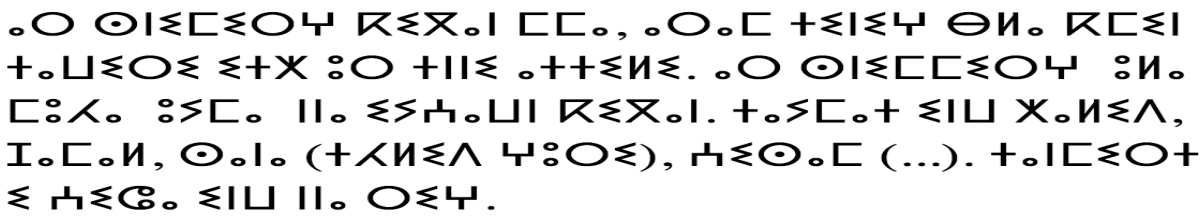

Abstract

The propagation of optical waves in coupled waveguides can be described by the coupled-mode theory. This formalism is mathematically analogous to the one for the quantum dynamics of the population of coupled atomic states, which is described by the Schrödinger equation within the so called Rotating Wave Approximation (RWA). This analogy has been pointed out in recent years. It was applied to coupled waveguide systems with constant effective refractive indices, which are fully analogous to resonant coupled quantum systems. This work extends this kind of studies to optical systems possessing an additional control parameter: the longitudinal modulation of the waveguide propagation constants. This approach is analogous to quantum systems with time dependent non-resonant excitation. As the population transfer between atomic states can be controlled by means of the Rabi frequencies and the laser frequency detunings, the light transfer between coupled waveguides can be controlled by means of the coupling constants and the propagation constants. Several such analogies are studied and exploited in this thesis for the demonstration of robust (broadband) adiabatic light transfer and splitting.

The first system is based on the recently introduced quantum process known as two-state STImulated Raman Adiabatic Passage (two-state STIRAP). This is implemented for the first time in classical optics with a set of two evanescently coupled waveguides with proper longitudinal modulation of the mode propagation constants and of the coupling coefficient between them. A broadband 50:50 beam splitter based on two-state STIRAP is theoretically proposed and experimentally demonstrated. The experiments are performed using reconfigurable and tuneable waveguide structures that are optically induced by a lateral illumination technique of a nonlinear photorefractive crystal. This experimental platform provides versatile guiding structures that can be erased and reconfigured to test various systems depending on the considered analogy.

A second quantum analogy based on the process of Rapid Adiabatic Passage (RAP) is theoretically studied and experimentally implemented for a set of two waveguides for

which the longitudinally varying detuning crosses zero at half propagation distance. The modulation of the detuning and of the coupling constant provide a very robust and highly achromatic mechanism for full light transfer between the waveguides (broadband directional coupler). This is analogous to the RAP-based robust inversion of two-level quantum systems.

The above RAP-like transfer applies to systems containing only two waveguides. It is also shown theoretically and numerically that the same functionality can be obtained in systems containing N waveguides with N$>$ 2. This relies on a technique called adiabatic elimination. It consists in the formal elimination of the N-2 internal waveguide(s) who reduces the system to an effective two-waveguide system where RAP can be applied. This is relevant because it permits a light transfer between the outer waveguides without excitation of the middle one(s). In contrast to the already known technique based on the conventional STIRAP process, the technique studied here works in a symmetric way and for an odd and even total number of guides N. Adiabatic elimination is achieved by a strong detuning between the two outer waveguides and the remaining one(s).

It can be concluded that the analogies of all the classical optical systems studied in this work with corresponding non-resonant quantum systems and processes give powerful tools to design new broadband photonic structures. Moreover, the present studies can pave the way for dealing with future novel functionalities in nonlinear optical waveguide systems, which involve in a natural way a spatial light-intensity-dependent variation of the waveguide propagation constants and detuning.

Résumé

La propagation d'ondes dans des guides d'ondes couplés peut être décrite par la théorie des modes couplés. Ce formalisme est mathématiquement analogue à l'équation de Schrödinger dans l'approximation des ondes tournantes (RWA) qui décrit la dynamique quantique du transfert de population entre des états atomiques couplés. Ces analogies ont été précédemment étudiées dans des systèmes de guides couplés possédant un indice effectif constant. Ces systèmes sont parfaitement analogues aux systèmes quantiques couplés en résonance. Nous étendons ce type d'études à des systèmes optiques possédant un paramètre de contrôle supplémentaire via la modulation longitudinale des constantes de propagation. Ces configurations sont analogues aux systèmes quantiques couplés avec une excitation variable et non résonnante. Le transfert de population entre les états atomiques est contrôlé par les fréquences de Rabi et le désaccord de fréquence entre le laser couplant les niveaux et la fréquence de transition. Et en optique, le transfert de lumière entre les guides est ajusté et contrôlé grâce aux constantes de couplage et de propagation des modes. Dans cette thèse, nous exploitons ces analogies pour réaliser des transferts robustes et adiabatiques de la lumière entre différents guides.

Le premier système étudié est basé sur le processus, récemment développé en physique quantique, de STIRAP à deux états (two-state STImulated Raman Adiabatic Passage). Cette analogie est mise en œuvre pour la première fois en optique grâce à une structure composée de deux guides, pour lesquels les constantes de couplage et de propagation sont modulées longitudinalement pour réaliser un diviseur de faisceau 50:50 large bande. Ce composant est d'abord étudié théoriquement puis démontré expérimentalement. Les expériences sont réalisées avec des structures de guide d'ondes reconfigurables et accordables, générés par la technique d'illumination latérale d'un cristal photoréfractif. Cette plateforme expérimentale innovante permet de générer des structures de guides qui peuvent être facilement effacés et reconfigurés pour tester différents systèmes.

Une seconde analogie, inspirée du processus de Passage Adiabatique Rapide (RAP), est ensuite théoriquement étudiée et expérimentalement réalisée. Nous exploitons un système à deux guides couplés, où le désaccord entre les constantes de propagation s'annule au centre de la propagation. Une telle modulation du désaccord entre les constantes de propagation et de la constante de couplage permet d'effectuer un transfert total de la lumière entre les guides (réalisation d'un coupleur directionnel large bande et robuste).

Le processus de RAP décrit précédemment s'applique à des systèmes à deux états. Nous démontrons théoriquement et numériquement que les analogies optiques du RAP peuvent être étendues à des systèmes contenant N guides (N$>$ 2) grâce à une technique quantique appelée élimination adiabatique. Elle consiste en l'élimination formelle du (des) guide(s) d'ondes intermédiaire(s). Cela réduit le système à un formalisme mathématique où seuls les deux guides externes restent, et où, par conséquent, le RAP peut être appliqué. Cette technique permet un transfert de lumière entre les guides externes sans excitation

du (des) guide(s) intermédiaires. Contrairement à la technique du STIRAP conventionnel, l'élimination adiabatique fonctionne de manière symétrique, et pour un nombre de guides N pair ou impair. L'élimination adiabatique requiert un désaccord important des constantes de propagation.

Ce travail contribue ainsi à démontrer que les analogies entre la mécanique quantique et l'optique guidée sont des outils puissants pour concevoir de nouvelles structures photoniques large bande et robustes. Elles peuvent être étendues à la réalisation future de nouvelles fonctions utilisant des guides en régime non linéaire, la propagation non linéaire induisant la variation spatiale (dépendante de l'intensité de la lumière).

Contents

Introduction

Even though classical and quantum physics are different in their essence, they often bear similar or identical mathematical formalisms leading to specific and useful analogies. For instance, the time independent Schrödinger equation and the Helmholtz equation share a common mathematical form. Classical optical diffraction, which is related to Fourier transformation, bears strong similarities with Heisenberg uncertainty principle, and so on. So, while particle entanglement is purely quantum in nature and do not have a classical counterpart, phenomena solely driven by quantum interference often find analogous classical phenomena. An example is the strong similarity between the electronic bandgaps in periodic crystalline potentials and the photonic bandgaps in periodic dielectric structures, the first being related to the quantum electron wavefunctions, the second to the classical electromagnetic waves. In this context optics was definitely a source of inspiration in the pioneering times of quantum mechanics, for instance when De Broglie proposed that any particle should have a wave nature. However, even though the richest analogies are found in the field of optics, other domain of classical physics bear useful quantum analogies. Several examples can be found in various fields, as for instance in acoustics where a classical acoustic Bloch waves [1] or an acoustic Casimir effect [2] can be identified. The interested reader may refer to the exhaustive list contained in Ref. [3].

Most analogies are found in the field of optics, much work in this context has recently been dedicated to photonic structures and lattices and a nice overview was given by Longhi [4]. Light propagation in such structures bears strong similarities with some general issues of quantum mechanics, such as the Aharonov-Bohm effect [5], the Berry phase [6, 7] or the spin Hall effect [8, 9]. In the same line, several analogs to phenomena in solid state physics were identified, such as the Bloch oscillations [10, 11], Anderson localization [12, 13], or surface physics effects [14, 15].

Among the photonic structures, those composed of a limited number of coupled optical waveguides aligned on a plane are of particular interest. Such structures provide a direct

analogy with quantum systems composed by an equivalent number of discrete states being coupled by a proper field, for instance some atomic levels coupled by resonant laser field. This kind of relationship is at the core of this thesis work and will be discussed in detail in this manuscript. In this context, a very important milestone has been the establishing of a relationship between a structure of three waveguides with a proper geometry and the celebrated quantum process of STIRAP (Stimulated Raman Adiabatic Passage) [16, 17, 18]. The first proposal highlighting this relationship was given by Paspalakis in 2006 [19] and the first experimental demonstration was given by Longhi et al. in 2007 [20] using waveguides formed by ion exchange on a glass substrate. Later, other studies have demonstrated analogies to the so called "half-STIRAP" [21] process or to multistate STIRAP [22, 23, 24].

The activities of the LMOPS laboratory in this field were started in the previous thesis by Charles Ciret [25], where experiments were performed using the same technique to record photoinduced waveguides that is used in this work.

In the previous thesis by Charles Ciret in our laboratory, optical analogies of multiple STImulated Raman Adiabatic Passage (multiple STIRAP), Autler-Townes effect, and Electromagnetically Induced Transparency (EIT) were theoretically studied and verified and successfully implemented for waveguides [24, 26, 27]. They conducted to the realization of planar achromatic multiple beam splitters and to broadband adiabatic light transfer. In these interesting outcomes, only the coupling constants between waveguides were spatially modulated. The coupling constants mimic the temporal modulation of the Rabi frequencies of their atomic systems analogs.

In this thesis, we use waveguides generated with lateral illumination technique for the demonstration of several additional analogies between quantum mechanics and waveguide optics in the case where the systems are subjected to a variable detuning. In this context, robust and achromatic coupled waveguide systems inspired by adiabatic evolving detuned coupled quantum systems are investigated theoretically and experimentally. Specifically, in these systems, not only the coupling constant is modulated but also the propagation constant of the waveguides evolves along the propagation distance. This new approach, offers more controllability, adds richness to these systems, and addresses new analogies while conserving the robustness associated to the adiabatic spatial evolution.

The main results of the present thesis concern the waveguide based implementation of three quantum techniques, the two–state STIRAP process [28, 29], the rapid adiabatic passage (RAP) process [30], and the adiabatic elimination of intermediate states [31, 32, 33, 34, 35]. The recently developed mechanism of two-state STIRAP of the quantum mechanics consists on an adiabatic creation of a coherent superposition in a coupled two-state system. It relies on a formal analogy between the STIRAP equations and the Bloch equations for a two-state system. In this thesis, we use this concept for a system of two evanescently coupled optical waveguides to propose a new kind of robust beam splitter

in which the exchange of optical power is controlled by means of a modulation of the propagation constant β along the propagation z-direction.

The other quantum-mechanical process, the RAP is used to inspire an achromatic directional coupler. The quantum RAP process produces an adiabatic and complete population transfer from an initial quantum state to a target final state. In our waveguide case, the wished power transfer is also assisted by means of the modulation of the propagation constant detuning and of the coupling constant. In both cases, the spatially modulated detuning provides a very robust mechanism of the optical power transfer, virtually insensitive to the variations of the maximum amplitude of detuning and to the light wavelength.

The process of adiabatic elimination of quantum physics consists on elimination of the intermediate states in a coupled N-state system due to the strong detuning of the intermediate states. The N-state system is reduced to an effective two-state system. This approach finds an analogy in waveguide structures in which the intermediate waveguides are "eliminated" by introducing a strong detuning between their propagation constants and the ones of the outer waveguides. This leads to an all achromatic light transfer between the outer waveguides.

For the experimental demonstration of the above concepts, specifically designed guiding structures with particular geometries are needed. Moreover, it is necessary to dispose of optical structures whose properties such as their curvature, refractive index, etc, can be easily modified. Depending on the material used, there are many technologies for the realization of optical waveguides, to name a few we may cite silicon-on-isolator waveguide compatible with CMOS technology (Complementary Metal Oxide Semiconductor), ion implantation, epitaxial growth, ion exchange, or thermal diffusion techniques. Some of the above techniques require quite sophisticated technologies and/or clean room facilities. They are therefore better adapted to a final product realization than for rapid prototyping and proof-of-principle demonstration. Furthermore, all the cited techniques lead to fixed structures that cannot be easily modified once they are created. Here, we use therefore an alternative technique permitting to generate optical waveguides at low costs and possessing the possibility for a quick reconfigurability. The used technique is the photo inscription of waveguides by lateral illumination which was developed first by Dittrich *et al.* [36] and was a subject of a previous thesis in the laboratory by Mohamed Gorram [37]. In the present thesis we exploit for the first time the dependence of the refractive index contrast on the local intensity of the lateral control light to obtain waveguide structures with variable propagation constant in the longitudinal direction.

This manuscript is organized as follows. The first chapter recalls the basic theory underlying the propagation of light in coupled–guiding structures. The modes of planar type waveguide are recalled and the coupling of light between neighboring waveguides is discussed. This is made on the base of the coupled mode theory, which represents the

basic element for the analogy with the corresponding quantum systems.

In the second chapter, we present the photorefractive and the electro-optic effects which are exploited for generation of the photoinduced waveguide structures used for the demonstration of our quantum-like mechanics in waveguide optics. At the end of this chapter, the experimental set-up for generation, characterization and measurements is presented in detail.

Through the third chapter, we introduce the analogies between quantum mechanics and waveguide optics. We show that the dynamics of coupled quantum systems described by the Schrödinger equation is perfectly similar to the dynamics of coupled optical waveguide systems described by the paraxial wave equation. We also identify the analogue parameters between an optical waveguide system and coupled quantum system showing a state population dynamics. By means of an example connecting a three level atomic system and its equivalent configuration composed of three coupled waveguides, it is shown that, on one hand, the role of the Rabi frequencies in the quantum system is taken by the coupling constants in the waveguide system. On the other hand, the time depending frequency detuning of near resonant coupling field (laser field) in the quantum system is analog to the spatially varying detuning of the propagation constants of the waveguides for the optical system.

In chapter 4, we present explicitly the analogy existing between a two level quantum system coupled by external laser fields evolving in time and an optical system composed of a set of two coupled waveguides in which the propagation constant of one of the waveguides evolves along the propagation distance. We introduce a spatial modulation of the coupling coefficients and we study theoretically and experimentally the effect of the propagation constants on the adiabatic light transfer between the coupled waveguides. Two concrete examples are investigated, the first one concerns the RAP process and the second one is based on the two-state STIRAP mentioned above. The optical structure is used to realize an efficient, robust, and achromatic light transfer in a set of two evanescently coupled waveguides. The RAP based system leads to a broadband directional coupler while the two-state STIRAP system leads to a broadband 50:50 beam splitter.

In the last chapter, we treat the phenomenon of adiabatic elimination of the quantum mechanics for a three state scheme with a strongly detuned intermediate state. This process is based on the elimination of the intermediate state due to the introduced strong detuning. By analogy, and in a three waveguide STIRAP-like scheme, full and robust light transfer between the outer waveguides can be achieved. Contrary to conventional STIRAP, the efficiency of light transfer does not depend on the order at which the coupling constants are applied and therefore works equally well from left to right and from right to left in the considered waveguide structure. The principle is then extended to a set of six waveguides. In both cases, the elimination of the intermediate waveguides is due to the strong detuning between the outer waveguides and the intermediate ones. Importantly,

these systems effectively behave like they would accomplish the RAP-like transfer that is the matter of one of the studies in chapter 4. The spectral dependence of this process is discussed with the help of realistic simulations.

Finally, appendix A presents some theoretical simulations studies that are less directly connected with the investigations performed in chapters 4 and 5. Two different optical systems are considered. The first one concerns waveguide systems in which an abrupt change of the detuning of the propagation constant is introduced. They mimic a coupled two/three state quantum systems in which the sign of the Rabi frequency changes abruptly. The second deals with backward propagation of light in the optical structure used for the demonstration of two-state STIRAP treated in chapter 4 as well as in a structure mimicking the so-called half-STIRAP quantum process. The role of the relative phase of the two back-propagating inputs is discussed and found to follow the expectations for conventional beam splitters. Appendix B gives a long résumé of the thesis in french and appendix C summarizes my publications and communications I attended during the thesis work.

1 Light guiding

Contents

1.1 Introduction

The discretization of electromagnetic waves into discrete guided modes was discovered for the first time when Maxwell's equations were solved for particular guiding structures. Such solutions were first obtained by Hondros and Debye [38] for circular dielectric cylinder in 1910. However, they were more interested in the propagation of radio-frequency waves along dielectric wires, as were Zahn (1916) [39] and Schrieven (1920), who first studied such wave propagation experimentally [40]. Most of the theoretical and experimental studies that followed well into the 1950s were likewise concerned with radio and micro wave propagation along dielectric waveguides. During this time, the optical aspect of dielectric waveguides received little attention except for the theoretical work of Buchholz (1938) [41].
The first dielectric optical waveguide in which discrete modes of propagation were studied at optical frequencies was the glass-cladded glass fiber developed originally for fiber optics imaging applications by Kapany in 1967 [42]. The work on optical waveguides received more attention after the advent of the laser in the 1960s and the related possibility of using coherent light in communications and other applications.
Dielectric optical waveguide is a structure that confines light along one or two directions transverse to propagation [43]. A planar waveguide is formed by uniform planar film with a constant or variable refractive index surrounded by two dielectric media of lower refractive indices [44]. The central medium is called the core and the surrounding upper and lower media are called the cladding. When the upper and lower media have the same optical constants, then the guiding structure forms a symmetric planar waveguide.

When light rays are incident on an interface of such a structure, at certain angles, the total internal reflection occurs and light is guided through the waveguide. This interpretation based on geometrical optics does not fully take into account the character of light as an electromagnetic wave. The more accurate description of light propagation within a waveguide is obtained using Maxwell's equations. The geometric boundary conditions at waveguide interfaces are introduced and only discrete solutions of the wave equations are permitted. This means that only discrete waves (modes) can be guided. These modes are characterized by specific profile amplitudes and discrete propagation constants [45, 46].

This chapter is organized as follows: we first determine the conditions of existence of modes when light propagates through an optical waveguide. Then, we use Maxwell's equations and electromagnetic analysis is presented. Propagating modes solutions are given by solving Helmholtz equation. Optical coupling of light is treated within the framework of coupled mode theory whose key quantity is the coupling constant for which an analytical expression can be given. Its role in light exchange between waveguides is illustrated through examples of optical directional couplers.

This chapter has as objective to remind some basics of waveguides optics. Mathemati-

cal tools, required for understanding light guiding and light coupling, are recalled. Coupled mode theory that points to describe the wave coupling between neighboring waveguides is discussed in some detail. As will be shown latter, coupled mode theory is at the heart of the analogies with the quantum phenomena that will be exploited in this thesis.

1.2 Modes of a dielectric planar waveguide

We start our conventional analysis of optical waveguides with the case of a planar waveguide, its simplicity as a guiding structure is very useful for illustrating the principles involved in light guidance and has applications in integrated optics. Also, the experiments described in this manuscript use planar waveguides. Since we can analyse the light propagation characteristics by seeing it as a supperposition of ray paths, it is quite important to appreciate the behavior of individual rays. In this section, we study the trajectories of rays within planar waveguide.

The planar optical waveguide under investigation is shown in Fig. 1.1. It consists typically of a core layer of thickness W surrounded by two layers which form the cladding. We assume that the cladding is unbounded, The planes $\pm W/2$ represent the waveguide interfaces. The waveguide extends indefinitely in all directions orthogonal to the x-axis. The z-axis is placed along the axis of the waveguide midway between the two interfaces. The refractive index profile in Fig. 1.1 is uniform across the core (n_1) and the cladding (n_2), with $n_1 > n_2$.

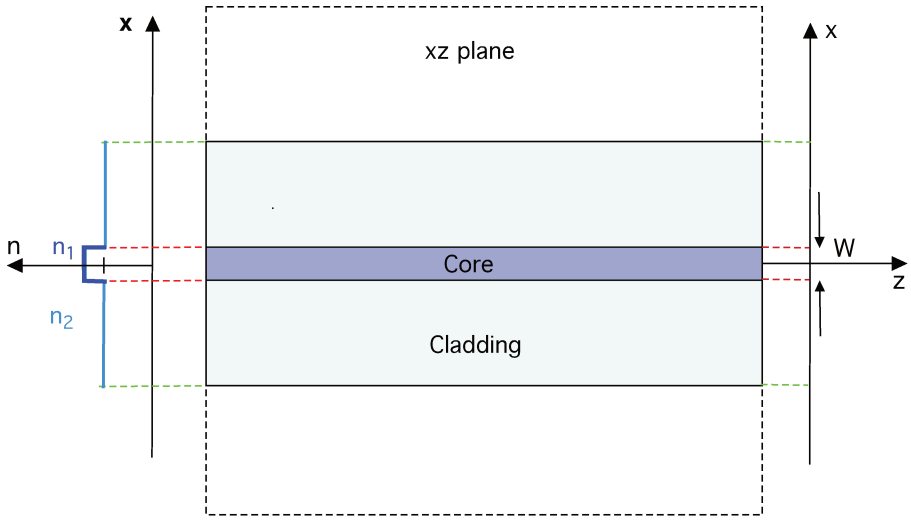

Figure 1.1: Planar waveguide in the plane xz, the refractive index for the core (n_1) and for the cladding (n_2) are uniform along the z-axis, $n_1 > n_2$.

1.2.1 Conditions for existence of mode

When a ray of light goes from a high to low refractive index medium it deviates away from the normal to the interface separating the two media. As the angle ϕ (see Fig. 1.2) of incidence in the highest refractive index region increases, the angle of refraction of the lower refractive index region increases too. At a certain angle ϕ_c, the angle of refraction becomes $\pi/2$, this angle ϕ_c is the critical angle for total reflection.

When the angle of incidence ϕ is below the critical angle ϕ_c the light ray is not guided, part of the ray continues its propagation in the outer cladding medium. If the angle of incidence ϕ exceeds the critical angle, then the light ray comes back into the same medium after reflection from the interface and it is guided guided by multiple total reflection

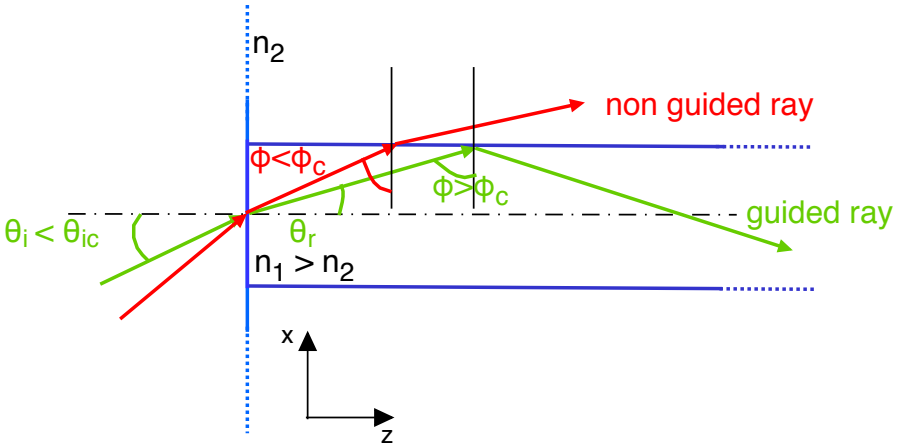

Figure 1.2: Guiding of light (the green ray) by total internal reflection. The angle of incidence of the guided ray is larger than the critical angle, $\phi > \phi_c$.

From Snell refraction law, the critical angle ϕ_c is directly related to the refractive indices n_1 and n_2. This gives

$$n_1 \sin(\phi_c) = n_2 \sin\left(\frac{\pi}{2}\right), \tag{1.1}$$

resulting in the well known expression

$$\phi_c = \sin^{-1}\left(\frac{n_2}{n_1}\right). \tag{1.2}$$

In order to maintain the propagation angle greater than the critical angle, the entrance angle in the waveguide must be less than the angle θ_{ic} corresponding to the critical angle

ϕ_c inside the waveguide. The entrance angle θ_{ic} satisfies the relation

$$\sin(\theta_{ic}) = n_1 \sin(\frac{\pi}{2} - \phi_c) = n_1 \cos(\phi_c) = \sqrt{n_1^2 - n_2^2} \equiv N.A., \tag{1.3}$$

$N.A.$ is called the numerical aperture of the waveguide.

In addition to the condition concerning the internal angles which must be larger than the critical angles, if one considers a specific wavelength of propagation, only rays propagating in direction of some specific angles remain in phase after two reflections on the waveguide interfaces. This is illustrated in Fig. 1.3. These propagation angles are called the mode angles of the waveguide.

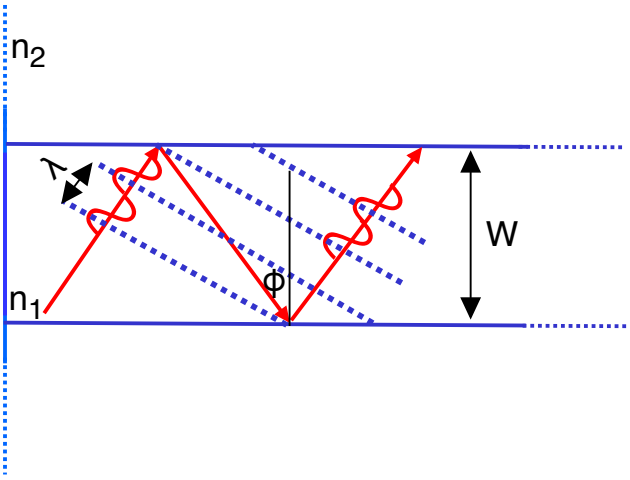

Figure 1.3: The propagation rays must remain in phase after multiple reflections on the waveguide interfaces.

The phase condition after multiple reflections on the interface can be written as follows

$$\frac{2\pi}{\lambda} W n_1 \cos\phi - \varphi = m\pi, \tag{1.4}$$

where λ is the wavelength, W is the waveguide width, φ is the phase shift upon reflection at the core/cladding interface and m is the order of the considered mode. Note that the first term in Eq. (1.4) corresponds to the half phase delay associated to the geometrical retardation after a single zig-zag cycle containing two reflections.
The phase shift upon total reflection is obtained from the Fresnel equations. For a transverse electric (TE) configuration for which the wave electric field has no longitudinal

component, we get

$$\tan\left(\frac{\varphi}{2}\right) = \sqrt{\frac{\cos^2(\phi_c) - \cos^2(\phi)}{\cos^2(\phi)}}. \tag{1.5}$$

By exchanging the place of the terms ϕ and $m\pi$ in Eq. (1.4), dividing the equation by 2, taking the tangent on both sides and inserting Eq. (1.5) one obtains the following transcendent equation

$$\tan\left(\frac{\pi}{\lambda} W n_1 \cos(\phi) - m\frac{\pi}{2}\right) = \sqrt{\frac{\cos^2(\phi_c) - \cos^2(\phi)}{\cos^2(\phi)}}. \tag{1.6}$$

This is the mode equation for a TE waveguide mode and permits to determine the characteristics angle ϕ for a specific mode. Equation (1.6) can be solved numerically or graphically by plotting the two sides of the equation separately, as done in Fig. 1.4, where we have as abscissa $\cos(\phi)$.

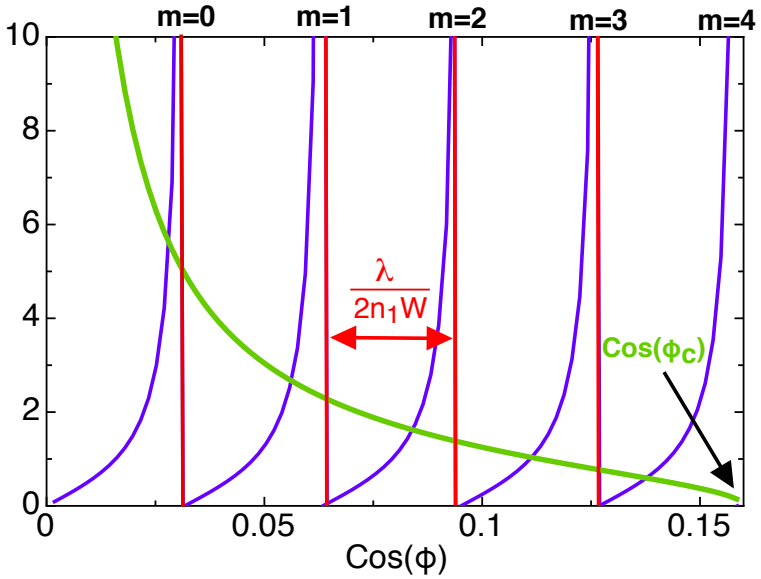

Figure 1.4: The two sides of Eq. (1.6) are plotted as separate functions for different values of m as a function of $\cos(\phi)$. The solid green curve corresponds to the function of the right-hand side of Eq. (1.6) while the solid blue curve corresponds to the tan *function on left-hand side. The intersections of the curves give the solutions of Eq. (1.6).*

In Fig. 1.4, the intersections between the two curves are the solutions of (1.6). The values of ϕ at each intersection allows the calculation of the guided ray's incident angle for that mode.

Until now, we used a "geometrical" analysis to describe and determine the supported modes in an optical guiding structure. This analysis exploits the interference behavior

between the involved rays including a geometrical term associated to the traveled distance and a term associated to the Fresnel phase shift upon total reflection. In order to determine the corresponding mode profiles we must rely on a full wave analysis based on the wave equation in both the core and the cladding of the waveguide. This is done in the next sub-section.

1.2.2 Mode profiles

In a simple view, each mode m can be thought of as a superposition of two plane waves that are either traveling upwards or downwards in the waveguide like the red arrows in Fig. 1.3. The resulting field is given by

$$E(x, z, t) = E_m(x) \exp\left[i\left(\omega t - \beta_m z\right)\right], \tag{1.7}$$

where ω is the frequency and β_m is the propagation constant for the m$^{\text{th}}$ mode. It corresponds to the z-component of the wavevector in the core, that is

$$\beta_m = n_1 k_0 \sin(\phi_m). \tag{1.8}$$

Since the propagation angle is in the range $\phi_c < \phi < \frac{\pi}{2}$, the propagation constant for a given mode is in the range

$$n_2 k_0 = n_1 k_0 \sin(\phi_c) < \beta_m < n_1 k_0 \sin(\frac{\pi}{2}) = n_1 k_0. \tag{1.9}$$

By consequence, the effective index for guided modes defined as $n_{eff} = \beta_m / k_0$ is in the range

$$n_2 < n_{eff} < n_1. \tag{1.10}$$

The effective refractive index is a key parameter in guided propagation just as the refractive index is in unguided wave travel. When the incidence angle tends to zero, rays traveling parallel to the slab (core) have an effective index that is close to the core index n_1. However, when the incidence angle tends to $\frac{\pi}{2} - \phi_c$, the effective index for critical angle approaches n_2.
Now that we have a qualitative understanding of waveguide modes, we calculate the supported modes, which will be characterized by the already discussed propagation constant β_m and their field distribution.

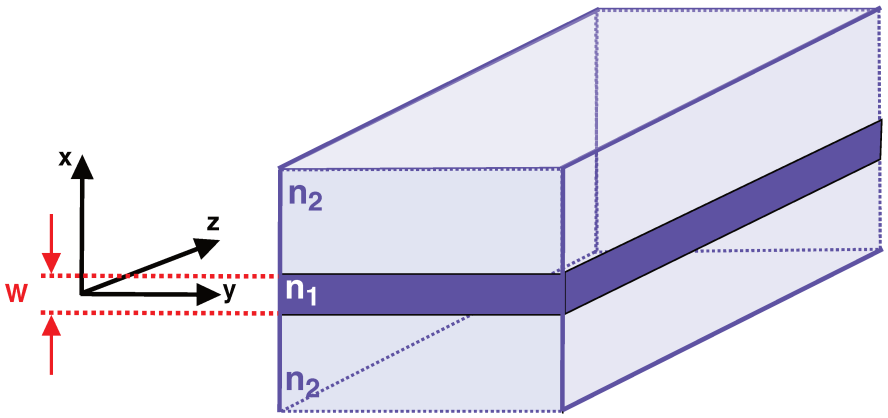

Figure 1.5: Waveguide structure and coordinate system used.

The electric field must satisfy the homogeneous wave equation

$$\nabla^2 \mathbf{E} + k_0^2 n^2 \mathbf{E} = 0. \tag{1.11}$$

Since the waveguide is homogeneous along the z direction, solutions of the wave equation can be taken as in (1.7) in the form

$$\mathbf{E}(x, z, t) = \mathbf{E}_m(x) \exp\left[i\left(\omega t - \beta_m z\right)\right], \tag{1.12}$$

where $\mathbf{E}_m = E_m \cdot \mathbf{e}$, and $\mathbf{e}$ is a unit vector in direction of the electric field. Plugging (1.12) into the wave equation (1.11), it results

$$\frac{\partial^2}{\partial x^2} E + \frac{\partial^2}{\partial z^2} E + k_0^2 n_i^2 E = 0, \tag{1.13}$$

which gives

$$\frac{\partial^2}{\partial x^2} E + \left(k_0^2 n_i^2 - \beta_m^2\right) E = 0. \tag{1.14}$$

Here n_i is either n_1 or n_2 depending on the region we are defining the field in.
For the fields in the core region ($|x| < \frac{W}{2}$) $n_i = n_1$ and the solution of Eq. (1.14) is

$$E_m(x) = A \sin\left(h_m x\right) + B \cos\left(h_m x\right), \tag{1.15}$$

where

$$h_m \equiv \sqrt{k_0^2 n_1^2 - \beta_m^2}, \tag{1.16}$$

is the modulus of the transverse wave vector. For the fields in the cladding region ($|x| > \frac{W}{2}$), the solution is of the form

$$E_m = A \exp\left[\gamma_m x\right] + B \exp\left[-\gamma_m x\right], \tag{1.17}$$

where

$$\gamma_m = \sqrt{\beta_m^2 - k_0^2 n_2^2}, \tag{1.18}$$

is the extinction factor, it specifies the rate at which the field decays with distance x, away from the core. The total electric field of the mode is then of the form

$$E_m = \begin{cases} A \sin\left(h_m x\right) + B \cos\left(h_m x\right) & |x| \leq \frac{W}{2} \\ C \exp\left[-\gamma_m x\right] & x > \frac{W}{2} \\ D \exp\left[\gamma_m x\right] & x < -\frac{W}{2}. \end{cases} \tag{1.19}$$

The quantities A, B, C, and D are constants to be determined by applying the boundary conditions. Since the latter depends on the vectorial quantities, we will break up the mode into two orthogonal polarization cases. A Transverse Electric (TE) polarization for which the electric field vector $\boldsymbol{E}$ is in the y-direction while the magnetic field vector $\boldsymbol{H}$ has both x and z components and a Transverse Magnetic (TM) polarization for which the magnetic field vector $\boldsymbol{H}$ is in the y-direction and the electric field vector $\boldsymbol{E}$ has both x and z components.

1.2.2.1 TE modes

As said above, the electric field for TE polarization is parallel to the y-direction and does not possess any component in the longitudinal z-direction, it is given by

$$E_{y,m} = \begin{cases} A \sin\left(h_m x\right) + B \cos\left(h_m x\right) & |x| \leq \frac{W}{2} \\ C \exp\left[-\gamma_m x\right] & x > \frac{W}{2} \\ D \exp\left[\gamma_m x\right] & x < -\frac{W}{2}. \end{cases} \tag{1.20}$$

The boundary conditions are that the tangential components of the electric field vector $\mathbf{E}$ and the magnetic field vector $\mathbf{H} = \frac{1}{-i\omega\mu}\nabla \times \boldsymbol{E}$ are equal across the boundary between the medium with refractive index n_1 and the medium with refractive index n_2. Applying these boundary conditions at $x = -\frac{W}{2}$ and at $x = \frac{W}{2}$ and for a fixed mode, we deduce the following relations

$$2A\sin\left(\frac{h_m W}{2}\right) = (C-D)\exp\left[-\frac{\gamma_m W}{2}\right] \tag{1.21}$$

$$2h_m A\cos\left(\frac{h_m W}{2}\right) = -\gamma_m(C-D)\exp\left[-\frac{\gamma_m W}{2}\right] \tag{1.22}$$

$$2B\cos\left(\frac{h_m W}{2}\right) = (C+D)\exp\left[-\frac{\gamma_m W}{2}\right] \tag{1.23}$$

$$2h_m B\sin\left(\frac{h_m W}{2}\right) = \gamma_m(C+D)\exp\left[-\frac{\gamma_m W}{2}\right] \tag{1.24}$$

In the case of a symmetric waveguide as shown in Fig. 1.5 ($A = 0$ and $C = D$), from the boundary conditions (E_y and $H_z = \frac{\partial}{\partial x}E_y$ are continuous at $x = \frac{W}{2}$), we obtain

$$h_m \tan(\frac{h_m W}{2}) = \gamma_m, \tag{1.25}$$

where

$$h_m^2 + \gamma_m^2 = k_0^2(n_2^2 - n_1^2). \tag{1.26}$$

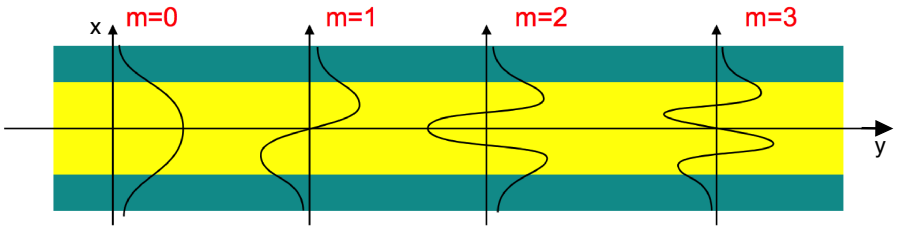

Figure 1.6: The electric field distribution for the first four modes.

The typical transverse field distribution for the first four modes is depicted in Fig. 1.6.

1.2.2.2 TM modes

We can repeat the whole process to establish the solutions for the transverse magnetic (TM) configuration in which the magnetic field vector **H** is parallel to the y-direction and does not possess any component in the longitudinal z-direction. We obtain

$$H_{y,m} = \begin{cases} A\sin(h_m x) + B\cos(h_m x) & |x| \le \frac{W}{2} \\ C\exp[-\gamma_m x] & x > \frac{W}{2} \\ D\exp[\gamma_m x] & x < -\frac{W}{2}. \end{cases} \tag{1.27}$$

The application of boundary conditions on the magnetic field **H** which its tangential component should be equal across the boundary, gives the following eigen equations

$$h_m \tan(\frac{h_m W}{2}) = \frac{n_1^2}{n_2^2}\gamma_m, \tag{1.28}$$

By combining the geometrical approach and the approach based on the electromagnetic analysis, we have seen the condition to be satisfied for the propagation of an optical wave in a dielectric planar waveguide. When we have more than one waveguide, placed close to each other, the wave propagating in one waveguide can act as a source for a second wave propagating in a neighboring waveguide. To describe this interaction and its consequences on the energy exchange, we introduce the coupled mode theory in Sec. 1.3.

1.3 Coupled optical waveguides

1.3.1 Introduction

In the preceding section, we have described how to calculate the TE and TM modes of a dielectric planar waveguide with step index. In this section, we present the coupled mode theory which is of great importance to understand how the lightwave is interacting in two copropagating light beams in adjacent waveguides. Great attention is given to the mode coupling coefficients and to the propagation constants. Their strong importance to predict energy exchange among the waveguides will become clear in the following.
The coupled mode theory for optical waveguides was developed by Snyder [47], Marcuse [48], Yariv [49], and Kogelnik [50] in the early 1970's. It has since been applied to a vast number of guided wave, optoelectronic, and optical fiber devices, such as, directional couplers made of thin film and channel waveguides [51, 52, 53], fiber couplers, or distributed feedback lasers [50, 54].
It is worth mentioning that the closely related coupled wave theory has also been very useful for understanding non linear optical wave propagation and interaction, such as second harmonic generation [55], parametric amplification [56], and modulation instability [57].
The physical models for coupled waveguide systems consist of two or more dielectric waveguides placed in close proximity. These waveguides may be parallel to each other or have a variable separation. Their refractive index contrast can be identical or different or even variable along the propagation direction. In these optically coupled waveguides, the power is transfered in a coherent fashion so that the direction of propagation is maintained for the input traveling wave and the output traveling wave. The analysis of coupled-waveguide systems is based on the modes of the individual, or uncoupled, waveguides. Once these waveguides modes, i.e., their propagation constants and field patterns are determined, the amplitudes of the modes in the coupled-waveguide systems are governed by the coupled mode equations. . The latter are obtained from Maxwell's equations in a perturbative approach. The following subsection gives mathematical expression of the coupling length and the one of the coupling coefficient. In addition to these two important parameters, the propagation constant of the waveguides plays a crucial role in energy transfer between waveguides. This property is at the core of the analogies between waveguides optics and

discrete quantum systems that will be treated in this work.

1.3.2 Modes coupling in optical waveguides

1.3.2.1 Derivation of coupled mode equation in two waveguides

If two waveguides are placed close to each other as shown in figure. 1.7, the optical modes of the waveguides either couple or interfere with each other. The characteristics of this coupling can be analyzed using the perturbation theory [58].
The simplest model of a coupled-waveguide system is the directional coupler which consists of two parallel waveguides in close proximity (figure. 1.7). The two waveguides can have different properties (refractive index distributions, widths, etc) but after identical waveguides are considered. The propagating mode of one of the waveguides has an evanescent part which extends to the neighbor waveguide and excites the mode of the second waveguide. By consequence, the optical coupling results from the mutual interaction of these evanescent fields. When the overlap between the evanescent fields is important the coupling is important too. In what follows, we present the conventional coupled mode theory which describes coupled waveguide systems in an intuitive and simple way. The formulations are general and expected to be valid under the weak coupling assumption [49].

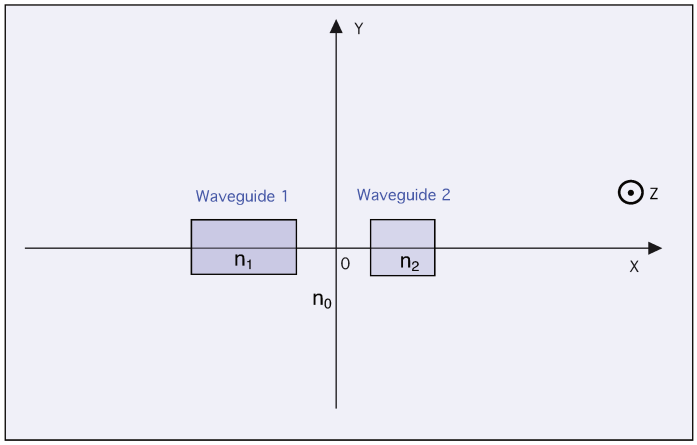

Figure 1.7: Model of co-directional coupler structure composed of two parallel waveguides with different distributions of the refractive index and different widths.

The eigenmodes in each waveguide taken individually are $\tilde{\mathbf{E}}_\mathbf{p}$, $\tilde{\mathbf{H}}_\mathbf{p}$ (p=1,2) satisfy the Maxwell's equations

$$\begin{aligned} \nabla \times \tilde{\mathbf{E}}_\mathbf{p} &= -i\omega\mu_0 \tilde{\mathbf{H}}_\mathbf{p}, \\ \nabla \times \tilde{\mathbf{H}}_\mathbf{p} &= -i\omega\varepsilon_0 n_p^2 \tilde{\mathbf{E}}_\mathbf{p}, \end{aligned} \tag{1.29}$$

where $n_p(x, y)$ represents the refractive index distribution of each waveguide. When the modes are coupled, the electromagnetic fields of the coupled waveguides are expressed as a superposition of the eigenmodes in each waveguide

$$\begin{aligned} \tilde{\mathbf{E}} &= A(z)\tilde{\mathbf{E}}_{\mathbf{1}} + B(z)\tilde{\mathbf{E}}_{\mathbf{2}}, \\ \tilde{\mathbf{H}} &= A(z)\tilde{\mathbf{H}}_{\mathbf{1}} + B(z)\tilde{\mathbf{H}}_{\mathbf{2}}. \end{aligned} \tag{1.30}$$

Substituting Eq. (1.30) into Eq. (1.29), we obtain

$$\begin{aligned} (u_z \times \tilde{\mathbf{E}}_{\mathbf{1}})\frac{dA(z)}{dz} + (u_z \times \tilde{\mathbf{E}}_{\mathbf{2}})\frac{dB(z)}{dz} = 0, \\ (u_z \times \tilde{\mathbf{H}}_{\mathbf{1}})\frac{dA(z)}{dz} - i\omega\varepsilon_0(n^2 - n_1^2)A(z)\tilde{\mathbf{E}}_{\mathbf{1}} + (u_z \times \tilde{\mathbf{H}}_{\mathbf{2}})\frac{dB(z)}{dz} - i\omega\varepsilon_0(n^2 - n_2^2)A(z)\tilde{\mathbf{E}}_{\mathbf{2}} = 0, \end{aligned} \tag{1.31}$$

where u_z is unit vector defining the propagation direction. By separating the transverse and the axial dependencies of the electromagnetic fields and taking the fields of the form

$$\begin{aligned} \tilde{\mathbf{E}}'_{\mathbf{p}} &= \tilde{\mathbf{E}}_{\mathbf{p}} \exp\left[-i\beta_p z\right], \\ \tilde{\mathbf{H}}'_{\mathbf{p}} &= \tilde{\mathbf{H}}_{\mathbf{p}} \exp\left[-i\beta p z\right], \end{aligned} \tag{1.32}$$

we obtain the following equations

$$\frac{dA(z)}{dz} + \kappa_{12}\frac{dB(z)}{dz}\exp\left[-i(\beta_2 - \beta_1)z\right] + i\chi_1 A(z) + iC_{12}B(z)\exp\left[-i(\beta_2 - \beta_1)z\right] = 0, \tag{1.33}$$

$$\frac{dB(z)}{dz} + \kappa_{21}\frac{dA(z)}{dz}\exp\left[i(\beta_2 - \beta_1)z\right] + i\chi_2 B(z) + iC_{21}A(z)\exp\left[i(\beta_2 - \beta_1)z\right] = 0, \tag{1.34}$$

where

$$C_{pq} = \frac{\omega\varepsilon_0 \int_{-\infty}^{+\infty}\int_{-\infty}^{+\infty}(n^2 - n_q^2)E_p^* E_q dxdy}{\int_{-\infty}^{+\infty}\int_{-\infty}^{+\infty} u_z.(E_p^* \times H_p + E_p \times H_p^*)dxdy}, \tag{1.35}$$

$$\kappa_{pq} = \frac{\omega\varepsilon_0 \int_{-\infty}^{+\infty}\int_{-\infty}^{+\infty}(E_p^* H_q + E_q H_p^*)dxdy}{\int_{-\infty}^{+\infty}\int_{-\infty}^{+\infty} u_z.(E_p^* \times H_p + E_p \times H_p^*)dxdy}, \tag{1.36}$$

$$\chi_p = \frac{\omega\varepsilon_0 \int_{-\infty}^{+\infty}\int_{-\infty}^{+\infty}(n^2 - n_p^2)E_p^* E_p dxdy}{\int_{-\infty}^{+\infty}\int_{-\infty}^{+\infty} u_z.(E_p^* \times H_p + E_p \times H_p^*)dxdy}. \tag{1.37}$$

The pair p and q are either (p,q)=(1,2) or (2,1). C_{pq} is a mode coupling coefficient (coupling constant) of the directional coupler. Along the propagation, the modes are interacting and from this interaction results the evolution of their amplitudes. The coefficient C_{pq} is related to the modes distribution overlap (see Fig. 1.9). The stronger is the overlap between the modes distribution is , the larger will be the coupling coefficient. The meaning of κ_{pq} is described as follows. Let us consider the waveguide configuration shown in Fig. 1.8, where waveguide 1 (WG1) exists only in the region $z < 0$ and waveguide 2 (WG2) in $z \geq 0$. When the eigenmode $(\tilde{E}_1, \tilde{H}_1)$ of WG1 propagates from the negative z-direction to $z = 0$, the electromagnetic field in the cladding excites the eigenmode $(\tilde{E}_2,\tilde{H}_2)$ at the point $z = 0$. This excitation efficiency is considered to be κ_{12}. Therefore, κ_{pq} represents the butt coupling coefficient between the two waveguides [59, 60] and it quantifies the excitation efficiency.
In most of the conventional analyses of the directional couplers, κ_{pq} and χ_p were neglected and they are assumed to be $\kappa_{pq} = \chi_p = 0$ during all the analysis in chapters 3 and 4 while in chapter 5 the used numerical method takes it into account. However, both κ_{pq} and χ_p should be taken into account in order to analyze the mode coupling effect strictly.

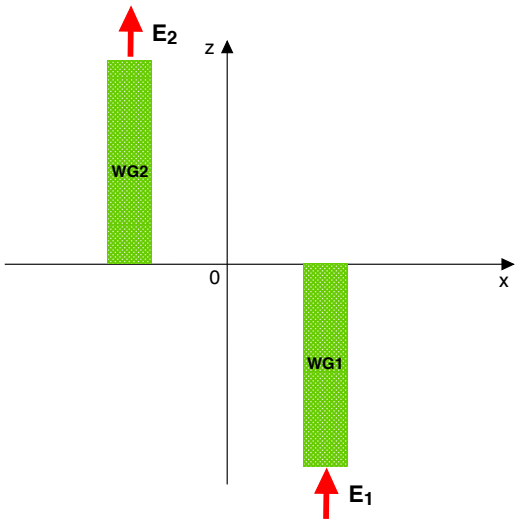

Figure 1.8: Two optically coupled waveguides illustrating the butt coupling coefficient κ_{12}.

The optical power carried by the eigenmode in the waveguide p (p=1,2) is expressed with the help of the spatially integrated Poynting vector

$$P_p = \frac{1}{2} \int_{-\infty}^{+\infty} \int_{-\infty}^{+\infty} u_z \cdot (\mathbf{E_p} \times \mathbf{H_p}^*) dx dy. \tag{1.38}$$

In the equations (1.35)-(1.37), the denominators are equal to $4P_p$. Henceforth, we assume

that the eigen modes in both waveguides are normalized to satisfy the condition

$$\int_{-\infty}^{+\infty}\int_{-\infty}^{+\infty} u_z \cdot (\mathbf{E_p}^* \times \mathbf{H_p} + \mathbf{E_p} \times \mathbf{H_p}^*) dxdy = 4P_p = 1. \tag{1.39}$$

By neglecting κ_{pq} and χ_p, the equations (1.33) and (1.34) become

$$\frac{dA(z)}{dz} + iC_{12}B(z)\exp\left[-i(\beta_2 - \beta_1)z\right] = 0, \tag{1.40}$$

$$\frac{dB(z)}{dz} + iC_{21}A(z)\exp\left[i(\beta_2 - \beta_1)z\right] = 0. \tag{1.41}$$

To see the overlap between the evanescent fields of the fundamental modes for two identical coupled waveguides, consider the situation shown in Fig. 1.9

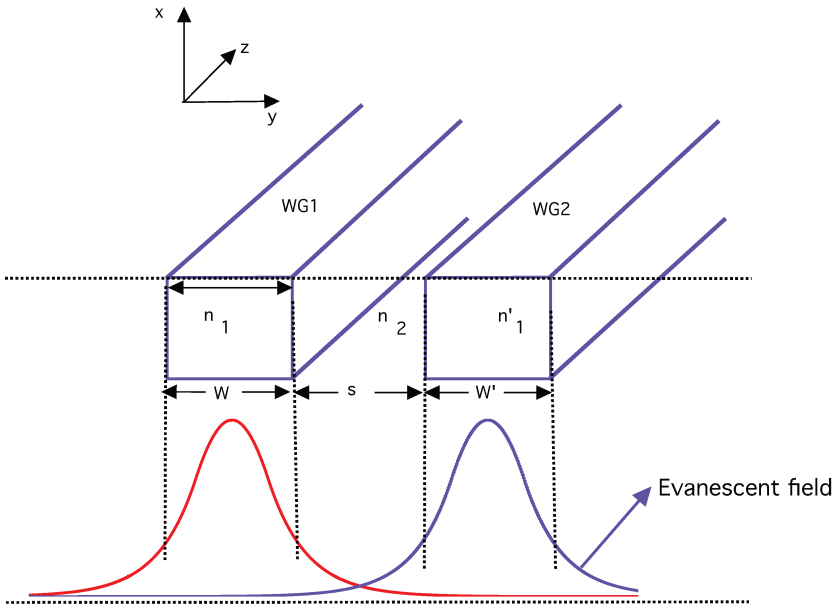

Figure 1.9: Diagram of a dual-channel directional coupler. The amplitudes of the electric field distributions for the fundamental mode of each waveguide are plotted.

Eqs. (1.40)-(1.41) can be written as

$$\begin{aligned} \frac{dA(z)}{dz} &= -iC_{12}B(z)\exp\left[-i\Delta\beta z\right] \\ \frac{dB(z)}{dz} &= -iC_{21}A(z)\exp\left[i\Delta\beta z\right], \end{aligned} \tag{1.42}$$

where $\Delta\beta = \beta_2 - \beta_1$ is the phase mismatch between the waveguides. The exponential term in (1.42) can be removed by making the transformation $\tilde{A}(z) = A(z)\exp\left[i\Delta\beta z/2\right]$

and $\tilde{B}(z) = B(z)\exp\left[-i\Delta\beta z/2\right]$, Eq. (1.42) becomes

$$\begin{aligned}\frac{d\tilde{A}(z)}{dz} &= -iC_{12}\tilde{B}(z) + i\frac{\Delta\beta}{2}\tilde{A}(z),\\ \frac{d\tilde{B}(z)}{dz} &= -iC_{21}\tilde{A}(z) - i\frac{\Delta\beta}{2}\tilde{B}(z),\end{aligned} \tag{1.43}$$

The quantities C_{12} and C_{21} are the coupling coefficients. Their expressions are given by Eq. (1.35). For identical waveguides, the reciprocity relation of the coupling coefficients is

$$C_{12} = C_{21}^{*} \tag{1.44}$$

In most of the directional couplers C_{pq} is real, therefore, $C_{12} = C_{21} = C$. This approximation corresponds to the orthogonal coupled-mode formulation which states that the coupling coefficients are symmetrical regardless of the difference of β_p [61].
The solutions of Eq. (1.42) are assumed in the forms

$$\begin{aligned}A(z) &= \left(a_1 e^{i\delta z} + a_2 e^{-i\delta z}\right)\exp[-i\frac{\Delta\beta}{2}z]\\ B(z) &= \left(b_1 e^{i\delta z} + b_2 e^{-i\delta z}\right)\exp[i\frac{\Delta\beta}{2}z]\end{aligned} \tag{1.45}$$

where δ is a parameter to be determined. a_1, a_2, b_1, and b_2 are constants given by initial conditions,

$$\begin{aligned}a_1 + a_2 &= A(z=0)\\ b_1 + b_2 &= B(z=0)\end{aligned} \tag{1.46}$$

By substituting Eq. (1.45) into the coupled-mode equation (1.42) and applying the initial conditions, we get

$$\begin{aligned}A(z) &= \left\{\left[\cos(\delta z) + i\frac{\Delta\beta}{2\delta}\sin(\delta z)\right]A(0) - i\frac{C}{\delta}\sin(\delta z)\,B(0)\right\}\exp\left[-i\frac{\Delta\beta}{2}z\right]\\ B(z) &= \left\{-i\frac{C}{\delta}\sin(\delta z)\,A(0) + \left[\cos(\delta z) - i\frac{\Delta\beta}{2\delta}\sin(\delta z)\right]B(0)\right\}\exp\left[i\frac{\Delta\beta}{2}z\right],\end{aligned} \tag{1.47}$$

with δ being given by

$$\delta = \sqrt{C^2 + \left(\frac{\Delta\beta}{2}\right)^2}. \tag{1.48}$$

We assume that all the optical intensity is initially injected only into waveguide 1 at $z = 0$. In this case $A(0) = A(z=0) = A_0$ and $B(0) = B(z=0) = 0$. Then, the optical intensity

evolution along z-direction is given by

$$I_1(z) = 1 - \left(\frac{C}{\delta}\right)^2 \sin^2(\delta z)$$
$$I_2(z) = \left(\frac{C}{\delta}\right)^2 \sin^2(\delta z)\,. \tag{1.49}$$

A qualitative explanation of the power exchange between the two waveguides can be given relying on Eq. (1.48) and we discuss two limiting cases.

(a) When $\Delta\beta >> C$ the coupling is weak and then the quantity C/δ tends to zero. Consequently, all the intensity initially injected in waveguide 1 remains in the same waveguide as seen in Fig. 1.10(b). There is only little exchange of power between the two waveguides.

(b) When $\Delta\beta << C$, C/δ tends to 1 and there is a strong exchange of power between the waveguides (see figure. 1.10(a)). The light oscillates between the waveguides along the propagation distance δz.

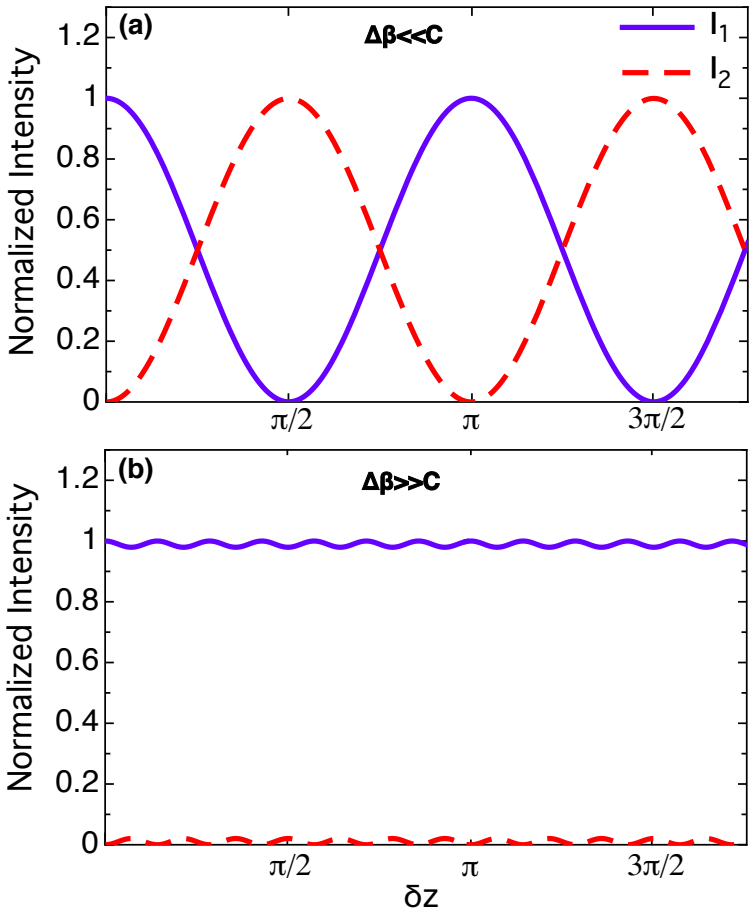

Figure 1.10: Variation of intensities in the directional coupler. (a) represents the case where $\Delta\beta << C$, in this case there is periodic exchange of energy between the two waveguides. (b) shows the case of $\Delta\beta >> C$, the energy exchange is inhibited and the light remains in waveguide 1.

The power-coupling efficiency from the input waveguide 1 to waveguide 2 reaches its maximum at $z = \frac{\pi}{2\delta}(2l+1)$, $(l = 0, 1, ...)$. The length z at $l = 0$ is called the coupling length, it is written as

$$L_c = \frac{\pi}{2\delta} = \frac{\pi}{2\sqrt{C^2 + \left(\frac{\Delta\beta}{2}\right)^2}}. \tag{1.50}$$

When the propagation constants of the two waveguides are identical ($\beta_1 = \beta_2$, $\Delta\beta = 0$), all the power integrally is transferred at the coupling length of

$$L_c = \frac{\pi}{2C}. \tag{1.51}$$

The variations of the coupling length according to the coupling constant C and the detuning $\Delta\beta$ is shown in Fig. 1.11

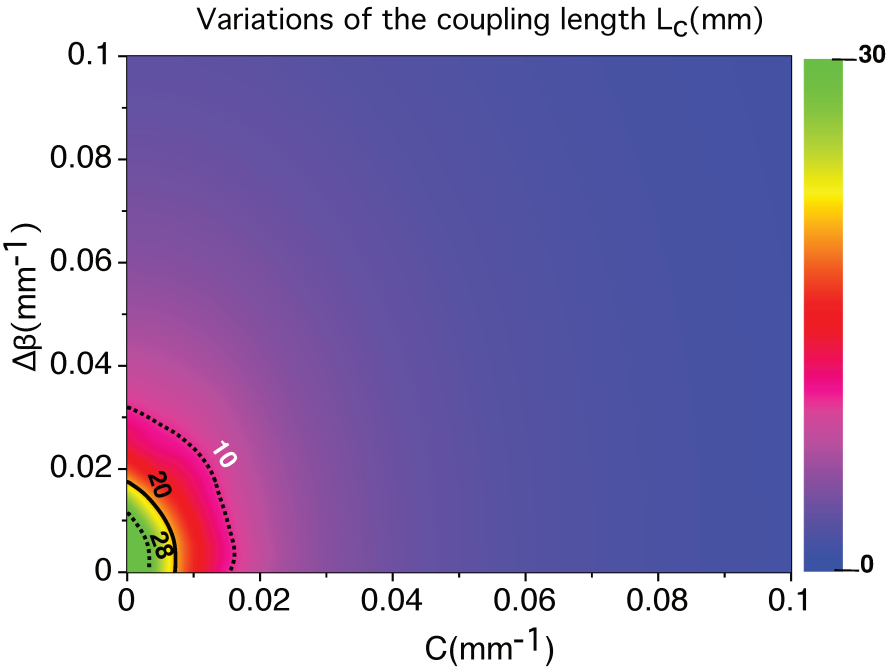

Figure 1.11: Coupling length dependence on the coupling constant C and the detuning $\Delta\beta$.

As depicted on Fig. 1.11, for small values of the coupling constant C, the coupling length L_c increases when $\Delta\beta$ decreases. For high values of the coupling constant C compared to $\Delta\beta$, the coupling length L_c depends mainly on C and very little on $\Delta\beta$.

For perfectly identical waveguides ($C_{12} = C_{21}$ and $\Delta\beta = 0$), Eq. (1.42) becomes

$$\begin{aligned} \frac{dA(z)}{dz} &= -iCB(z) \\ \frac{dB(z)}{dz} &= iCA(z), \end{aligned} \tag{1.52}$$

where C is the coupling constant. It is possible in this case to find an analytical expression for C in the "tight binding" approximation, for which the extension of the modes amplitude outside the core of the waveguide is not too large [49] is given by

$$C = \frac{2h_m^2\gamma_m}{\beta_m(W + 2/\gamma_m)(h_m^2 + \gamma_m^2)} e^{-\gamma_m s}. \tag{1.53}$$

Here h_m is the modulus of the transverse wave vector for the mth mode, γ_m is the extinction constant, it gives the rate at which the field decays with the transverse distance, β_m is the propagation constant, W is the waveguide width, and s is the separation distance (border to border) between the waveguides. The dominant term in the above coupling constant expression is the exponential term in which appears the the extinction coefficient γ_m and the separation distance s, C decreases exponentially with s.

The coupling constant is a key parameter in transfer and control of light through waveguides. It depends on physical properties of the waveguides. In the next section, we discuss its variations as a function of various waveguide parameters.

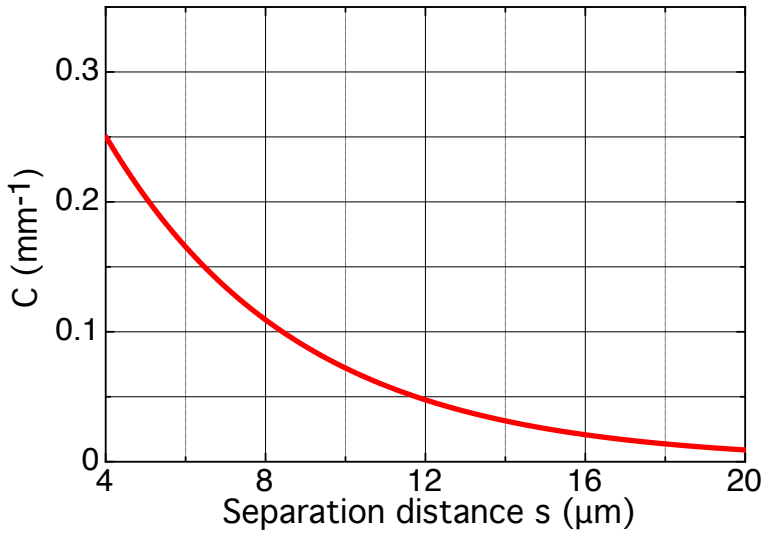

Figure 1.12: Coupling constant dependence on the waveguides separation distance s showing the exponential decrease with s. Waveguides parameters : waveguide width W= 7 µm, $\Delta n = 2 \cdot 10^{-4}$, $\lambda = 633$ nm.

When the waveguides are very close to each other, the evanescent waves overlap is important leading to a strong coupling constant. However, when the distance separating

the waveguides becomes bigger, this overlap between the evanescent fields of each waveguide decreases and by the consequence the coupling constant becomes weaker as Fig. 1.12 shows.

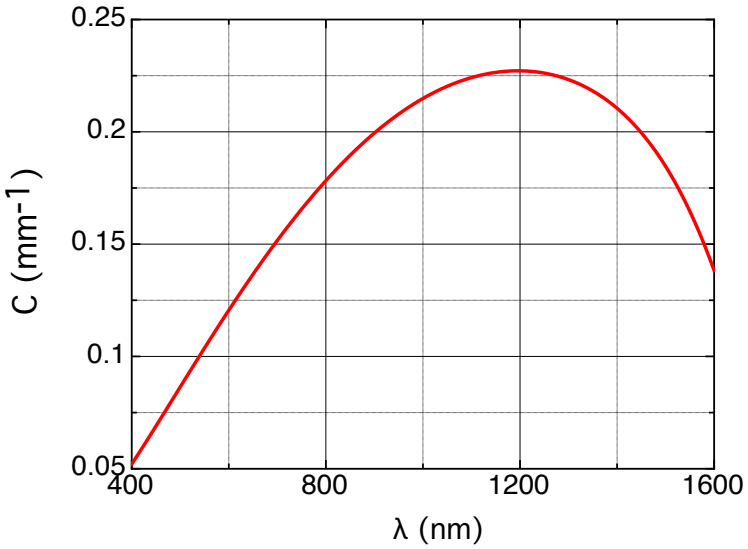

Figure 1.13: Coupling coefficient as a function of wavelength. The waveguide width W= 7 µm, $\Delta n = 2 \cdot 10^{-4}$, *and the separation distance is fixed to* $s = 7$ µm.

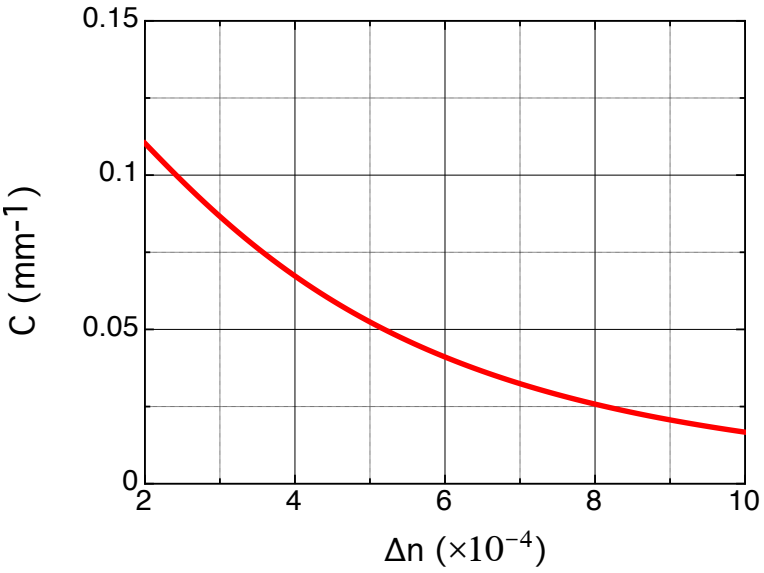

Figure 1.14: Coupling constant dependence on the refractive index Δn. *Waveguide parameters : waveguide width* W= 7 µm, *separation distance* s= 7 µm, $\lambda = 633$ nm.

When the wavelength increases, the guided mode gets less confined due to its natural tendency to exhibit a strong diffraction. This leads to smaller values for the extinction factor γ_m and consequently the coupling constant increases as seen in Fig. 1.13. The decrease

seen at the longest wavelengths is due to the failure of the tight-binding approximation at these wavelengths due to the looser mode confinement. Finally, when the refractive index contrast is large, the guided mode is more confined and the evanescent wave does not overlap much with the neighboring waveguide. In this case the extinction factor γ_m is increasing with increasing Δn and the coupling constant is therefore a decreasing function of Δn, as Fig. 1.14 shows.

1.3.2.2 Coupled mode theory in waveguide array

In the previous section, we have discussed about evanescent light coupling among two waveguides. We have recalled the differential equations satisfied by the mode amplitudes and have discussed the various dependencies of the coupling coefficient. In this section, we give briefly the coupled modes equations in the case of a multi waveguide structure, as well as their solutions.
Let us consider an infinite array of planar identical waveguides positioned with equal separations between each other so that the coupling constants between them are equal (see Fig. 1.15).

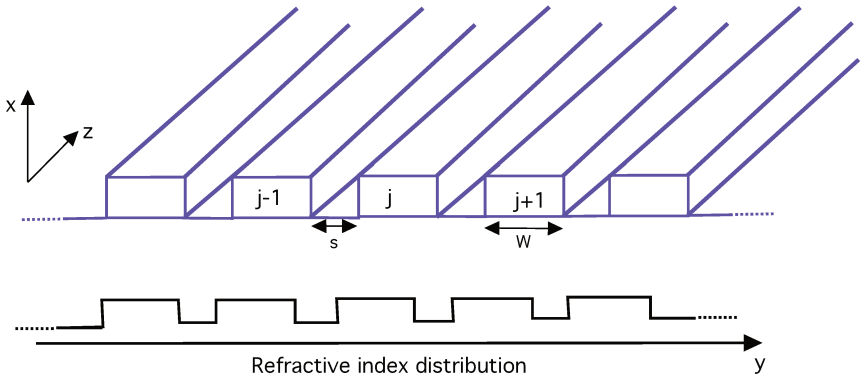

Figure 1.15: Array of coupled and identical optical waveguides.

In this system all the waveguides support the same fundamental and transverse electric optical mode, and energy can be exchanged between neighboring guides through the overlap of their modes. The optical coupled-mode set of equations for the mode amplitude A_n in the n^{th} waveguide is [61, 62]

$$i\frac{dA_n}{dz} = -C(A_{n-1} + A_{n+1}), \tag{1.54}$$

where C is the coupling constant and β is the propagation constant. The equation (1.54) is a generalization of the equation (1.52) with phase synchronism between the coupled modes. The infinite set of these ordinary differential equations is analytically integrable [63]. The solution for the n^{th} waveguide, when only one waveguide is excited, is a set of Bessel functions. If we set $A_n = A_0$ for $n = 0$ and $A_{i\neq n} = 0$ for $n \neq 0$ at $z = 0$,

$$A_n(z) = i^n J_n(2Cz)A_0, \tag{1.55}$$

where $J_n(x)$ is the Bessel function of first kind of order n.

We can simulate a structure composed of multiple waveguides, where all the waveguides possess the same properties (refractive index contrast, width, ...) and the mutual separation distance is constant. Initially, the wave is injected in the central waveguide. Along the propagation distance, the light experiences "discrete diffraction" and moves towards the outer waveguides. The stronger the coupling, the further the light will move from the central input waveguide ($n = 0$). Figure. 1.16 shows the light intensity evolution along the propagation distance.

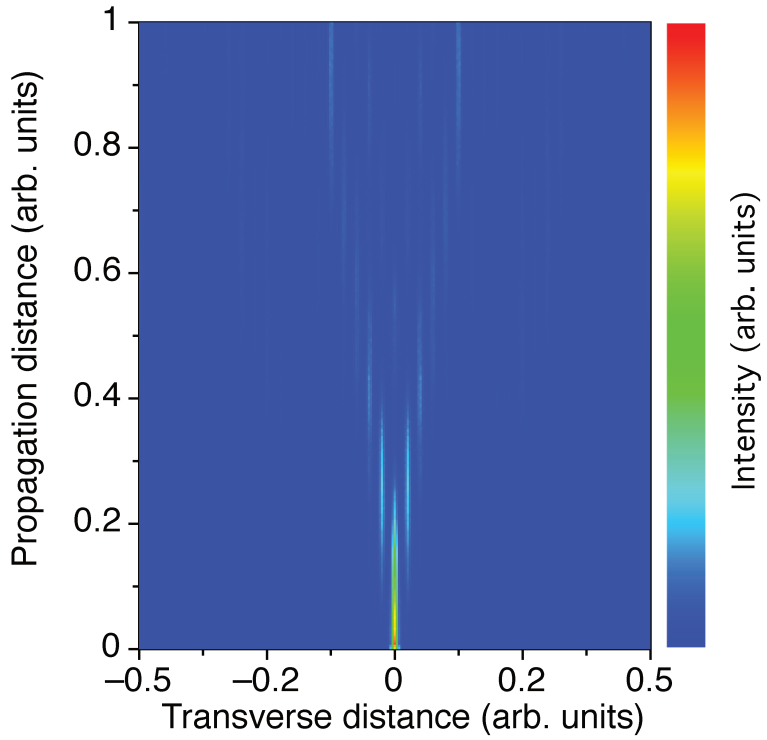

Figure 1.16: Simulation of a diffracted wave in an array of waveguides. The light is initially injected in the central waveguide.

As the beam propagates, the maximum intensity is clearly located in two main lobes that are moving away from the central waveguide. This is a striking difference compared

to bulk media in which upon diffraction the maximum intensity is always located in the center of the beam.

1.4 Conclusion

In this chapter, we have recalled the main features of guided wave theory and light coupling among dielectric waveguides. According to established theory, only some discrete values of the incident angle ϕ, of the transverse wavevector h_m, and of the propagation constant β_m are possible. These discrete values define the guided modes of the waveguide. Using an electromagnetic analysis, the solution of Helmholtz equation describing the field evolution in the waveguide is obtained. The form of the field depends on the regions defining the guiding structure; a spatially oscillating field is obtained in the core while an exponentially decaying field exists in the cladding. The evanescent field in the cladding constitutes the part which is mainly responsible of the optical coupling if another waveguide is placed nearby.
This optical coupling is studied in the second part of the chapter. It was illustrated using two parallel optical waveguides whose fields interact by means of their evanescent fields. The derivation based on Maxwell's equations leads to the establishment of the coupled mode equations which contain two key parameters ; the coupling constant C_{pq} and the phase mismatch $\Delta\beta$ reflecting the difference in longitudinal propagation constants. As has been demonstrated, these parameters are crucial to control the energy transfer from one waveguide to an other in a given optical structure.

Understanding the fundamentals of guiding light in optical waveguides is important with respect to the experiments that will follow. The presented basics give guidance for the design, generation, and exploitation of optical guiding structures under variation of the main parameters C and $\Delta\beta$.

2 Light induced photorefractive waveguides

Contents

2.1 Introduction

This chapter presents the non linear optical tools for the generation of light induced waveguides. The induced structures will serve for light guiding and demonstration of some quantum-optical analogies that will be presented in the next chapter. The linear electro-optic effect is presented and conjointly its role in the refractive index modulation. Then, the photorefractive process is exposed and interpreted in the framework of the conventional model of Kukhtarev. The formation of the space charge field, which is the key element in this process, as well as the experimental setup and the lateral illumination technique used in the experiments are presented in detail. This technique is applied to $Sr_xBa_{1-x}Nb_2O_6$ (SBN) crystal with $x = 0.61$, which possesses strong photorefractive and electro-optic properties. This crystal is the one used for all the experiments. Different guiding structures will be generated using this technique and their shape and role will depend on the wished light output intensity. These structures are generally associated to a given analogy with discrete quantum processes. Two parameters strongly involved on the demonstrations of the analogies are the coupling constant and the refractive index contrast, at the end of this chapter these two parameters are experimentally characterized. Their characterization will be useful for the design of robust and achromatic structures.

2.2 The linear electro-optic effect

The application of an electric field [64] to an acentric crystal provokes the displacement of the ionic constituents to locations determined by the external field strength, the charge on the ions, and the restoring force [65]. The external electric field induces changes in the anisotropy and this change can be seen in terms of the modification of the principal refractive index. This modification can be described to first order for crystals that do not present an inversion of symmetry. In other words, the refractive index modifications are linearly proportional to the applied electric field and the crystal exhibits the linear electrooptic effect also known as Pockels effect. The change of the refractive indices can be described by the change in the tensor of the optical indicatrix $1/(\epsilon)_{ij}$ under an applied electric field $\mathbf{E} = (E_x, E_y, E_z,)$, this change can be expressed using the electro-optic tensor and the applied electric field as

$$\Delta \left(\frac{1}{n^2}\right)_{ij} = \sum_k \mathrm{r}_{ijk} E_k, \tag{2.1}$$

where r_{ijk} is a 3^{rd} rank tensor, its elements r_{ijk} are expressed in meters per volts. The linear electro-optic effect can be interpreted using the polarization induced by the presence of the electric field which on its turn is responsible for modification of the refractive index.

Using the polarization $\mathbf{P}$, one can write

$$\Delta\left(\frac{1}{n}\right)_{ij} = \sum_k f_{ijk} P_k, \tag{2.2}$$

where f_{ijk} are the polarization optical coefficients expressed in m^2/C. As the electric field is related to the polarization by the dielectric tensor ϵ, the tensors r and f are related by the relation

$$r_{ijk} = \epsilon_0 \sum_l f_{ijl}(\epsilon_{lk} - \delta_{lk}), \tag{2.3}$$

where δ_{kl} is the Kronecker delta (=1 for $k = l$, 0 for $k \neq l$). Equation (2.3) shows that a large value of ϵ is of interest to get a large value of r, near phase transitions, we get large r.

The crystal SBN:61 exhibits a phase transition relatively close to room temperature ($T_c \sim 350K$), which is the main reason for the large electro-optic coefficients in this crystal. From Eq. (2.1) and for small variations, the modification of the refractive index is given by [66]

$$\Delta n = -\frac{n^3}{2} r_{eff} E, \tag{2.4}$$

where r_{eff} is the effective electro-optic coefficient associated with the given configuration. For instance, if the field is applied along the $3-axis$ and we are interested in the change of the refractive index for extraordinary polarization parallel to the $3-axis$, the electro-optic coefficient r_{eff} corresponds to r_{333}. The electro-optic effect can be used to modulate the polarization of a propagating light wave in a crystal.

To create waveguides using the electro-optic effect, the material should allow the formation of an internal space-charge field under illumination. This is possible in some photorefractive materials that exhibit the photorefractive effect, which is presented in the next section.

2.3 Photorefractive effect

The photorefractive effect gives rise to a spatial modulation of the refractive index due to charge transport induced by spatially inhomogeneous light intensity as well as the above electro-optic effect. These spatial variations in light intensity are found for instance when two beams of light create an interference pattern. Photorefraction has given rise to several attractive effects such as wave-guiding [67], phase conjugation [68, 69], beam amplification [70], and four wave mixing energy exchange [71]. Also, the effect is useful for several interesting applications like holographic storage, laser beam clean up, optical correlation, or reconfigurable waveguides and switches [37, 72, 73, 74], just to name a few.

The photorefractive effect was first observed by Ashkin and co-workers [75] in samples of $LiTaO_3$ and $LiNbO_3$ crystals. At that time, the effect was considered as highly deleterious to the non linear devices based upon these crystals [76, 77] and the early studies focused on its elimination. It was observed in forms of inhomogeneities of the index of refraction when a focused laser beam shines $LiNbO_3$ and $LiTaO_3$ crystals. These variations were localized along the path of the applied laser light. Shortly afterwards, experiments carried out by Chen and co-workers on KTN [78] showed similar optical damage as in $LiTaO_3$ and $LiNbO_3$. The difference was that in the case of KTN an external electric field was necessary.
In the following section, the standard theory of photorefractive effect using the band-transport model will be presented in some details.

2.3.1 Phenomenological description of the photorefractive effect

We consider the simplest model, where a single donor and trap level between the valence band and the conduction band is considered. The traps are acting as electron donors and the bound electron can be excited in the conduction band by a photon with appropriate energy. Despite of its simplicity, this model gives a good picture on the kind of properties which can be expected from the photorefractive effect in many materials. This model was presented first by Kukhtarev and co-workers [79], we describe it by considering the equations describing the different involved processes.

Figure 2.1 illustrates the main steps associated to the photorefractive charge transport within the above model.

- Photogeneration of charge carriers (step (a) in Fig. 2.1)
- Charge transport (step (b))
- Re-trapping of charge carriers (step (c))
- Once the charges are redistributed, the generated internal electric field leads to a change of refractive index via the Pockels effect discussed in section 2.2.

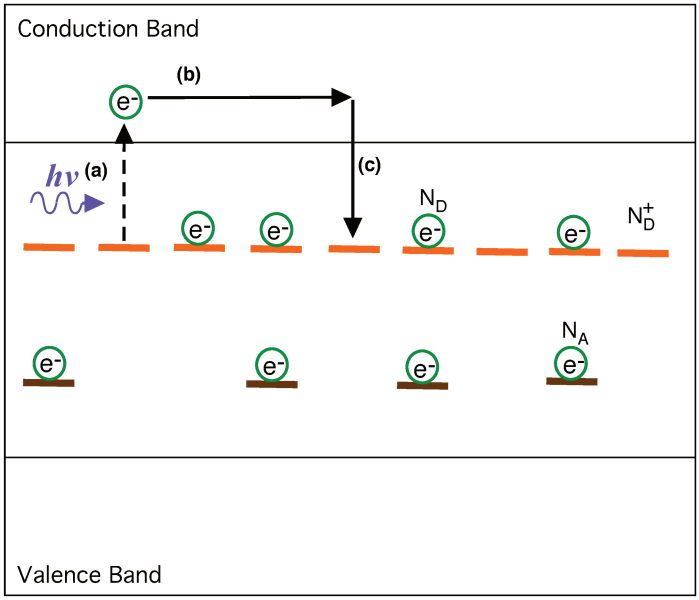

Figure 2.1: Band scheme of a single level photorefractive process. (a) photoexcitation of a trapped electron. (b) charge transport in the conduction band. (c) Retrapping in an empty trap.

In the following, we discuss briefly the three main processes (a), (b), and (c) of Fig. 2.1.

2.3.1.1 Photogeneration of charge carriers, charge transport and retrapping

The conventional photorefractive effect [80] relies on a redistribution of charges due to photo-excitation from a donor level of a dielectric or semiconductor material to the conduction or to the valence band. The mobile state to which the charge carriers are excited is the quasi empty conduction band for electrons or the quasi full valence band for holes. There are mainly two processes involved in the material during the creation of the mobile charge carriers, the photo-excitation of charge carriers which are trapped in defects at some level in the band gap or the direct excitation from the valence band to the conduction band. The energy hν of the incident photon decides which of these mechanisms can take place. If this energy is higher than the band gap energy then all the excitation processes are present simultaneously. In contrast, for photon energy smaller than the band gap energy, the excitation from the valence band to conduction band cannot take place. In the present work we will deal only with this case. Decreasing the photon energy even more, it is possible to exclude at a certain point also the excitation of trapped charge carriers depending on their position in the band gap [1] The photoexcitation process can be

[1]The minimal photon energy needed for exciting a trapped charge carrier cannot be directly related to his position in the energy band scheme due to important contribution from the Franck-Condon shift.

described by the equation

$$\frac{\partial N_D^+}{\partial t} = (s_e I + \beta_e)\left(N_D - N_D^+\right) - \gamma_e n N_D^+, \tag{2.5}$$

where N_D^+ is the concentration of ionized donors, s_e is the photoionization constant for electrons, I is the space dependent illumination light intensity, N_D corresponds to the donor concentration, γ_e represents the recombination constant for electrons, β_e the electronic dark generation rate, and n is the free electron concentration in the conduction band. The first term of the right side of Eq. (2.5) ($(s_e I + \beta_e)(N_D - N_D^+)$) describes the photoionization process and the thermal excitation of electrons from the donor level. The second term takes into account the recombination of electrons (γ_e) into the traps.

The charge transport is driven by electric forces, by diffusion and by the photogalvanic effect [2]. The electric forces are produced by an external applied field and/or by the internal space charge field generated by the charge redistribution. The diffusion is produced by the random walk of the charge carriers as a consequence of their thermal energy.
The key quantities for interpretation of the charge transport are the mobility and the carrier life time. These two properties can be quantified using holographic time-of-flight measurements [81]. With this type of measurements, the dynamics of the excited charge carriers can be determined over several time decades in order to determine the carrier lifetime and the band mobility. The impact of shallow traps on the mobility and charge recombination can then be considered by introducing an effective mobility and an effective recombination rate.
Since the charges in the conduction band are mobile (see process (**b**) in Fig. 2.1) the continuity equation for the electron density in the conduction band contains an additional term proportional to the divergence of the current density $\mathbf{J}_e$ with respect to the two terms already present in Eq. (2.5). The balance equation of the electron density in the conduction band is therefore

$$\frac{\partial n_e}{\partial t} = (s_e I + \beta_e)\left(N_D - N_D^+\right) - \gamma_e n N_D^+ + \frac{1}{e}\nabla \mathbf{J}_e, . \tag{2.6}$$

where the electron current density $\mathbf{J}_e$ is given as

$$\mathbf{J}_e = e n \mu_e \mathbf{E}_{sc} + k_B T \mu_e \nabla n + e s_e I \left(N_D - N_D^+\right) \mathbf{L}_{ph}, \tag{2.7}$$

where $\mathbf{E}_{sc}$ is the space charge field vector, μ_e is the electron mobility tensor, $\mathbf{L}_{ph}$ is the photogalvanic transport length vector, ϵ_0 is the vacuum dielectric permittivity, ϵ_{eff} is the effective dielectric constant that applies to the given configuration, e is the unit charge,

[2] After excitation the charge carrier can show an initial momentum in a preferential direction due to a local asymmetry. This is called the photogalvanic effect and can be used to produce charge separation in an effective way in some crystals.

k_B the Boltzmann constant, and T the absolute temperature.
Equation (2.7) defines the electric current in the conduction band, and has the form of the continuity equation when introduced in Eq. (2.6). The first term gives the drift current in the total electric field $\mathbf{E}_{sc} + \mathbf{E}_0$, where $\mathbf{E}_0$ is the applied electric field. The second term describes the diffusion process of the electrons generated by the electron concentration gradient, it gives a contribution only in the case of an inhomogeneous illumination. The last step in the photorefractive charge transport consists on re-trapping the already excited charge carriers. This re-trapping process can happen in radiative or non radiative way. In all cases the recombination rate is proportional to the number density of free charge carriers and the one of empty traps as seen in Eq. (2.5).

The resulting space-charge internal field is obtained from Gauss equation as

$$\nabla \cdot (\epsilon_0 \epsilon_{eff} \mathbf{E}_{sc}) = e \left(N_D^+ - n - N_A \right), \tag{2.8}$$

The four equations presented above describes the model of Kukhtarev, they are valid for isotropic photoexcitation, *i.e.*, if the photoionization constant s_e is independent on the light polarization.

2.3.1.2 Space charge field description for periodic illumination

A solution of the system of Eqs. (2.5)- (2.8) can be established if the material is illuminated with a periodic intensity distribution,

$$I(\mathbf{x}) = I_0 \left(1 + m \exp\left[i\mathbf{K}\mathbf{x}\right]\right), \tag{2.9}$$

which can be easily obtained by interference of "two plane waves". Here $\mathbf{K}$ is the grating vector ($\mathbf{K}$=$\mathbf{K}/K$), $\mathbf{x}$ is the position vector, and m is the modulation depth. In this case, the complex amplitude E_{sc} of the space charge field vector $\mathbf{E_{sc}} = E_{sc} \exp\left[i\mathbf{K}\cdot\mathbf{x}\right] \hat{\mathbf{e}}$ with $\mathbf{e}$ is a unit vector. For small modulation depth m, E_{sc} is given by [82]

$$E_{sc} = -im \frac{E_q \left(E_D - iE_0\right)}{E_q + E_D - iE_0}, \tag{2.10}$$

where E_0 is the amplitude of an eventually applied electric field. The above equation shows that the complex amplitude of the space charge field E_{sc} is related to the trap limited field amplitude E_q and the diffusion field amplitude E_D. The latter is defined as

$$E_D = \frac{k_B T}{e} K, \tag{2.11}$$

with $K = \|\mathbf{K}\|$. This field corresponds to the field amplitude of a sinusoidal electric field that exactly counteracts the effect of the charge diffusion process. The trap limited field is

$$E_q = \frac{e}{\epsilon_{eff}\epsilon_0 K} N_{eff}, \tag{2.12}$$

it gives a limit for the maximum of $\mathbf{E_{sc}}$ that can be generated with the available traps. In Eq. (2.12) N_{eff} is the effective trap density defined as

$$N_{eff} = \frac{N_{D0}^{+}\left(N_D - N_{D0}^{+}\right)}{N_D} \tag{2.13}$$

where $N_{D0}^{+} = n_0 + N_A$ is the the spatial average of ionized donors density in the presence of the illumination. Although n_0, the spatial average density of electrons in the conduction band when the light is on, is dependent on the intensity I_0 of the light, n_0 is in most cases much smaller than the acceptor density N_A, so that $N_{D0}^{+} \simeq N_A$. The quantities N_{eff} and E_q are independent of the light intensity in the conventional model. It is useful to consider the limit of the solution (2.10) for the case where an external electric field such that $E_q \gg E_0 \gg E_D$ is applied. This is a common situation in photorefractive experiments. In this case we have

$$E_{sc} = -mE_0. \tag{2.14}$$

The fact that the amplitude in (2.14) is real reflects the fact that the response in this case is local with a minimum of the field exactly at the positions where the light intensity is maximum (field screening). In contrast, if no electric field is applied, the space charge field given by Eq. (2.10) simplifies to

$$E_{sc} = -im\frac{E_q E_D}{E_q + E_D}. \tag{2.15}$$

Here the factor i on the right-hand side indicates that the response is non local, *i.e.* the space charge field is $\frac{\pi}{2}$ out of phase with respect to the light distribution. From Eq. (2.15), we can also conclude that if one of the two fields E_q or E_D is much smaller than the other, the total space-charge field is limited by this field. An other important parameter involved during the photorefractive process is the build-up time τ_D. In the simplest approximation the build-up evolution is given by

$$E_{sc}(t) = E_{sc,0}\left(1 - \exp\left[-t/\tau_D\right]\right), \tag{2.16}$$

where τ_D is the dielectric relaxation time given by

$$\tau_D = \frac{\epsilon_0 \epsilon_{eff}}{\sigma} = \frac{\epsilon_0 \epsilon_{eff}}{e\mu_e n_0}. \tag{2.17}$$

It holds

$$\tau_D \propto \frac{1}{I_0}. \tag{2.18}$$

While expression (2.17) is valid in absence of applied field and for large enough grating spacing $\Lambda = \frac{2\pi}{\|\mathbf{K}\|}$, it can be shown that the correction factor in the build-up time for smaller grating spacing is in the order of 1 and is independent on the light intensity.

2.3.1.3 Space-charge field and refractive index change for localized illumination

A photorefractive refractive index change by a lateral illumination technique [36, 37, 83] can be used for light guiding. Indeed, when an electric field E_0 is applied to a photorefractive crystal along its $\vec{c}$ axis,the illuminated areas see their electric field decreasing as seen in (2.14) and consequently their refractive index modified. From Equations (2.10) and (2.4), by neglecting diffusion and photogalvanic currents, the resulting refractive index variations can be expressed as

$$\Delta n = -\frac{n^3}{2} r_{eff} E_0 \frac{I_D}{I_D + I(x)}. \tag{2.19}$$

Here I_D is the dark intensity [84] *i.e.* the light intensity which is needed to generate a photocurrent equal to the already present "dark current". For non illuminated zones (I(x)=0), we can therefore deduce easily

$$\Delta n_{I(x)=0} = -\frac{n^3}{2} r_{eff} E_0. \tag{2.20}$$

Therefore, the difference of refractive index between the illuminated and non illuminated zones is

$$\begin{aligned} \Delta n &= \frac{n^3}{2} r_{eff} E_0 \frac{I(x)}{I_D + I(x)}, \\ &= \frac{n^3}{2} r_{eff} E_0 \frac{1}{1 + \frac{I_D}{I(x)}} \end{aligned} \tag{2.21}$$

From Eq. (2.21), it can be seen that the refractive index difference between the illuminated and non illuminated areas depends on the illuminating light profile $I(x)$ and two cases are to be discussed. For $I(\mathbf{x}) \gg I_D$, the ratio $\frac{I_D}{I(\mathbf{x})}$ tends to zero and consequently Δn tends the value $\frac{n^3}{2} r_{eff} E_0$. In contrast, For $I(\mathbf{x}) \ll I_D$, the ratio $\frac{I_D}{I(\mathbf{x})}$ tends to infinite and in this case there is a negligible difference between the refractive index of the illuminated an non illuminated zones, Δn does not depend on the illuminating light profile $I(x)$. However, for our experiments, we will mainly assist the modification of the refractive index by adjusting the level of the background illumination I_D[3] while the profile of the $I(x)$ will be chosen in a way that takes into account the experimental constraints (imaging, ...). The level of the background intensity I_D is chosen in order to get a maximum difference of the refractive index between the illuminated area and non illuminated area.

[3]The "dark intensity" I_D can be artificially increased by a homogeneous illumination that rises the homogeneous photoconductivity above the dark conductivity level.

2.4 Experimental generation of optical waveguides

The above discussed photorefractive index change is at the base of our technique to generate photoinduced reconfigurable waveguides. By lateral illumination technique[4], we induce the change of the refractive index in preliminarily designed structures, which can be of different shapes and will be used for various purposes.

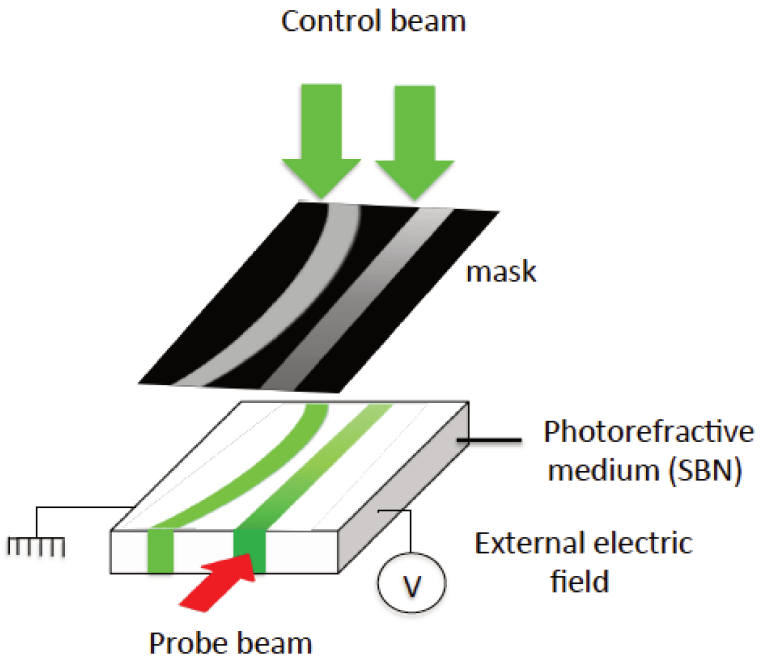

Figure 2.2: Principle of creation of optical waveguides using lateral illumination technique. The example shown corresponds to the creation of two coupled waveguides.

There exist other techniques for photoinduction of optical waveguides. So it is possible to change the refractive index by changing locally the structure of the material, this includes ion diffusion [85, 86], proton exchange [87, 88, 89], and ion implementation [90, 91]. Another technique involves direct laser writing using a scanned femtosecond laser beam on a transparent substrate [92, 93]. Finally, there are also techniques where a layer of higher refractive index is deposited on a substrate such as epitaxial deposition [94, 95, 96] or sol-gel technique [97, 98], most of above methods lead to fixed guiding structures which are not easy to modify. Therefore a technique offering more reconfigurability and giving easily modifiable structures is highly welcomed. The light-induced lateral illumination approach that we use permits to generate easily reconfigurable waveguide structures with

[4]This technique was developed in the laboratory within the thesis of Mohamed Gorram and was employed in a previous thesis. It will be used for all the experiments of this thesis.

simple and limited number of steps.

2.4.1 Technique for reconfigurable waveguides

We present how to generate reconfigurable photo-induced guiding structures using the lateral illumination technique. These structures were made using a photorefractive crystal of SBN (Strontium Baryum Niobate) with a wavelength of the inscription of 532 nm. Even though, as shown by Gorram *et al.* [37], this technique can be used to generate waveguides confined in both transverse dimensions, in this work we consider only waveguides confined in one dimension. Figure 2.2 shows how this technique works, the direction of the beam creating the waveguide is perpendicular to the direction of the waveguide itself. The dimensions of the waveguides made with this technique depends on the size of the light stripes reaching the crystal and imaged from the mask. As already mentioned, the material on which the waveguides are written is photorefractive and possesses electro-optic properties. A control beam (see Fig.2.2) reproduces the image of a designed mask on the crystal to which an external electric field is applied. Then, the structure is probed by a second laser beam (probe beam). More details on this technique will be given when presenting the experimental set-up in the next section.

2.4.2 Material used and experimental set up

2.4.2.1 SBN material

Strontium Baryum Niobate, $Sr_xBa_{1-x}Nb_2O_6$ (SBN) is a ferroelectric material possessing electro-optic and photorefractive properties. Its high electro-optic ($r_{333} = 235\,\mathrm{pmV^{-1}}$ for x=0.61) and piezoelectric coefficients [99, 100, 101] makes it a favorite material for many applications related to holography [102]. SBN belongs to the group of relaxor ferroelectrics. A first structural characterization was conceived by Jamieson and co-workers [103] for the composition x=0.75. It belongs to the structure type of tetragonal tungsten bronze (TTB) (see fig. 2.3) with the space group P4bm at room temperature. The positions taken by the Sr, Ba, Nb, and O are shown in Fig. 2.3. This configuration was also confirmed for SBN crystals with x=0.61 [104] and for a Strontium content x extending from 0.25 to 0.75 [100].

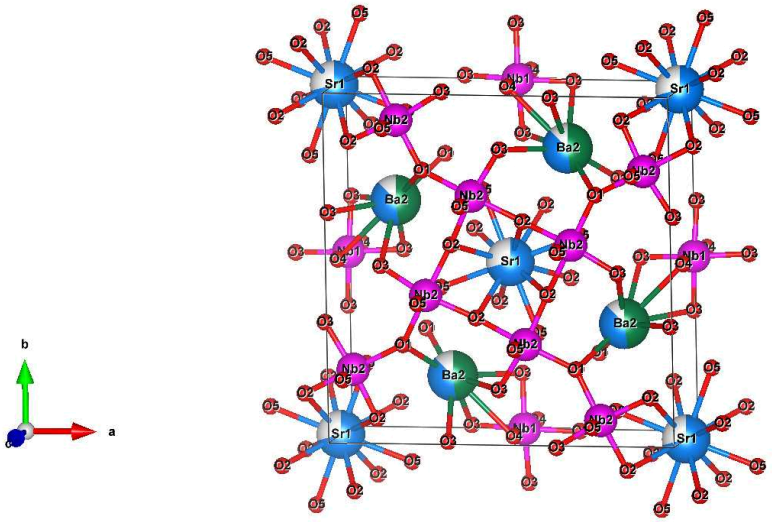

Figure 2.3: Crystal structure of the tetragonal tungsten bronze (TTB). This structure was confirmed for SBN with ratio of Strontium going from 0.25 to 0.75.

Single crystals of SBN can be grown using Czochralski technique with resistance heating [105] or the Stepanov technique [106]. $Sr_xBa_{1-x}Nb_2O_6$, x=0.61, or SBN:61 is relatively easy to grow compared to other photorefractive ferroelectric oxides because it mixes congruently at $T \sim 1510°C$. SBN can be doped with different elements such as Cerium, Cobalt,..., its quality defined by its photoconduction, electro-optic, and photorefractive time response, depends strongly on the dopant nature and dopant quantity. Table 2.1 gives the values of some characteristic parameters for SBN:61. The r_{333} electro-optic coefficient is 5 times higher than the r_{113} coefficient. For the experimental realization of waveguides, we use therefore a configuration where the r_{333} coefficient is active. The birefringence Δn of SBN:61 is negative ($n_e < n_o$). For experimental generation of optical guiding structures and for all the experiments, we use a cerium doped SBN:61 crystal with a Ce concentration of 0.002 mol%.

Table 2.1: Physical characteristic parameters of SBN:61. The electro-optic coefficients are measured at $\lambda = 514$ nm, the refractive indices at $\lambda = 633$ nm [101].

Composition	ϵ_{33}	r_{113} [pm/V]	r_{333} [pm/V]	n_e	n_o
SBN:61	800	47	235	2.2953	2.3116

2.4.2.2 SLM device and experimental setup

This section introduces the experimental techniques and tools used in this thesis. We mainly focus on the key elements of the experimental setup. One of the important elements

used in the experiment setup is the Spatial Light Modulator (SLM). It is a transmissive or reflective device used to spatially modulate the amplitude and/or phase of an optical wave front. An SLM can be programmed to produce light beams with various optical wave fronts like optical vortices or high order Bessel beams or other different functions.

For our experiments, we use the SLM in a reflective configuration to project the initially prepared waveguide images on an SBN:61 crystal. These images have the advantage of being easily reconfigurable, so different images with different shapes can be sent to the SLM. In figure. 2.4, examples of images that can be reproduced on the screen of an SLM are shown, these images are then reflected by the SLM and can be used as different functions depending on the experiment requirements. Figure. 2.4(a) provides diffractive axicon, figure. 2.4(b) shows the image of three coupled waveguides with curvatures, and figure. 2.4(c) is an image of array composed of equally separated and identical waveguides.

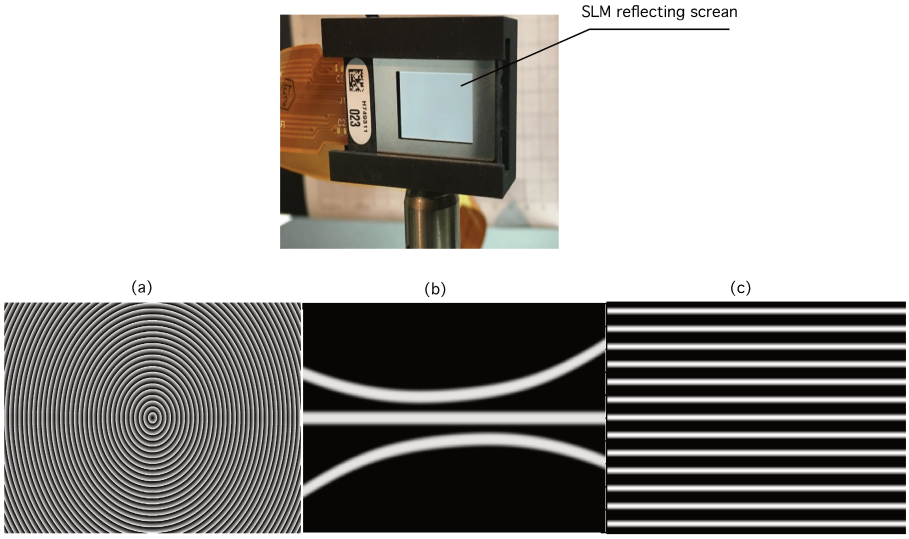

Figure 2.4: The SLM device is shown with examples of masks (a), (b), and (c) sent to the SLM screen. (a) provides diffractive axicon, (b) shows waveguides with curvatures, and (c) is an image of array composed of equally separated and identical waveguides.

The active part in the SLM is composed of liquid crystals. They are responsible of the modulation mechanism. Liquid crystals are molecules that are in a state of matter between a liquid and solid. Like a solid, they have an orientation order, where the long axis of each molecules is oriented in the direction of what is known as the molecular director. For our experiments, we use an LCoS-SLM (Liquid Crystal on Silicon SLM) which has a structure in which a liquid crystal layer is arranged on a silicon substrate. An electric field across the liquid crystal layer can be applied pixel by pixel (the number of pixel defines its screen size). This causes the liquid crystal molecules to tilt according to the electric field so that in general the phase of the reflected light can be modulated. By consequence, a difference

in the liquid crystal refractive indexes occurs in different tilt angles which induces a phase difference. However, if the polarization direction of the linearly polarized incident light is not aligned parallel to the direction of the liquid crystal molecules, the polarization state of the reflected light changes in accordance to the applied electric field to each pixel.

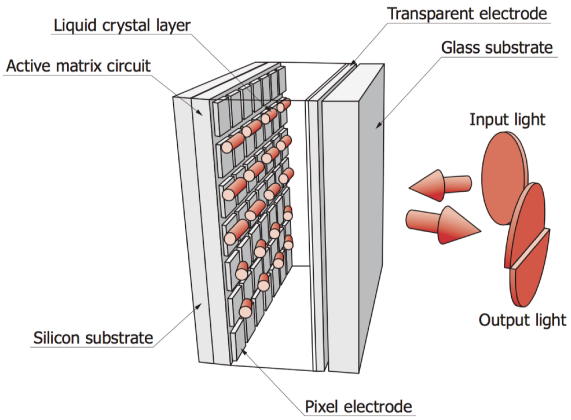

Figure 2.5: LCoS-SLM device structure.

Figure 2.5 shows the components of LCOS-SLM device, the input light is reflected by the liquid crystal layer so that the output light has its polarization modified. The device on Fig. 2.5 is connected to PC via DVI-D interface so that the SLM device can be directly controlled and receive different images previously designed with other softwares. These images are 256 gray level scaled so that the intensity of the reflected light can be related to the gray level of the image. The size of the used SLM device (HOLOEYE-LC-R1080) is 16.39 mm × 10.56 mm which corresponds to 1920pixel×1200pixel, with a pixel pitch of 8.5 µm. The full experimental setup of the lateral illumination technique is

Table 2.2: Factor of proportionality between the image size on the SLM and its size on the crystal and the observing CCD camera.

Size on SLM	Size on crystal (transverse)	Size on CCD camera
1 pixel	1.2 µm	1.6 pixel

depicted on figure 2.6. A vertically polarized control beam coming from a laser source at $\lambda = 532$ nm is incident on the polarized beam splitter (PBS). The beam splitter transmits the vertically oriented polarization and reflects the horizontally oriented one. The SLM reflects all the incident light and its polarization is locally modified according to the SLM's image configuration. The variation of the polarization of the reflected light is converted on an intensity variation by means of the PBS so the shape and contrast of the image on SLM is reproduced on the crystal. One of the two cylindrical lenses is oriented vertically and reduces the lateral dimension (along x direction). The other is oriented horizontally

such as to fit the length of the crystal.
The imaging ratio gives the relationship between the transverse dimension of the image size on the SLM and the corresponding size on the crystal. Also, there is a factor between the image size on the crystal and its size on the recording CCD camera. With the value of the lens focal length and imaging measurement, we get the imaging ratios given in Table. 2.2. The geometry of the control illumination is then inscribed in the crystal of SBN to which an external electric field is applied with a background illumination according to the processes described in Sec. 2.3.1.3. The background illumination is provided by an adjustable white light lamp with a fiber output allowing a good homogeneous illumination of the crystal.The background illumination allows to improve the resolution of the edges of the waveguide.
Once the guiding structure is generated, a second laser beam is used to probe it. Two different laser probe wavelengths 633 nm and 850 nm are used. These well separated wavelengths allow to establish the achromatic behavior of the recorded structures. The polarization of the probing light is parallel to the $\vec{c}$ axis of the SBN crystal. Along this axis, the active electro-optic coefficient is r_{333} as discussed in Sec. 2.2.

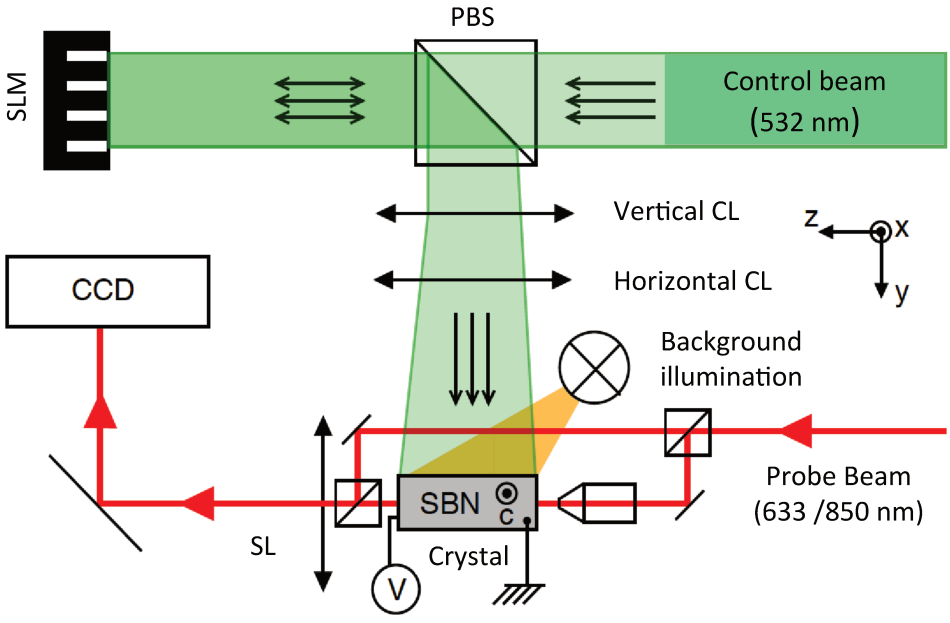

Figure 2.6: Simplified experimental set-up for generation of planar photo induced waveguides by lateral illumination technique [25]. SLM: Spatial light modulator, PBS: Polarized beam splitter, CL: Cylindrical lens, SL: Spherical lens, V: Applied voltage on a photorefractive crystal of SBN.

A Mach-Zehnder interferometer setup (see Fig. 2.7) involving the probing beam for interferometric measures is used. The laser light issued from the source at $\lambda = 633/850\,\text{nm}$ is splitted into two beams, one propagates in the free space and the other passes through the SBN crystal where the waveguide is generated. Upon recombination, the two paths of the probing beam produce an interference pattern. During the formation of the waveguide, its refractive index evolves and the fringes scroll at the place where the waveguide forms. Counting the number of scrolling fringes permits to estimate the induced change in refractive index. In the next section, we proceed to the characterization of the generated waveguide.

2.4.2.3 Characterization of the photo induced waveguides

Two important quantities are experimentally characterized, the induced change of refractive index and the coupling constant in the case of two identical parallel coupled waveguides. The experimental estimation of these two quantities is necessary for implementation of some analogies existing between quantum mechanics and waveguide optics. The principle of these analogies will be discussed in details in the next chapter.
First, we are interested in the measurement of the refractive index change of a waveguide generated in a crystal of SBN:61 induced by the photorefractive effect. To achieve this goal, we proceed to its estimation by creating different images of waveguides with different gray level. These images are probed and by interferometric measures we estimate the refractive index of the waveguide compared to the one of the bulk. The estimation of the refractive index is obtained as follows.

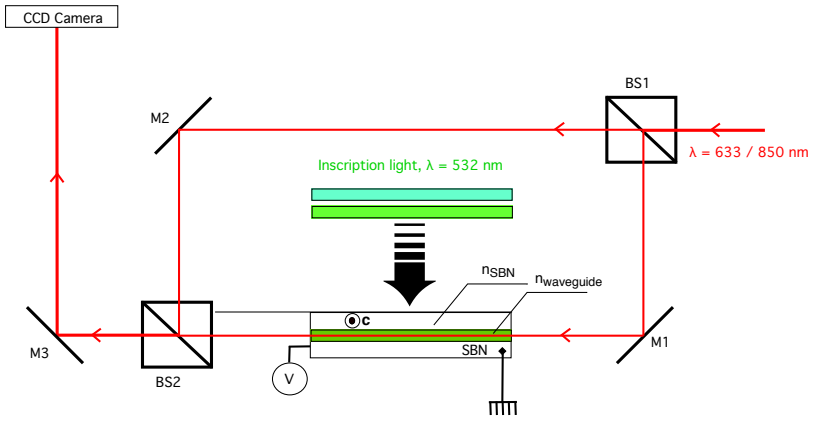

Figure 2.7: Part of the experimental set-up for the determination of the refractive index change of the photo induced waveguides with the Mach-Zehnder interferometer

We design a set of images of waveguides with same geometry but with different contrast of the gray level going from 50% to 100%. A value of 100% means that the corresponding pixel on the image sent to the SLM is fully white. For 0% the pixel is fully black and

for intermediate values we have all the intermediate gray levels. These images are sent one after the other to the SLM and projected using a laser light of $\lambda = 532$ nm on the SBN crystal. Then, with a second laser beam at $\lambda = 633\,\text{nm}$ or $850\,\text{nm}$, we probe the created waveguide and measure thanks to Mach-Zehnder interferometer the phase shift between the light propagating in the waveguide and the one propagating nearby in the bulk of the crystal (see example in Fig. 2.8). The refractive index difference is estimated by counting the number of fringes after the waveguide is fully established. Figure 2.9 shows an example of the dependence of $n_{waveguide}$-n_{SBN} (n_{SBN} corresponds to the extraordinary index of SBN) according to the gray level of the waveguide's image which is directly proportional to the local light intensity contrast. For the gray level situated in the range [50%, 75%], the index difference varies linearly with the incident light intensity of the control beam.

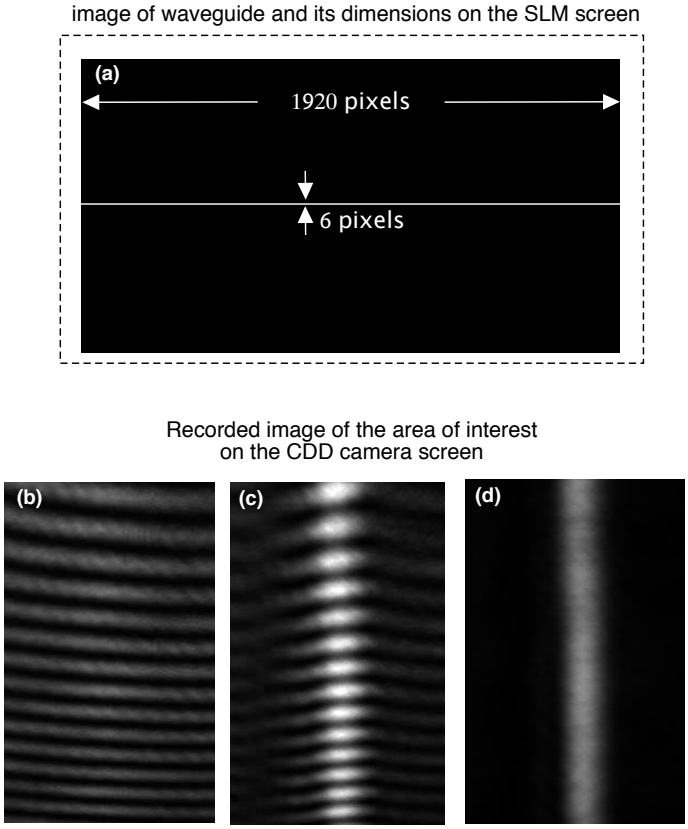

Figure 2.8: (a) SLM image of a straight waveguide, the dimensions of the waveguides measured in pixel are 6×1920 *which correspond to* $7.2\,\mu\text{m}\times23\,\text{mm}$ *once projected in the SBN crystal. (b), (c), and (d) are recorded images of the output of the crystal on the CCD Camera. (b) and (c) show the interference configuration before and after the waveguide is formed, (d) shows the output of the waveguide in absence of the beam in the second arm of the interferometer.*

We note that the characterization of the induced refractive index change is deduced

from the difference between the propagation constants $\beta_{waveguide}$-β_{SBN}, the quantity directly measured. This calibration corresponds to a given background illumination and a given intensity of the green laser light falling on the SLM. It is therefore necessary to repeat this kind of calibration at regular intervals and every time any of the important parameters change (background intensity, control light intensity, waveguide width, ...).

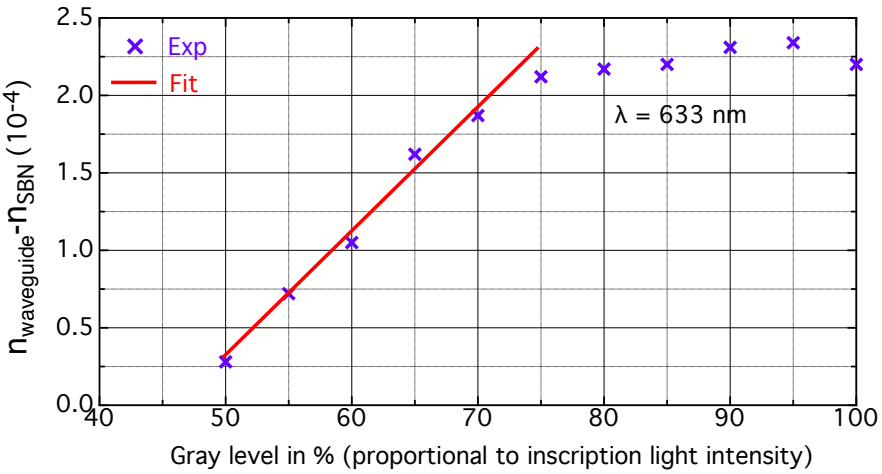

Figure 2.9: Example of calibration curves of the refractive index change for a wavelength $\lambda = 633\,\text{nm}$. The induced refractive index change is measured as a function the gray level of the SLM waveguide image. The calibration is achieved by interferometric measures using Mach-Zehnder interferometer. The response is nearly linear (red line) for a range of gray levels between 50% and 75%.

As we have seen in subsection 1.3.2 of chapter 1, the other important parameter for the waveguides and particularly for light coupling is the coupling constant. In its expression given in Eq.(1.53), the dominant term is the exponential term in which the extinction coefficient γ_m appears. The estimation of this coefficient is important for the coupling constant estimation and therefore for the prediction of light transfer between waveguides.

We proceed to the estimation of the γ_m by creating a set of identical directional couplers in which only the distance between the waveguides s is changed (see examples in figure. 2.10(b), the other parameters such as the width, the refractive index contrast are maintained constant and correspond to an SLM image of 100% of gray level. We initially inject the light with intensity I_0 in the input of waveguide 1 (WG1 of Fig. 2.10(b)) and measure the relative amount of light at the outputs of WG2 after a propagation distance of 23 mm.

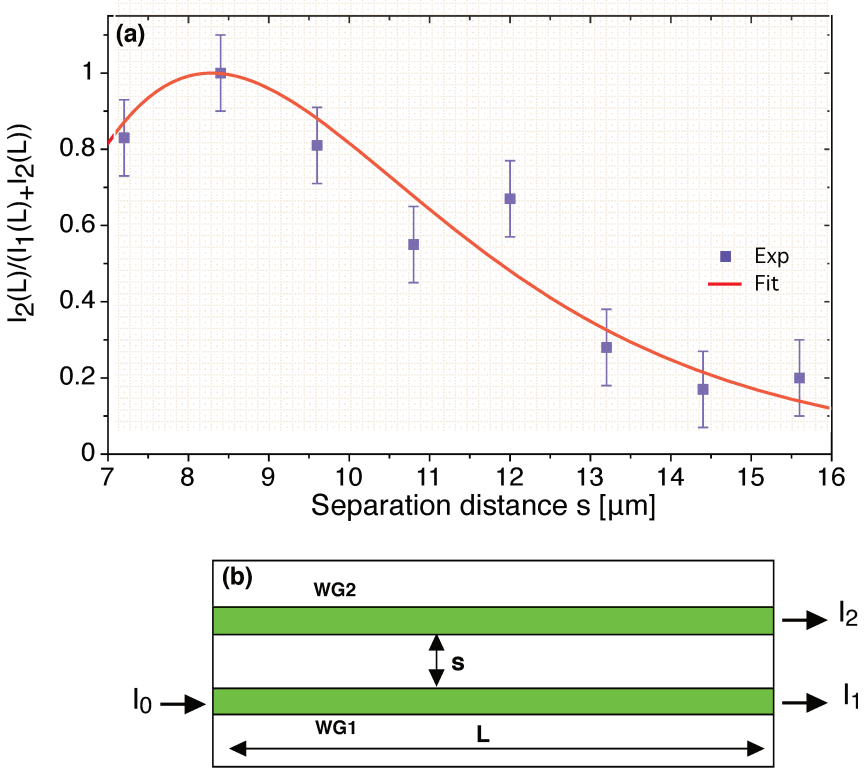

Figure 2.10: (a) Variations of relative output intensity in WG2 for directional couplers shown in (b). The output intensity of WG2 I_2 is plotted according to the waveguide's separation distance s. The experimental data are fitted with an appropriate function with respect to Eq. (2.22) for the case where $\Delta\beta = 0$ and $L = 23\,\mathrm{mm}$

.

Figure. 2.10(a) shows an example of the results taken in the range of parameters for which the crystal length corresponds to less than one or a little more than one coupling length and coupling constant is dominated by the term $e^{-\gamma_m s}$. The figure shows the measured relative output intensity of WG2 of the directional couplers shown in Fig. 2.10(b). The output intensity in WG2 as a function of the separation distance s decreases with the increase of the separation distance s. In contrast with Fig. 1.12 presented in section 1.3.2 in which the theoretical coupling constant variations with the separation s is calculated with assumed square profile of refractive index while for the experimental measurements, the waveguide refractive index profile is slightly smoothed on the borders due to the peaticities related to the involved photorefractive charge transport. For high separation distances, both results should be in good agreement as will be seen in the following.

To estimate the extinction factor γ_m, we fit the experimental recorded data of Fig. 2.10(a) with an exponential decay function of the form

$$\tilde{I}_2(s) = \sin^2\left(C_0 \exp(-\gamma_m s)L\right), \tag{2.22}$$

where $\tilde{I}_2$ is the relative intensity in waveguide 2, C_0 is an arbitrary maximal amplitude of the coupling constant and L is the full propagation length taken equal to 23 mm. Equation (2.22) is a combination of Eq. (1.49) and Eq. (1.53)
From the fit parameters shown in Fig. 2.10(a), we deduce the values of γ_m and C_0

$$C_0 = 0.34 \pm 0.07 \text{ mm}^{-1} \tag{2.23}$$

$$\gamma_m = 0.19 \pm 0.04 \text{ µm}^{-1} \tag{2.24}$$

The value of γ_m estimated using the coupled mode theory is $0.22\,\text{µm}^{-1}$ which is in good agreement with the experimental value. Note that the theoretical value (as in Fig. 1.12) is obtained by assuming a perfect square of the refractive index contrast. In reality in a photorefractively induced waveguide the borders of the refractive index profile are slightly smoothed as a result of the involved charge transport physics. Therefore, the agreement between the expected and experimentally determined values for the leading quantity γ_m can be considered very good. From the experimentally estimated values of γ_m and C_0, we reproduce the expected variation of the coupling constant as a function of the separation distance s, similarly to the theoretical curve in Fig. 1.12. Note that each type of waveguides associated to different experimental parameters (gray level, background illumination, applied field, waveguide width, ...) has a different calibration curve.

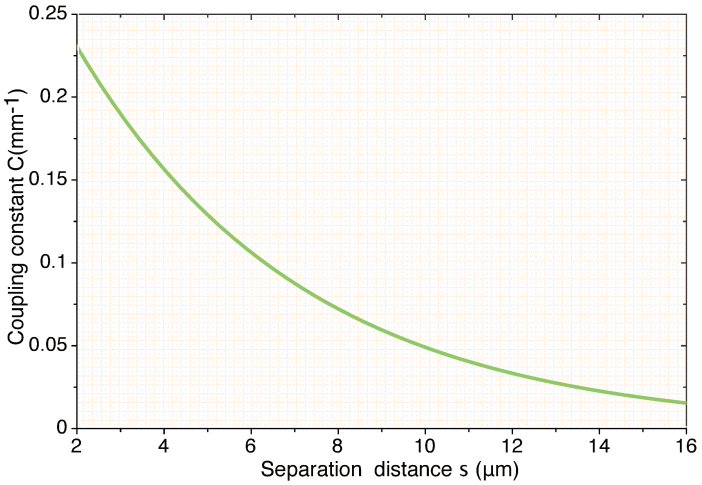

Figure 2.11: Fitted coupling constant as a function of separation distance s as extrapolated from measurement of the extinction factor γ_m and its maximal amplitude C_0 with help of directional couplers of Fig. 2.10(b).

2.5 Conclusion

The first part of this chapter has reminded the basis of the linear electro-optic effect (Pockels effect) and of the photorefractive effect in the framework of the conventional

band transport model of Kukhtarev [82]. In the second part, we have shown how these two effects can be used for the generation of optical waveguides by the lateral illumination technique.

The characterization of the photo induced guiding structures is achieved by quantifying their induced change of refractive index by means of an interferometric calibration procedure. We also estimated the coupling constant for two identical coupled waveguides in which we experimentally studied the optical power exchange. This kind of calibrations of the refractive index change and the coupling constant will serve to guide the design of optical structures which will be used for experimental demonstration of some analogies between coupled quantum systems and coupled optical waveguide systems.

3 Analogy between quantum and optical systems

Contents

3.1 Introduction

Quantum-classical analogies have paved the way for the establishment of classical systems that behaves similarly as their quantum analogs and vice-versa. The analogy between geometric optics and Newtonian particle dynamics initiated the development of the wave mechanics [107]. Other examples of analogies have been studied, demonstrated, and exploited. To name a few, scattering and localization of light is analog to one of electrons. Non linear resonant tunneling is similar to non linear soliton dynamics in optical fibers, etc. Moreover, a coupled two mode optical system is demonstrated to be the analog of a two-level quantum system. This latter analogy will attract most of the attention in this thesis.

The present work deals with the important analogy between quantum mechanics and guided wave optics. This analogy is based on the similarity between the time-dependent Schrodinger equation describing the dynamics of the atomic system and the paraxial wave equation describing the dynamics of the light when it propagates in guiding structures. Thereby, the processes and approaches developed in quantum mechanics can serve as source of inspiration for optics and vice-versa. The exploitation of this kind on analogy has led to the design of multi layered optical structures with the same transmission characteristics as their analogs in quantum mechanics with 0D, 1D or 2D dimensions [108]. A particularly important case concerns analogues to the coherent control of atomic or molecular systems by means of laser fields. Examples are rapid adiabatic passage (RAP) [30, 109], population trapping and coherent population transfer such as Stimulated Raman adiabatic passage (STIRAP) [110, 111]. Generally, advantage in optics is a much easier characterization of the systems since the structures are generally orders-of-magnitude larger than their corresponding quantum structures. To name a few, the transverse modes of aspherical laser resonators are similar to the eigenstates of the stationary Schrödinger equation with a potential well determined by the mirror profile. Also, the Franck-Condon principle has found its analog in paraxial optics in the mismatch of a mode passing through two fibers with different refractive index distribution [112] . Moreover, the quantum squeezed states have been extended to solutions of the Helmholtz equation that contain them in the paraxial approximation [113]. The Helmholtz equation reduces in the paraxial approximation to a form equivalent to the time-dependent Schrödinger equation, with the distance along the optical axis, the wavelength, and the refractive index playing the roles of time, Planck's constant and potential, respectively, in direction of the ray. Ray optics and classical mechanics are recovered in the limits $\lambda \longrightarrow 0$ and $\hbar \longrightarrow 0$, respectively.

We start this chapter by discussing the adiabaticity condition, essential for the population/light transfer in the atomic/optical system, to be robust. It is shown that under certain conditions that the parameters of the system should fulfill (Rabi frequencies and detuning in quantum mechanics, coupling constants and difference in the longitudinal propagation constant in optics), the evolution becomes adiabatic. In the following, we illustrate the analogies between quantum mechanics and wave optics by considering the example of the dynamics of a three level system and its analog in optics consisting of a set of three waveguides. It will be seen that the involved dynamic equations are similar, the coupling constants of the waveguides in the case of the optical system are analog to the Rabi frequencies in the case of the atomic system.

3.2 Adiabatic evolution of a quantum system

3.2.1 Adiabaticity theory

We consider a quantum system for which the Hamiltonian $\mathsf{H}(\tau) = \mathsf{H}(t/T)$ evolves slowly and continuously in time and during a time evolution T. During its evolution, the system is qualified to be adiabatic when the time of its evolution tends to the infinity. We note $E_1(t)$, $E_2(t)$, ..., $E_n(t)$, ... the instantaneous eigenvalues of the Hamiltonian with its corresponding eigenstates $|\psi_n(t)\rangle$, and by $P_1(t)$, $P_2(t)$, ..., $P_n(t)$, ..., their associated projectors

$$\mathsf{H}|\psi_n(t)\rangle = E_n|\psi_n(t)\rangle, \tag{3.1}$$

$$\langle\psi_n(t)|\psi_m(t)\rangle = \delta_{nm}, \tag{3.2}$$

$$P_n(t) = |\psi_n(t)\rangle\langle\psi_n(t)|\,. \tag{3.3}$$

Therefore, applying the projector $P_n(t)$ on $|\psi(t)\rangle$ gives

$$P_n(t)\,|\psi(t)\rangle = \langle\psi_n(t)|\psi(t)\rangle\,|\psi_n(t)\rangle\,, \tag{3.4}$$

and applying the same projector a second time gives

$$P_n^2(t)\,|\psi(t)\rangle = \langle\psi_n(t)|\psi(t)\rangle\,\langle\psi_n(t)|\psi_n(t)\rangle\,|\psi_n(t)\rangle\,, \tag{3.5}$$

$$= P_n(t)\,|\psi(t)\rangle\,, \tag{3.6}$$

which is unchanged with respect to (3.4), as expected for a projector. The propagator of the quantum system $U(t,t_i)$, gives the state $|\psi(t)\rangle$ at a later time for a known initial state $|\psi(t_i)\rangle$,

$$|\psi(t)\rangle = U(t,t_i)|\psi(t_i)\rangle \tag{3.7}$$

We suppose that :

- The instantaneous eigenvalues do not cross each other *i.e.*$|E_n(t) - E_m(t)| > \delta_0\ \forall$ t,
- The derivatives $\frac{d}{dt}P_n$, $\frac{d^2}{dt^2}P_n$ are defined (they are norm twice differentiable) and continuous, so that when T approaches infinity, the propagator $U(t,t_i)$ has the following asymptotic property : $\forall\ n \in \mathbb{N}$ when $T \to \infty$, the propagator $U(t,t_i)$ satisfies the relation [114]

$$U(t,t_i)P_n(t_i) - P_n(t)U(t,t_i) = \mathscr{O}(\frac{1}{T}). \tag{3.8}$$

Equation (3.8) constitutes the adiabatic theorem. When the evolution time T tends to infinity, the term $\mathscr{O}(\frac{1}{T})$ on the right-hand side of Eq. (3.8) approaches 0 and consequently, the quantity $U(t,t_i)P_n(t_i)$ tends to the quantity $P_n(t)U(t,t_i)$. It is therefore equivalent to

project first the state $|\psi(t)\rangle$ on the various eigenstates and then to apply the propagator $U(t,t_i)$ on each of them, or to apply first the propagator $U(t,t_i)$ on the state $|\psi(t)\rangle$ and project at the end. This implies that, if the system state $|\psi(t)\rangle$ is initially connected to a state $|\psi_n(t)\rangle$, it will follow this state during the evolution of the system, in the adiabatic limit $T \longrightarrow \infty$.

3.2.2 Adiabatic evolution : The example of a two state system

In this section, we apply the adiabatic theorem to a two level quantum system. We particularly point out how the adiabatic passage allows to control the transition between the eigenvalues. We consider a system composed of two energy levels, coupled by means of a laser field possessing a time varying envelope. The ground state $|\ \psi_1\rangle$ is linked to the excited state $|\ \psi_2\rangle$ with a detuning Δ (see Fig. 3.1). The Hamiltonian of the system in the rotating Wave Approximation (RWA) [115, 116], written in the basis $|\ \psi_1\rangle, |\ \psi_2\rangle$ is given by

$$\mathsf{H}(t/T) = \mathsf{H}(\tau) = \frac{1}{2}\begin{bmatrix} 0 & \Omega(\tau) \\ \Omega(\tau) & 2\Delta(\tau)) \end{bmatrix}. \tag{3.9}$$

where T is a characteristic time of the system which can be the laser pulse duration for example, and τ is the normalized time $\tau = t/T$. $\Omega(\tau)$ is the Rabi frequency corresponding to the coupling laser field. It is related to its slowly varying amplitude of the light electric field $\varepsilon(\tau)$ by the relation

$$\Omega(\tau) = -d_{12}\varepsilon(\tau)/\hbar, \tag{3.10}$$

where d_{12} is the component of the dipole-transition moment along its electric-field vector. The Hamiltonian of Eq. (3.9) has the eigenvalues

$$\varepsilon_{\pm} = \frac{1}{2}\Delta(\tau) \pm \frac{1}{2}\sqrt{\Delta^2(\tau) + \Omega^2(\tau)} \tag{3.11}$$

with the corresponding eigenstates

$$|\ \psi_+\rangle = \begin{bmatrix} \cos(\vartheta(\tau)/2) \\ \sin(\vartheta(\tau)/2) \end{bmatrix}, |\ \psi_-\rangle = \begin{bmatrix} -\sin(\vartheta(\tau)/2) \\ \cos(\vartheta(\tau)/2) \end{bmatrix}, \tag{3.12}$$

where ϑ is the dynamical angle, given by

$$\tan(\vartheta(\tau)) = -\frac{\Omega(\tau)}{\Delta(\tau)}, \qquad 0 \leq \vartheta(\tau) \leq \pi. \tag{3.13}$$

We denote by $|\ \Psi(\tau)\rangle$ the wave function describing the system and satisfying the Schrödinger equation

$$\frac{i}{T}\frac{\partial}{\partial\tau}|\Psi(\tau)\rangle = H(\tau)\ |\ \Psi(\tau)\rangle. \tag{3.14}$$

In the following, we suppose that the system is initially connected to the state $\mid \psi_+\rangle$, *i.e.*. $\mid \Psi(-\infty)\rangle = \mid \psi_+(-\infty)\rangle = \mid \psi_1\rangle$. We consider the particular case where the detuning Δ starts with negative values, *i.e.*. $\Delta(-\infty) < 0$. We get

$$\mid \tilde{\Psi}(\tau)\rangle = R^{\dagger}(\tau) \mid \Psi(\tau)\rangle \tag{3.15}$$

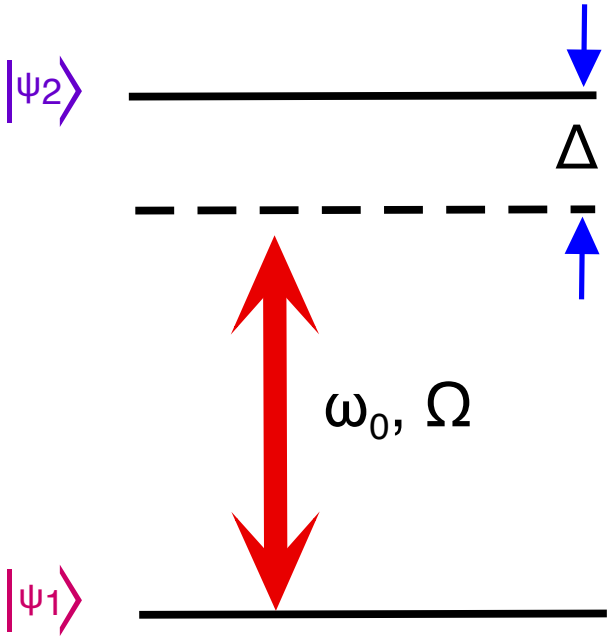

Figure 3.1: Scheme of two level system used to illustrate the adiabatic theorem. The laser at frequency ω_0 possessing the Rabi frequency Ω couples the ground state $\mid \psi_1\rangle$ to the excited state $\mid \psi_2\rangle$ with a detuning Δ.

where R($\vartheta(\tau)$) is the unitary transformation (rotation matrix), defined by

$$R(\tau) = \begin{bmatrix} \cos(\vartheta(\tau)/2) & -\sin(\vartheta(\tau)/2) \\ \sin(\vartheta(\tau)/2) & \cos(\vartheta(\tau)/2) \end{bmatrix}. \tag{3.16}$$

Using (3.16) in (3.15) and replacing $\mid \Psi(\tau)\rangle$ by $\left(R^{\dagger}\right)^{-1} \mid \tilde{\Psi}(\tau)\rangle$ in (3.14), we get

$$\frac{i}{T}\frac{\partial}{\partial\tau}\left|\tilde{\Psi}(\tau)\right\rangle = \begin{bmatrix} \varepsilon_+(\tau) & \frac{i}{T}\frac{\dot{\vartheta}(\tau)}{2} \\ -\frac{i}{T}\frac{\dot{\vartheta}(\tau)}{2} & \varepsilon_-(\tau) \end{bmatrix} \left|\tilde{\Psi}(\tau)\right\rangle. \tag{3.17}$$

In the adiabatic limit $T \longrightarrow \infty$, the off-diagonal terms in equation (3.17), known as non adiabatic coupling terms, can be neglected comparing to the quantity $\mid \varepsilon_+ - \varepsilon_- \mid$. This gives the adiabaticity condition

$$|\varepsilon_+ - \varepsilon_-| \gg \left|\frac{\dot{\vartheta}}{T}\right|. \tag{3.18}$$

When the condition of equation (3.18) holds, the solution of the Schrödinger equation becomes easier to solve and the wave function is of the form

$$|\Psi(\tau)\rangle = \exp\left(-iT\int_{-\infty}^{\tau}\varepsilon_+(s)ds\right)|\psi_+(\tau)\rangle + \mathscr{O}(\frac{1}{T}). \tag{3.19}$$

Thus, in the adiabatic limit, the system evolves by following the state to which it was initially connected ($|\psi_+\rangle$).

3.2.3 Adiabatic passage

In this section, we demonstrate how to realize an asymptotic transition between the two levels by following adiabatically an initial state for example, the state $|\Psi(\tau \longrightarrow -\infty)\rangle = |\psi_+(-\infty)\rangle = |\psi_1\rangle$ and end up in the state $|\Psi(\tau \longrightarrow +\infty)\rangle = |\psi_+(+\infty)\rangle = |\psi_2\rangle$. This, in the case where the coupling Ω satisfies $\Omega(\pm\infty) = 0$ and the detuning Δ changes linearly from negative values to positive values with an intermediate crossing of the resonance ($\Delta = 0$). The adiabatic eigenvalues of equation (3.11) are plotted versus time on figures 3.2(c) and (d) with the diabatic ones which correspond to the adiabatic eigenvalues in the absence of the coupling ($\Omega = 0$).

$$a_1 = \varepsilon_+^{(\Omega=0)}(\tau) = 0, \quad a_2 = \varepsilon_-^{(\Omega=0)}(\tau) = \Delta(\tau) \tag{3.20a}$$

$$\left|\psi_+^{(\Omega=0)}\right\rangle = \begin{pmatrix}1\\0\end{pmatrix} \equiv |\psi_1\rangle\,, \quad \left|\varphi_-^{(\Omega=0)}\right\rangle = \begin{pmatrix}0\\1\end{pmatrix} \equiv |\psi_2\rangle\,. \tag{3.20b}$$

Let us consider an example where the shapes of the pulses are of the form $\Omega(\tau) = \Omega_0\,\mathrm{sech}(\tau)$ and $\Delta(\tau) = \Delta_0\tau$. The adiabatic eigenvalue ε_- and ε_+ form a crossing of a width Ω_0 at $\tau = 0$. If we follow continuously each of the adiabatic eigenvalues from very earlier times ($\tau \to -\infty$) to very late times ($\tau \to +\infty$) by positive values, the dynamics follows each branch in the adiabatic regime we will observe a rotation of the eigenvalues and the asymptotic limit of the mixing angle ϑ is

$$\tan(\vartheta(\tau \longrightarrow -\infty)) = -\frac{\Omega(\tau \longrightarrow -\infty)}{\Delta(\tau \longrightarrow -\infty)} = -\frac{0}{-\Delta_0} = 0^+ \Longrightarrow \vartheta = 0. \tag{3.21}$$

This leads to

$$|\psi_+(-\infty)\rangle = \begin{pmatrix}1\\0\end{pmatrix} \equiv |\psi_1\rangle\,, \tag{3.22}$$

and

$$\tan(\vartheta(\tau \longrightarrow +\infty)) = -\frac{\Omega(\tau \longrightarrow +\infty)}{\Delta(\tau \longrightarrow +\infty)} = -\frac{0}{+\Delta_0} = 0^- \Longrightarrow \vartheta = \pi, \tag{3.23}$$

which implies

$$|\psi_+(+\infty)\rangle = \begin{pmatrix}0\\1\end{pmatrix} \equiv |\psi_2\rangle\,. \tag{3.24}$$

We similarly obtain $|\psi_-\rangle$

$$|\psi_-(-\infty)\rangle = \begin{pmatrix} 0 \\ 1 \end{pmatrix} \equiv |\psi_2\rangle, \qquad |\psi_-(+\infty)\rangle = \begin{pmatrix} -1 \\ 0 \end{pmatrix} \equiv -|\psi_1\rangle\,. \tag{3.25}$$

The system goes continuously from the state $|\psi_1\rangle$ to the state $|\psi_2\rangle$ and reciprocally (in absolute value). We can conclude that from a given initial condition, the evolution is sufficiently adiabatic to lead the system to an asymptotic transition.

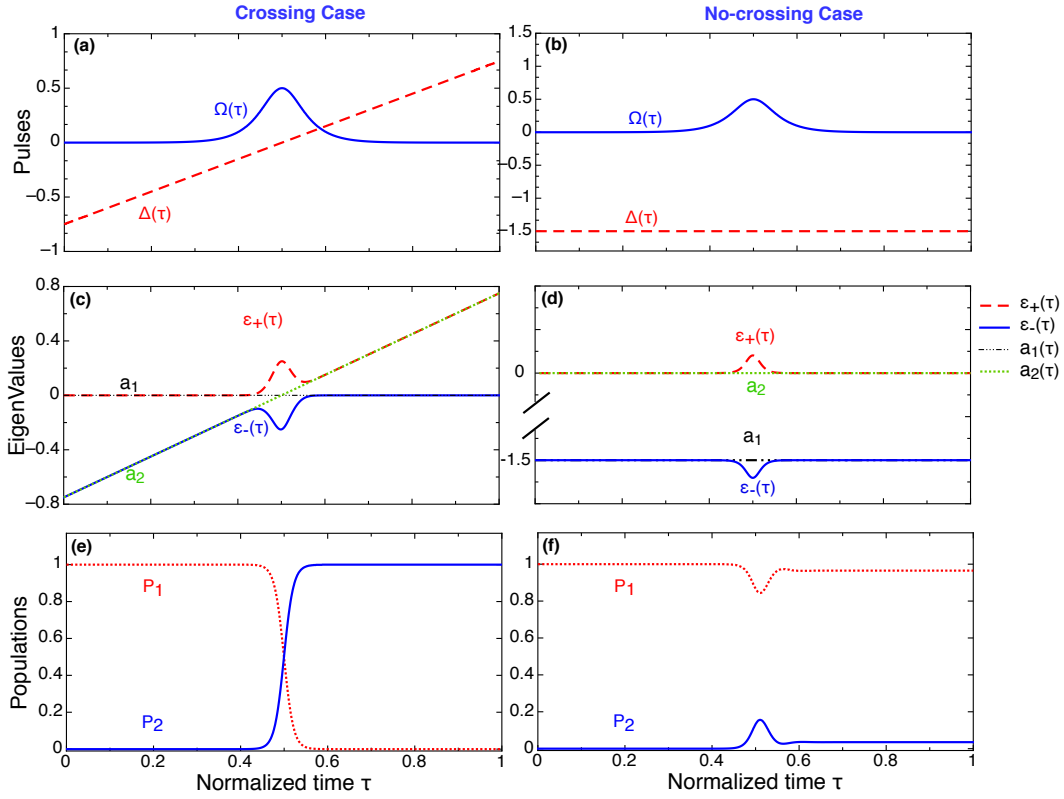

Figure 3.2: (a) shapes of the detuning and the Rabi pulse for the values $\Omega T = 10$ and $\Delta_0 T = 25$. The eigenvalues of the system shown in figure 3.1 versus time (c) for the crossing case and (d) for the no-crossing case. (e) and (f) the time evolution of the population from the ground state to the excited state.

⇨ Crossing CASE :

This case occurs when the detuning $\Delta(\tau)$ changes from negative values to positives values and crosses zero at the maximum of coupling $\Omega(\tau)$ as illustrated in Fig. 3.2(a). As shown in Fig. 3.2(c), the diabatic eigenvalues of (3.9) which are 0 and $\hbar\Delta(\tau)$ cross each other when the detuning $\Delta(\tau)$ is zero (when the coupling $\Omega(\tau)$ reaches its maximum value). When $\Delta(\tau)$ is large (compared to $\Omega(\tau)$), the diabatic eigenvalues and the adiabatic eigenvalues are equal and deviate from each other when $\Omega(\tau)$ is present. As Eqs. (3.21)-(3.24) show, a complete population transfer from ψ_1 to ψ_2 occurs. Figure. 3.2(e) shows this situation.

➪ **No-Crossing CASE :**

For this case, the diabatic eigenvalues do not cross each other, this case is shown in Figure. 3.2(d). A constant detuning $\Delta(\tau)$ and a hyperbolic secant shape of coupling $\Omega(\tau)$ are considered. The diabatic eigenvalues are separated and parallel to each other. When the coupling $\Omega(\tau)$ is zero, the diabatic and adiabatic eigenvalues are equal. When the coupling $\Omega(\tau)$ is present, the adiabatic eigenvalues deviate from the diabatic ones (see Fig. 3.2(d)). As Equation. (3.12) shows, at early and late times, $|\psi_+(-\infty)\rangle = |\psi_+(+\infty)\rangle = |\psi_1\rangle$ because in both cases ϑ tends to the same value 0. At intermediate times, when the coupling $\Omega(\tau)$ is present, the slight change in ϑ induces as expected a little transfer of population to the state $|\psi_2\rangle$ which almost returns when $\Omega(\tau)$ returns to zero. This return of population can be seen in Fig. 3.2(f).

3.3 Dynamics of atomic quantum systems and optical waveguide systems

The objective of this section is to point out the analogy between quantum mechanics and waveguide optics by means of the three state system. This quantum system was extensively investigated theoretically [117, 118, 119, 120] and experimentally [110, 121, 122]. In one hand, we remind the master equations that govern its dynamics and give the mathematical quantities involved in the population transfer between its energy levels. The STImulated Raman Adiabatic Passage (STIRAP) technique is presented, we shows through some simulation results that this technique can provide an efficient and robust population transfer. On the other hand, we present the analogue of the previous quantum system in optical waveguides and we point out that their dynamics are perfectly similar. We will see in the quantum case that the role taken by the Rabi pulses corresponds to the one taken by the coupling constants in the case of optical coupled waveguides, the detuning between the central frequency of the laser field coupling the quantum levels and the transition frequency finds its counterpart in the difference between the longitudinal propagation constants of the waveguides. For the optical system, we give the equations describing light transfer between waveguides and the parameters that control this transfer. As in the case of quantum system, the light can be transferred between waveguides adiabatically and efficiently. The STIRAP process for waveguides is illustrated through some simulation results.

3.3.1 Dynamics of population transfer in atomic systems

3.3.1.1 Example of three state system

We consider the atomic system composed of three electronic levels known also as "Λ system" (see Figure 3.3 (a)) in which only the level ψ_1 (initial state) is initially populated. The coupling between the states ψ_1 and ψ_2 is provided by a laser pulse P_1 while the interaction between the states ψ_2 and ψ_3 is provided by a second laser pulse P_2. The intermediate state ψ_2 may undergo spontaneous emission to the states ψ_1 and ψ_3 or to other states. The objective is to transfer all of the population from state ψ_1 into state ψ_3 without losing population by spontaneous emission from state ψ_2. The system evolves in time and its dynamics is given by the time-dependent Schrödinger equation:

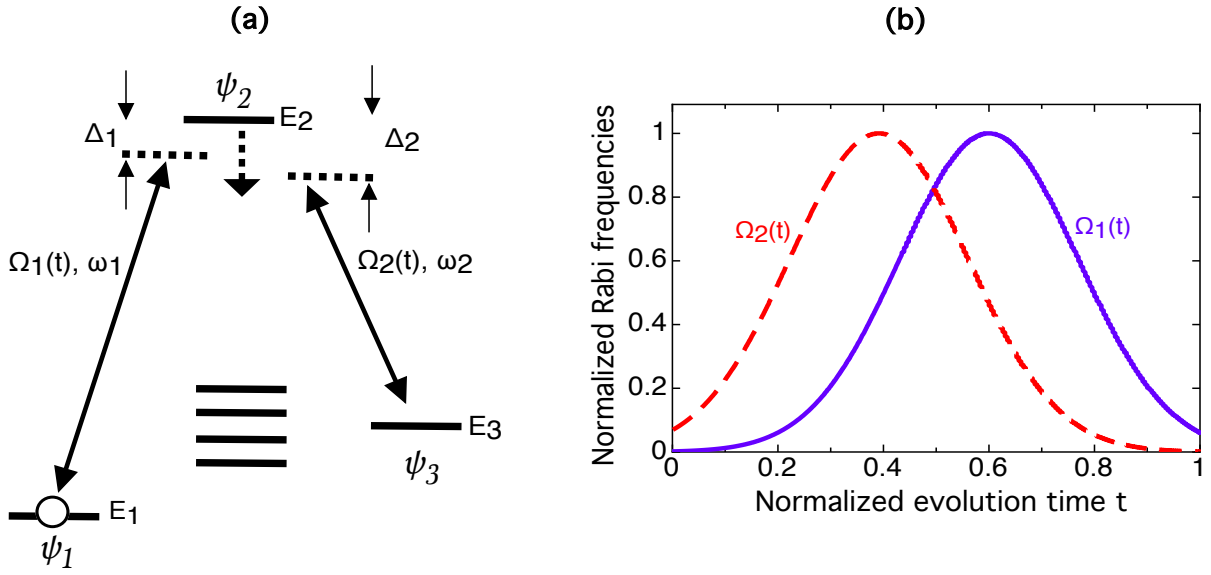

Figure 3.3: Three-state quantum system scheme. (a) the laser pulse with the Rabi frequency $\Omega_1(t)$ ensures the connection between the initially populated state ψ_1 and the final, target, state ψ_3 which is linked to the intermediate state ψ_2 by a second laser pulse with the Rabi frequency $\Omega_2(t)$. (b) Time evolution of the Rabi frequencies for a three state STIRAP process. The detuning of the laser frequencies $\omega_1(t)$ and $\omega_2(t)$ of the two pulses from the transition frequencies $(E_2 - E_1)/\hbar$ and $(E_2 - E_3)/\hbar$ are respectively Δ_1 and Δ_2. The state ψ_2 may decay spontaneously to states ψ_1 and ψ_3 or to other levels.

$$i\hbar\frac{d}{dt}\psi(t) = \mathsf{H(t)}\psi(t), \tag{3.26}$$

where $\psi(t) = [p_1(t), p_2(t), p_3(t)]^T$ is a vector whose elements represent the probability amplitudes of the three states ψ_1, ψ_2 and ψ_3, and $\mathsf{H(t)}$ is the time dependent Hamiltonian of the coupled system given in the rotating wave approximation (RWA) [115, 116] which neglects the very fast oscillating term in the Hamiltonian by

$$H(t) = \hbar \begin{bmatrix} 0 & \Omega_1(t) & 0 \\ \Omega_1(t) & \Delta_1 & \Omega_2(t) \\ 0 & \Omega_2(t) & \Delta_1 - \Delta_2 \end{bmatrix}. \tag{3.27}$$

Here $\Omega_1(t)$ and $\Omega_2(t)$ are the Rabi frequencies of the pulses P_1 and P_2, respectively. They are related to their slowly varying amplitudes of the light electric field $\varepsilon_1(t)$ and $\varepsilon_2(t)$ by the relations

$$\Omega_1(t) = -d_{12}\varepsilon_1(t)/\hbar, \qquad \Omega_2(t) = -d_{23}\varepsilon_2(t)/\hbar, \tag{3.28}$$

where d_{12} and d_{23} are components of the dipole-transition moments along their respective electric-field vectors. Δ_1 and Δ_2 are the single photon detunings of the laser pulses from their respective transitions, $\hbar\Delta_1 = E_2 - E_1 - \hbar\omega_1$, $\hbar\Delta_2 = E_2 - E_3 - \hbar\omega_2$, ω_1 and ω_2 are the central frequencies of the laser pulses P_1 and P_2, respectively. E_1, E_2 and E_3 are the energies of the states ψ_1, ψ_2, and ψ_3, respectively.
The matrix of (Eq. 3.27) is expressed in the basis formed by a combination of the unperturbed states $\psi_{i=1,3}$. As in Sec. 3.2.1 this matrix can be expressed in the so-called adiabatic basis using the rotation matrix

$$R(t) = \begin{bmatrix} \sin(\vartheta(t))\sin(\varphi(t)) & \cos(\vartheta(t)) & \sin(\vartheta(t))\sin(\varphi(t)) \\ \cos(\varphi(t)) & 0 & -\sin(\varphi(t)) \\ \cos(\vartheta(t))\sin(\varphi(t)) & sin(\vartheta(t)) & \cos(\vartheta(t))\cos(\varphi(t)) \end{bmatrix}. \tag{3.29}$$

The eigenstates of Eq. (3.26) are then

$$\Psi_+(t) = \psi_1 \sin(\vartheta(t))\sin(\varphi(t)) + \psi_2 \cos(\varphi(t)) + \psi_3 \cos(\vartheta(t))\sin(\varphi(t)), \tag{3.30}$$

$$\Psi_0(t) = \psi_1 \cos(\vartheta(t)) - \psi_3 \sin(\vartheta(t)), \tag{3.31}$$

$$\Psi_-(t) = \psi_1 \sin(\vartheta(t))\cos(\varphi(t)) - \psi_2 \sin(\varphi(t)) + \psi_3 \cos(\vartheta(t))\cos(\varphi(t)). \tag{3.32}$$

Where ϑ and φ are the mixing angles, their expressions in the case of a two photon resonance [123], $\Delta_1(t) = \Delta_2(t) = \Delta(t)$, are

$$\vartheta(t) = \arctan(\frac{\Omega_1(t)}{\Omega_2(t)}), \tag{3.33}$$

$$\varphi(t) = \frac{1}{2}\arctan\left(\frac{\sqrt{\Omega_1^2(t) + \Omega_2^2(t)}}{\Delta(t)}\right), \tag{3.34}$$

where not only the Rabi frequencies but also the detuning can be time dependent. The eigenvalues associated to the three adiabatic states are

$$\varepsilon_0 = 0, \tag{3.35}$$

$$\varepsilon_- = \frac{1}{2}\Delta(t) - \frac{1}{2}\sqrt{\Delta^2(t) + \Omega_1^2(t) + \Omega_2(t)^2}, \tag{3.36}$$

$$\varepsilon_+ = \frac{1}{2}\Delta(t) + \frac{1}{2}\sqrt{\Delta^2(t) + \Omega_1^2(t) + \Omega_2^2(t)}. \tag{3.37}$$

The detuning $\Delta(t)$ can depend on time, we discuss that case in the next chapter for a two level quantum system. For simplicity and illustration, we take here the case where the detuning $\Delta(t) = 0$.

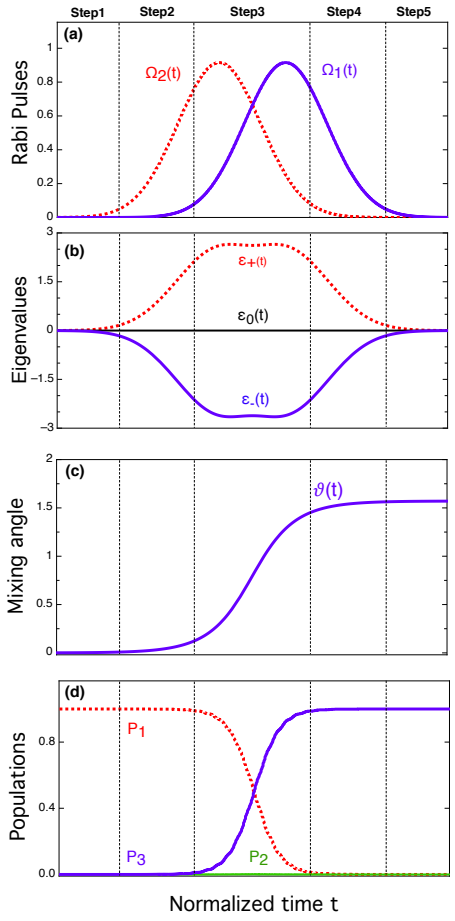

Figure 3.4: (a) Time evolution of the Stokes ($\Omega_2(t)$) and pump ($\Omega_1(t)$) pulses for the STIRAP process, (b) corresponding evolution of the adiabatic frequencies ε_-, ε_0, and ε_+ and (c) the variations of the the mixing angle $\vartheta(t)$. The state conversion from ψ_1 to ψ_3 is accompanied with the mixing angle inversion from the value 0 to the value $\frac{\pi}{2}$. (d) Population transfer from the ground state ψ_1 to the final state ψ_3.

The eigenstate Ψ_0 in (3.31) is of great importance because it only involves the eigenstates ψ_1 and ψ_3. One could use this state to go from state ψ_1 to ψ_3 by control of the

mixing angle $\vartheta(t)$ which depends only on the Rabi frequencies $\Omega_1(t)$ and $\Omega_2(t)$. If the laser pulses are shaped carefully in a way that the value of ϑ tends to zero at the beginning of the evolution and to $\frac{\pi}{2}$ at the end of the process, the passage from the state ψ_1 to ψ_3 will be achieved without contribution of the state ψ_2.

3.3.2 STImulated Raman Adiabatic Passage technique

In the system shown in figure 3.3, we consider the case where the laser frequencies are tuned to resonance with the respective one-photon transitions ($\Delta_1 = \Delta_2 = 0$), this ensures a strong coupling between the levels.
The STIRAP process consists on a complete and efficient transfer of population from an initially populated state ψ_1 into the final, target, state ψ_3 by means of coherent radiations issued usually from laser light that couple the intermediate state ψ_2 to the states ψ_1 and ψ_3. In the STIRAP process, no population is placed in the state ψ_2 and no decay from this intermediate to other states is possible. For the process to work properly and give rise to an efficient population transfer, the coupling laser pulses should evolve adiabatically in time and be applied in a specific order (the counter intuitive order shown on Fig 3.3(b))

The key element of STIRAP process is the eigenstate Ψ_0 of (3.31), this state is called the *dark state*[124], it is immune against loss of population through spontaneous emission because,during the evolution, the state vector $\psi(t)$ stays constantly aligned to the dark state Ψ_0 that does not involve the state Ψ_2.

The process of STIRAP can be considered to occur in five steps [125, 126], each step is limited by a dashed vertical line in Fig. 3.4, these steps are the following

- **Step1 :**

Only the Stokes pluse $\Omega_2(t)$ is present. It couples the final state ψ_3 to the intermediate state ψ_2, inducing Autler-Townes splitting [127] of the energy levels (3.36) and (3.37). All the population remains in the ground state and the state vector $\psi(t)$ is aligned with Ψ_0 and equals to ψ_1 as we can see in Fig. 3.5.

- **Step2 :**

$\Omega_2(t)$ continues to increase and becomes strong while $\Omega_1(t)$ has just switched on and is still much weaker than $\Omega_2(t)$. The state vector $\psi(t) \equiv \Psi_0$ deviates only little from the state ψ_1. There is no transition to ψ_2 because the corresponding transition is inhibited due to the electromagnetically induced transparency (EIT)[1][128, 129].

[1] In a three level Λ-type atomic system in which the coupling between the intermediate state ψ_2 and the final state ψ_3 is much stronger compared to the coupling between the ground state ψ_1 and the intermediate state ψ_2, EIT can be seen as destructive interference (between the quantum events (transitions)) between the two different paths $\psi_1 \rightarrow \psi_2$ and $\psi_1 \rightarrow \psi_2 \rightarrow \psi_3 \rightarrow \psi_2$ to reach ψ_2. This results in a inhibition of the transition from ψ_1 to ψ_2 (transparency) due to the strong coupling between ψ_2 and ψ_3.

- **Step3 :**

The two pulses are present and strong with $\Omega_1(t)$ increasing and $\Omega_2(t)$ decreasing. By consequence, the mixing angle $\vartheta(t)$ switches slowly from 0 to $\frac{\pi}{2}$ (see Figs. 3.5 and 3.4(c)) and the state vector $\psi(t) \equiv \Psi_0$ goes from ψ_1 to $-\psi_3$ without contribution from state ψ_2.

- **Step4 :**

The state vector $\psi(t)$ is now aligned with ψ_3. $\Omega_2(t)$ is too weak to induce a transition to state ψ_2 because $\Omega_1(t)$ couples strongly the states ψ_1 and ψ_2 leading to EIT-based inhibition as in Step2.

- **Step5 :**

The Stokes pluse disappear and the induced Autler-Townes splitting by the pump pulse is reduced to zero. The state vector $\psi(t) \equiv \Psi_0$ is equal to $-\psi_3$.

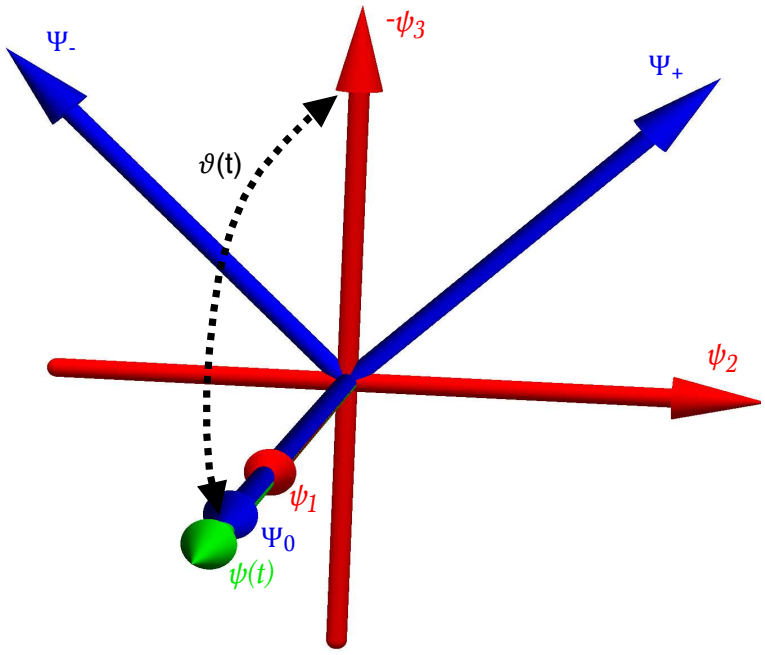

Figure 3.5: Scheme of Hilbert space for the three state system of Fig. 3.3 in the basis formed by state $|\psi_1\rangle$, $|\psi_2\rangle$, and $|\psi_3\rangle$ and in the basis formed by $|\Psi_-\rangle$, $|\Psi_0\rangle$, and $|\Psi_+\rangle$. At earlier times, the mixing angle $\vartheta(t)$ tends to 0 and consequently the state vector $|\psi_1\rangle$ is aligned with $|\Psi_0\rangle$ and at later times $\vartheta(t)$ tends to $\frac{\pi}{2}$ and the same state vector Ψ_0 is aligned with the state ψ_3.

⇨ **Condition of adiabaticity for three state-STIRAP :**

For STIRAP to occur, the local adiabaticity should hold during all the steps. The corresponding adiabatic condition was derived in [130] and reads

$$\left(\Omega_1^2(t)+\Omega_2^2(t)\right)^{1/2} \gg \left|\dot{\vartheta}(t)\right| = \frac{\left|\Omega_2(t)\dot{\Omega}_1(t)-\Omega_1(t)\dot{\Omega}_2(t)\right|}{\Omega_1^2(t)+\Omega_2^2(t)} \tag{3.38}$$

This condition should be satisfied for any given variation of the Rabi frequencies with time. A more useful or "global" condition can be obtained by integrating Eq. (3.38) over the interaction time. It is expressed by means of the effective Rabi frequency area,

$$\mathscr{A} = \int_{-\infty}^{+\infty} \left(\Omega_1^2(t)+\Omega_2^2(t)\right)^{1/2} dt, \tag{3.39}$$

as the integral over $\dot{\vartheta}(t)$ gives $\frac{\pi}{2}$, the condition (3.38) becomes

$$\mathscr{A} \gg \frac{\pi}{2}. \tag{3.40}$$

When the relation (3.40) is not verified, the evolution is not completely adiabatic and the population transfer from ψ_1 to ψ_3 might be incomplete. This global adiabatic condition needs a large pulses area ($\mathscr{A}_{\Omega_1,\Omega_2} = \int_{-\infty}^{+\infty} \Omega_{1,2}(t)dt \gg 1$) for the STIRAP process (with $\Delta = 0$). Under this last condition, the transfer of population from ψ_1 to ψ_3 is complete and efficient.

3.3.3 Dynamics of light transfer in optical waveguides

3.3.3.1 Example of three waveguide system

By analogy with the quantum system studied before, we proceed in the same way for the optical system. We investigate an optical system composed of three identical coupled waveguides (WG). The variable of time in the quantum system is replaced by the variable of space in the optical system. The role of the Rabi frequencies is taken by the coupling constants (see Sec.1.3 in chapter 1). The equations describing the dynamics are equivalent.

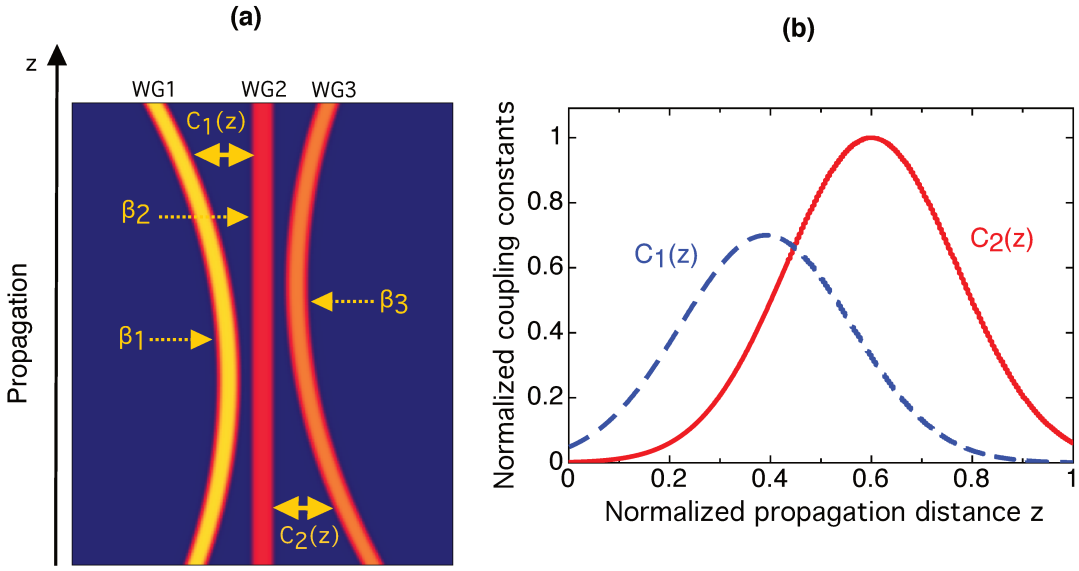

Figure 3.6: (a) Set of three coupled optical waveguides, WG1 is connected to WG2 via the coupling $C_1(z)$ and WG2 is connected to WG3 via the coupling $C_2(z)$, here we take the geometrical averages of the coupling constants $C_1(z) = \sqrt{(C_{12}(z)C_{21}(z))}$ and $C_2(z) = \sqrt{(C_{23}(z)C_{32}(z))}$. The longitudinal propagation constants $\beta_1(z)$, $\beta_2(z)$, and $\beta_3(z)$ are associated to WG1, WG2, and WG3, respectively. (b) The shape of coupling constants $C_1(z)$ and $C_2(z)$ as a function of the normalized propagation distance. This optical system mimics the quantum system shown on figure. 3.3. The optical detunings $\Delta\beta_{21}(z) = \beta_2(z) - \beta_1(z)$ and $\Delta\beta_{23}(z) = \beta_2(z) - \beta_3(z)$ mimic the quantum detunings $\Delta_1(t)$ and $\Delta_2(t)$, respectively.

We start the illustration of quantum-optical analogy by exposing the Schrödinger-like wave equation describing the light propagation along the paraxial direction z (Fig. 3.6). Similarly to (1.43), in the slowly varying envelope approximation, the evolution of the amplitudes of the optical fields a_n, with $n = 1, 2, 3$ in the waveguides, is given by the coupled mode theory and can be written in the form [19]

$$i\frac{da_1}{dz} = C_1(z)a_2, \tag{3.41}$$

$$i\frac{da_2}{dz} = C_1(z)a_1 + \Delta\beta_{21}a_2 + C_2(z)a_3, \tag{3.42}$$

$$i\frac{da_3}{dz} = C_2(z)a_2 + (\Delta\beta_{21} - \Delta\beta_{32})a_3. \tag{3.43}$$

Equations (3.41)-(3.43) have the same form as equations in (1.43), they can be written in their matricial form

$$i\frac{d}{dz}A(z) = \mathsf{H(z)}A(z), \tag{3.44}$$

the Hamiltonian $\mathsf{H(z)}$ in the case of waveguides system reads,

$$\mathsf{H(z)} = \begin{bmatrix} 0 & C_1(z) & 0 \\ C_1(z) & \Delta\beta_{21}(z) & C_2(z) \\ 0 & C_2(z) & \Delta\beta_{21}(z) - \Delta\beta_{23}(z) \end{bmatrix}. \tag{3.45}$$

where $C_1(z) = \sqrt{C_{12}(z)C_{21}(z)}$ and $C_2(z) = \sqrt{C_{23}(z)C_{32}(z)}$ are the geometrical aver ages of the coupling constants representing the mutual influence between the propagating modes in WG1 and WG2 and in WG2 and WG3, respectively. $\mathbf{A}(z) = [a_1(z), a_2(z), a_3(z)]^T$ is a vector state whose components a_1, a_2, and a_3 indicate the amplitudes of the fundamental modes in the three waveguides. $\Delta\beta_{21}(z)$ and $\Delta\beta_{23}(z)$ are the detunings of the longitudinal propagation constant (associated to the phase) between the waveguides WG1 and WG2 and WG2 and WG3, respectively. These detuning are induced by the difference in the propagation constants of the waveguides, if the three waveguides have a same and identical propagation constant $\beta_1(z) = \beta_2(z) = \beta_3(z) = \beta(z)$ these detunings vanish. This situation corresponds to the case of resonant excitation in the quantum atomic system.

In the system shown in figure 3.6, the separation between waveguides is shaped in such a way that the engendered couplings constants evolve similarly as the Rabi frequencies in the atomic system. For waveguides the evolution is in the spatial domain, while in the atomic system it is in the temporal domain. The waveguides shape produces two nearly gaussian pulses of the coupling constant shifted along the z-longitudinal coordinate. In the case of equal detunings

$$\Delta\beta_{21} = \Delta\beta_{23} = \Delta\beta, \tag{3.46}$$

the three adiabatic states for Eq.(3.45) are

$$\mathbf{B}_+(z) = \mathbf{A}_1 \sin(\theta(z)) \sin(\phi(z)) + \mathbf{A}_2 \cos(\phi(z)) + \mathbf{A}_3 \cos(\theta(z)) \sin(\phi(z)), \tag{3.47}$$

$$\mathbf{B}_0(z) = \mathbf{A}_1 \cos(\theta(z)) - \mathbf{A}_3 \sin(\theta(z)), \tag{3.48}$$

$$\mathbf{B}_-(z) = \mathbf{A}_1 \sin(\theta(z)) \cos(\phi(z)) - \mathbf{A}_2 \sin(\phi(z)) + \mathbf{A}_3 \cos(\theta(z)) \cos(\phi(z)), \tag{3.49}$$

where $\mathbf{A}_1 = [1,0,0]^T$, $\mathbf{A}_2 = [0,1,0]^T$, $\mathbf{A}_3 = [0,0,1]^T$ are three unitary vectors in the diabatic basis. The mixing angles $\theta(z)$ and $\phi(z)$ are defined as

$$\theta(z) = \arctan\left(\frac{C_1(z)}{C_2(z)}\right), \tag{3.50}$$

$$\phi(t) = \frac{1}{2}\arctan\left(\frac{\sqrt{C_1(z)^2 + C_2(z)^2}}{\Delta\beta(z)}\right). \tag{3.51}$$

The expressions (3.47)-(3.51) are equivalent to (3.30)-(3.34) for the atomic system. Simi-

larly to (3.35)-(3.37) one can express the corresponding eigenvalues as

$$\epsilon_0 = 0, \tag{3.52}$$

$$\epsilon_-(z) = \frac{1}{2}\Delta\beta(z) - \frac{1}{2}\sqrt{\Delta\beta(z)^2 + C_1(z)^2 + C_2(z)^2}, \tag{3.53}$$

$$\epsilon_+(z) = \frac{1}{2}\Delta\beta(z) + \frac{1}{2}\sqrt{\Delta\beta(z)^2 + C_1(z)^2 + C_2(z)^2}. \tag{3.54}$$

The adiabatic condition can be written[131]

$$|\epsilon_0 - \epsilon_\pm(z)| \gg \left\langle \dot{\mathrm{B}}_\mathbf{0}(z) | \mathrm{B}_\pm(z) \right\rangle, \tag{3.55}$$

which can be simplified for a null detuning ($\Delta\beta = 0$)

$$\sqrt{C_1^2(z) + C_2^2(z)} \gg |\dot{\theta}|. \tag{3.56}$$

This condition is similar to (3.38). We verify its validity by taking an example of two gaussian forms of the coupling constants $C_1(z)$ and $C_2(z)$ with the same maximum amplitude C_0 and the same spatial FWHM of 5mm. $C_1(z)$ reaches its maximum at the distance z=8mm and $C_2(z)$ at z=14.8mm for a full propagation distance of 23mm. The following figure shows the variations of the ratio $\sqrt{C_1^2(z) + C_2^2(z)}/|\dot{\theta}|$ versus the propagation distance

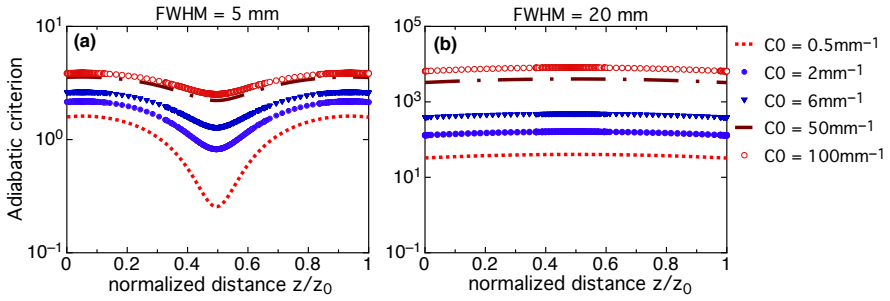

Figure 3.7: The validity of the adiabaticity condition of equation (3.56) versus the propagation distance. The ratio $\sqrt{C_1^2(z) + C_2^2(z)}/|\dot{\theta}|$ is plotted for two different values of FWHM and compared to 1. In the case (a) of $FWHM = 5\,\mathrm{mm}$ and for values of C_0 greater than $C_0 = 2\,\mathrm{mm}^{-1}$, the adiabatic condition is always satisfied. For $C_0 = 0.5\,\mathrm{mm}^{-1}$, it is not satisfied for some distances at the middle of propagation. In the case (b) of $FWHM = 20\,\mathrm{mm}$, the adiabatic condition is always satisfied whatever the value of C_0. C_0 is the maximum amplitude of the coupling constants taken as gaussians for a full propagation $z_0 = 23\,\mathrm{mm}$.

The condition of (3.56) should be fulfilled all along the propagation distance to ensure an efficient and complete light transfer from WG1 to WG3. From Fig. 3.7, this condition is

strongly respected for high values of the maximum amplitude of the coupling constant C_0. For both FWHM, the adiabatic condition gets mores satisfied when C_0 increases as can be seen in Fig. 3.7(a) and (b). In the case of FWHM = 5 mm, and for a C_0 greater than $2\,\mathrm{mm}^{-1}$ the relation $\sqrt{C_1^2(z) + C_2^2(z)}/|\dot{\theta}| \gg 1$ is always verified. For $C_0 = 0.5\,\mathrm{mm}^{-1}$, the condition of adiabaticity is violated for some distances at the middle of the propagation. In the case of FWHM = 20 mm the condition is always fulfilled whatever the value of C_0. Therefore, a sufficiently smooth evolution (broad pulses) and sufficient pulse overlap allow to satisfy the adiabatic conditions all over the propagation even for moderate values of the peak coupling constant C_0.

3.4 Conclusion

Along this chapter, we have presented an example of analogies between quantum mechanics and wave optics. For the case of coupled atomic system, driving population in a three level system from an initial state to a final, target, state is carried out by means of of external laser fields. The Rabi frequencies of the laser fields involved in the process of population control are of great importance, and can be designed in function of the wanted final state. On the same line, waveguides and their reciprocal coupling constant and detuning can be designed as a function of the wished output state. In the case of waveguides, the light transfer is controlled by the spatially varying coupling constants in analogy with the population transfer controlled by the Rabi pulses of the external laser fields.
During the process of population and light transfer in both systems, fulfillment of an adiabatic condition is an essential element. In this way the initial state evolves adiabatically and ends up in the desired final state. The adiabatic condition related either to the Rabi pulses (quantum system) or to coupling constant (optical system) should as good as possible hold along the whole evolution of the system. This, ensures an efficient and optimal population transfer or light transfer.

4 Adiabatic light transfer in non resonant optical waveguides

Contents

4.1 Introduction

In the previous chapter, we have described a concrete example of analogy between quantum mechanics and waveguide optics. It was shown that a three state atomic system is similar to a waveguide system composed of three coupled waveguides, with equivalent variables in the optical system to the quantum system ones. In the quantum case, the dynamics is temporal and governed by Schrödinger equation, while in the optical case, the evolution is spatial and is given by the paraxial wave equation. Moreover, the example of three state STIRAP technique, presented, illustrates this similarity. Several studies in waveguides were inspired by the above STIRAP process [16, 17, 30]. As we have seen for the system presented previously in section 3.3.1, the population can be effectively driven from an initial state to a final target state. The first proposals [19, 132] and the first experimental demonstration [20] of a STIRAP-like process in waveguides have stimulated several studies on adiabatic light passage in waveguides by slight modifications of this concept. These include theoretical and experimental studies related to the fractional STIRAP process [21], multi-state STIRAP [24, 133, 134], beam-splitting [21, 135, 136, 137, 138], adiabatic mode

conversion [134, 139] or the role of nonlinear effects [140]. Generally these approaches profit from the high robustness of the adiabatic process, leading for instance to a broadband behavior of the light spatial adiabatic passage process. However, since the necessary adiabatic condition is better fulfilled at longer than at shorter wavelengths [24], the use of such systems for spectral low-pass or high-pass filtering was also proposed [141, 142].

For these analogies to work properly, the adiabaticity criterion we treated in section 3.2.1 of the precedent chapter should be fulfilled. In the case of waveguides, this requires a smooth spatial evolution of the coupling constant C between neighboring waveguides. Previous studies generally relied uniquely on the spatial variation of C to ensure adiabaticity. As follows from the coupled-mode theory [49], presented in subsection 1.3.2, the coupling constant C is mainly connected to the distance between the evanescently coupled waveguides. Consequently, an adiabatic evolution of the distance separating the waveguides should satisfy this adiabatic criterion. The counterpart of coupling constant in atomic physics is a temporal evolving Rabi frequency Ω which couples the quantum states to each other.
In the case of atomic physics the atom-laser detuning $\Delta\omega$ provides a useful and versatile additional parameter for the adiabatic control of the system evolution. This detuning is given by a temporal dependent mismatch of the central frequency of the driving field from the transition frequency. The corresponding parameter in waveguides is represented by spatial evolution of a detuning $\Delta\beta$ of the propagation constants in the individual waveguides. The introduction of this new parameter will make the system more rich in term of number of controlling parameters at disposal. Therefore, it is expected that also for waveguides the detuning parameter shall increase the possibilities for controlling the adiabatic evolution of the propagating light fields. Moreover, the combination of these two parameters will help to explore and address new phenomena and analogies. Its is worth to point out that the interest of directional couplers with linearly varying propagation constant has been recognized for tapered waveguides [143, 144, 145] and transfer of light has been investigated. Nevertheless, the combination with a spatially evolving coupling constant received little attention.

In this chapter we address this issue in relation with existing quantum phenomena for the first time to our knowledge. We consider two coupled waveguides with spatially modulated coupling coefficients and we study theoretically and experimentally the effect of a spatially modulated detuning $\Delta\beta(z)$ (associated to a longitudinal variation of the index contrast) on the adiabatic light transfer between them. We choose two concrete examples of analogies. The first mimics the Rapid Adiabatic Passage (RAP) process [30] in quantum physics for which the detuning crosses zero at the moment the coupling constant reaches its maximum strength, which leads to a robust and rapid way to adiabatically invert a two-state system. Such a population transfer by adiabatic passage via a level crossing was initially implemented in nuclear magnetic resonance [146]. Laser-driven adiabatic passage

in atoms and molecules was proposed by Treacy [147] and demonstrated first in the infrared by Stark-shifting the transition frequency [148], or by sweeping the laser frequency through resonance [149]. Also, adiabatic passage was observed also in the near-infrared [150] and with visible light [151]. Further details can be found in Refs. [30, 152, 153]. The second example of analogy mimics the so-called two-state STIRAP process [28, 29], which leads finally to an equal coherent superposition of the two states. Two-state STIRAP was experimentally demonstrated by Yamazaki et al. [154] with a trapped $^{40}Ca^{+}$ ion. In the case of waveguides the RAP process implements an achromatic directional coupler, while the two-state STIRAP process implements a broadband one-to-two beam splitter. The experiments for implementation of two-state STIRAP and RAP are performed with the help of reconfigurable photoinduced waveguides recorded through the photorefractive effect using the lateral illumination technique [24, 155, 156] that we have extensively described in section 2.4. Two probing wavelengths more than 200 nm apart are used for both structures in order to verify the expected achromaticity. We start in section 4.2 by recalling the general framework for the studies in which we expose the mathematical formalism and the parameters involved in these processes. Then in section 4.3, we address the case of the RAP-like process, we give the theoretical and experimental results and discuss them in the framework of the adiabatic approach. The following section 4.4 treats the case of two-state STIRAP, we present its theoretical and experimental results and discuss the robustness and adiabaticity. The experimental results are in good agreement with the theoretical expectations in both cases. These results show the crucial role of the waveguide detuning $\Delta\beta(z)$ in driving the system adiabatically to the desired output configuration while remaining robust and achromatic. Most of the results of this chapter were exposed in [157].

4.2 General framework

We consider two neighboring waveguides with different longitudinal propagation constants $\beta_1(z)$ and $\beta_2(z)$ for their fundamental mode. In paraxial approximation, the propagation of a monochromatic light wave in such a structure can be analyzed in the framework of the coupled mode theory (see Sec. 1.3) (CMT)[49] which treats the problem in a discrete way by involving the evanescent coupling between the waveguides. The corresponding evolution of the waves amplitudes can then be described by two coupled differential equations, which, similarly as in [19, 156, 158], read as follows in the present case

$$i\frac{d}{dz}\begin{bmatrix} a_1(z) \\ a_2(z) \end{bmatrix} = \begin{bmatrix} \beta_1(z) & C(z) \\ C(z) & \beta_2(z) \end{bmatrix} \begin{bmatrix} a_1(z) \\ a_2(z) \end{bmatrix} . \tag{4.1}$$

Equation (4.1) can be rewritten following the same procedures as in [19, 156, 158] to get the following form

$$i\frac{d}{dz}\begin{bmatrix} a_1(z) \\ a_2(z) \end{bmatrix} = \begin{bmatrix} -\Delta\beta(z)/2 & C(z) \\ C(z) & \Delta\beta(z)/2 \end{bmatrix} \begin{bmatrix} a_1(z) \\ a_2(z) \end{bmatrix} \ . \tag{4.2}$$

Here the components of $\mathbf{A}(z) = [a_1(z), a_2(z)]^T$ are, besides for an unimportant phase, proportional to the amplitudes of the fundamental modes in the two waveguides. We call $\mathbf{H}(z)$ the coupling matrix in the above equation, which takes the role of the Hamiltonian and describes the interaction between the waveguide modes. It depends on the detuning parameter $\Delta\beta(z) = \beta_2(z) - \beta_1(z)$ as well as on the space-dependent coupling constant $C(z)$ between the two waveguides. Note that the latter corresponds to the geometrical average of the values for the coupling from waveguide 1 to 2 and from waveguide 2 to 1 [156], $C(z) = \sqrt{C_{12}(z)C_{21}(z)}$, which can be different due to the local asymmetry. By substituting the space coordinate z for the time coordinate t in the Schrödinger-type equation (B.2), the two-waveguides system is fully equivalent to a coupled quantum two-level system, which population amplitude dynamics is described by the same equation within the rotating wave approximation [30, 159]. As discussed, the role of the coupling constant $C(z)$ is then taken by the Rabi frequency $\Omega(t)$ and the waveguide detuning $\Delta\beta(z)$ is equivalent to the atom-laser detuning $\Delta\omega(t)$.

Equation (B.2) is expressed in the natural basis formed by the modes of the two waveguides, called diabatic basis. However, we can rewrite it in another basis, called adiabatic basis, where the basis vectors are the local (instantaneous) eigenvectors of the space-varying Hamiltonian. This leads to

$$i\frac{d}{dz}\begin{bmatrix} b_1(z) \\ b_2(z) \end{bmatrix} = \begin{bmatrix} -\epsilon(z) & -i\ d\theta/dz \\ i\ d\theta/dz & \epsilon(z) \end{bmatrix} \begin{bmatrix} b_1(z) \\ b_2(z) \end{bmatrix} \ , \tag{4.3}$$

where the quantities ϵ and θ are given by

$$\epsilon(z) = \left(C^2(z) + (\Delta\beta/2)^2\right)^{1/2} \ , \tag{4.4}$$

and

$$\theta(z) = \frac{1}{2}\arctan\left(2C(z)/\Delta\beta(z)\right) \ . \tag{4.5}$$

The vector $\mathbf{B}(z) = [b_1(z), b_2(z)]^T$ contains the modes amplitudes in the adiabatic basis. Equation (4.3) is perfectly similar to Eq. (3.17) seen in section 3.2.2 for the time evolving quantum system. The amplitudes in the adiabatic and diabatic basis are connected by a space-dependent rotation operator such that $\mathbf{A}(z) = \mathbf{R}(\theta(z))\mathbf{B}(z)$, with

$$\mathbf{R}(\theta(z)) = \begin{bmatrix} \cos\theta(z) & \sin\theta(z) \\ -\sin\theta(z) & \cos\theta(z) \end{bmatrix} \ . \tag{4.6}$$

For an adiabatic evolution, the amplitudes $C(z)$ and $\Delta\beta(z)$ should vary slowly so that $\theta(z)$ evolves smoothly in order to ensure that the adiabatic state vector $\mathbf{B}(z)$ remains fixed in the adiabatic basis. To do so, the following condition [1] should be fulfilled [30]

$$\frac{1}{2}\left|\frac{\partial C}{\partial z}\Delta\beta - C\frac{\partial \Delta\beta}{\partial z}\right| \ll \left(C^2 + \left(\frac{\Delta\beta}{2}\right)^2\right)^{3/2} . \tag{4.7}$$

When the adiabatic condition holds, the state vector $\mathbf{B}(z)$ remains fixed in the space-varying basis formed by the adiabatic states. In particular, if the state vector $\mathbf{B}(z)$ coincides with a single adiabatic state at some distance z, then it will remain in that adiabatic state as long as the evolution is adiabatic, the state vector $\mathbf{B}(z)$ will adiabatically follow this state.

The two eigenstates (the adiabatic states) of the rotation matrix (4.6) are

$$\mathbf{B}_-(z) = \mathbf{A}_1 \cos\theta(z) - \mathbf{A}_2 \sin\theta(z) , \tag{4.8a}$$
$$\mathbf{B}_+(z) = \mathbf{A}_1 \sin\theta(z) + \mathbf{A}_2 \cos\theta(z) , \tag{4.8b}$$

where $\mathbf{A}_1$ and $\mathbf{A}_2$ are the two diabatic states of the system. In general, the state vector $\mathbf{B}(z)$ is aligned with an initial state at the beginning of the propagation and aligned with a specified target state at the end of the propagation. Under appropriate conditions, this alignement can be provided by a single adiabatic state or by a superposition of the adiabatic states. In the first situation, this state is called an *adiabatic transfer state*.

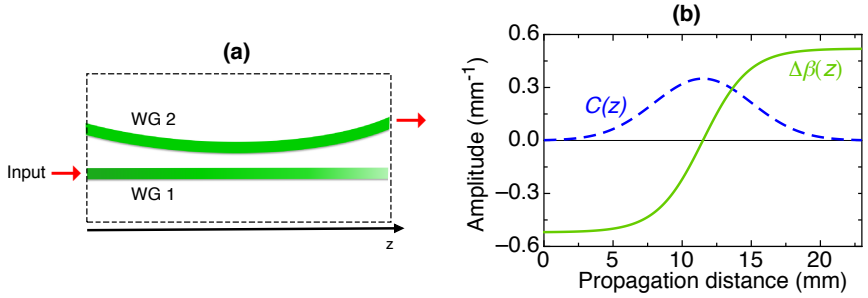

Figure 4.1: (a) Schematic of the waveguide structure providing an optical analogy to the RAP process. (b) Corresponding longitudinal evolution of the coupling constant $C(z)$ and of the detuning $\Delta\beta(z)$. Note that on the scheme (a) the longitudinal and transverse dimensions are not in scale.

In the next sections we will apply and verify the above general behavior to the specific cases of the RAP-like and two-state STIRAP-like light transfer. The waveguide structure being studied for RAP-like process is shown schematically in Fig. B.3(a). It is composed

[1] This condition stems from the requirement that the outer diagonal elements in the matrix in Eq. (4.3) should be small with respect to the diagonal elements

of two planar waveguides where the light is confined only in the plane of the drawing. One of the waveguide is straight (WG1) while the other is weakly curved (WG2), so that the distance separating them and the coupling constant C evolves with z. The propagation constant β_1 of WG1 changes with z, which is achieved in our case by means of a variation of its refractive index contrast. The propagation constant β_2 is left constant.

4.3 RAP-like light transfer

The waveguide structure used to simulate the RAP process is shown schematically in Fig. B.3(a). The corresponding evolution of the parameters $C(z)$ and $\Delta\beta(z)$ are shown in Fig. B.3(b). These parameters mimic the experimental situation discussed below. For the RAP process to occur, it is essential that the detuning should cross zero during the evolution, which is the case for the function $\Delta\beta(z)$ in Fig. B.3(b), that follows normally a tanh function with its zero corresponding to the maximum of $C(z)$ (nearest distance between the waveguides).

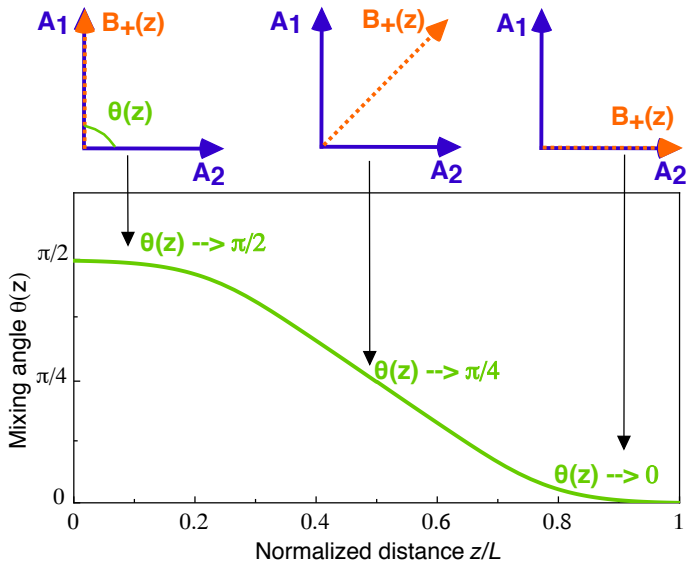

Figure 4.2: Representation of the state inversion as the mixing angle $\theta(z)$ evolves along the propagation distance. In the basis formed by ($\mathbf{A}_1$,$\mathbf{A}_2$), the adiabatic state $\mathbf{B}_+(z)$ is aligned with $\mathbf{A}_1$ when $z \to 0$ and $\theta(z \to 0) \to \frac{\pi}{2}$. At half distance, where the detuning $\Delta\beta(z = L/2)$ is zero, $\mathbf{B}_+$ is equally distributed on the states $\mathbf{A}_1$ and $\mathbf{A}_2$. $\mathbf{B}_+(z)$ ends up in $\mathbf{A}_2$ at the end of the propagation and $\theta(z \to L) \longrightarrow 0$, so that a complete light transfer is achieved. L is the full propagation distance, taken equal to 23 mm in our experiments.

At early and late distances the magnitude $|\Delta\beta(z)|$ is much larger than $C(z)$, while the contrary is true near the zero-crossing point. Since the mixing angle $\theta(z)$ depends

strongly on the ratio $C/\Delta\beta$ (see Eq. (4.5)), $\theta(z)$ evolves during the propagation (see Fig. 4.2). Initially ($z = 0$), this ratio tends to 0 and 2θ is nearly equal to π, so that $\theta \approx \pi/2$ (situation depicted in the left side of Fig. 4.2). With increasing z, $C(z)$ and $\Delta\beta(z)$ increase ($\Delta\beta(z)$ approaches zero from the negative side), which leads to a decrease of $\theta(z)$. At half distance, $\Delta\beta(z)$ vanishes and $C(z)$ reaches its maximum, so that $2\theta = \pi/2$ and $\theta = \pi/4$ which corresponds to the situation shown in the intermediate stage in Fig. 4.2. In the following $\Delta\beta(z)$ continues to increase and becomes again much larger than $C(z)$, which is decreasing, so that θ tends to zero at large distances (configuration in the right side of Fig. 4.2). Consequently, starting initially from state A_1 (all light in WG1), the system follows adiabatically the adiabatic state $B_+(z)$ of Eq. (4.8b) and eventually ends up in state A_2 (all light in WG2). This implies that a complete light transfer should take place. This adiabatic process is intrinsically robust and is expected to take place over a wide range of the design parameters and of the propagating wavelengths for a given design, which means that the behavior should be highly achromatic.

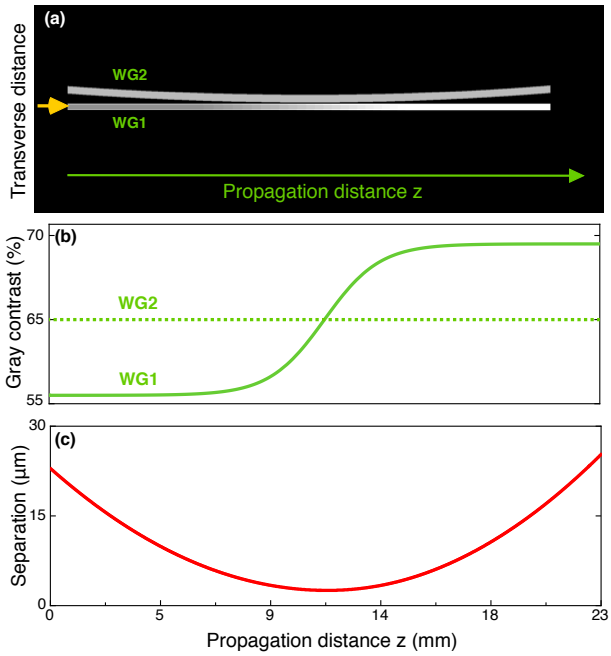

Figure 4.3: (a) Designed SLM images of two waveguides for experimental demonstration of RAP process. (b) shows the variations of the gray level (which induces variation in refractive index contrast) of SLM images, the curved waveguide has a constant gray level where the straight waveguide has a modulated gray level. (c) shows the modulated separation distance variations along the propagation distance.

We have verified the above expectations by using photoinduced dynamic waveguides recorded by a properly structured lateral control illumination technique (see Sec. 2.4) on a $Sr_xBa_{1-x}Nb_2O_6$ (SBN) crystal with $x = 0.61$. Essentially, the combination of a local illumination by the control beam and of the electric field applied to the photorefractive

SBN crystal leads to a local modification of the refractive index landscape of the crystals. This modification is such that maxima of the refractive index are found at the positions of maximum illumination, leading therefore to a guiding waveguide structure. Variations of the index contrast (and of the propagation constant) can be achieved by varying locally the intensity (grey level) of the control light being directed from the spatial light modulator (SLM) to the crystal. Since the recording and erasure of the structures takes only few tens of seconds in SBN, the technique provides the advantage of being able to produce reconfigurable structures in a unique crystal. Moreover, the dynamics of the waveguide recording process can be exploited to characterize the index contrast interferometrically as described in Subsec. 2.4.2.

An example of image sent to SLM is presented in Fig. 4.3(a), it corresponds to the one we use for generation of the structure in which RAP should take place. It is similar to figure. B.3(a) but with parameters directly involved in the optical RAP-like structure generation. One of the two waveguides (WG2) presents a curvature while the other (WG1) is straight. The gray level of the image leading to WG1 changes along the z-distance while the gray level is constant for WG2. The coupling constant C is related to the distance between waveguides by Eq. (1.53), the separation distance profile shown in Fig. 4.3(c) reproduces a gaussian profile for the parameter $C(z)$. The gray level profiles in Fig. 4.3(b) gives constant propagation constant for WG2 and approximates an hyperbolic tangent for WG1.

The design of the waveguide configuration used to demonstrate the RAP-like effect is such that both $C(z)$ and $\Delta\beta(z)$ have a smooth evolution to satisfy at best the adiabaticity criterion of Eq. (4.7) within the limits permitted by the physics of our experimental approach. The nominal z-dependences corresponding to Fig. B.3(b) are $C(z) = C_{max}\exp[-((z-z_0)/\sigma_0)^2]$ and $\Delta\beta(z) = \Delta\beta_{max}\tanh[2\pi(z-z_0)/L]$, where C_{max} is the maximum of the coupling constant reached at half the propagation distance $z_0 = 11.5$ mm, it corresponds to the minimum separation distance as shown in Fig. 4.3(c). $\sigma_0 = 5$ mm is the 1/e half-width of the gaussian coupling-constant pulse, $\Delta\beta_{max}$ is the maximum of detuning, the function $\Delta\beta$ crosses *zero* and the half distance of propagation, when the coupling constant C reaches it maximum, and $L = 23$ mm is the full propagation distance in the crystal. The parameters C_{max} and $\Delta\beta_{max}$ depend not only on the design of the waveguide but also on the probe wavelength. Their values were estimated by carrying out preliminary experiments in non-modulated waveguides. The estimation of coupling constant is done by observation of coupling of waves in uniform parallel directional couplers, we create a set of two identical parallel waveguides with different separations as described in Subsec. 2.4.2.2. For the estimation of $\Delta\beta$, we carry out interferometric measures using a *Mach–Zehnder* scheme during the formation process of the waveguides. We create a set of waveguides with same geometry but with different contrast of their refractive index, and measure the refractive index shift with respect to a reference value (see Subsec. 2.4.2.2).

For our experimental conditions we estimate the parameters within a precision of roughly 15%, $C_{max} = 0.35 \pm 0.05$ mm^{-1} and $\Delta\beta_{max} = 0.52 \pm 0.08$ mm^{-1} for the probe wavelength of 633 nm, as well as $C_{max} = 0.49 \pm 0.07$ mm^{-1} and $\Delta\beta_{max} = 0.32 \pm 0.05$ mm^{-1} for the probing at 850 nm. With the above parameters the expected evolution of the light intensity in the two-waveguide structure of Fig. B.3(a)+(b) can be obtained from Eq. (B.2) and is shown in Figs. 4.4(a) and 4.4(b), for the wavelengths 633 and 850 nm, respectively. In both cases at the output of the structure one expects essentially a switch from WG1 to WG2. The corresponding experimental results are shown on Fig. 4.4(c) and 4.4(d), which depict the intensity profile at the output of the crystal. The dashed blue lines give the output of the reference waveguide, that is WG1 in absence of WG2. When the RAP-like structure including the WG2 is produced, the light output switches to WG2 for both wavelengths (solid red lines).

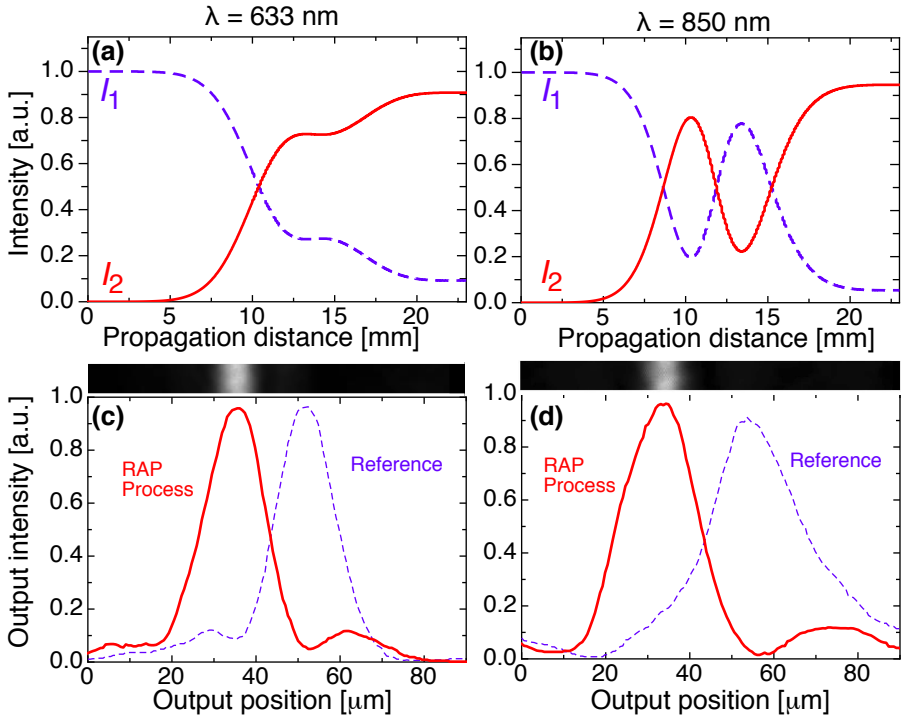

Figure 4.4: Theoretical expectation and experimental verification of the RAP-like light transfer for the parameter given in the text. (a) Numerically calculated spatial evolution of the intensity in WG1 (blue dashed curve) and WG2 (solid red curve) for λ=633 nm. (b) Same for λ=850 nm. (c) Measured intensity output distribution with WG1 but in the absence of WG2 (reference, blue dashed line) and with the presence of both waveguides (solid red line). (d) Same for λ=850 nm and the same structure.

It is worth verifying that the detuning is essential for the above RAP-like light transfer to occur. Figure 4.5 shows the expected and measured behavior for the same kind of

two-waveguide structure leading to the results in Fig. 4.4, but in the absence of detuning ($\Delta\beta(z) = 0$). As seen in Fig. 4.5 in this case the RAP process does not take place and the results are not robust as will be detailed in the next section. An essentially complete return of the light to the straight waveguide is expected for λ=633 nm, while a strong transfer to the curved waveguide is expected for λ=850 nm (see Fig. 4.5(a) and (b)). This is confirmed by the experimental results of Fig. 4.5(c) and 4.5(d), respectively. Therefore, such a structure essentially leads to a damped Rabi-like oscillation between the two waveguides, with very different output distributions for the two probing wavelengths.

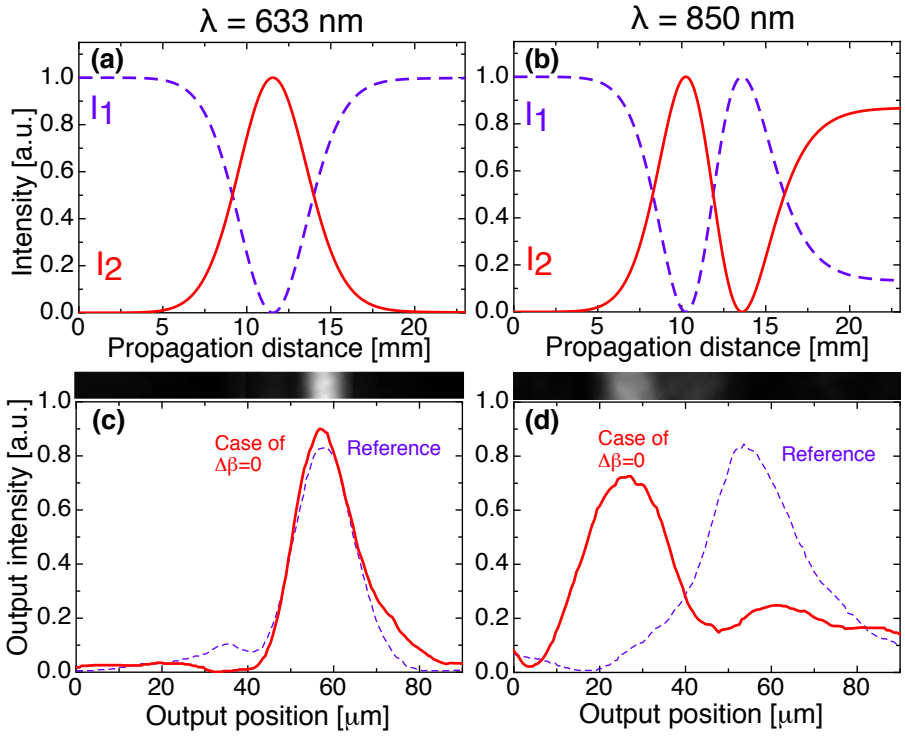

Figure 4.5: Counter example to the RAP process in absence of the detuning ($\Delta\beta(z) = 0$). (a) Expected evolution of the intensity in WG1 (blue dashed curve) and WG2 (solid red curve) according to Eq. (B.2) for λ=633 nm. (b) Same for λ=850 nm. (c) Measured intensity output distribution with WG1 but in the absence of WG2 (reference, blue dashed line) and with the presence of both waveguides (solid red line). (d) Same for λ=850 nm and the same structure.

Even though the experiments on the RAP-like light transfer of Fig. 4.4 give satisfactory results, the corresponding experimental parameters are still at the edge of the zone for which the adiabatic condition is fulfilled at best in the $(C_{max}, \Delta\beta_{max})$-space. In order to illustrate this, we study the robustness with respect to these two parameters by plotting the expected intensity transferred to WG2 as a function of C_{max} and $\Delta\beta_{max}$. Figure 4.6 gives a contour plot of the theoretically expected transferred intensity as a function of

these two parameters. Clearly the experimental parameters (blue circle for 633 nm and green square for 850 nm) are at the border of the red region of maximum adiabaticity. The counter example in absence of detuning corresponds to points on the abscissa of the diagram of Fig. 4.6. It is also worth noting that upon an increase of the wavelength, one gets a higher coupling constant (see Sec. 1.3.2) but a lower detuning. This means that the increase of wavelength corresponds to moving transversally with respect to the direction leading to a maximum fulfillment of the adiabatic condition. The decrease in the detuning is due on one hand to the proportionality of β on $1/\lambda$, and, on the other hand, to a slight decrease of the electro-optic response and of the index contrast in the SBN material for longer wavelengths.

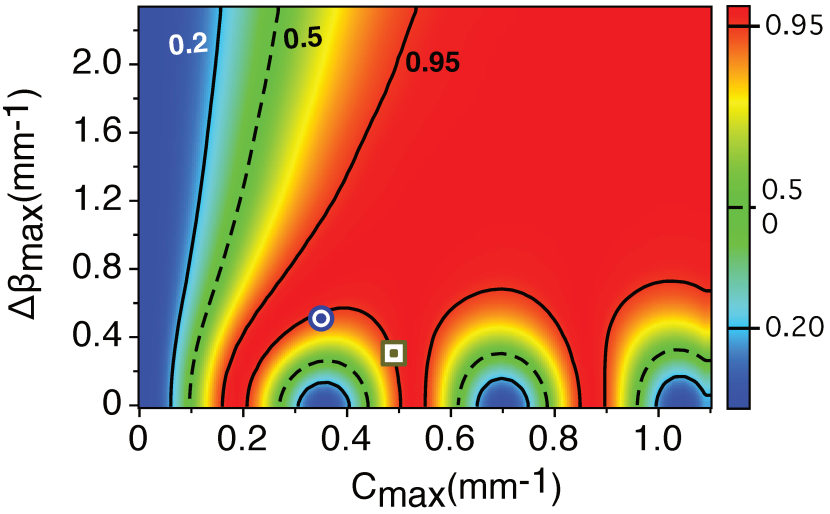

Figure 4.6: Landscape of the expected output intensity of WG2 for the RAP-process as calculated using coupled mode theory under variation of the parameters C_{max} and $\Delta\beta_{max}$. The red area correspond to the region where the adiabatic condition is fulfilled the best and the light transfer is complete. The blue circle and the green square correspond to the experimental conditions of Fig. 4.4 for probing at 633 nm and 850 nm, respectively.

4.4 Two-state STIRAP-like beam splitting

The concept of two-state STIRAP [28] relies on a mathematical analogy between the equations governing the population dynamics of a two-level system with a temporally varying detuned coupling field and a resonantly coupled chainwise-linked three-level system leading to the standard STIRAP process. As discussed above, the two-level system is described by a time-dependent Schrödinger equation of two complex variables. The latter can be recast as three coupled equations of three real variables [159, 160] in the form of

the optical Bloch equation. This, on its turn, can be brought in a form equivalent to the Schrödinger equation applying to the standard STIRAP process in a three-level system. In this way, knowledge about the STIRAP process can be directly inherited for the chirped two-state excitation [17, 28]. Ultimately the detuning of the two-level excitation can be identified with the Stokes pulse of a three-level STIRAP system (the Rabi-frequency pulse that couples the target state and the intermediate state), while the Rabi-frequency of the two-level system is identified with the corresponding pump pulse of STIRAP, which couples the initial and the intermediate state. For the analogy between the two-state STIRAP process and the coupling within a pair of detuned waveguides we can consider two distinct cases. The first one, *Case A*, is the one where the waveguide detuning $\Delta\beta(z)$ is spatially preceding the coupling constant $C(z)$. This case is equivalent to a counter-intuitive sequence in the standard three-state STIRAP process [16, 17]. It corresponds to the situation shown in Fig. 4.8(a) and Fig. 4.8(b).

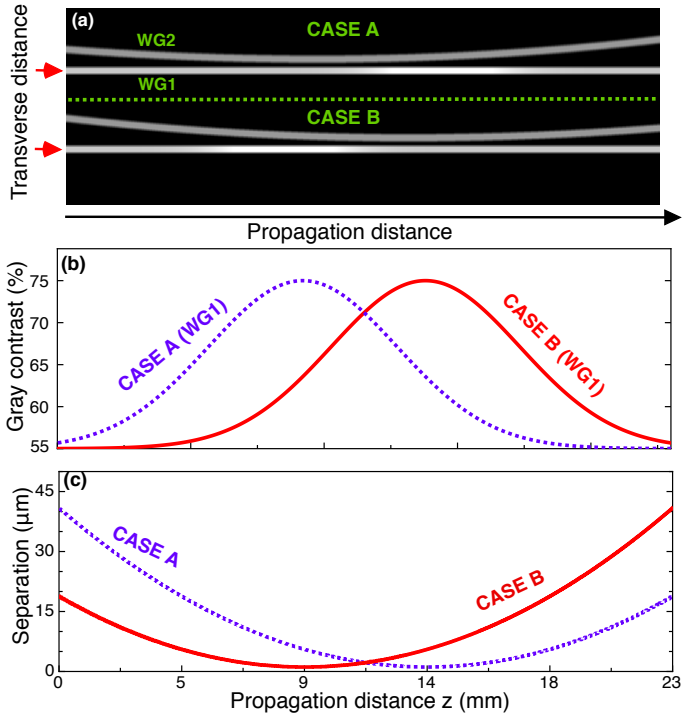

Figure 4.7: Designed images of two waveguides for experimental demonstration of two–state STIRAP process. (a) shows the designed structures for case A and case B, (b) and (c) show the dependence of the gray contrast and the separation distance between the waveguide along the propagation distance for both cases.

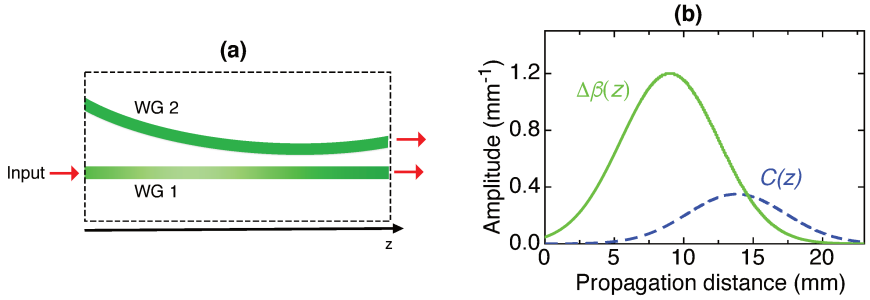

Figure 4.8: (a) Schematic of the waveguide structure providing an optical analogy to the two-state STIRAP process in the case A. (b) Corresponding longitudinal evolution of the coupling constant $C(z)$ and of the detuning $\Delta\beta(z)$. Note that on the schemes (a) the longitudinal and transverse dimensions are not in scale.

The second case, *Case B*, has the coupling preceding the detuning and would correspond to an intuitive order of the pulses for an atomic three-level system. The waveguide structure designed for two-state STIRAP implementation is shown in Fig. 4.7. The gray contrast level of the curved waveguide is maintained fixed, the one of the straight waveguide is variable (see Fig. 4.7), its dependence on the propagation distance is shown in Fig. 4.7(b). The distance separating WG1 and WG2 also varies, its dependence is shown in Fig. 4.7(c).

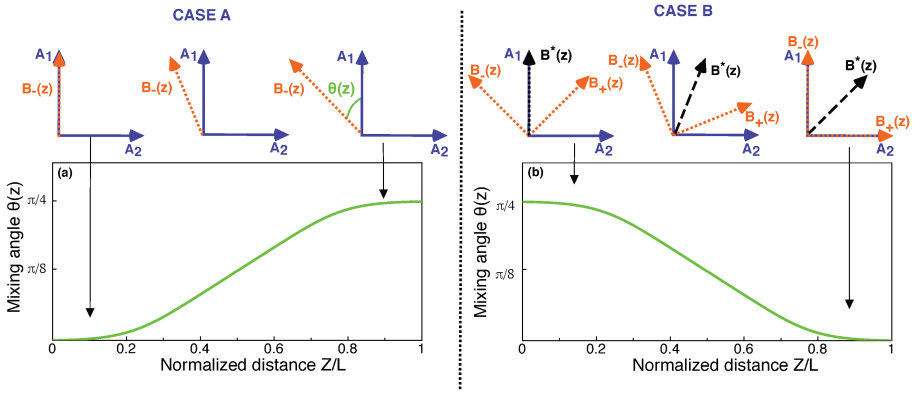

Figure 4.9: (a) Evolution of the mixing angle $\theta(z)$ with the propagation distance z. (b) Evolution of the adiabatic state used for light transfer in the base formed by the diabatic states ($\mathbf{A}_1$, $\mathbf{A}_2$) according to the mixing angle $\theta(z)$.

We start by discussing *Case A* with the help of the general relationships given in Section 4.2. Initially only $\Delta\beta(z)$ is present (see Fig. 4.8(b)) and its amplitude increases continuously, while $C(z)$ is negligibly small. Therefore the ratio $\Delta\beta(z)/C(z) \to +\infty$ and the mixing angle $\theta(z)$ in (4.9(a)) is initially equal to zero, as shown in the left diagram of Fig. 4.9. With (4.8a) this implies that the state $\mathbf{B}_-$ is initially aligned with $\mathbf{A}_1$ as illustrated in Fig. 4.9 for Case A. If we inject light in waveguide 1 the system is therefore

initially in the adiabatic state $\mathbf{B}_-$ and the diabatic state $\mathbf{A}_1$. Subsequently, $\Delta\beta(z)$ increases towards its maximum value, as long as $C(z)$ is still small, $\mathbf{B}_-$ deviated only little from the state $\mathbf{A}_1$. When $\Delta\beta(z)$ is behind its maximum and $C(z)$ reaches comparable values, the angle θ rises and the adiabatic transfer state $\mathbf{B}_-$ is no longer aligned with $\mathbf{A}_1$ but becomes a superposition of $\mathbf{A}_1$ and $\mathbf{A}_2$. At the final stage, $\Delta\beta(L)$ tends to zero and $\Delta\beta(L)/C(L) \to 0$, so that $\theta(L)$ tends to $\pi/4$ (as seen Fig. 4.9). Consequently, the system shall tend to $\mathbf{B}_-(L) = (\mathbf{A}_1 - \mathbf{A}_2)/\sqrt{2}$, which leads to an equal intensity of the light in the two waveguides, as shown in Fig. 4.10(a).

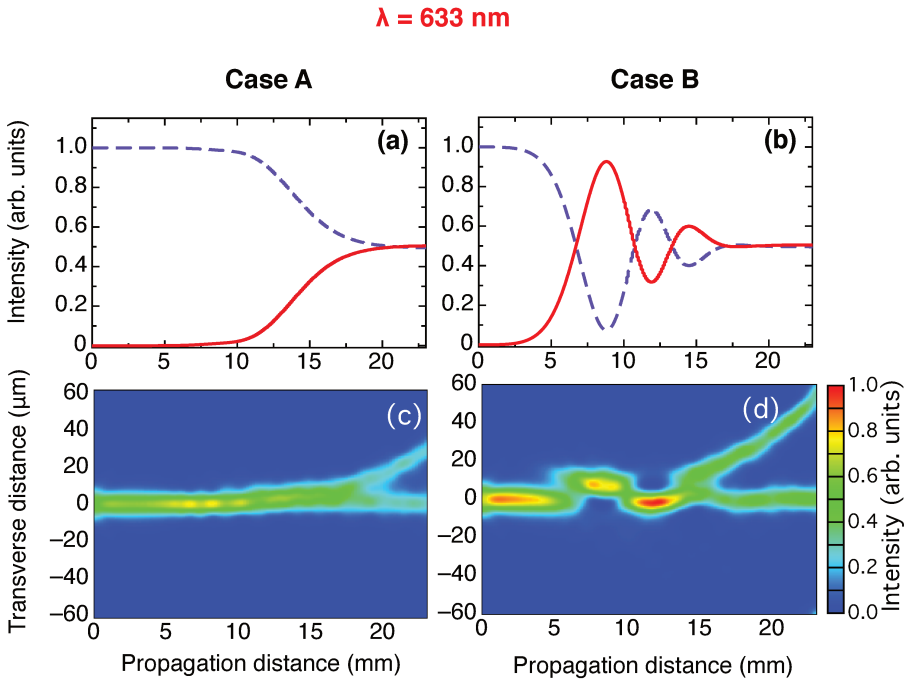

Figure 4.10: Theoretical expectations for a two-state STIRAP-like waveguide structure modeled for propagation of light at the 633 nm wavelength. Panels (a) and (c) correspond to case A, panels (b) and (d) to case B. (a) and (b) show the intensity evolution in WG1 (dashed blue line) and WG2 (solid red line) obtained from coupled mode theory. Panels (c) and (d) show the corresponding evolution of the light distribution obtained with the alternative beam propagation method (BPM). For both cases the system leads to an equal splitting of the input intensity among the two waveguides.

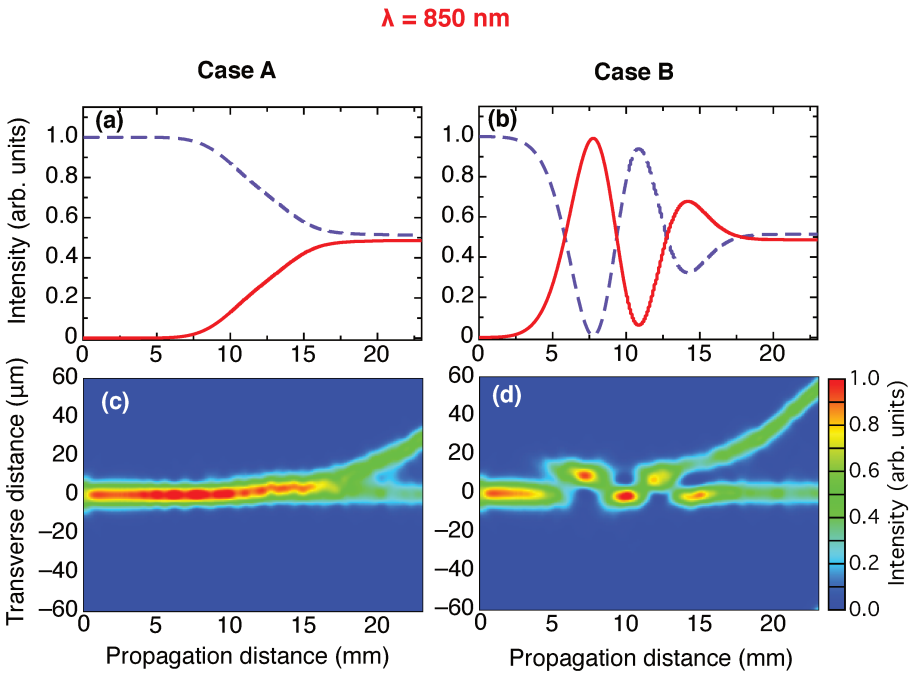

Figure 4.11: Theoretical expectations for a two-state STIRAP-like waveguide structure modeled for propagation of light at the 850 nm wavelength. Panels (a) and (c) correspond to case A, panels (b) and (d) to case B. (a) and (b) show the intensity evolution in WG1 (dashed blue line) and WG2 (solid red line) obtained from coupled mode theory. Panels (c) and (d) show the corresponding evolution of the light distribution obtained with the alternative beam propagation method (BPM). For both cases the system leads to an equal splitting of the input intensity among the two waveguides.

The *Case B* corresponds to the situation where the light is injected in WG1 from the right side of the structure in Fig. 4.8(a). In this case, the ratio $\Delta\beta(z)/C(z)$ goes from 0 to $+\infty$ and $\theta(z)$ (see figure 4.9(b)) from $\pi/4$ to 0. Importantly, in this situation the initial state $\mathbf{A}_1$ (injection in WG1) does not correspond to one of the adiabatic states $\mathbf{B}_-$ or $\mathbf{B}_+$, but to a superposition $\mathbf{B}^*$ of them given by

$$\mathbf{B}^*(z) = \frac{1}{\sqrt{2}}(\mathbf{B}_-(z) + \mathbf{B}_+(z)) \ . \tag{4.9}$$

Therefore, unlike for case A where only one adiabatic state is involved, here the system is expected to remain in the superposition state $\mathbf{B}^*$ as long as the system evolves adiabatically. Since at the end of the structure $\theta(L) = 0$, the system shall converge towards $\mathbf{B}^*(L) = (\mathbf{A}_1 + \mathbf{A}_2)/\sqrt{2}$, which is again an equal intensity distribution of the light in the two waveguides, as shown in Fig. 4.10(b). However, unlike for case A, the evolution towards this 50:50 splitting presents here some transient oscillations.

The curves shown in Fig. 4.10(a) and (b) are modeled according to the parameters used for the experiments given below and the following functions, $\Delta\beta(z) = \Delta\beta_{max} \exp[-((z -$

$z_1)/\sigma_0)^2]$ and $C(z) = C_{max}\exp[-((z-z_2)/\sigma_0)^2]$, where $z_1 = 9$ mm and $z_2 = 13.8$ mm for case A, and $z_1 = 13.8$ mm and $z_2 = 9$ mm for case B. A common $1/e^2$ half-width of $\sigma_0 = 5$ mm is used. The values of $\Delta\beta_{max}$ and C_{max} are those for the wavelength of 633 nm, which are shown as a blue point on the landscape applying to the two-state STIRAP case in Fig. 4.12. These are $\Delta\beta_{max} = 1.2 \pm 0.18$ mm^{-1}, and $C_{max} = 0.35 \pm 0.05$ mm^{-1}. The corresponding values for the same structure but for the wavelength of 850 nm (green square in Fig. 4.12) are $\Delta\beta_{max} = 0.73 \pm 0.11$ mm^{-1} and $C_{max} = 0.52 \pm 0.08$ mm^{-1}, where the errors correspond to the experimental conditions. Figure 4.10 also contains numerical calculations of the beam propagation in waveguide structures corresponding to case A and case B using the Beam Propagation Method (BPM) [161, 162]. We use this second method to design optical waveguides and predict the light evolution in such structures. The structure design only takes as an input the form and the index profile of the waveguides and does not assume anything with respect to coupled wave theory. As can be seen in Figs. 4.10(c) and 4.10(d), the BPM calculations also correctly predict the smooth evolution for case A, and the initial oscillations for case B, in agreement with the curves in Figs. 4.10(a) and 4.10(b) obtained from coupled wave theory.

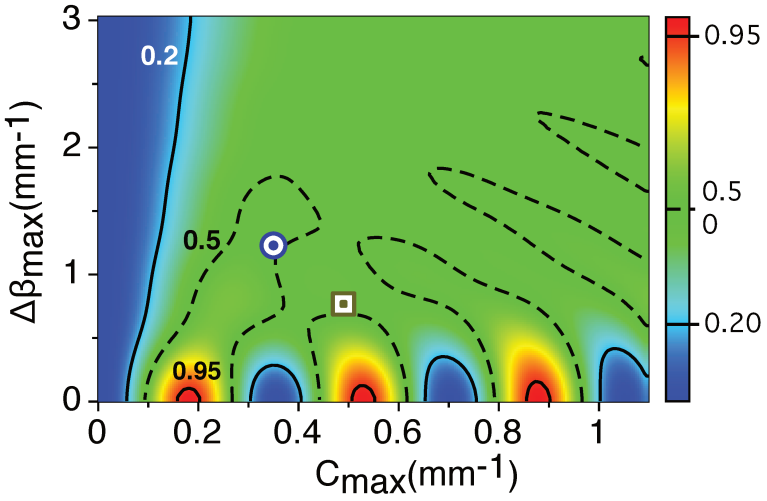

Figure 4.12: Landscape of the expected output intensity of WG2 for the two-state STIRAP process (case A) showing the relative intensity transferred from WG1 to WG2. The green area gives the region where the adiabatic condition is best fulfilled and the waveguide structure gives essentially a 50:50 beam splitter. The blue circle and the green square correspond to the experimental conditions of Fig. 4.13 for probing at 633 nm and 850 nm, respectively.

Figures 4.11 shows that the same effect seen in 4.10 for propagation at λ=633 nm is expected also for propagation at λ=850 nm. Figures 4.11(a) and 4.11(b) are obtained using the coupled mode theory. For both cases, the output intensity tends to an equal

distribution among the two waveguides. As in the case of λ=633 nm, the case A does not present any oscillations whereas case B does. Simulations by the BPM method are shown in Figs. 4.11 (c) and (d). As for the case of λ=633 nm, they are in good agreement with the corresponding coupled mode theory expectations in Figs. 4.11(a) and 4.11(b). Summarizing, the theory predicts that at the output of the waveguide structures that mimic two-state STIRAP one should obtain a similar splitting irrespective of case A or B, and irrespective of the wavelength (see Fig. 4.12), provided that the system fulfills sufficiently well the adiabatic condition. Figure 4.13 gives the experimental output distributions for propagation in photoinduced waveguide structures corresponding to cases A and B at the probe wavelengths of 633 and 850 nm. It is seen that the beam splitting is satisfactorily obtained for both cases at both wavelengths, thus confirming the robustness of the process. In absence of detuning the behavior would be expected to be highly dependent on wavelength, similar to the case of Fig. 4.5 for RAP. Therefore, the observed broadband behavior is a direct consequence of the waveguide detuning, which permits to place the experiments outside the region near the abscissa in Fig. 4.12, for which Rabi-like oscillations strongly dependent on wavelength would be expected.

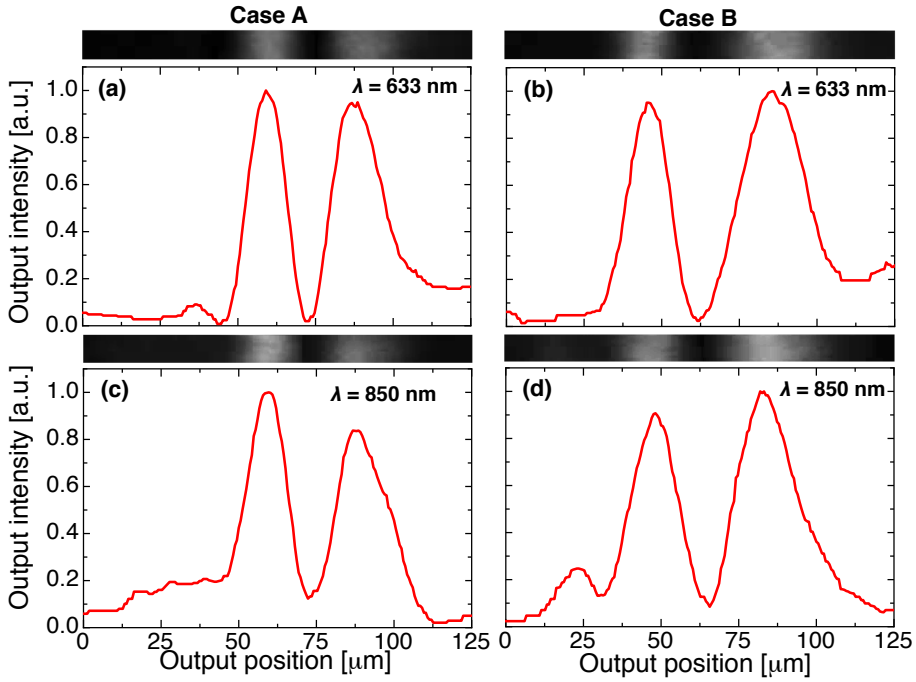

Figure 4.13: Experimental output intensity distribution for the case of two-state STIRAP as probed for cases A and B at two different wavelengths. (a) and (b): probing at λ = 633 nm, (c) and (d): probing at λ = 850 nm. Panels (a) and (c) correspond to case A, while panels (b) and (d) correspond to case B (see text).

4.5 Conclusion

We have discussed the role of waveguide detuning for the adiabatic light transfer among a pair of coupled waveguides in analogy with adiabatic quantum population dynamics processes. By the examples of the Rapid Adiabatic Passage and the two-state STIRAP processes the theoretical expectations have been successfully verified experimentally using photo-induced reconfigurable waveguides recorded in a photorefractive crystal. The corresponding structures act as broadband directional couplers and broadband beam splitters, respectively. The robustness and achromaticity brought about by the adiabatic evolution mediated by the detuning and the coupling strength have been confirmed. Generally, the combination of the effects of longitudinally varying coupling and longitudinally varying detuning permits to access a much wider range of possibilities for the adiabatic evolution of the light fields as compared to systems where only the coupling constant is modulated. As proposed recently for the case of three-waveguide couplers [158], this kind of concept can be extended to a larger number of waveguides, leading potentially to several new rich functionalities.

The introduction of a longitudinally varying detuning $\Delta\beta$ permitted to implement the RAP-like and the two-state STIRAP-like effects of the quantum mechanics for waveguides. It also offers more possibilities to address new analogies between quantum mechanics and waveguide optics. In the next chapter, we study the phenomenon of adiabatic elimination in a coupled multi waveguide system. It consists to reduce an N-waveguide system to an effective two waveguide system by elimination of the intermediate waveguides. This is achieved by introducing a strong and uniform detuning $\Delta\beta$ between the intermediate waveguides and the outer waveguides, the detuning is assisted by a longitudinally modulated coupling constant $C(z)$. It will be shown that this approach containing a pseudo space-depending detuning reduces the N-waveguide system to a two waveguide system. This system behaves like the system studied for RAP process.

5 Adiabatic Elimination

Contents

5.1 Introduction

In the previous chapter, we exposed the theoretical and experimental results of optical structures based on the quantum processes of RAP and two–state STIRAP. In the case of RAP, we realized an optical structure which operates as a broadband directional couplers and a broadband beam splitter for two–state STIRAP. In both cases, the modulation of the longitudinal detuning $\Delta\beta$ between waveguides and of the coupling constant C was crucial for the successful implementation of these two quantum–inspired processes. In this chapter, we propose another approach that gives a similar behavior as the above RAP effect even though no explicit modulation of the propagation constants of the waveguides is present. The proposed approach is based on the quantum technique of adiabatic elimination [31, 32, 33, 34, 35] and in the case of waveguides leads to an effective z-dependent pseudo-detuning. The underlying ideas concerns an N–level coupled quantum system, for

which the population of the intermediate states (2 to $N-1$) can be neglected if their detunings with respect to the first and final state are constant and much stronger compared to their corresponding couplings Rabi frequencies. In the case of optical waveguides, it involves a detuning between the propagation constants of the outer waveguides and the central waveguide(s) that is large but constant over the propagation. In comparison to RAP process, it requires a strong detuning $\Delta\beta$ (with respect to the coupling constant C) between the outer waveguides and the inner ones but no longitudinal modulation is necessary. Importantly, in contrast to multiple STIRAP, which can be used successfully to transfer light between the outer waveguides only if the total number of waveguides in the array is odd [24, 133, 135, 136], the present approach works equally well for odd and even number of waveguides in the array. While most earlier studies on adiabatic elimination in waveguides optics considered only parallel waveguides [163, 164, 165], here we take advantage of the simple control parameter of a varying coupling strength to the outer waveguides, which can be realized by varying the distance between these outer waveguides and the central ones [166]. It is shown that these spatially varying coupling constants lead to the above mentioned space-dependent pseudo-detuning of the propagation constants in an effective two-waveguide system. For our specific waveguide design this effective system is fully analogous to the rapid adiabatic passage process (RAP) in two-level quantum systems [30]. Therefore the behavior of our proposed structures is formally equivalent to the one of a two-waveguide structure with explicit longitudinal variation and zero crossing of the waveguide detuning parameter described in section 3.2.3. recent work [157].
First, we expose the theory underlying the adiabatic elimination technique in a system composed of three coupled waveguides. Through the first section, we also discuss the conditions under which the adiabatic elimination can take place and which guarantee an adiabatic evolution of the system. The fulfillment of both these conditions is required for the process to take place properly. Also, we present the designed optical structure based on the parameters values that best satisfy these two criteria. We show through the example of three waveguides that it reduces to an effective two–state waveguide system equivalent to the one treated in section 4.3. Next, we numerically verify the expectations by means of the beam propagation method (BPM) and describe the expected spectral dependence. The example calculations are performed for fused silica waveguides with propagation around the telecommunication wavelengths. Even though, waveguide photoinduction technique does not allow to reach the values of $\Delta\beta$ required for adiabatic elimination, other types of "fixed" waveguides can reach such values. therefore, we model such systems in the case of fused silica waveguides. In section 5.3, we expand the technique to a system containing a total number N of waveguides and proceed in the same way as for the three waveguide system. For both systems, we show that the combination of adiabatic elimination and of the slow adiabatic spatial evolution of the Stokes and pump coupling constants leads to a robust bi-directional light exchange between the outer waveguides over a broad spectral

range. Most of these results discussed in this chapter were recently published [167].

5.2 Adiabatic elimination in three–waveguide structure

5.2.1 Theory

5.2.1.1 The dynamics of the system

We consider a system of three evanescently coupled dielectric waveguides as the one shown in Fig. 5.1, for which the outer waveguides 1 and 3 have an identical refractive index profile which differs from the one of the central one. We assume that the light propagation constant in the outer waveguides be β_0 and the one of the central waveguide be $\beta_0 + \Delta\beta$. In the framework of coupled-wave theory the propagation of the electric-field amplitudes $a_1(z)$, $a_2(z)$ and $a_3(z)$ of the waves traveling in the three above waveguides is described by a system of three coupled differential equations written in a matrix form as [49]

$$i\frac{d}{dz}\begin{bmatrix} a_1(z) \\ a_2(z) \\ a_3(z) \end{bmatrix} = \begin{bmatrix} 0 & C_{12}(z)e^{-i\Delta_{\beta z}} & 0 \\ C_{21}(z)e^{i\Delta_{\beta z}} & 0 & C_{23}(z)e^{i\Delta_{\beta z}} \\ 0 & C_{32}(z)e^{-i\Delta_{\beta z}} & 0 \end{bmatrix} \begin{bmatrix} a_1(z) \\ a_2(z) \\ a_3(z) \end{bmatrix}, \tag{5.1}$$

where the $C_{ij}(z)$ are the z-dependent coupling coefficients from waveguide j to waveguide i and in general $C_{ij}(z) \neq C_{ji}(z)$. As usual, the longitudinal z-variation of the coupling constants is associated to the changing distance between the waveguides seen in Fig. 5.1. The direct coupling between waveguide 1 and 3 is neglected because the structure is assumed to be planar and their distance is supposed to be sufficiently large.

Similarly to the approach given in [156], the above Eq. (5.1) can be brought in a more symmetric form by performing the simple transformation $a_1'(z) = \sqrt{C_{21}(z)/C_{12}(z)}\; a_1(z)$, $a_2'(z) = \exp(-i\Delta\beta z)\; a_2(z)$, $a_3'(z) = \sqrt{C_{23}(z)/C_{32}}\; a_3(z)$. This leads to the form [19]

$$i\frac{d}{dz}\begin{bmatrix} a_1'(z) \\ a_2'(z) \\ a_3'(z) \end{bmatrix} = \begin{bmatrix} 0 & C_P(z) & 0 \\ C_P(z) & \Delta\beta & C_S(z) \\ 0 & C_S(z) & 0 \end{bmatrix} \begin{bmatrix} a_1'(z) \\ a_2'(z) \\ a_3'(z) \end{bmatrix}, \tag{5.2}$$

where the pump ($C_P(z)$) and the Stokes ($C_S(z)$) coupling constants are geometrical averages of the above coefficients $C_{ij}(z)$, i.e. $C_P(z) \equiv \sqrt{C_{12}(z)C_{21}(z)}$ and $C_S(z) \equiv \sqrt{C_{23}(z)C_{32}(z)}$. The system of (5.2) can be reduced to an effective two–waveguide system under some conditions about the detuning $\Delta\beta$ and the coupling constants $C_p(z)$ and $C_s(z)$. For this to happen we need a condition to eliminate the intermediate waveguide (its electric field amplitude $a_2'(z)$) of the three waveguide system in Fig. 5.1. Moreover, these parameters should ensure a spatial adiabatic evolution . In the following, we investigate these conditions.

5.2.1.2 Adiabatic evolution and adiabatic elimination criteria

➪ **Adiabatic elimination condition :**

In order to suppress the intermediate waveguide and reduce the above system to an effective two waveguide system, we consider a strong propagation constants mismatch $\Delta\beta$ with respect to the pump and Stokes coupling constants, we can set

$$\frac{|\Delta\beta|}{\sqrt{C_P^2(z)+C_S^2(z)}} \gg 1, \tag{5.3}$$

as we shall assume for our case, then the derivative of $a_2'(z)$ varies rapidly and the average value of $a_2'(z)$ and $a_2(z)$ over many cycles will be zero, thus the average of the derivative vanishes. If no light is initially input in the middle waveguide this extreme limit leads to a strong suppression of the wave amplitude in this waveguide, this effect is known in quantum physics as adiabatic elimination [31, 32, 33, 34, 35]. The easiest mathematical way to perform the adiabatic elimination of the middle waveguide is to set $da_2'(z)/dz = 0$

$$i\frac{d}{dz}a_2(z)' = 0 = C_P(z)a_1'(z) + \Delta\beta a_2' + C_S(z)a_3'(z)$$

$$\Rightarrow a_2'(z) = -\frac{C_P(z)}{\Delta\beta}a_1'(z) - \frac{C_S(z)}{\Delta\beta}a_3'(z), \tag{5.4}$$

and replace the resulting expression for $a_2'(z)$ in the other two equations of (5.2). After an unimportant phase shift of the electric field amplitudes such that

$$\tilde{a}_i(z) \equiv \exp\left[-i((C_P^2(z)+C_S^2(z))z/(2\Delta\beta)\right] a_i'(z),$$

this leads to an equation characterizing an effective two state system given by

$$i\frac{d}{dz}\begin{bmatrix}\tilde{a}_1\\ \tilde{a}_3\end{bmatrix} = \begin{bmatrix}-\Delta_{eff} & C_{eff}\\ C_{eff} & \Delta_{eff}\end{bmatrix}\begin{bmatrix}\tilde{a}_1\\ \tilde{a}_3\end{bmatrix}, \tag{5.5}$$

where

$$\Delta_{eff} = \frac{C_P^2(z)-C_S^2(z)}{2\Delta\beta} \tag{5.6}$$

is an effective detuning and

$$C_{eff} = -\frac{C_P(z)C_S(z)}{\Delta\beta} \tag{5.7}$$

is an effective coupling coefficient. The effective detuning Δ_{eff} and the effective coupling constant C_{eff} play the same role as the detuning $\Delta\beta$ and the coupling constant C in (B.2), also equations (5.5) and (B.2) are perfectly similar.

➪ **Adiabatic evolution condition :**

Similarly to the procedure seen in section 4.2, we write Eq. (5.5) in the *adiabatic basis* [30, 35, 126],

$$i\frac{d}{dz}\begin{bmatrix} b_1(z) \\ b_3(z) \end{bmatrix} = \begin{bmatrix} -\sqrt{C_{eff}^2(z)+\Delta_{eff}^2} & -i\frac{d\vartheta(z)}{dz} \\ i\frac{d\vartheta(z)}{dz} & \sqrt{C_{eff}^2(z)+{\Delta_{eff}}^2} \end{bmatrix}\begin{bmatrix} b_1(z) \\ b_3(z) \end{bmatrix}, \tag{5.8}$$

where

$$\vartheta(z) = \frac{1}{2}\arctan\left(\frac{C_{eff}(z)}{\Delta_{eff}}\right). \tag{5.9}$$

The connection between the amplitudes $\tilde{a}_1(z)$ and $\tilde{a}_3(z)$ and the adiabatic ones $b_1(z)$ and $b_3(z)$ is given by

$$b_1(z) = \tilde{a}_1(z)\cos\vartheta(z) - \tilde{a}_3(z)\sin\vartheta(z), \tag{5.10a}$$

$$b_3(z) = \tilde{a}_1(z)\sin\vartheta(z) + \tilde{a}_3(z)\cos\vartheta(z). \tag{5.10b}$$

When the evolution of the system is adiabatic, $|b_1(z)|^2$ and $|b_3(z)|^2$ remain constant [30, 35, 126]. Mathematically, adiabatic evolution means that the non-diagonal terms in Eq. (5.8) are small compared to the diagonal terms and can be neglected. This restriction amounts to the following *adiabatic condition* on the process parameters [30, 35, 126]

$$\left|\frac{d}{dz}\vartheta(z)\right| \ll \left(C_{eff}^2(z)+\Delta_{eff}^2\right)^{1/2}, \tag{5.11}$$

which, using Eq. (5.9), takes the explicit form

$$\frac{2\left(C_{eff}^2(z)+\Delta_{eff}^2\right)^{3/2}}{\left|\Delta_{eff}\frac{d}{dz}C_{eff}(z) - C_{eff}(z)\frac{d}{dz}\Delta_{eff}\right|} \gg 1. \tag{5.12}$$

Hence adiabatic evolution requires a smooth enough z dependence of the effective phase mismatch Δ_{eff} and of the effective coupling coefficient $C_{eff}(z)$, a long enough waveguide length, and a large enough coupling. In the adiabatic regime $|b_{1,3}(z)|^2$ =const, but the light intensity contained in waveguide 1 and waveguide 3 ($\propto |\tilde{a}_{1,3}(z)|^2$) will vary if the mixing angle ϑ varies, thus adiabatic evolution can produce energy transfer between the outer waveguides. Note that $C_{eff}^2(z)+\Delta_{eff}^2$ decreases by increasing $\Delta\beta$, therefore a sort of compromise must be found to optimize both criteria (B.3) and (5.12).

5.2.2 Examples

5.2.2.1 Strucutre of three waveguides

The chosen designed structure for adiabatic elimination demonstration is shown in Fig. 5.1. The outer waveguides (WG1 and WG3) are curved while the inner waveguide (WG2) is

straight, this results in a z–dependences of the coupling constants $C_s(z)$ (between WG1 and WG2) and $C_p(z)$ (between WG2 and WG3). The refractive index change of the central waveguide is six times higher than the one of the outer waveguides, this leads to as strong detuning $\Delta\beta$ with the waveguides.

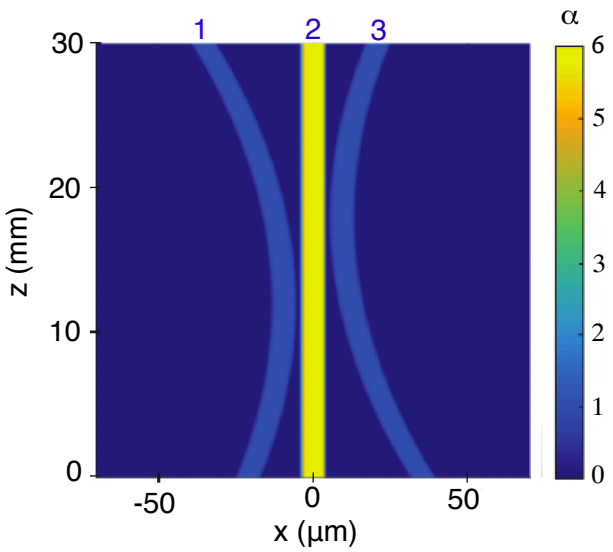

Figure 5.1: Waveguide structure for adiabatic elimination in an array of three waveguides. The color code visualizes the normalized refractive index contrast α. $\alpha = 1$ is the maximum refractive index change of the outer waveguides and $\alpha = 6$ the one for the central one leading to a mismatch $\Delta\beta$ of the propagation constants. Injection into the left waveguide 1 at $z = 0$ corresponds to an intuitive order of coupling while injection into the right waveguide corresponds to a counterintuitive order of coupling.

The waveguides are assumed to be written in fused silica for which the cladding refractive index is 1.4440 at 1550 nm [168]. In the transverse x-dimension, the form of the refractive index profile of each waveguide i is assumed to be

$$\Delta n_i(x) = \alpha_i \Delta n_0 \exp(-(x/d)^8), \tag{5.13}$$

where $\Delta n_i(x)$ is the amplitude of the refractive index contrast for waveguide i and $\Delta n_0 = 0.004$. For the sake of simplicity we consider that all waveguides have the same 1/e half-width $d = 4$ µm but the internal waveguide has a larger refractive index contrast (by a factor $\alpha = 6$) with respect to the outer ones (for which $\alpha = 1$). This produces the mismatch $\Delta\beta$ in the mode propagation constants. While waveguide 2 is straight, we assume that the two outer waveguides have a parabolic geometrical form given by

$$\delta x_1(z) = -8.10^{-8}(z - L/2 - L/10)^2, \quad \text{for WG1} \tag{5.14a}$$

$$\delta x_3(z) = 8.10^{-8}(z - L/2 + L/10)^2, \quad \text{for WG3,} \tag{5.14b}$$

where all distances should be expressed in micrometers and the total propagation length is $L = 30$ mm. This gives a longitudinal separation distance between the maximum of the coupling constants C_P and C_S of 6 mm. In the x-transverse dimension, the minimum separation between two adjacent waveguides is 9.6 µm (from the center to the center of the waveguides). With regard to the separating distances between the waveguides, large values of the coupling constants are involved. Also, the large refractive index change ($2.4 \cdot 10^{-2}$ at maximum) permits high order modes to propagate in the structure. This implies taking into account the multimode behavior of the structure in order to understand which modes can lead to the adiabatic elimination process and/or to the adiabatic evolution of the system.

5.2.2.2 Multimode behavior of the structure

The satisfaction of the previously discussed criteria of Eqs. (5.12) and (B.3) requires high values of the detuning $\Delta\beta$ and therefore high values of the refractive index change Δn for the waveguides. In order to understand the influence of these modes on these criteria we show the dependences of the parameters $\Delta\beta$ and C on the wavelength and different modes.

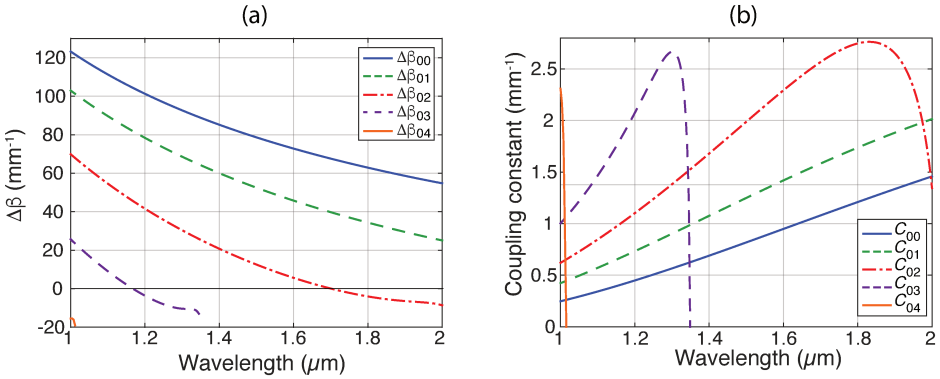

Figure 5.2: Evolution (a) of the detuning $\Delta\beta_{0i}$ and (b) the corresponding coupling constants C_{0i} between the fundamental mode ($m = 0$) of waveguide 1 (or 3) and the mode i ($m = i$) of waveguide 2 as a function of wavelength. The planar step index waveguide width is 7.64 µm. The refractive index change of the outer waveguides in Fig. 5.1 with respect to the bulk is $\Delta n_1 = \Delta n_3 = \Delta n_0 = 4 \cdot 10^{-3}$ and $\Delta n_2 = 6\Delta n_0 = 2.4 \cdot 10^{-2}$ for the central waveguide. The coupling constants shown here are the maximum of C_P and C_S.

Figure 5.2(a) shows the λ-dependence of the detuning $\Delta\beta_{0i}$ between the fundamental mode of the outer waveguide (1 or 3) and the excited mode i in central waveguide (2) while Fig. 5.2(b) shows their corresponding coupling constants. The propagation constants are calculated by resolving the transcendental equations of planar step index waveguides. The

coupling constants and the perturbations on the propagation constants due to the other waveguide are calculated using the coupled mode theory presented in section 1.3. Note that, as discussed in chapter 1, the perturbative coupled mode theory can not be applied without errors just below the cutoff wavelengths, where the coupling constant appear artificially to decrease. In the following section, we consider $\lambda = 1.55\,\mu m$ so three modes should be considered for WG2 while WG1 and WG3 remain essentially single mode, so only the fundamental mode is considered for WG1 and WG3. We also discuss the variations of the criteria depending on the considered mode. Moreover, The dispersion of the refractive index is given by ref. [168], but we neglect the wavelength variation of Δn_0, $\Delta n_0 = 0.004$ for all wavelengths.

5.2.2.3 Fulfillment of the criteria

In order to understand how the two previously discussed criteria can be satisfied and for which values of C_{eff} and Δ_{eff} they are both enough satisfied, we plot the ratio of the left-hand side of Eqs. (B.3) and (5.12) as a function of the propagation distance z. These parameters are plotted for the structure shown in Fig. 5.1

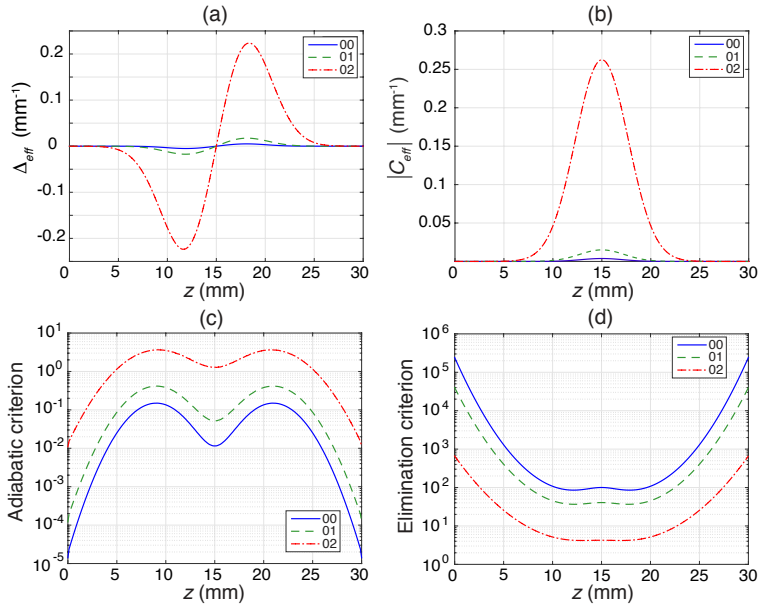

Figure 5.3: Visualization of the adiabatic parameters for the structure shown in Fig. 5.1 for the different possible mode couplings deduced from the calculations of Fig. 5.2 for $\lambda = 1550$ nm. The "0i" curves consider the coupling between the fundamental mode ($m = 0$) of the outer waveguide (1 or 3) and the mode i of the central waveguide 2 ($m = i$). z-dependence of (a) Δ_{eff}(Eq. (B.4)), (b) $|C_{eff}|$ (Eq. (B.5)), (c) of the adiabatic elimination criterion of Eq. (B.3) and, (d), the adiabatic criterion of Eq. (5.12).

As shown in Fig. 5.3(a), the effective phase mismatch Δ_{eff} sweeps from some negative to some positive values, in this process the mixing angle $\vartheta(z)$ changes from $\pi/2$ to 0. With the light initially in waveguide 1, the system will stay adiabatically in state $b_3(z)$, so that the light will switch to waveguide 3 when $\vartheta(z)$ approaches zero. Therefore the effective phase mismatch sweep will produce complete light switching. This is exactly the mechanism that is at work also in the RAP-like two-waveguides system with explicit detuning that was reported in chapter 4. It is worth noting that adiabatic transfer does not bring about any specific restriction to the shape of the effective phase mismatch Δ_{eff} as far as the condition (5.12) is fulfilled and the mixing angle $\vartheta(z)$ changes from $\pi/2$ to 0 (or vice versa).

As Fig. 5.3(d) shows, the minimum value of the ratio $|\Delta\beta| / (C_P^2 + C_S^2)^{1/2}$ being approximately 4 (obtained at the z-locations where either C_P or C_S is maximal). Note that, as discussed in more detail below, this minimum (worst case) ratio corresponds to the coupling of the fundamental mode of the outer waveguides (mode number $m = 0$) with the second excited mode of the central waveguide ($m = 2$). The minimum of the above ratio for the coupling between the fundamental modes of all waveguides is roughly 20 times larger(see Fig. 5.3(d)). The corresponding evolution of the adiabatic criterion (5.12) is shown in Fig. 5.3(c). If we consider the coupling between the modes $m = 0$ and $m = 2$, the ratio in (5.12) varies between 1.5 and 4 over the interacting distance where the longitudinal shift between waveguides 1 and 3 leads to a variation of the effective z-dependent detuning Δ_{eff}. In contrast, the ratio of Eq. (5.12) would be less than one if two fundamental modes are considered for which the coupling is weaker and the detuning is larger. Therefore for this coupling among the modes $m = 0$ there is an increase of the ratio of Eq. (B.3) that goes at the expense of the adiabatic criterion (5.12).
The above values for the criteria (B.3) and (5.12) have been approximated by calculating the propagation and coupling constants of the different modes of a planar step index waveguide with a refractive index contrast of Δn_0 and a width equal to the Full-Width-at-Half-Maximum of the waveguides used in the BPM simulations (FWHM=7.64 µm).

5.2.2.4 Adiabatic elimination vs RAP

The structure shown in Fig. 5.1 operates as the structure for RAP-like process seen in section 4.3. With the parameters of Figs. 5.3(a) and (b) for $\Delta_{eff_{02}}$ and $C_{eff_{02}}$, we design a two waveguide structure similar to the one presented in Fig. B.3(a). This equivalent structure is shown in Fig. 5.4(b).

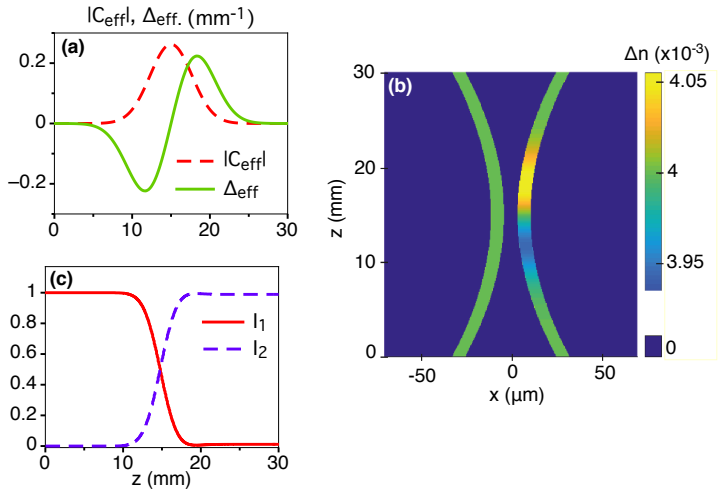

Figure 5.4: (a) the z-dependence of the effective detuning Δ_{eff} and the effective coupling constant C_{eff} considering the coupling between the fundamental mode of the (m=0) of the outer waveguides and the second mode (m=2) of the central waveguide of Fig. 5.1. (b) the corresponding RAP-like structure. (c) the intensities variations of the waveguides in (b) as a function of the propagation distance z.

As seen in Fig. 5.4(b) the effective phase mismatch Δ_{eff} sweeps from negative values to some positive values as seen in Fig. 5.4(a) (or vice versa). At the crossing ($\Delta_{eff} = 0$), the effective coupling constant C_{eff} reaches its maximum and similarly to RAP this leads to a complete light transfer to the other waveguide as Fig. 5.4(c) shows. In the case where Δ_{eff} sweeps from positive values to negatives values, there is also a complete light transfer. The consequence is that the intuitive and the counterintuitive order of coupling will lead both to the same final outcome, a complete switching of the light between the outer waveguides in the three–waveguide structure since the structure in Fig. 5.4 is equivalent to the structure of Fig. 5.1. As will be verified in the next section by means of BPM simulations, this property is not found in the case of the conventional STIRAP process.

5.2.3 Verifications by BPM simulations

In this section we verify the expectations discussed in section 5.2.1 by performing numerical simulations of the wave propagation in the structure of Fig. 5.1. A BPM method using a split-step Fourier method is used for the simulations [161, 162].

First, we consider the situation where $\alpha = 1$ for all waveguides, that is all waveguides have an identical index profile and thus $\Delta\beta = 0$. Obviously in this case adiabatic elimination cannot take place since the condition (B.3) is not satisfied. Despite of that, when the light is injected in the right outer waveguide (counterintuitive order) a complete light transfer to the left most waveguide without excitation of the middle one is obtained. This is seen in Fig. 5.5(a) simulated for a light wavelength of 1550 nm and corresponds to

the standard STIRAP process in a three–waveguide directional coupler discussed earlier [19, 20, 132]. In contrast, as can be seen in Fig. 5.5(b) the reverse situation where the light is injected in the left waveguide (intuitive order) is much more complex and does not lead to a corresponding transfer to the opposite outer waveguide. This is a manifestation of the mentioned asymmetry of the STIRAP process with respect to waveguide exchange.

Figures 5.5(c) and 5.5(d) show the situation like the one of Fig. 5.5(a) and 5.5(b), but for the case of an increased index contrast for the central waveguide ($\alpha = 6$). In this case the light transfer occurs both from left to right and from right to left in a symmetric way with almost no excitation of the middle waveguide, as expected from the theory in subsection 5.2.1.
In fact, for the situation of Figs. 5.5(c) and 5.5(d) the adiabatic elimination condition (B.3) is satisfied. Figure 5.5(d) clearly shows that the mode with $m = 2$ appears weakly in the transient regime. Therefore, under the above conditions the system chooses the channel over the intermediate mode $m = 2$ that leads to the optimum transfer and fulfills satisfactorily both criteria as discussed in subsubsection 5.2.2.3.

Obviously, besides adiabatic elimination, also a large enough effective detuning Δ_{eff} in (B.4) is essential for the symmetric transfer observed in Figs. 5.5(c) and 5.5(d). To show this we also consider as a counter-example the fully symmetric structure where the distances between the two outer waveguides and the central one are identical for all z ($\delta x_1(z) = -\delta x_2(z) = -8.10^{-8}(z - L/2)^2$). In this case the pump and Stokes coupling constants are the same and the pseudo-detuning Δ_{eff} in Eq. (5.5) vanishes everywhere. Therefore the system cannot behave like a RAP process, even though adiabatic elimination of the middle waveguide is still at work. This is seen in Figs. 5.5(e) and 5.5(f), which shows how the light is getting distributed among the two outer waveguides.

As already mentioned, an important point is that for our simulated cases the outer waveguides are essentially single mode, however, the internal waveguides are no longer single mode as soon as $\alpha > 1$. This can be seen for instance in Fig. 5.5(d) where the transient light in the central waveguide for the intuitive case (right column) propagates in the third order mode (with a propagation constant β_2). This is the higher supported mode of waveguide 2, and this mode has therefore the smallest $\Delta\beta$ with the propagation constant β_0 of waveguides 1 and 3. As a matter of principle the fundamental mode in the input waveguide can couple to any of the modes of the internal ones. The RAP-like switching behavior can be obtained provided that the criterion (B.3) is satisfied for any of the modes, in other words all the propagation constant must be sufficiently far from the propagation constant of the fundamental mode in the outer waveguides.

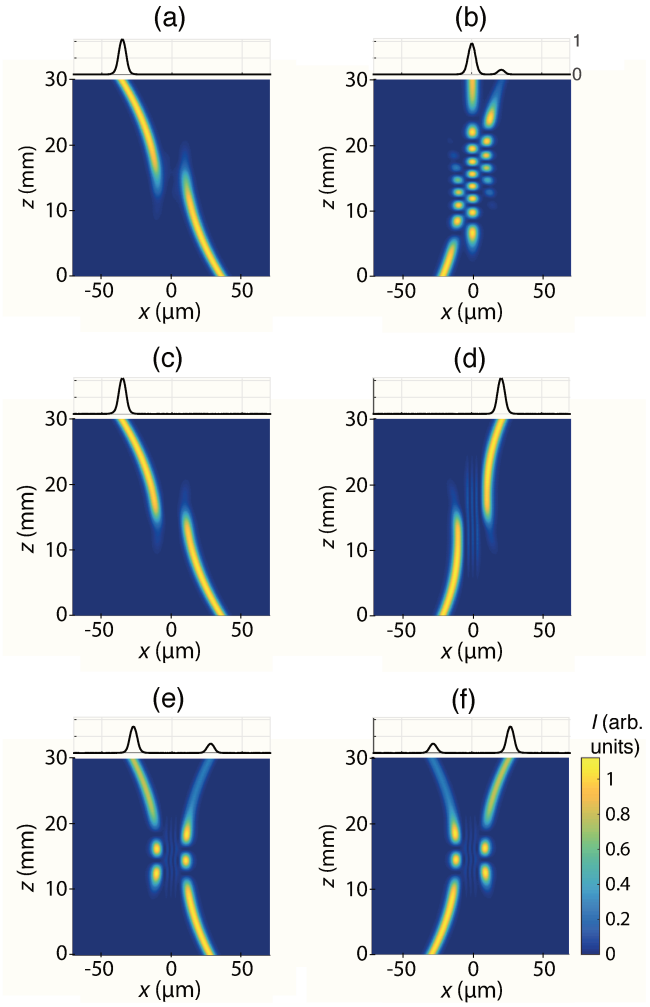

Figure 5.5: Wave propagation in a three-waveguide structure calculated by the BPM method at the wavelength $\lambda = 1550$ nm for light injection into the right waveguide (left column) and into the left waveguide (right column). (a) and (b) are for the case $\alpha = 1$, for which all waveguides have the same index contrast and therefore $\Delta\beta = 0$. (c) and (d) are for $\alpha = 6$ (refractive index design corresponding to the one of Fig. 5.1). This gives the RAP-like light switching between the outer waveguides. (e) and (f) are for a fully symmetric waveguide structure for which $\Delta_{eff} = 0$ in (5.5) and for which the RAP-like transfer cannot take place ($\alpha = 6$). The small top diagrams represent the intensity profiles at the end of the 30-mm propagation. The intensity color scale is the same for all the surface plots.

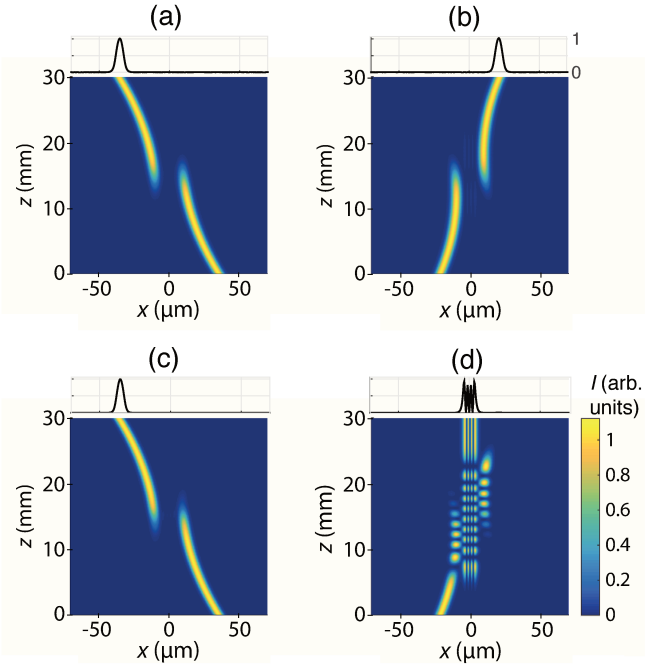

Figure 5.6: Wave propagation in a three-waveguide structure as in Figs. 5.5(c) and 5.5(d) ($\alpha = 6$) but for different wavelengths. (a) and (b) are at $\lambda = 1300$ nm (c) and (d) are are at $\lambda = 1137$ nm.

Figures 5.6(a) and 5.6(b) represent the same situations as Figs. 5.5(c) and 5.5(d) but for a propagating wavelength of 1300 nm instead of 1550 nm. Also here a symmetric transfer is achieved. The results are even better for this set of parameters, with less transient light in the central waveguide in the intuitive case. This is expected since the minimum value of the ratio in Eq. (B.3) is now approximately 22, again for the coupling of the modes $m = 0$ and $m = 2$. Note that transfer is efficient despite for the fact that the ratio of Eq. (5.12) is not so large in this case ($\lesssim 1$). The behavior seen in Figs. 5.5(c) and 5.5(d) and Figs. 5.6(a) and 5.6(b) proves the robustness of the process resulting in a broadband behavior, which will be discussed in more detail below. This robustness is associated to the adiabatic evolution of the parameters in the RAP-like light transfer between the outer waveguides.

⇨ Adiabatic elimination transfer efficiency vs wavelength

The influence of the competition between modes affects the robustness of the transfer efficiencies which are defined by $\eta_{CI} = P_1(z = L)/P_N(z = 0)$ for the counter-intuitive case and $\eta_I = P_N(z = L)/P_1(z = 0)$ for the intuitive case, where $P_i(z)$ is the power in waveguide i at the propagation distance z. This is illustrated in Fig. 5.7 representing the transfer efficiencies η_{CI} and η_I as a function of wavelength.

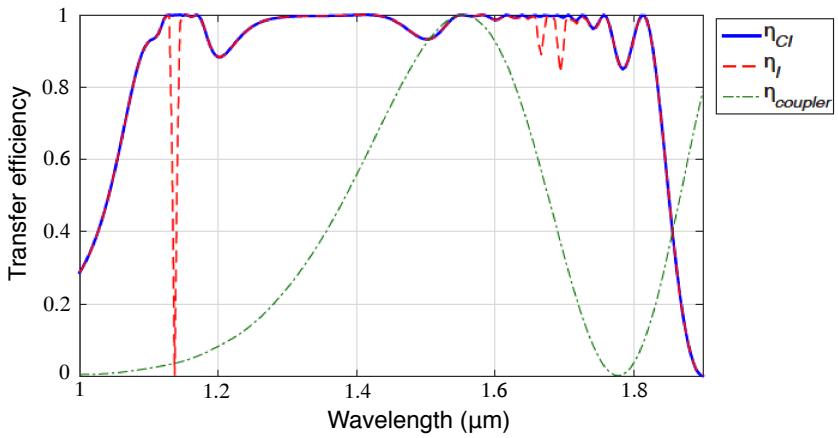

Figure 5.7: Evolution of the transfer efficiencies with wavelength for a three waveguide structure. The refractive index profiles correspond to the ones of Fig. 5.1. η_{CI} (resp. η_I) is the transfer efficiency for the counter-intuitive case (resp. the intuitive case). The efficiency spectrum is compared to the one a directional coupler ($\eta_{coupler}$) composed of two straight waveguides and tuned to the wavelength of 1.55 μm.

The robustness of the transfer by adiabatic elimination is clearly seen Fig. 5.7, where a rather flat profile is obtained over more than 600 nm. We interpret the efficiency drop for short wavelengths ($\leq$ 1150 nm) as being due to a combination of two factors and with the help of Fig. 5.2. The first is the decrease of the coupling constants with decreasing wavelengths (see Fig. 5.2), the second is the appearance of the fourth mode in the central waveguide, whose propagation constant β_3 starts close to the fundamental one β_0 of the outer ones, preventing so the adiabatic elimination. For the intuitive case, the efficiency even drops to zero for a specific wavelength around 1.14 μm due to the association of an extremely small detuning in the propagation constants β_3 and β_0 and a coupling effect driving all the light in the central waveguide at the end of the propagation (see Fig. 5.6(d)). For the counter-intuitive case, the efficiency η_{CI} is still 1 as illustrated on Fig. 5.6(c), since there is never light in waveguide 2 in the counter-intuitive case (as for STIRAP). Therefore, for specific wavelengths and/or specific values of α, the structure might act as a mode converter or a mode filter rather than as a robust directional coupler. For longer wavelengths, the efficiency drops again since the wavelength approaches the cut-off frequency of the third mode and $\beta_2 \to \beta_0$. This is also due to a too strong coupling. Indeed for $\lambda > 1.8$ μm, for the couter-intuitive case (resp. the intuitive case), the light is integrally transferred from waveguide 1 (resp. waveguide 3) to waveguide 3 (resp. waveguide 1) during the propagation but comes back to waveguide 1, thus decreasing η.

The case where all waveguides remain single mode has not been considered since as explained the large required detuning $\Delta\beta$ lead naturally to a multimode structure of the stronger waveguides, at least for realistic simple waveguide profiles as the one considered in this work. Even though the spectral dependence of our proposed coupler is influenced by

the multimode behavior and by the wavelength dependence of the coupling, its bandwidth is much larger that the one of a coupler consisting of only two waveguides as shown with the curve of $\eta_{coupler}$ in Fig 5.7. The latter has been obtained by simulating the wave propagation in two straight coupled waveguides separated by 19.2 µm (instead of 9.6 µm). All the others parameters remain the same, especially the refractive index profile $\Delta_n(x)$ is the one of waveguides 1 and 3. The separation distance has been adjusted to get one coupling length for the 30-mm propagation length at $\lambda = 1550$ nm.

⇨ Optimization of the structure dimensions :

The above examples show that adiabatic elimination can be used to realize a symmetric coupler, but no attempt was done to optimize the dimensions of the related structures. Generally, it is well known that robust adiabatic approaches tend to require longer propagation lengths than non adiabatic ones. In this context, computational approaches such as those based on shortcuts to adiabacity [169, 170] can reduce the device footprint. To judge the possibility of using shorter structures in our specific case, we may consider first the evolution of the effective parameters Δ_{eff} and C_{eff} in Figs. 5.3(a) and 5.3(b). One sees that these parameters vary significantly only in a spatial region of the order of 15 mm around the center of the 30-mm long structure. One may therefore expect that a certain reduction of the structure length should be possible.

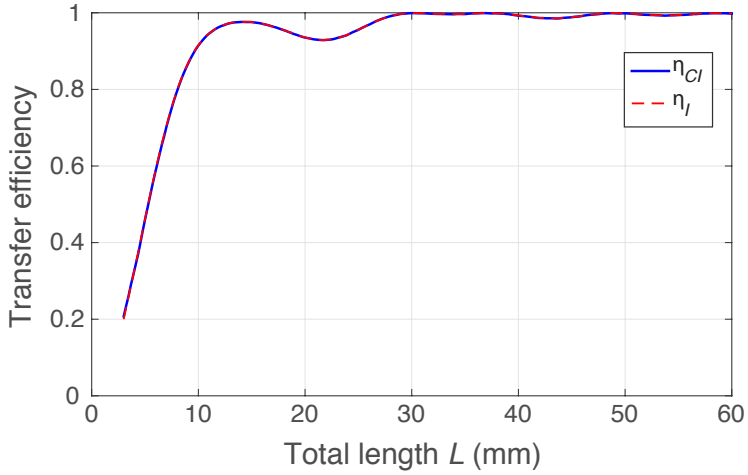

Figure 5.8: Dependence of the transfer efficiencies η_{CI} and η_I on the total length L for $\lambda = 1.55$ µm. The geometrical functions $\delta x_1(z)$ and $\delta x_3(z)$ are given by the parabolas of Eqs. (5.14). The waveguide's shape still correspond to the one of Fig. 5.1 if z is replaced by a normalized propagation distance z/L and the same x dimension in micrometers is kept.

We investigate the tolerance of the coupler for the structure of Fig. 5.1 with respect to a variation of the total length L with the help of Fig. 5.8. The latter represents the variation of the transfer efficiency η for the intuitive and counterintuitive cases as a function

of L and for $\lambda = 1.55$ µm. The curvatures of the two outer waveguides are still expressed by Eqs. (5.14). Therefore, a decrease (increase) of L corresponds to a compression (expansion) of the structure of Fig. 5.1(a) in z-direction, while keeping the x dimensions unchanged. In this way the distances between the waveguides at the entrance and output of the structure, as well as their minimum separations near $z = L/2$ remain the same. Importantly, the central waveguide elimination criterion of Eq. (B.3) is not modified by a change of the total length L since it is principally affected by the difference in refractive index contrast between the central and the outer waveguides. In contrast, the adiabatic condition of Eq. (5.12) depends on the geometrical shape and is decreasing by shortening L, thus the curves of Fig. 5.8 can be considered as a test of adiabaticity.
It is clearly seen that $\eta_{CI}(L)$ and $\eta_I(L)$ overlap for all lengths L. This is related to the fact that the criterion (B.3) remains valid and therefore the coupler efficiency remains symmetric with only negligible transient light in waveguide 2, as in Fig. 5.5(c) and 5.5(d). The transfer efficiency in both directions remain high and exceeds 90 % down to a length of about 10 mm. Afterwards, the steep drop in efficiency seen for $L < 10$ mm is due to the lost of the adiabatic condition. Indeed, for $L = 10$ mm, the adiabatic criterion (5.12) varies between 0.5 and 1.2 over the interacting (coupling) distance.

For the chosen set of waveguide parameters, this limit value of 10 mm is consistent with the above discussion in connection to Fig. 5.3(a) and (b) since the crucial part of the 30-mm long coupler is roughly 10-15 mm. We verified also that the footprint of the 3-waveguide-coupler could be reduced as well by zooming on the central part of the coupler, effectively cutting away the initial and final part of propagation with respect to Fig. 5.1. In this case the waveguide curvatures are not changed. Also in this situation we have found a drop below $\eta < 90\%$ for $L < 10$ mm. Note that in this case, for such a 10-mm-long coupler, the two outer waveguides are separated by 25 µm (center to center) at $z = 0$ or $z = L$ instead of the ≈55 µm in Fig. 5.1. Note also that, even though the parameters of our original structure are optimized for a chosen length of 30 mm, for shorter lengths (but $L \geq 10$ mm) the obtained efficiency may be further optimized by modifying (for each L) the curvature parameters in Eqs. (5.14) or by using a more complex geometrical function than the simple parabola considered in this proof of principle study.

5.3 Adiabatic elimination for array of N waveguides

5.3.1 Theory

In the last section, we have seen that the adiabatic elimination reduces the three–waveguide system to an effective two–waveguide system. This is established by setting the amplitude of the electric field in the central waveguide to zero due to the strong detuning between

the outer waveguides and the central one. In this section, we apply the same procedure for a four and six–waveguide systems but it can be generalized to an array composed of N waveguides by analogy with the case of N–state system in the quantum physics [171]. Before embarking in discussion of the simulation results for six–waveguide system, it is worth remembering that a multistate STIRAP permits to achieve a robust transfer from the initial to the target state via the so called adiabatic dark state only if the total number of states is odd and the Stokes coupling precedes the pump coupling (counter-intuitive order) [24, 171]. For our calculations we choose therefore an even total number of waveguides ($N = 6$) (see Fig. 5.9) in order to proof that for the present approach there is no limitation on the parity of the waveguide number.

5.3.1.1 The dynamics for an array of N waveguides

Similarly to the case of Eq.(5.2) the equation describing the evolution of the normalized wave amplitudes $a_i'(z)$ in an array of 4 waveguides can be brought in the form

$$i\frac{d}{dz}\begin{bmatrix} a_1' \\ a_2' \\ a_3' \\ a_4' \end{bmatrix} = \begin{bmatrix} 0 & C_P & 0 & 0 \\ C_P & \Delta\beta & C_I & 0 \\ 0 & C_I & \Delta\beta & C_S \\ 0 & 0 & C_S & 0 \end{bmatrix} \begin{bmatrix} a_1' \\ a_2' \\ a_3' \\ a_4' \end{bmatrix}, \tag{5.15}$$

where $C_P \equiv \sqrt{C_{12}C_{21}}$, $C_S \equiv \sqrt{C_{34}C_{43}}$ are the pump and Stokes couplings, respectively, and $C_I = C_{23} = C_{32}$ is the coupling coefficient between the internal waveguides, which are assumed to be identical and are detuned by $\Delta\beta$ with respect to the outer ones. Here the adiabatic elimination of the intermediate waveguides is done by setting $da_2'/dz = 0$ and $da_3'/dz = 0$ in Eq. (5.15) determining the amplitudes a_2' and a_3' in terms of a_1' and a_4' from the resulting set of linear algebraic equations, and replacing them in the equations for da_1'/dz and da_4'/dz. This permits to reduce the four-states problem to an effective two-states system which takes a form identical to Eq. (5.5),

$$i\frac{d}{dz}\begin{bmatrix} \tilde{a}_1 \\ \tilde{a}_4 \end{bmatrix} = \begin{bmatrix} -\Delta_{eff} & C_{eff} \\ C_{eff} & \Delta_{eff} \end{bmatrix} \begin{bmatrix} \tilde{a}_1 \\ \tilde{a}_4 \end{bmatrix}, \tag{5.16}$$

where the relation between the amplitudes $\tilde{a}_i$ and a_i' is again a simple phase shift and

$$\Delta_{eff} = \frac{\Delta\beta\,(C_P^2 - C_S^2)}{2\,(\Delta\beta^2 - C_I^2)}, \tag{5.17}$$

$$C_{eff} = \frac{C_P C_I C_S}{\Delta\beta^2 - C_I^2}. \tag{5.18}$$

The equivalent equation of (5.15) for $N = 6$ is,

$$i\frac{d}{dz}\begin{bmatrix} a_1' \\ a_2' \\ a_3' \\ a_4' \\ a_5' \\ a_6' \end{bmatrix} = \begin{bmatrix} 0 & C_P & 0 & 0 & 0 & 0 \\ C_P & \Delta\beta & C_I & 0 & 0 & 0 \\ 0 & C_I & \Delta\beta & C_I & 0 & 0 \\ 0 & 0 & C_I & \Delta\beta & C_I & 0 \\ 0 & 0 & 0 & C_I & \Delta\beta & C_S \\ 0 & 0 & 0 & 0 & C_S & 0 \end{bmatrix} \begin{bmatrix} a_1' \\ a_2' \\ a_3' \\ a_4' \\ a_5' \\ a_6' \end{bmatrix}. \tag{5.19}$$

Again, by a similar procedure as the one described above one obtains the corresponding effective two–waveguide system,

$$i\frac{d}{dz}\begin{bmatrix} \tilde{a}_1 \\ \tilde{a}_6 \end{bmatrix} = \begin{bmatrix} -\Delta_{eff} & C_{eff} \\ C_{eff} & \Delta_{eff} \end{bmatrix} \begin{bmatrix} \tilde{a}_1 \\ \tilde{a}_6 \end{bmatrix}, \tag{5.20}$$

where

$$\Delta_{eff} = \frac{\Delta\beta(\Delta\beta^2 - 2C_I^2)}{2\left[(\Delta\beta^2 - C_I^2)^2 - \Delta\beta^2 C_I^2\right]}(C_P^2 - C_S^2), \tag{5.21}$$

is its corresponding effective detuning, and

$$C_{eff} = \frac{C_P C_I^3 C_S}{(\Delta\beta^2 - C_I^2)^2 - \Delta\beta^2 C_I^2}, \tag{5.22}$$

its corresponding effective coupling constant. Since Eqs. (5.5), (5.16), and (5.20) are identical, as was the case for the three-waveguide situation of Sec. 5.2, in the adiabatic regime the present situation is expected to lead to a RAP-like switch of the wave amplitude between waveguides 1 and 6 (1 and 4), both for the counterintuitive and intuitive order of couplings.

5.3.1.2 Criteria of adiabatic evolution and adiabatic elimination

The structure considered for $N = 6$ is shown in Fig. 5.9, the central waveguides have the same refractive index which differs from the one of the outer waveguides. The curvatures and refractive index change of WG1 and WGN are identical to those of WG1 and WG3 of the three waveguide case and WG2 to WG(N-1) are identical to WG2.

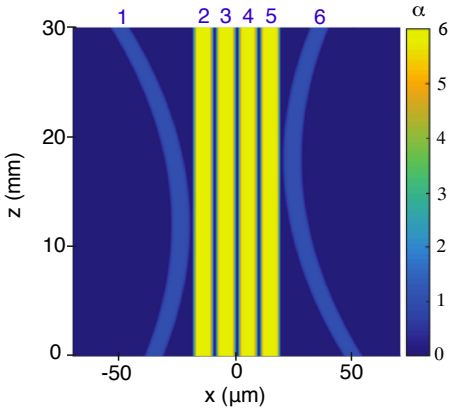

Figure 5.9: Waveguide structure for adiabatic elimination in an array of six waveguides. The color code visualizes the normalized refractive index contrast α. $\alpha = 1$ is the maximum refractive index change of the outer waveguides and $\alpha = 6$ the one of the four central ones leading to a mismatch $\Delta\beta$ of the propagation constants. Injection into the left waveguide 1 at $z = 0$ corresponds to an intuitive order of coupling while injection into the right waveguide corresponds to a counterintuitive order of coupling.

For $N = 6$, the elimination criterion must be adapted due to the additional coupling between the central straight waveguides. Therefore, in accordance with Eq.(5.19), three elimination criteria should be satisfied. They are defined by,

$$\frac{|\Delta\beta|}{\sqrt{C_P^2 + C_I^2}} \gg 1 \tag{5.23}$$

$$\frac{|\Delta\beta|}{\sqrt{C_I^2 + C_S^2}} \gg 1 \tag{5.24}$$

$$\frac{|\Delta\beta|}{C_I\sqrt{2}} \gg 1 \tag{5.25}$$

These 3 criteria give close values as can be seen in Fig. 5.10(d). The main difference with the criterion (B.3) is that they remains almost constant along the propagation since the C_I are constant.

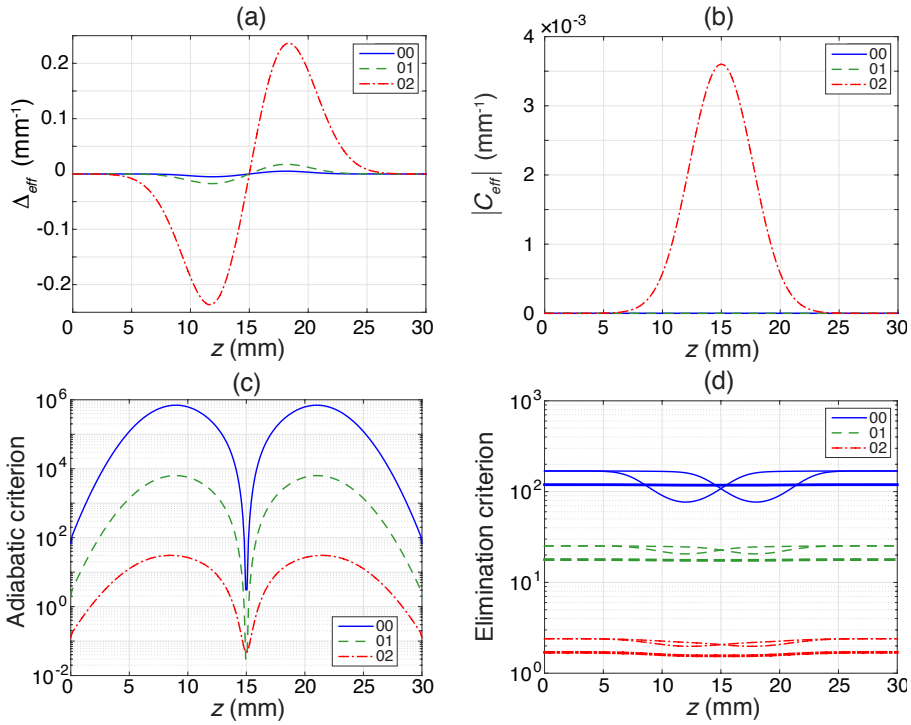

Figure 5.10: Similar visualization of the adiabatic parameters for the 6-waveguide case ($N = 6$) as in Fig. 5.3.
The elimination criterion of eq. (5.12) has been modified to take into account the coupling constant C_I between the central waveguides. We therefore get three close criteria : $|\Delta\beta|/\sqrt{C_P^2 + C_I^2}$, $|\Delta\beta|/\sqrt{C_I^2 + C_S^2}$ and $|\Delta\beta|/C_I\sqrt{2}$, represented in (d). The thickest lines in (d) correspond to $|\Delta\beta|/C_I\sqrt{2}$.

In Fig 5.10(c), the adiabatic criterion becomes very high and moreover increases as the mode order diminishes. In the case of $N = 3$, the criteria of Eq. (B.3) evolves in an opposite way, since the criteria increases with the mode order (see Fig. 5.3). This difference is associated with the fact that $C_{eff} \sim 0$ for the coupling for the first two modes ($m = 0, 1$) of the internal waveguides. Therefore, as for $N = 3$ the denominator in Eq. (B.3) diminishes with the mode orders. However this decrease is much faster for $N = 6$ than for $N = 3$, and much faster than the decrease of the value of the numerator, leading to an opposite dynamic of Eq. (B.3) with the mode order for $N = 3$ and $N = 6$. Note that the adiabatic criteria labelled 00 and 01 in Fig 5.10(c) are not really relevant since $C_{eff} \sim 0$ prevents the coupling in the effective two–state system of Eq. (5.20) for this case. Therefore, the main information of Fig 5.10(c) is that for the coupling between the fundamental mode of waveguides 1 and N ($m = 0$) and the second higher mode ($m = 2$) of the internal waveguides, it gives in average similar values for the adiabatic criterion of Eq. (B.3) than for the 3-waveguide case. However, with respect to the top curve in Fig. 5.3, here we observe a deep minimum for $z = L/2$ which can affect the light

propagation. However, the elimination criteria are identical for $N = 3$ and $N = 6$.

5.3.2 Verifications by BPM simulations

Figures 5.11(a) and 5.11(b) show again the case where there is no adiabatic elimination because all the waveguides have the same index contrast ($\alpha = 1$) and thus $\Delta\beta = 0$. In this case the propagation behavior is very sensitive to the waveguide geometries and in general one obtains a quite complex distribution of the light among the various outputs. In contrast, by increasing the propagation constant mismatch by means of the factor $\alpha = 6$, the switch of the wave between the outer waveguides expected from the RAP-like process is observed. This is seen in Fig. 5.11(c) and 5.11(d) for $\lambda = 1550$ nm.

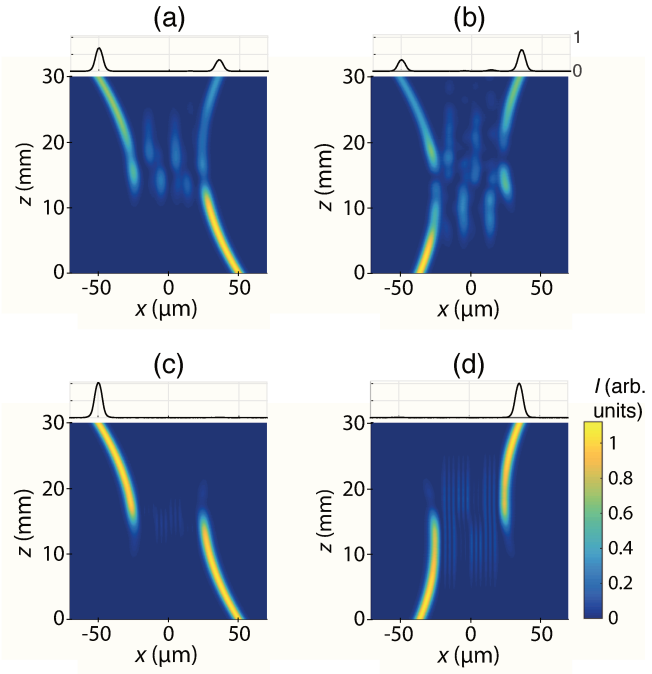

Figure 5.11: Wave propagation in a six–waveguide structure calculated by the BPM method for light injection into the right waveguide (left column) and into the left waveguide (right column). The wavelength is $\lambda = 1550$ nm. (a) and (b) are for the case $\alpha = 1$. (c) and (d) are for $\alpha = 6$ (refractive index design corresponding to the one of Fig. 5.9). This give the RAP-like light switching between the outer waveguides.

⇨ Adiabatic elimination transfer efficiency vs wavelength

Similarly to the case of three waveguides, we study the transfer efficiencies which are defined by $\eta_{CI} = P_1(z = L)/P_N(z = 0)$ for the counter-intuitive case and $\eta_I = P_N(z = L)/P_1(z = 0)$ for the intuitive case, where $P_i(z)$ is the power in waveguide i at the

propagation distance z. This is illustrated in Fig. 5.12 representing the transfer efficiencies η_{CI} and η_I as a function of wavelength.

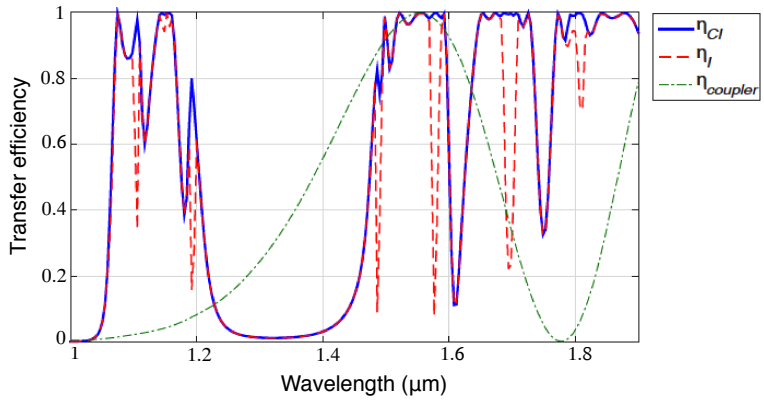

Figure 5.12: Evolution of the transfer efficiencies with wavelength for six–waveguide system of Fig. 5.9. η_{CI} (resp. η_I) is the transfer efficiency for the counter-intuitive case (resp. the intuitive case). The efficiency spectrum is compared to the one a directional coupler ($\eta_{coupler}$) composed of two straight waveguides and tuned to the wavelength of 1.55 μm.

For the 6–waveguide case, the expected bandwidth is much smaller than for the 3–waveguide case. This is related to the fact that, as for the case of a multi-STIRAP process [24, 171], the adiabatic condition is more difficult to fulfill with an increased number of waveguides leading to a less robust behavior. The adiabatic criterion (5.12) for $N = 6$ can reach high values ($\gg 1$) at the z-locations of the maximum of C_P and C_S, but drops to $\ll 1$ at $z = L/2$ (see the deep minimum in the middle of propagation in Fig. 5.10(c)). η is therefore much more affected by the wavelength dependence of the coupling constants than for $N = 3$. Nevertheless, as for $N = 3$, for specific (pseudo-periodic) wavelength ranges an almost flat transfer efficiency close to 1 is observed also in this case.

5.4 Conclusion

Through this chapter, we have studied theoretically and numerically a new method for light switching between the outer waveguides of a N-waveguide array which provides the optical analog of the adiabatic elimination process used in quantum physics. The adiabatic elimination reduces the problem from a true N-waveguides system to an effective two-waveguides system with an effective pseudo-detuning of the propagation constants. It was shown that, upon an appropriate choice of the longitudinal evolution of the coupling constants involving the outer waveguides, the above effective two-waveguides system behaves like a coupled two-level quantum system subjected to the rapid adiabatic passage

process seen in chapter 4. In the case of present effective two–waveguide system, no spatial modulation of the detuning $\Delta\beta$ between waveguides is necessary while a spatial varying coupling constant is required. The involved values of $\Delta\beta$ for the process of adiabatic elimination are huge in comparison to RAP which prevents its experimental implementation with our technique of photo induction of waveguides. In contrast to the case of the conventional STIRAP process, for the present approach the photonic transport is found to be symmetric with respect to an interchange of the outer waveguides. It works independently on the intuitive or counter-intuitive order of the coupling constants. Moreover, the theoretical expectations have been successfully verified by means of wave propagation simulations by the beam propagation method applied to structures containing an odd ($N = 3$) or even ($N = 6$) number of waveguides. We recall that for conventional STIRAP an odd number of waveguides is required. We have shown that for $N = 3$ the system is very broadband and the transfer efficiency can be kept close to 100 % over a wavelength range spanning more than 600 nm around the telecommunication wavelengths. For an increased number of waveguides N in the structure the bandwidth diminishes but several wavelength regions with nearly flat transfer efficiency near 100 % are still observed. Moreover, since the system behavior is influenced by higher order modes in the central waveguide(s), slight modifications of the present technique might be useful also for novel approaches for mode conversion and filtering applications.

General Conclusions and Perspectives

Along this thesis, we have used photo induced optical waveguides generated with lateral illumination technique for demonstration of analogies between quantum mechanics and waveguide optics. We have seen that propagation of electromagnetic waves in optical waveguides presenting a space varying propagation constant is analog to population evolution in quantum atomic systems with laser detuning frequency evolving in time. Then, we exploited techniques and approaches developed in the field of quantum mechanics for waveguide optics.

In the optical structures we used for demonstration of these analogies, the optical coupling of light was studied within the framework of coupled–mode theory, it involves the evanescent wave of the guided modes. The equations derived from coupled-mode theory which describe the electric field amplitude evolution are similar to those derived from Schrödinger equation describing the probability amplitude evolution for atomic systems composed of discrete energy levels. In the optical case, the waveguides were coupled to each others by means of the coupling constant, while in the quantum case, the Rabi frequencies of the coupling laser fields plays this role.

Thanks to a lateral illumination technique which offers highly reconfigurable optical structures, we can easily modify their geometry and their refractive index distribution and adapt them to experimental needs depending on the analogy to be implemented. The control beam intensity distribution was used to control the shape of waveguides whereas the intensity itself controls the photorefractively induced refractive index change.

The recently developed two–state STIRAP technique of the quantum physics was adapted to the waveguide case by using a two–waveguide structure where both, the reciprocal coupling constant and the detuning of their longitudinal propagation constant, were properly modulated. In this way, we have demonstrated theoretically and verified experimentally an achromatic beam splitter based on this adiabatic two–state STIRAP process.

Also, the optical analogy of RAP was investigated for an optical system composed of two coupled waveguides in which a detuning changing sign at half propagation distance was introduced between the waveguides. It was shown that this gives a complete adiabatic transfer of the light to the second waveguide. Again, this was successfully implemented and used as achromatic directional coupler.

In the last chapter, the quantum phenomenon of adiabatic elimination which consists on eliminating adiabatically the population of the intermediate state(s) under the assumptions of a large constant detuning between the outer states and the intermediate state(s). In waveguides, this leads to full light transfer from an input waveguide where light is initially injected to an output waveguide essentially without coupling any light into the intermediate waveguide(s). For the condition of adiabatic elimination to hold, a very large detuning of the propagation constant β is necessary. This fact prevents the possibility of an experimental implementation with our technique of photo induction of waveguides. Note also that, contrary to the standard three–waveguide STIRAP, intuitive or counterintuitive sequence work equally well.

In terms of perspectives several comments can be made. First of all it is useful to remark that the systems demonstrated experimentally with our reconfigurable photoinduced technique prove the validity of the underlying principles. In principle all these structures can be realized also with standard techniques used for integrated optics, even though for some of them a solution for creating a controllable variation of the refractive index contrast would require additional efforts. In all cases a slight readjusting of the waveguide parameters would be required to accommodate the specificity of each individual technology.

All the studies conducted in this thesis have involved a linear propagation of the probe light guided in the waveguide structures. This was insured by limiting the power of the probe beam below the onset of any nonlinear phenomenon. In a next step it would be interesting to release this condition. If the guided probe light can modify the refractive index contrast that it feels, the overall output distribution among the waveguide may be modified according to the input power, leading to a nonlinear switching device. For instance, in the case of a RAP-like transfer one can imagine that the RAP waveguide structure would be active at low probe beam intensity, while at high intensity an increase of the refractive index contrast would prevent the zero crossing of the $\Delta\beta$ function, what would kill the transfer. Depending on the material used, the nature of the involved nonlinearity might be associated to the photorefractive effect, the optical Kerr effect, thermal effects or other kind of nonlinearities. This approach will be particularly interesting if one considers also the case of light propagating inside the structure in both directions, forward and backward. The nonlinearity can in this case provide a nonreciprocal behavior leading for instance to an effective optical isolation in an integrated device.

The case of adiabatic elimination in waveguides also offers interesting perspectives. In our case the intermediate waveguides were multimode and we have seen that the system

chooses one of these modes for the transfer, under our conditions this was generally the second excited mode m=2. At present it is not fully clear under which criteria this choice is privileged and additional investigations are needed. A question one may try to answer is the following. Is there some kind of "minimum energy" criterion deciding over which channel the transfer should occur? The mode selectivity that we have observed also offers an interesting opportunity. It is likely that a small modification of our approach might allow realizing a system able to separate different modes into different outputs in a broadband manner. This kind of approach might be used for mode filtering or mode conversion, properties highly demanded in modern telecommunication research.

A

Complementary Studies

Contents

A.1 Introduction

This brief appendix describes few additional theoretical investigations performed in the course of the thesis which are only partially connected with the previous chapters.

The first part describes the behavior of systems of two or three waveguides with an abrupt discontinuity of their propagation constants at half propagation distance. In atom physics such kind of systems with an abrupt switch of the sign (phase) of the Rabi frequency have been proposed as an alternative technique to Rapid Adiabatic Passage to achieve robust coherent population inversion [172, 173] in the case of a two level system. It was shown that the system describing the population transfer evolution is exactly solvable if the coupling has an hyperbolic-secant shape. This kind of idea was recently applied also to the case of nonlinear optical frequency conversion by three-wave mixing in the undepleted pump approximation [174]. In this regime the system of three coupled differential equations for the sum frequency conversion $\omega_3 = \omega_1 + \omega_2$ effectively reduces to a two-state system for photon conversion from the signal frequency ω_2 to the sum frequency ω_3 and the inversion of the sign of the coupling coefficient at half propagation distance leads to a robust conversion with increased bandwidth. In the case of waveguides the corresponding approach for a robust achromatic light transfer was proposed in a recent work by Huang and coworkers [175]. The authors have discussed theoretically the case where a sign jump

in the detuning $\Delta\beta$ leads to a light transfer (two waveguides) or beam splitting (three waveguides). In the next section we briefly discuss this kind of systems in view of the parameters that can be achieved with a reconfigurable waveguide recording system like ours. As we will discuss, the range of parameters giving the most robust behavior for the systems of Ref. [175] are not within reach for photorefractive light-induced waveguides since they require a too strong coupling constant associated to a sizable detuning $\Delta\beta$. Nevertheless, some regions in parameter space associated to a relatively robust behavior despite for weaker required coupling constants are identified. However, since these regions are on "bridges" in the parameter landscape rather on flat zones, the overall robustness is expected to be weaker with respect to the approaches inspired by RAP and two-state STIRAP developed in the main corpus of this thesis.

In the second part of this appendix we discuss in some detail the case of backward propagation. We consider only waveguide structures that lead to a splitting of the wave amplitude into two output ports in the forward direction. Backward injection of the light from the two output ports transfers the light to the original input port, to the other port, or to a mixture of the two ports depending on the relative phase shift between the two backward propagating inputs. We discuss this behavior specifically for structures that mimic the two-state STIRAP process that were treated in Sec. 4.4 of chapter 4. We recall that, as seen in chapter 4, in forward direction the two-state STIRAP-like waveguide structure leads theoretically to two equally intense output waves with a relative phase shift of either π or zero, depending on the case. Imposing this phase shift in backward direction leads to a wave evolution that corresponds to the expected time reversal behavior. Besides for the two-state STIRAP inspired structures we consider also the case of structures being equivalent to the so called half-STIRAP or fractional STIRAP process [176, 177, 178]. The latter consists in interrupting the conventional three state STIRAP process (see section 3.3) after half its evolution and leads to a coherent superposition of the initial state 1 and the target state 3. The analogy with the half-STIRAP process was demonstrated in the case of waveguides by Dreisow et al. [179]. Also in the case of half-STIRAP-like structures the reciprocal phase dependent evolution is confirmed. Here the light can populate also the usually silent intermediate waveguide in the case where the relative phase of the two backward waves is not properly selected. All in all the simulations discussed below confirm that such waveguide structures act exactly like an optical beam splitter (in linear optical regime). The case where the waveguides will act in the nonlinear regime promises to be much more interesting, in this case we may expect a non reciprocal behavior that can open several new perspectives.

A.2 Light passage in waveguide structures with abrupt propagation constant discontinuity

In this section we discuss waveguide structures with an adiabatic evolution of the coupling constant and a non-zero detuning $\Delta\beta$ that switches its sign at half propagation distance $L/2$. Such structures in the case of waveguides were proposed in [175]. We start by discussing the case of a two waveguide directional coupler shown in Fig. A.1. The two waveguides switch their refractive index profiles at $L/2$ while the coupling constant C evolves smoothly and adiabatically. The corresponding propagation constants β_1 and β_2 for WG1 and WG2 are $\beta_0 \pm \Delta\beta/2$ in the first half of the structure and $\beta_0 \mp \Delta\beta/2$ in the second half. This kind of structure can be seen as a simplified binary version of the RAP process discussed in section 4.3, where the smooth evolution of the coupling constant is replaced by a single jump. It is important to note that, unlike for the RAP, STIRAP and two-state STIRAP systems discussed earlier, the light amplitude evolution in the present kind of system is not governed by an adiabatic transfer state. Even though the coupling constant evolves adiabatically, the jump in $\Delta\beta$ at $L/2$ breaks the adiabaticity at that point. Nevertheless, as will be discussed below, the jump in the detuning gives a second control parameter which is essential to reach robust (and broadband) regions for the light transfer in the parameter landscape.

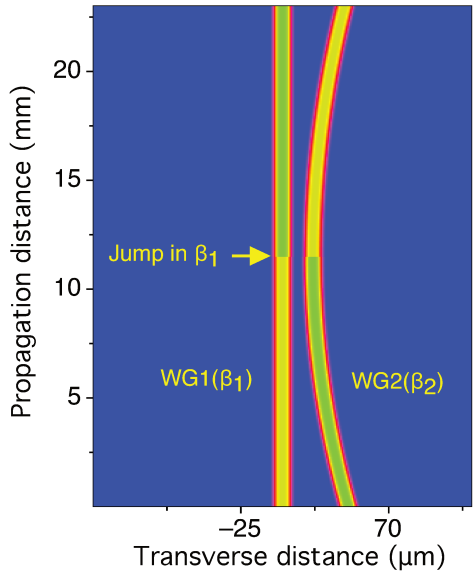

Figure A.1: Two-waveguide directional coupler with a sign jump of the waveguide detuning. The two waveguides possess a jump in their propagation constants β_1 and β_2 at half propagation distance. If light is injected in WG1 it should transfer to WG2 at the end of propagation and vice-versa.

Like for its quantum counterpart in atomic physics [172, 173], it was shown in [175] that

the waveguide structure of Fig. A.1 admits an analytic solution for the transferred intensity at the end of propagation provided that the coupling constant evolves as a hyperbolic secant function. This is given by

$$C(z) = C_{max}\,\mathrm{sech}\,[(z - L/2)/\sigma] = C_{max}/\cosh\,[(z - L/2)/\sigma], \tag{A.1}$$

where L is the length of the structure and σ is the half-width of the function $C(z)$ at the level corresponding to 64.8 % of its maximum. The analytic solution holds for vanishing coupling at the beginning and end of the structure ($C(0) = C(L) \approx 0$) and thus $L \gg \sigma$. If injection is in WG1 with an intensity $I_1(0) = 1$, in the limit of large maximum coupling, i.e. $C_{max} \gg \Delta\beta$ the analytic solution for the intensity $I_2(L)$ in WG2 at the output of the structure can be approximated as [175]

$$I_2(L) \cong \frac{C_{max}^2}{C_{max}^2 + (\Delta\beta/2)^2}\left[1 - \frac{\Delta\beta}{C_{max}} e^{-\pi\Delta_{\beta\sigma}/4}\cos\left(\frac{\pi C_{max}\sigma}{2}\right) + \mathscr{O}^2\right]^2, \tag{A.2}$$

where $\mathscr{O}^2$ is a quadratic term in the ratio $\Delta\beta/C_{max}$. Since $I_2(L)$ in Eq. (A.2) approaches 1, the light transfer efficiency approaches 100 % in its regime of validity ($C_{max} \gg \Delta\beta_{max}$). To illustrate this we show in Fig. A.2 some cases corresponding to this regime. Before discussing in detail this figure we would like to point out that the corresponding situations illustrated in Ref. [175] correspond to very long lengths L of the waveguide structures, typically between 20 cm and 70 cm for reasonable values of the coupling constant C_{max}. For this reason we have chosen for Fig. A.2 a more practical length $L = 2.3$ cm, which is the same as to the one used for the investigations in chapter 4. The left column in Fig. A.2 corresponds to a directional coupler like the one shown in Fig. A.1 with a non zero $\Delta\beta$ switching its sign at $z = L/2$, while the right column gives the counter-example for structures with an identical evolution of the coupling constant $C(z)$ but a vanishing $\Delta\beta$, so that the waveguides propagation constants are matched. For the four upper panels (Fig. A.2(a)-(d)) the function $C(z)$ corresponds to the hyperbolic secant function discussed above with $\sigma = 0.23$ cm. In contrast, for the four lower panels (Fig. A.2(e)-(h)) $C(z)$ correspond to a gaussian function having nearly the same full-width-at-half-maximum, with the expression $C(z) = C_{max}\exp\,[-(z - L/2)^2/\tilde{\sigma}^2]$, with $\tilde{\sigma} = 0.26$ cm. Panels (a), (b), (e) and (f) in Fig. A.2 show the spatial evolutions of $C(z)$ and $\Delta\beta(z)$, while panels (c), (d), (g) and (h) show the corresponding intensity evolution in the two waveguides. The latter was calculated numerically using coupled mode theory in the same way as was done in the previous chapters. It can be clearly recognized that both for the case of the hyperbolic secant profile (Fig. A.2(c)), and for the case of the gaussian profile (Fig. A.2(g)) the light is transferred correctly to the target waveguide 2. The kick associated to the non-adiabatic switch at $z = L/2$ can be clearly recognized in both cases. Therefore, while the sech profile sustains an analytic solution, any other similar profile will give essentially the same final result provided that the $\Delta\beta$ discontinuity is maintained. The necessity of the detuning

$\Delta\beta$ is clearly evidenced by the counter-examples in Fig. A.2(d) and A.2(h). In this case, due to the large value of the coupling constant, very rapid oscillations of the wave between the two waveguides occur in the central region and the output state does not correspond to the light transfer from WG1 to WG2.

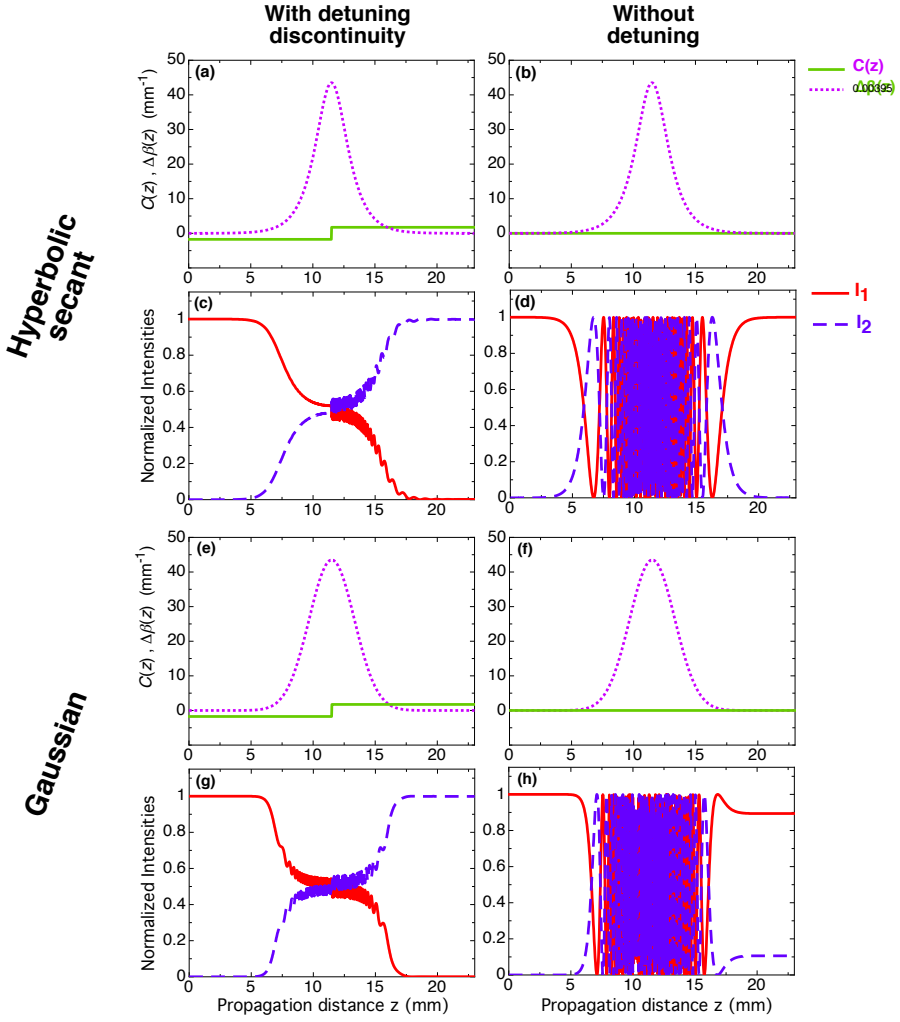

Figure A.2: Two-waveguide directional coupler with (left column) and without (right column) a discontinuity of the detuning $\Delta\beta$. Panels (a), (b), (e) and (f) give the spatial evolution of the coupling constant $C(z)$ (violet dotted lines) and $\Delta\beta(z)$ (solid green lines). Panels (c), (d), (g) and (h) give the numerically calculated spatial evolution of the intensity in WG1 (solid red curves) and WG2 (blue dashed curves). The evolution is calculated based on coupled mode theory (CMT). For the upper four panels the function $C(z)$ has a hyperbolic secant shape, for the lower four panels the shape is gaussian. The robust light transfer from WG1 to WG2 is obtained only in the presence of the detuning step as seen in (c) and (g).

As can be seen in Fig. A.2(a) and (e), the above calculations were performed for the case where the maximum of the coupling largely exceeds the value of the detuning jump. The corresponding maximum coupling constants of more than 40 mm^{-1} are out of reach for most waveguide recording techniques and well above those that can be obtained with our experimental approach. To verify if an experimental implementation of such a system would be feasible within our constraints we have simulated the same kind of system with more realistic parameters, similar to those used in chapter 4. This is shown in Fig. A.3, where a gaussian shape for the function $C(z)$ is assumed and the parameters C_{max} and $\Delta\beta$ have the same order of magnitude. Despite for the weaker values of these two parameters, an almost full transfer of the intensity from WG1 to WG2 is predicted again (Fig. A.3(c)). In contrast, the counter-example in absence of detuning (see Fig. A.3(b) and (d)) shows that in this case the transfer does not occur. Here the evolution is controlled merely by means of the coupling constant C and the light finally distributes among the two waveguides at the output.

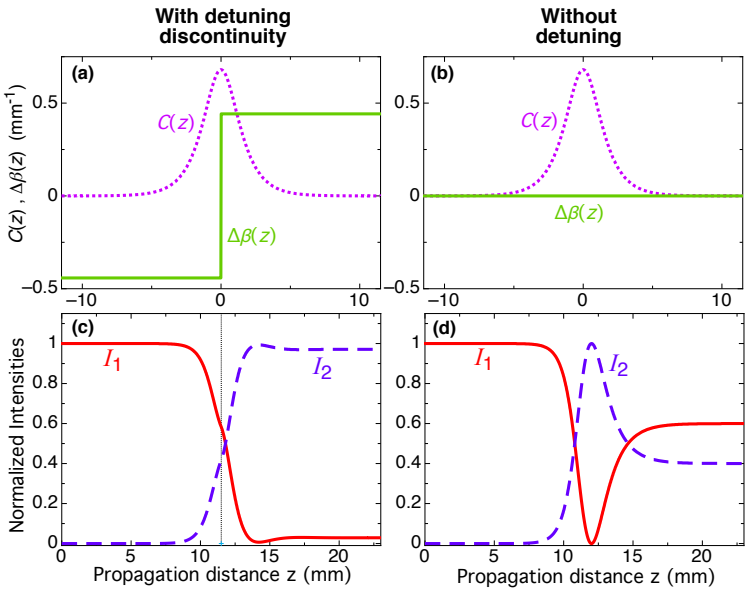

Figure A.3: Two-waveguide directional coupler as in Fig. A.2 but for smaller and comparable values of the coupling constant and of the detuning. For the left column a gaussian-shaped coupling constant with $C(z) = C_{max}\,\mathrm{sech}[10(z-11.5)/L]$ *and a detuning expressed by* $\Delta\beta(z) = \Delta\beta[2U(z-11.5)-1]$ *are assumed, where* $U(z)$ *is the Heaviside step function and all explicit distances are expressed in millimeters. The parameter values are* $C_{max} = 0.6\ mm^{-1}$ *and* $\Delta\beta = 0.44\ mm^{-1}$*, respectively. For the right column the function* $C(z)$ *is the same but* $\Delta\beta(z) \equiv 0$*. The quasi-adiabatic light transfer occurs only for case with the jump in* $\Delta\beta$*.*

The parameters used for Fig. A.3(a) and (c) are rather interesting and are, as we

will see below, at the boarder of a small region in parameter space where the transfer is complete. In order to study more in detail the robustness of the structures of the type shown in Fig. A.1, we scan the two parameters C_{max} and $\Delta\beta$ that control the light transfer to WG2. Figure A.4 shows the landscape describing how the output intensity in WG2 depends on these two parameters. A hyperbolic secant function with the same width as in Fig. A.3 is used for the calculations. Clearly the most robust region (homogeneous green area) is found for large values of C_{max} and smaller, but non zero values of $\Delta\beta$. This could be expected from the argumentations at the beginning of this section and from the simulations in Fig. A.2. On the other hand, the practically more feasible parameter area around the blue point is at the border of a bridge region of optimum transfer. As it extends over a smaller area of the landscape, such a bridge region is intrinsically less robust than wider homogeneous regions as those that we have identified for the RAP or two-state STIRAP in chapter 4 (see Figs. 4.7 and 4.12). Therefore, light transfer by the present approach based on the detuning discontinuity does not seem to bring any advantages over the RAP approach discussed earlier in this thesis, at least within the framework of our experimental system.

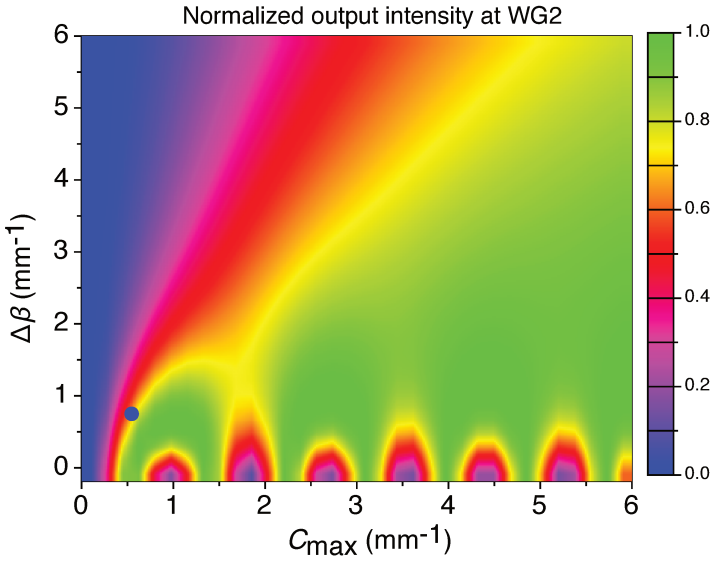

Figure A.4: Normalized output intensity in WG2 of Fig. A.1 as a function of the maximum of coupling constant C_{max} and of the detuning $\Delta\beta$. The structures are supposed to have a longitudinal z-dependence of these two parameters as in Fig. A.3. The blue point corresponds to the parameters of Fig. A.3. The most robust zone for the light transfer (homogeneous green region) is found for large C_{max} and non zero $\Delta\beta$. The practical case of Fig. A.3 corresponds to the border of a bridge zone with only relative robustness.

In the following we consider the extension of the above approach to the case of three waveguides with adiabatic evolution of the coupling constants and a discontinuity of the propagation constants at half distance. The corresponding schematic structure is shown in Fig. A.5. The geometry of the curved outer waveguides (WG1 and WG3) is symmetric with respect to the straight central waveguide (WG2). The discontinuities in β are for $z = L/2$, which is the distance where the three waveguides are closest together and have the largest coupling constants. The aim of this device is to split a wave injected in the central waveguide towards the two outer waveguides and its principle of operation can be understood by very simple intuitive arguments. Let us suppose first that the WG1 would be absent and that we would inject all light into WG2. In this case, as we have discusses above, under appropriate choice of the parameters the light would fully transfer to WG3. If we now add symmetrical WG1 on the left the same effect is expected, however, the light would move away from WG2 with equal probability to WG1 and to WG3. We expect therefore a beam splitting behavior that can be an alternative to the two-state STIRAP based approach treated in chapter 4 and to other approaches leading to broadband beam splitting.

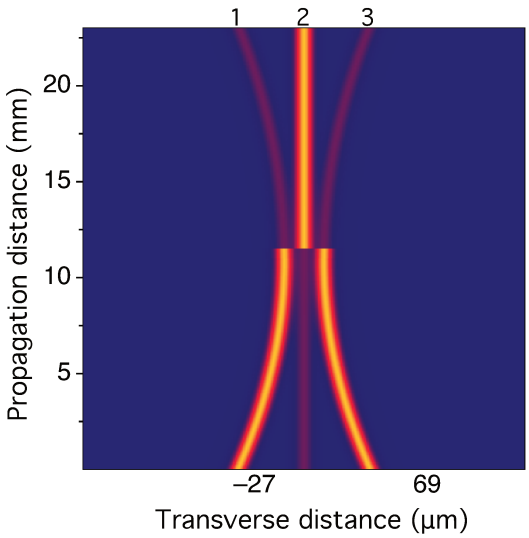

Figure A.5: Three waveguide structure for achromatic beam splitting of light injected in WG2 towards the outer waveguides WG1 and WG3. All waveguides possess a discontinuity of their propagation constants at the distance $L/2$, where the three waveguides are nearest to each other.

To illustrate that this is really happening we simulate the light intensity evolution in the three waveguide again using the coupled mode method. The results are shown in Fig. A.6 and contain again also the counter-example in absence of detuning. The coupling constants C_{12} between the waveguides 1 and 2 and C_{23} between the waveguides 2 and 3 are identical and are chosen to have a gaussian form, $C_{12}(z) = C_{23}(z) = C(z) =$

$C_{max}\exp[-(z-11.5)/4.5]^2$. The propagation constant detuning is given by $\Delta\beta(z) = \Delta\beta[2U(z-11.5)-1]$, where $U(z)$ is the Heavyside step function. All lengths in the two above expressions are expressed in millimeters. Two sets of parameters are used to calculate the evolution in Fig. A.6. These sets mimic the use of wavelengths more than 200 nm apart, i.e. 633 nm (upper row) and 850 nm (lower row), as in chapter 4. Figures A.6 (a) and (c) in the left column confirm that the structure acts as a beam splitter for both sets of parameters, with nearly 50 % of the intensity being transferred to each of the outer waveguides. This is no longer true for the counter-examples in the right column which show that in absence of detuning much of the light remains in the input waveguide 2 at the output of the structure. In this case the output light distribution is totally controlled only by the coupling constant $C(z)$.

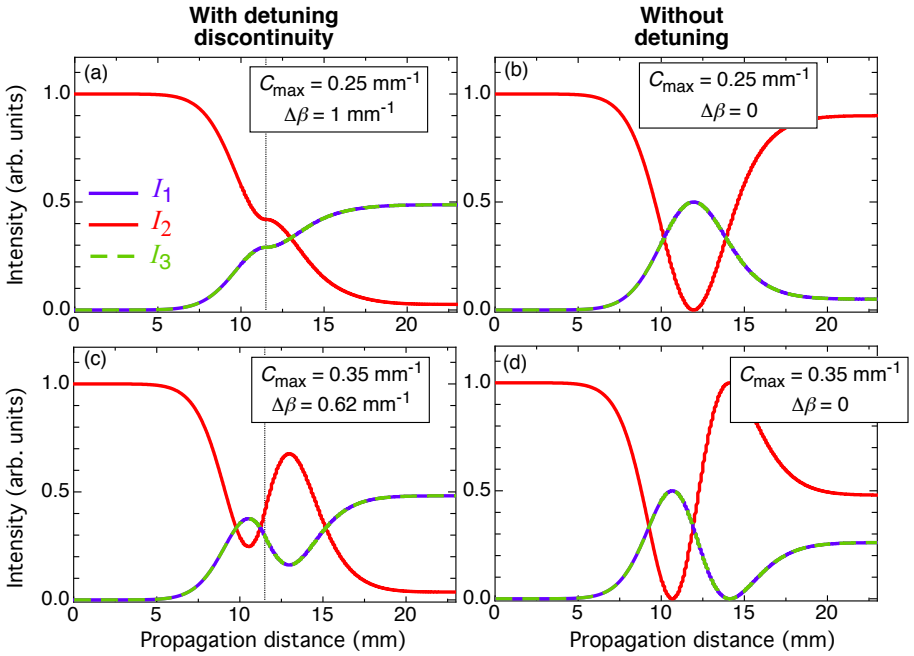

Figure A.6: Calculated longitudinal evolution of the light intensity in the waveguides of Fig. A.5. The left column gives the case where there is a propagation constant detuning discontinuity at half propagation distance. The right column is the case of three matched waveguides ($\Delta\beta = 0$). The input wave is injected into the central waveguide 2. Panels (a) and (b) in the upper row correspond to parameters associated to a wavelength $\lambda = 633$ nm and panels (c) and (d) in the lower row correspond to parameters for $\lambda = 850$ nm. The mathematical form for the functions $C(z)$ and $\Delta\beta(z)$ are given in the text and the parameters are given in the insets.

To judge more closely the robustness of the above conditions we have made a scan over the values of C_{max} and $\Delta\beta$ similarly to what was done in Fig. A.4 for the case of

two waveguides. The results are presented in Fig. A.7, where the output intensity in WG1 is represented as a function of the parameters C_{max} and $\Delta\beta$. As was the case for the two-waveguide configuration, also here the most robust region where nearly 50 % of the intensity is transferred to each of the outer waveguide is found for rather large values C_{max} associated to a sizable detuning and correspond to the nearly homogeneous green region in Fig. A.4. On the abscissa, for *zero* detuning the system manifests Rabi-like oscillations as was the case for the two-waveguides system. The practical parameters of Fig. A.6 are again on the first bridge region, therefore they are intrinsically less robust than configurations that would be associated to larger areas with homogeneous and flat landscape.

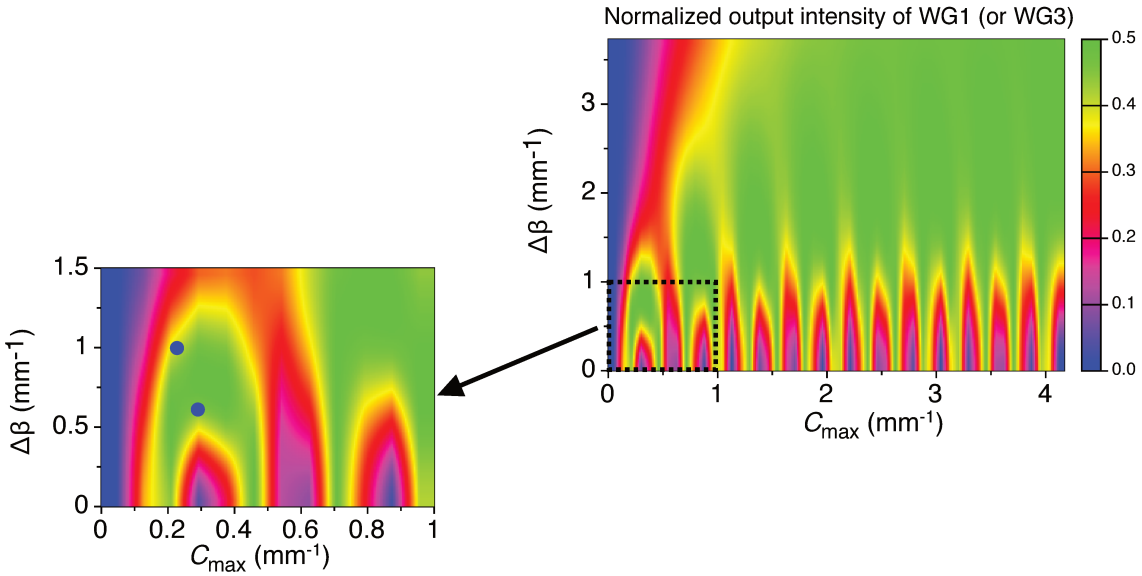

Figure A.7: Color plot of the normalized output intensity in WG1 and WG 3 as a function of the parameters C_{max} and $\Delta\beta$. The inset shows an enlargement of the zone near the parameters used for Fig. A.6 given by the two blue points.

To conclude this section one can say that the use of the technique based on an intermediate jump and sign reversal of the waveguide detuning does in principle deliver a mean to realize robust and broadband directional couplers and beam splitters when using two or three waveguides, respectively. However, to work in its more robust parameter regime, the technique requires generally larger coupling constants and significantly longer propagation lengths than the corresponding adiabatic techniques inspired by RAP and two-state STIRAP that were treated in the main corpus of this thesis. Nevertheless, some specific parameters being compatible with the dimensions and properties of our photo-induced structures can be found. However, the corresponding conditions lie on a relatively isolated and small "bridge" region in the landscape characterizing the efficiency of the process as a function of the two relevant parameters, the maximum coupling constant amplitude and

the magnitude of the jump in the difference between the propagation constants of the waveguides. The consequence is that such structures would have a lower tolerance with respect to errors in the design, as well as a smaller bandwidth with respect to structures associated to larger flatter regions of the same landscape. All this gives some of the reasons for which we have preferred the adiabatic approaches with continuously varying detuning rather than the present approach with binary-type detuning for our experimental studies.

A.3 Backward propagation in adiabatic waveguide structures

In this section we will discuss theoretically backward propagation in some specific waveguide structures, these are the one corresponding to the two-state STIRAP analogy that we studied in section 4.4, as well as a three-waveguides structure that mimics the half-STIRAP process. Both these structures act as a broadband beam-splitter if taken in the forward direction, light is injected in one input port and exists from two output ports. Here we take the structures in reversed direction and inject light waves in backward direction into each of the two active output ports. Our brief investigations will focus on how the backward propagating waves do evolve upon variation of the relative phase impinged on the two backward inputs.

We start by considering the case of two-state STIRAP-analog waveguides. For the forward direction we know from the theoretical argumentation in chapter 4 that, for injection solely in WG1 and for case A (detuning maximum preceding the coupling maximum), we expect to obtain two output waves of equal amplitude in WG1 and WG2, but opposite phase. This is related to the fact that the output state is the adiabatic state $\mathbf{B}_{-}(L) = (\mathbf{A}_1 - \mathbf{A}_2)/\sqrt{2}$ and the amplitudes associated to the two diabatic states $\mathbf{A}_1$ and $\mathbf{A}_2$ have opposite sign and thus a phase shift $\Delta\phi = \pi$ as given in the paragraph before Eq. (4.9) in section 4.4. For the case B the situation is reversed and the wave amplitudes at the output of WG1 and WG2 are expected to be reciprocally in phase because the output wave state is given by $\mathbf{B}^*(L) = (\mathbf{A}_1 + \mathbf{A}_2)/\sqrt{2}$.[1] In the following we discuss only the case A but the same conclusions would be drawn also for case B. We recall first in Fig. A.8 the behavior in the case of forward propagation by employing the same parameters as those used in the theoretical section of the section. 4.4.

[1]It is worth noting that the above reciprocal phase shift applies for the case where the function $\Delta\beta(z)$ has positive values, that is $\beta_2(z) \geq \beta_1(z)$. The two-state STIRAP approach is equally valid also if $\Delta\beta(z)$ is negative everywhere. In this case one would obtain an output mutual phase shift $\Delta\phi = 0$ for case A and of $\Delta\phi = \pi$ for case B.

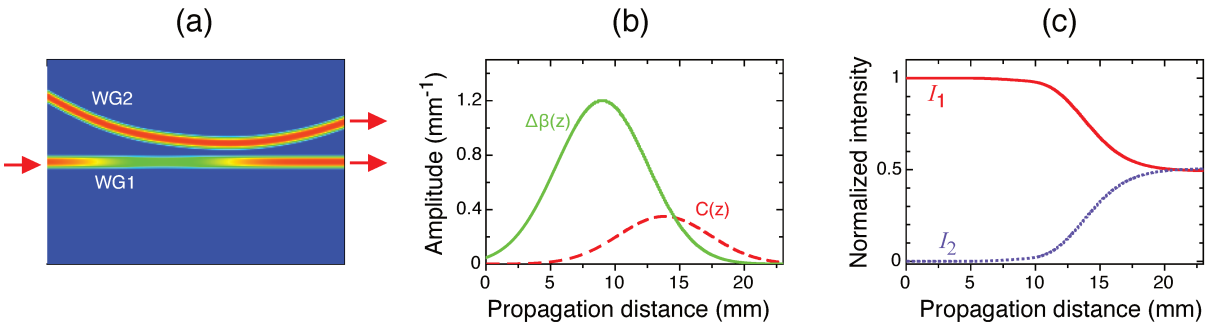

Figure A.8: Forward propagation in the case two-state STIRAP inspired waveguide system (case A). (a) Waveguide structure. (b) Longitudinal dependence of the detuning $\Delta\beta(z) = \beta_2(z) - \beta_1(z)$ and of the coupling constant $C(z)$. (c) Evolution of the intensities I_1 and I_2 in WG1 and WG2, respectively, upon forward injection in WG1. In the present case the two equally intense output waves have a mutual phase shift of $\Delta\phi \approx \pi$.

Let us now take the same structure and inject two waves from the output ports in the backward direction. If we represent this situation again by drawing the propagation direction from left to right we get the picture given in Fig. A.9(a). We allow in this case to impose a relative phase shift $\Delta\phi$ between the two input waves. Figure A.9(c) shows the intensity evolution in the two waveguides upon backward propagation. The solid red and blue lines corresponds to the case $\Delta\phi = \pi$, which is the phase-shift expected after forward propagation in the same structure. It is seen that waves evolve to bring back all the power to WG1, which is the waveguide were the light was injected in forward direction. However, we see that there are some weak oscillations in the spatial dynamics of both intensities I_1 and I_2, which are not present in the forward direction (cf. Fig. A.8(c)). The reason for this difference is related to the fact that our simulated structure is not a perfect two-state STIRAP system but only an approximation to it. Specifically, as seen in Fig. A.8(b) and Fig. A.9(b), both $\Delta\beta(z)$ and $C(z)$ still deviate a bit from zero either at the beginning or at the end of the propagation. As a consequence the exact mutual phase shift of the output waves after forward propagation differs by few percent from the expected value of π. If this is taken into account at the input of the backward process, one obtains the smooth curves given by the violet and light blue dashed lines in Fig. A.9(c). These curves depict in fact the time reversal process to the one in Fig. A.8(c) showing that the structure acts as an ideal linear optical lossless element.

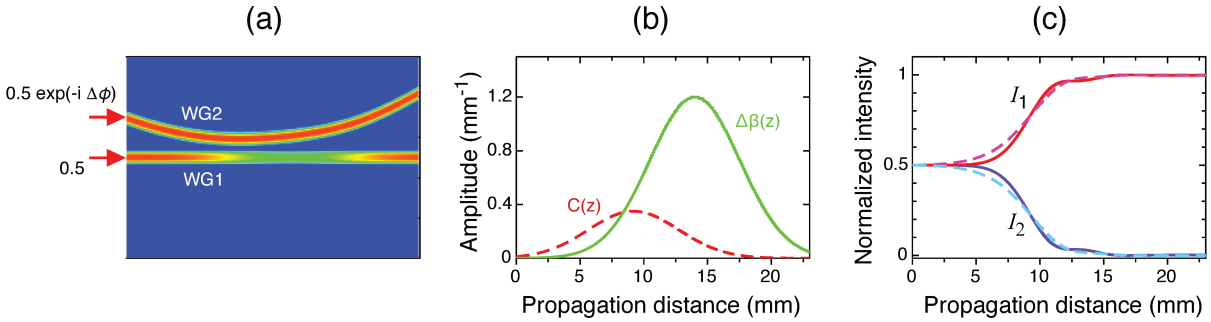

Figure A.9: Backward propagation for the two-state STIRAP waveguide structure of Fig. A.8. (a) Waveguide structure, two waves with equal amplitude and a mutual phase shift $\Delta\phi$ are injected into the two waveguides. (b) Longitudinal dependence of the detuning $\Delta\beta(z) = \beta_2(z) - \beta_1(z)$ and of the coupling constant $C(z)$. (c) Evolution of the intensities I_1 and I_2 in WG1 and WG2, respectively, upon backward injection in WG1 and WG2. The solid red and blue lines are for $\Delta\phi = \pi$ and give the longitudinal dependences of the intensities in WG1 and WG2, respectively. The dashed violet and light blue curves give the corresponding evolution for the more precise value $\Delta\phi = 1.036\pi$ for the relative phase.

For the above example we have chosen the correct imposed phase shift $\Delta\phi$ that corresponded to the one naturally occurring in the same structure upon forward propagation of a wave initially injected in WG1. Therefore the light goes back to WG1 in backward direction. This is no longer true if the imposed mutual phase shift is varied, in this case the backward propagation will generally lead at the other end of the structure to a distribution of the intensities among the two waveguides which will depend on the value of $\Delta\phi$. This is illustrated in Fig. A.10 where the output intensities I_1 and I_2 after back propagation are depicted as a function of $\Delta\phi$. The figure also illustrates the spatial evolution of the two intensities for three selected values of $\Delta\phi$. From the main bottom graph in Fig. A.10 it can be easily recognized that the two output intensities I_1 and I_2 follow a relationship of the type

$$I_j(\Delta\phi) = \frac{1}{2}\left[1 + (-1)^j \cos\Delta\phi\right] \ , \tag{A.3}$$

where $j = 1, 2$. This is exactly the same kind of transmission function like the one for a conventional beam splitter with two input ports and two output ports illuminated simultaneously in both input ports.[2] Therefore the two-state STIRAP structure takes exactly the role of a reciprocal broadband beam splitter.

[2]Actually the curves in the main graph of Fig. A.10 are slightly shifted with respect to the relationship (A.3). This is related to the already discussed fact that for our simulated structure the output waves mutual phase shift in forward direction is not exactly π. Consequences of this are the small oscillations seen in the inset for $\Delta\phi = \pi$, as well as the fact that the output intensities I_1 and I_2 for $\Delta\phi = \pi/2$ are not exactly the same, as it would be expected for an ideal two-state STIRAP equivalent structure.

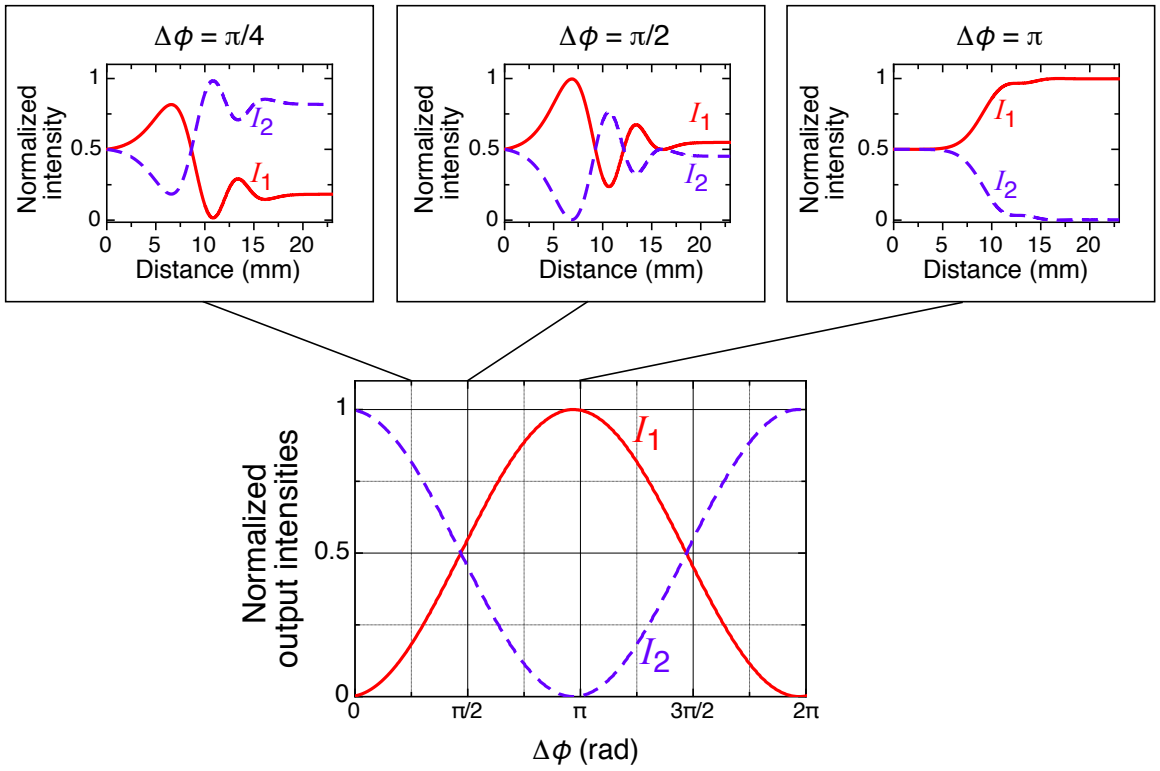

Figure A.10: Normalized output intensities I_1 and I_2 as a function of the mutual phase shift $\Delta\phi$ upon back-propagation in the two-state STIRAP waveguide structure of Fig. A.8. The three insets give the spatial evolution of the intensities in the two waveguides for the values of $\Delta\phi$ equal to $\pi/4$, $\pi/2$ or π.

The above argumentations can be extended to waveguide structures with additional input and output ports. Here we bring only the example of the half-STIRAP (also known as fractional STIRAP) structure, which has three input and output ports but only one specific input ports and two of the output ports can be used for broadband 1-to-2 splitting [179]. Another example would be the adiabatic multiple beam splitter described by Ciret et al.[26] that has 7 (or $2N+1$) input ports and 7 (or $2N+1$) output ports but only one input port and three (or N) of the output ports are used for the 1-to-3 (1-to-N) broadband beam splitting.

The waveguide configuration that mimics the half-STIRAP quantum process contains three waveguides and can be easily understood based on the knowledge on the STIRAP-like adiabatic light passage that we have described in the previous chapters (chapter 4/Sec. 4.4 and chapter 3/Sec. 3.3.3.1). As illustrated in Fig. A.11, the half-STIRAP structure simply consists in interrupting the waveguide STIRAP process at half propagation distance. Since the waveguide 2 does not get any light throughout all the propagation, cutting the structure at half leads to a splitting of the wave that was originally injected in WG1 into an equal amount of intensity in waveguides 1 and 3. Obviously, since at half propagation

the spatial evolution of the intensities I_1 and I_3 is quite steep, it is very important to cut the structure exactly at half. At this point the theory predicts that the waves in WG1 and WG3 should be out-of-phase by π.

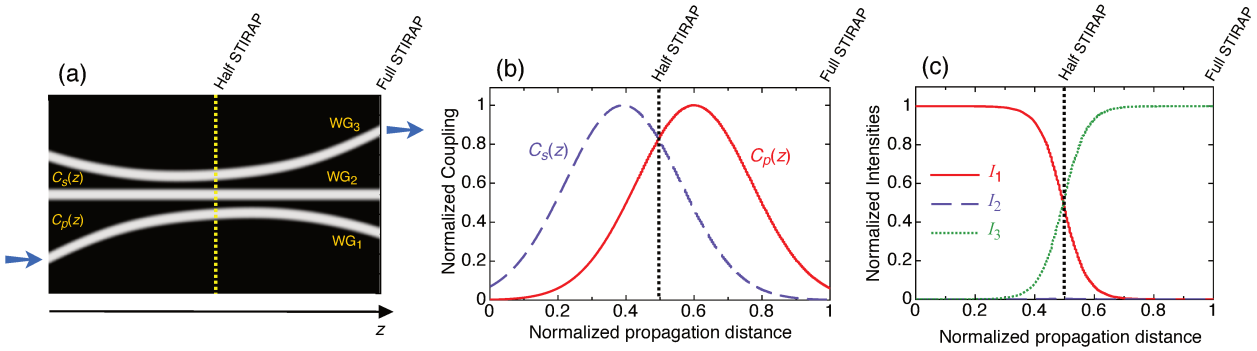

Figure A.11: Concept of a half-STIRAP waveguide structure as compared to a (full) STIRAP structure. (a) Waveguide design, the Stokes coupling $C_s(z)$ precedes the pump coupling $C_p(z)$ and the half-STIRAP structure is cut at half distance. (b) Corresponding evolution of the coupling constants. (c) Corresponding evolution of the intensities in the three waveguides. At half distance the intensity is equally distributed among the the waveguides 1 and 3 with a phase shift of π between the two waves.

If the half-STIRAP structure is injected in backward direction on waveguides 1 and 3 with this phase shift of π, the propagation leads to a reconstruction of the power in WG1, as it can be expected from a time reversal argumentation. This is shown in the graph for $\Delta\phi = \pi$ in Fig. A.12(b), which shows the light intensity evolution in the three waveguides in this case. Figure A.12 is the equivalent of Fig. A.10 for the case of half-STIRAP and was obtained for a structure with the coupling constants as depicted in Fig. A.11(b) with a maximum of the coupling constants equal to $C_{max} = 6$ mm^{-1} and a propagation distance (half length) $L/2 = 11.5$ mm. If the mutual phase shift between the re-injected waves in WG1 and WG3 differ from π the power in WG1 always experiences a damped spatial oscillation towards a certain output level depending on $\Delta\phi$. At the same time the power in the two remaining waveguides oscillates rapidly between them. This is a crucial difference to the case of two-state STIRAP summarized in Fig. A.10. While for the two-state STIRAP the light has only two waveguides to choose with, here there is also the central waveguide which is silent in forward direction upon initial excitation of WG1. However, this waveguide is no longer silent in backward direction if the phase shift is not chosen appropriately. As seen in Fig. A.12(a) the backward output intensity in WG1 follows again a function of the type (A.3) which corresponds to the usual linear superposition of two equally intense waves. The output intensities in WG3 and WG2 also follow the same kind of function, their sum makes up for the missing intensity in WG1. This kind of behavior can be generalized to adiabatic waveguide configurations with additional input

and output ports, like the case of the multiple beam splitter demonstrated experimentally in Ref. [26].

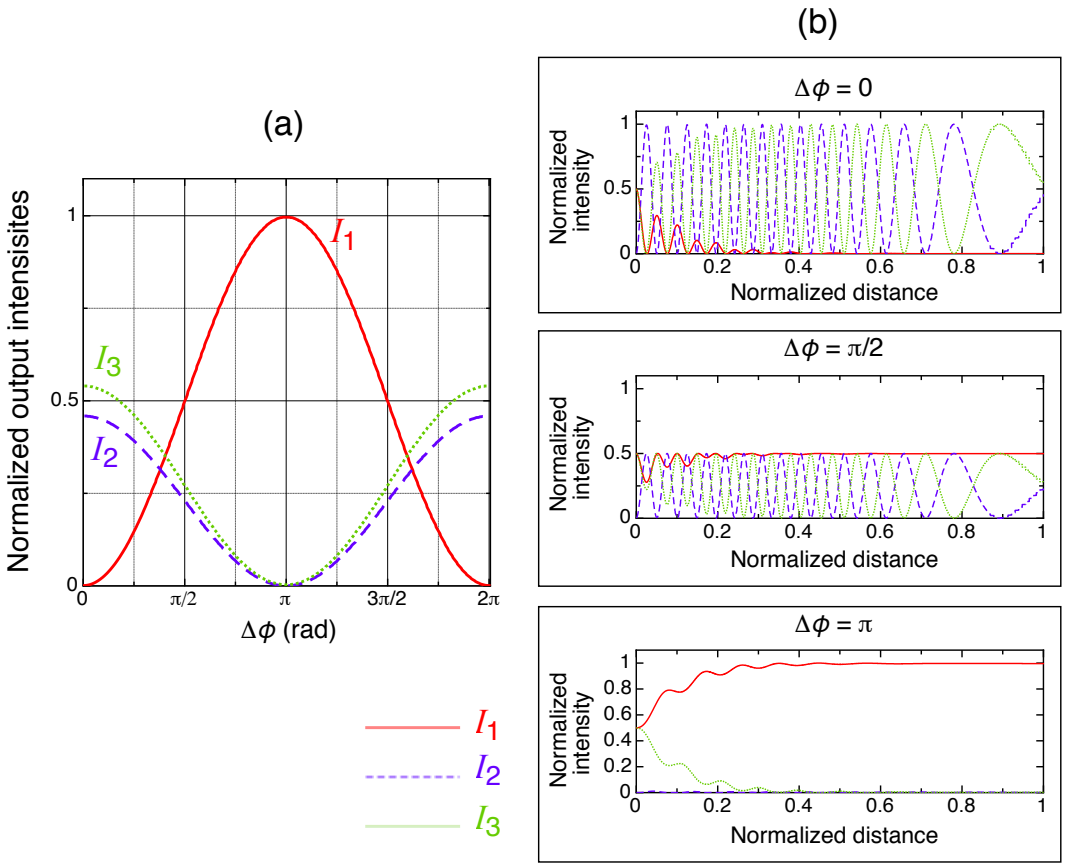

Figure A.12: (a) Normalized output intensities I_1, I_2 and I_3 in waveguides 1 to 3 as a function of the mutual phase shift $\Delta\phi$ between the waves injected backward in WG1 and WG3 in the half-STIRAP waveguide structure of Fig. A.11. The three graphs in (b) give the spatial evolution of the intensities in the three waveguides for $\Delta\phi$ equal to 0, $\pi/2$ and π.

To conclude this section one can say that adiabatic waveguide configurations leading to a beam splitter behavior, like the two-state STIRAP and the half-STIRAP one, conserve all the features of a linear beam splitter even if used as beam recombiner in backward direction. Some interesting features appear if the number of waveguides (input and output ports) is larger than two because ports which are usually not active in the forward 50:50 broadband beam splitting process can be activated by changing the phase of one of the backward propagating wave. However, all these devices act as reciprocal lossless linear optical elements that fulfill the invariance with respect to time reversal. One can anticipate that very interesting new features can be expected if the structures are made to react non linearly to the propagating light waves. In this case reciprocity would be lost, which would open the way for several useful effects, like for instance the realization of optical diodes

(one way transmission) in such kind of waveguide configurations or different new features associated to the control of light by light in an integrated optical domain.

A.4 Conclusion

In this appendix, we have summarized some complementary theoretical investigations performed in the course of this thesis. In the first section we have analyzed systems of two or three waveguides with a jump of the sign of a non-zero waveguide detuning at half propagation distance. In the second section we have analyzed the back propagation upon injection of two waves in structures that lead to broadband 50:50 beam splitting when taken in the forward direction with the appropriate input wave.

It is found that the approach with the detuning discontinuity can work in principle to realize broadband directional coupling or an alternative way for broadband beam splitting, which is true even for parameters compatible with the experimental platform at our disposal. However the related conditions are in a small "bridge" region in the landscape that describes the efficiency of the processes as a function of the relevant parameters. Therefore such structures are expected to be less robust and more critical as compared to the alternative approaches based on RAP or two-state STIRAP that we have discussed theoretically and experimentally in chapter 4.

For the study of the backward propagation in beam splitting structures we have considered specifically the cases where such structures are the analogs of the two-state STIRAP or the half-STIRAP process in quantum physics. We have clearly shown that such devices behave exactly in the way expected for conventional (eventually multi-port) beam splitters. In this case several interesting new perspectives would become feasible if the waveguides are made to respond nonlinearly to the propagating light.

B

French Summary – Résumé en français

Contents

This annex presents a long abstract of the thesis. / Cette annexe présente un résumé long de mon manuscrit de thèse.

B.1 Introduction

La physique classique et la physique quantique sont différentes par essence, même si elles ont souvent des formalismes mathématiques similaires, pouvant conduire à des analogies spécifiques et utiles. A titre d'exemple, l'équation de Schrödinger indépendante du temps et l'équation de Helmholtz ont une forme mathématique commune. Le phénomène classique de diffraction, qui est liée à la transformée de Fourier, présente de fortes similitudes avec le principe d'incertitude de Heisenberg. Alors que les états intriqués des particules sont de nature purement quantique et n'ont pas d'analogie classiques, les phénomènes basés sur les interférences quantiques trouvent leur analogies en physique classique. Un exemple est la forte similitude entre les bandes interdites électroniques associées aux potentiels périodiques dans les structures cristallines et les bandes interdites photoniques des

structures diélectriques périodiques, le premier phénomène étant lié aux fonctions d'onde d'électrons quantiques, le second aux ondes électromagnétiques classiques. Dans ce contexte, l'optique a été une source d'inspiration des pionniers de la mécanique quantique, par exemple lorsque De Broglie a proposé que toute particule devrait avoir une nature ondulatoire.

De nombreux exemples d'analogies couvrent divers domaines, comme les ondes acoustiques de Bloch [1] ou l'effet Casimir acoustique [2]. Une liste exhaustive des analogies quantiques-classiques peut être trouvée dans la réf. [3]. Les analogies les plus riches sont trouvées dans le domaine de l'optique, notamment en ce qui concernent les structures et réseaux photoniques. Un bon aperçu de ce domaine peut être trouvé dans l'article de revue de Longhi [4]. La propagation de la lumière dans de telles structures présente de fortes similitudes avec certains problèmes généraux de la mécanique quantique, comme l'étude Aharonov-Bohm [5], la phase de Berry [6, 7] ou l'effet Hall [8, 9]. Dans la même ligne, plusieurs analogues avec des phénomènes de la physique du solide ont été identifiés, comme les oscillations de Bloch [10, 11], la localisation d'Anderson [12, 13], ou les effets de la physique de surface [14, 15].

Parmi les structures photoniques, celles composées d'un nombre limité de guides d'onde plans couplées présentent un grand intérêt. De telles structures fournissent une analogie avec les systèmes quantiques composés d'un nombre équivalent d'états discrets couplés par un champ externe, qui peut être une radiation laser quasi résonante. Dans ce contexte, une étape très importante a été l'établissement d'une relation entre une structure de trois guides d'ondes avec une géométrie particulière et le fameux processus quantique de STIRAP (Stimulated Raman Adiabatic Passage) [16, 17, 18]. La première proposition mettant en évidence cette relation a été donnée par Paspalakis en 2006 [19] et la première démonstration expérimentale a été donnée par Longhi et *al.* en 2007 [20] en utilisant des guides d'ondes formés par échange d'ions sur un substrat de verre. D'autres études ont conduit à la démonstration des analogies avec le processus dit "half-STIRAP" [21] ou "multi-state STIRAP" [22, 23, 24]. Ce type de d'analogie est au coeur de ce travail de thèse et est discuté en détails dans ce manuscrit.

Les activités du laboratoire LMOPS dans ce domaine ont débuté avec la thèse de Charles Ciret [25], où des analogies avec la physique quantique ont été démontrées par des expériences en utilisant des structures guidantes générées par la technique de photo-induction par illumination latérale. Dans ces travaux antérieurs, des analogies optiques avec le multi-STIRAP, l'effet Autler-Townes, et la transparence induite électromagnétiquement (EIT) ont été étudiées théoriquement et implémentées expérimentalement avec succès pour des guides d'ondes [24, 26, 27]. Ils ont mené à la démonstration de diviseurs de faisceaux multiples achromatiques,le transfert de lumière entre les guides étant adiabatique et fonctionnant sur une large bande spectrale. Dans ces travaux, seules les constantes de couplage entre guides d'ondes ont été modulés spatialement. Les constantes de couplage des guides

imitent la modulation temporelle des fréquences de Rabi dans les systèmes atomiques. Dans cette thèse, nous utilisons des guides d'ondes générés par technique d'illumination latérale pour la démonstration d'autres analogies intéressantes entre la mécanique quantique et les guide d'onde optiques. Ici, non seulement les constantes de couplage sont modulées spatialement mais aussi les constantes de propagations des guides. Cette modulation est équivalente à l'évolution temporelle du désaccord en fréquence (désaccord entre la fréquence centrale du laser de couplage et la fréquence de transition) dans les systèmes atomiques. Ceci permet d'explorer de nouvelles analogies et d'ajouter un nouveau paramètre de contrôle des systèmes optiques étudiés. Ainsi, cette nouvelle approche ajoute de la richesse aux systèmes tout en conservant l'aspect adiabatique et la robustesse associée.

Les principaux résultats de la présente thèse concernent l'étude d'analogies optiques de trois phénomènes quantiques : le processus du STIRAP à deux niveaux [28, 29], le passage adiabatique rapide (RAP) [30], et l'élimination adiabatique des états intermédiaires [31, 32, 33, 34, 35].

Le mécanisme récemment développé de STIRAP à deux états de la mécanique quantique consiste en une création adiabatique d'une superposition cohérente d'états dans un système couplé [30, 35]. Il repose sur une analogie formelle entre les équations décrivant le processus STIRAP et les équations de Bloch dans un système à deux niveaux. Dans cette thèse, nous utilisons ce concept pour un système de deux guides d'ondes optiques couplés par champs évanescents pour proposer un nouveau type de diviseur de faisceau robuste dans lequel la division de puissance optique est contrôlée au moyen d'une modulation de la constante de propagation le long de la direction de propagation z.

Le processus de RAP [30] est exploité quant à lui pour réaliser un coupleur directionnel hautement achromatique. En physique quantique, le processus du RAP produit un transfert adiabatique et efficace de population d'un état initial vers un état cible en suivant les états adiabatiques du système. Dans notre cas de deux guides d'onde, le transfert de puissance visé est effectué grâce à la modulation de la constante de propagation longitudinale d'une des deux guides assisté par la modulation de la constante de couplage. Dans les deux cas, la modulation spatiale du désaccord entre les guides fournit un mécanisme de transfert de puissance très robuste, peu aux variations de l'amplitude maximale du désaccord et à la longueur d'onde.

Le processus d'élimination adiabatique de la physique quantique consiste à éliminer les états intermédiaires dans un système à N états couplés en raison du fort désaccord entre les états intermédiaires et les états externes (état initial et état cible). Ce système est réduit à un système effectif à deux états. Cette approche trouve toute son analogie dans les structures de guide d'ondes dans lesquelles les guides d'ondes intermédiaires sont "éliminés" en introduisant un fort désaccord entre leurs constantes de propagation et celles des guides externes. Cela conduit, là encore, à un transfert de lumière achromatique entre

les guides d'ondes externes. A différence des cas des systèmes inspirés par le phénomène de STIRAP, ce transfert est symétrique et fonctionne pour un nombre total de guides impairs ou pairs.

B.2 Principe des analogies entre des guides d'ondes et des systèmes atomiques couplés

Nous illustrons l'une des analogies entre la mécanique quantique et l'optique guidée au moyen de l'exemple d'un système atomique à deux niveaux et son analogue optique composé de deux guides d'onde. La figure B.1 illustre cet exemple d'analogie.

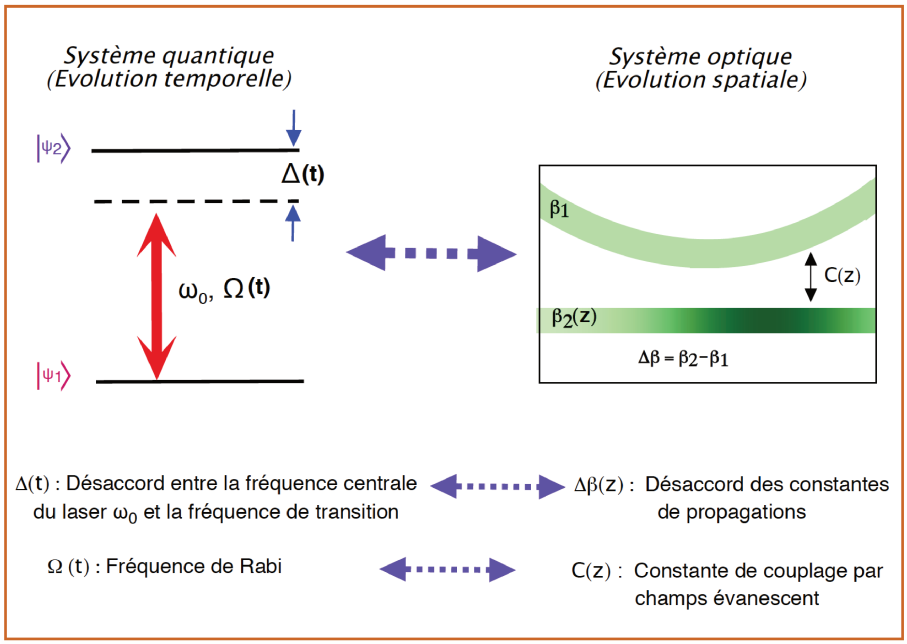

Figure B.1: (à gauche) Schéma du système quantique à deux états présentant un désaccord $\Delta(t)$ évoluant dans le temps, couplé par un champs laser possédant une fréquence de Rabi $\Omega(t)$ elle aussi dépendante du temps .(à droite) Schéma de guides d'onde couplés via la constante de couplage $C(z)$, présentant une évolution spatiale du désaccord entres les constantes de propagation longitudinales $\Delta\beta(z)$.

Dans le système atomique situé à gauche de la figure B.1, la fréquence de Rabi Ω (liée à l'intensité du champ de couplage) du champ laser impliqué dans le processus du transfert de population de l'état fondamental $|\psi_1\rangle$ vers l'état final $|\psi_2\rangle$ (voir Fig. B.1) est ajustée en fonction du pourcentage de population à placer dans l'état final $|\psi_2\rangle$. De façon similaire, pour les guides d'onde, la constante de couplage C peut être conçue en fonction de la distribution de lumière souhaitée à la sortie des guides. Le transfert de lumière entre les guides est contrôlé en partie au moyen de la constante de couplage variable spatialement

en analogie avec le transfert de population contrôlé par la fréquence de Rabi variable dans le temps. La constante de couplage est ajustée essentiellement en réglant la distance entre les guides, puisque la partie évanescente de l'onde se propageant dans un guide vue par l'autre guide qui implique le couplage : plus les guides sont proches plus le couplage est fort.

Le désaccord Δ entre le champ laser de fréquence ω_0 et la transition atomique fournit un paramètre supplémentaire pour contrôler de façon adiabatique l'évolution du système. Ce désaccord, dépendant du temps, est donné par la différence entre la fréquence centrale du laser et la fréquence de transition. Le paramètre correspondant dans le cas des guides d'onde est représenté par une évolution spatiale du désaccord $\Delta\beta$ des constantes de propagation des guides. Ici les constantes de propagation sont ajustées en ajustant le contraste d'indice des guides qui évolue longitudinalement. L'introduction de ce nouveau paramètre ajoute un degré de liberté supplémentaire. De plus, l'ajustement de la constante de couplage et les constantes de propagation permet d'explorer et traiter de nouveaux phénomènes et analogies.

Dans le système atomique de la figure B.1 (gauche), la population (électrons, molécules,...) évolue dans le temps d'un état initial donné vers un état final cible. La dynamique du système est décrite par l'équation de Schrödinger dépendante du temps qui peut s'écrire dans la *base adiabatique*[1] sous l'approximation des ondes tournantes (RWA) [115, 116] sous la forme matricielle suivante

$$i\frac{d}{dt}\begin{bmatrix} p_1(t) \\ p_2(t) \end{bmatrix} = \frac{1}{2}\begin{bmatrix} 0 & \Omega(t) \\ \Omega(t) & 2\Delta(t) \end{bmatrix}\begin{bmatrix} p_1(t) \\ p_2(t) \end{bmatrix} \tag{B.1}$$

où $p_1(t)$ et $p_2(t)$ représentent les amplitudes de probabilité des états $|\psi_1\rangle$ et $|\psi_2\rangle$, respectivement. Par le biais de la modulation temporelle de la fréquence de Rabi Ω et du désaccord Δ, les valeurs de p_1 et de p_2 sont ajustées.

L'analogue optique (figure B.1(droite)) est une structure composée de deux guides d'onde pour lesquels la constante de propagation $\beta_2(z)$ varie le long de la distance de propagation z, ceci produit une variation spatiale du détuning $\Delta\beta(z)$ entre les guides. La courbure du guide 1 conduit à une modulation spatiale de la constante de couplage $C(z)$ entre les guides. La dynamique de la lumière dans la structure optique est décrite par la théorie des modes couplés (CMT) [49]

$$i\frac{d}{dz}\begin{bmatrix} a_1(z) \\ a_2(z) \end{bmatrix} = \begin{bmatrix} 0 & C(z) \\ C(z) & \Delta\beta(z) \end{bmatrix}\begin{bmatrix} a_1(z) \\ a_2(z) \end{bmatrix} . \tag{B.2}$$

a_1 et a_2 sont les amplitudes des modes dans les guides 1 et 2, respectivement. En fonction des profils spatiaux de C et de $\Delta\beta$, la quantité de lumière transférée du guide initial (guide

[1] cette base est constituée des vecteurs adiabatiques évoluant dans le temps. Quand l'évolution est suffisamment lente, les vecteurs diabatiques suivent les vecteurs adiabatiques.

1) au guide 2 peut être contrôlée.

Les équations (B.1) et (B.2) sont similaires et les paramètres optiques C et $\Delta\beta$ jouent les rôles de paramètres quantiques Ω et Δ, respectivement.

B.3 Transfert de lumière équivalent au passage adiabatique rapide (RAP)

B.3.1 Le processus quantique du RAP

Dans le phénomène du RAP (Fig. B.2), le couplage Ω et le détuning Δ évoluent dans le temps pour transférer de manière robuste et efficace toute la population initialement préparée dans l'état initial $|\psi_1\rangle$ vers l'état final cible $|\psi_2\rangle$. Δ doit évoluer d'une valeur négative à une valeur positive tout en passant par zéro (voir Fig. B.2(b)) (ou réciproquement en passant d'une valeur positive à une valeur négative).

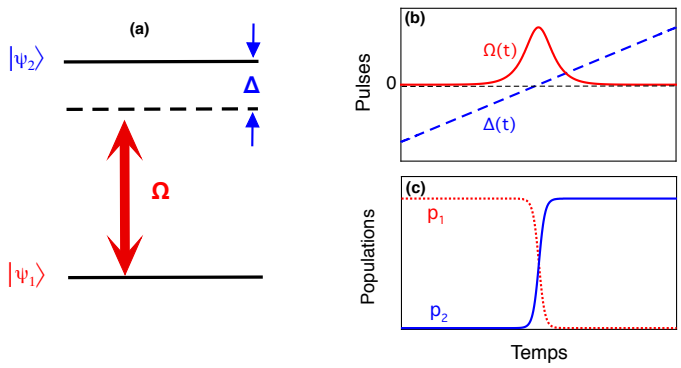

Figure B.2: (a) modélisation d'un système à deux niveaux non résonant où le processus du RAP peut avoir lieu. (b) évolution temporelle du détuning $\Delta(t)$ et de la fréquence de Rabi $\Omega(t)$ et (c) l'évolution des populations des états $|\psi_1\rangle$ et $|\psi_2\rangle$.

La figure B.2(c) montre un transfert complet de la population de l'état $|\psi_1\rangle$ à l'état $|\psi_2\rangle$. Les paramètres qui contrôlent ce transfert de population doivent varier lentement dans le temps pour que le transfert puisse se faire de manière robuste et efficace.

Pour les guides d'onde, le processus du RAP peut être exploité pour réaliser un transfert complet de la lumière d'un guide à l'autre. Ceci peut être réalisé en modulant les paramètres optiques C et $\Delta\beta$ de telle sorte à reproduire la configuration quantique.

B.3.2 L'analogie optique du RAP

Le système optique équivalent est composé de deux guides d'ondes couplés par champs évanescents et pour lequel la constante de propagation longitudinale de l'un des guides

évolue le long de la distance de propagation. Pour imiter l'évolution temporelle de la fréquence de Rabi dans le cas quantique, nous introduisons une modulation spatiale de la constante de couplage (qui est reliée à la séparation entre les guides). Nous étudions théoriquement et expérimentalement l'effet de ces modulations sur le transfert de lumière entre les guides d'ondes couplés et sur la robustesse du transfert. La structure optique utilisée, basée sur le processus du RAP permet de réaliser un transfert de lumière efficace, robuste et achromatique. Elle fonctionne comme un coupleur directionnel large bande. Sur la figure B.3, la structure utilisée est montrée ainsi que les évolutions spatiales de détuning $\Delta\beta$ et de la constante de couplage C utilisées.

Comme montré sur la figure B.3(b), le détuning $\Delta\beta(z)$ s'annule au milieu de la propagation, cette condition est importante pour que le processus du RAP prenne place dans les guides d'onde.

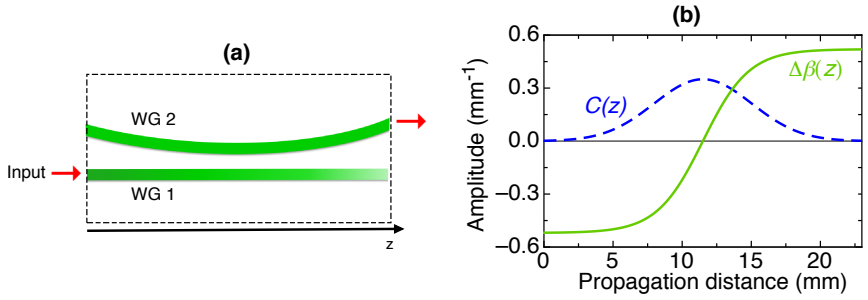

Figure B.3: (a) Schéma de la structure des guides fournissant l'analogie optique au processus du RAP. (b) Evolution longitudinale correspondante de la constante de couplage $C(z)$et du detuning $\Delta\beta(z)$.

Le système d'équation (B.2) pour la structure de la figure B.3(a) pour deux longueurs d'onde différentes pour tester l'achromaticité du système. Expérimentalement, la structure utilisée est générée en utilisant la photo-inscription des guides par illumination latérale [37] sur un cristal de niobate de strontium baryum de formule chimique $Sr_xBa_{1-x}Nb_2O_6$ (SBN) possédant des propriétés photo-réfractives. Le contraste d'indice des guides induits est de l'ordre de 10^{-4} avec la largeur typique des guides générés est de 7 µm. Les profils d'intensité sont obtenus expérimentalement en imageant la face de sortie des guides sur une caméra CCD, ce qui permet d'avoir la distribution de la lumière entre les guides après une distance de propagation z.

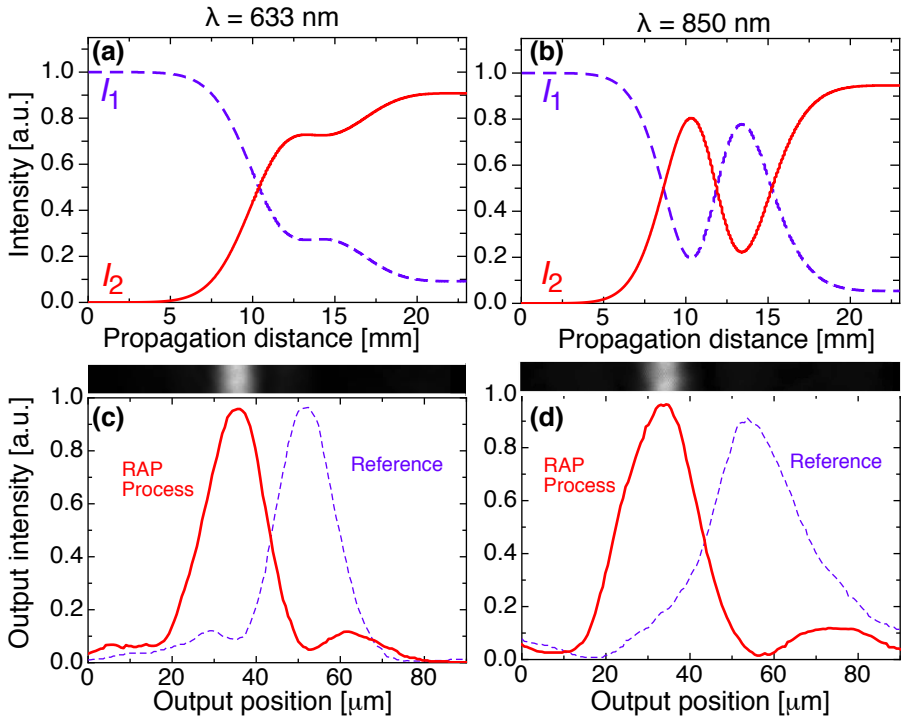

Figure B.4: Intensités simulées dans les guides de la structure montrée sur la figure B.3 pour une longueur d'onde (a) de 633 nm*, (b) de* 850 nm*. (c) et (d) distributions de l'intensité en sortie du cristal mesurée en présence des deux guides (courbe rouge) en l'absence du guide 2 (courbe en traits bleus) pour les deux longueurs d'onde.*

La figure B.4 montre les résultats théoriques et expérimentaux pour l'intensité lumineuse des guides 1 et 2 de la structure montrée en Fig. B.3(a). Pour les deux longueurs d'onde utilisées, les courbes théoriques des figures B.4(a) et (b) prévoient un transfert presque total de l'intensité lumineuse du guide 1 vers le guide 2. Les profils expérimentaux de la distribution de l'intensité lumineuse à la sortie des guides montre un transfert presque complet pour les deux longueurs d'onde du guide 1 vers le guide 2.Le processus quantique du RAP a été étudié théoriquement et implémenté expérimentalement avec succès grâce à la modulation longitudinale de $\Delta\beta$, assisté par une modulation de la constante de couplage C. La structure optique générée expérimentalement par la technique de photo-inscription par illumination latérale agit comme coupleur directionnel large bande.

Grâce à l'introduction du detuning $\Delta\beta$ et sa modulation, le processus du RAP a pu avoir lieu dans la structure de la figure B.3(a). La figure B.5 montre les profils théoriques et expérimentaux de l'intensité lumineuse dans les guides 1 et 2 en l'absence de la modulation de $\Delta\beta$ ($\Delta\beta = 0$). Pour le cas de $\lambda = 633\,\text{nm}$, on observe un retour complet de la lumière vers le guide où elle a été injectée initialement tandis qu'une quantité importante est transférée dans le guide 2 pour $\lambda = 850\,\text{nm}$. Ainsi, le processus du RAP n'a pas lieu dans la structure et un transfert robuste ne peut avoir lieu [157].

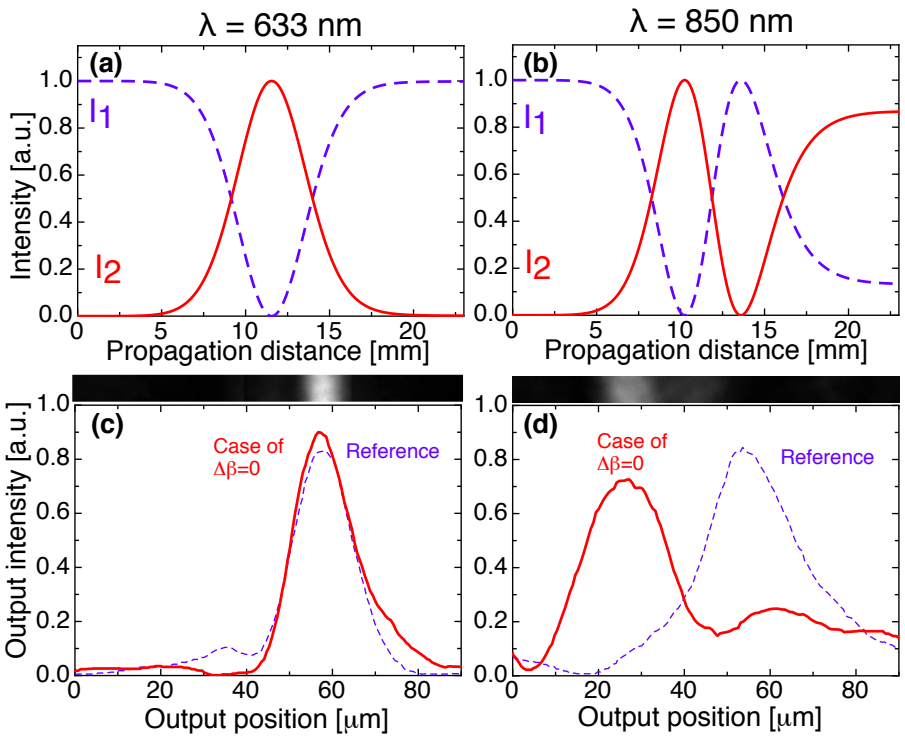

Figure B.5: Intensités simulées dans les guides de la structure montrée sur la figure B.3 sans la modulation de $\Delta\beta$ pour une longueur d'onde (a) de 633 nm*, (b) de* 850 nm*. (c) et (d) distributions de l'intensité mesurée dans le guide 2 (courbe rouge) en l'absence du guide 1 (courbe en traits bleus) pour les deux longueurs d'onde.*

B.4 Diviseur de faisceau basé sur le STIRAP à deux états

Le second processus étudié est celui du "two-state STIRAP". Il basé sur la similitude qu'il y a entre l'équation décrivant la dynamique temporelle de la population dans un système à deux niveaux avec un détuning Δ et celle d'un système à trois niveaux présentant le processus du STIRAP conventionnel. Le système à deux niveaux en question est décrit par le même type d'équation que (B.1). L'objectif est de réaliser un mélange égal des états à la fin du processus quantique, autrement dit une distribution égale de la population entre les deux états. Encore une fois, nous considérons une modulation de $\Delta\beta$ pour les guides afin d'imiter la modulation temporelle de Δ pour pouvoir concevoir et implémenter la structure optique équivalente.

On considère alors deux cas distincts pour la démonstration dans le cas des guides de l'analogie au two-state STIRAP.

➪ **Cas A :**

La configuration des guides correspondant à ce cas est montrée sur la figure B.6(a), le détuning $\Delta\beta(z)$ atteint son maximum avant celui de la constante de couplage $C(z)$. Ce cas est équivalent au cas contre intuitif pour le processus conventionnel du three-state STIRAP [16, 17].

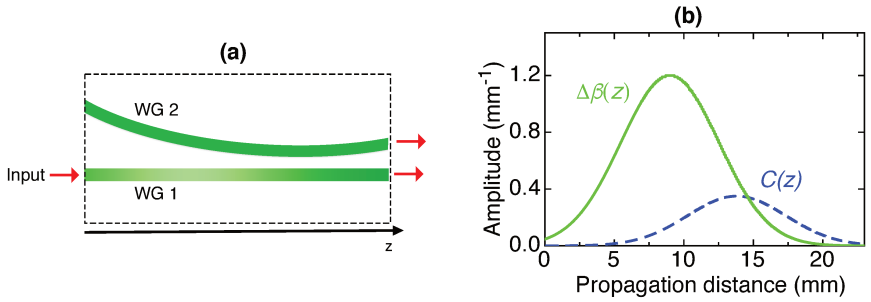

Figure B.6: (a) Schéma de la structure des guides fournissant l'analogie optique au processus du two-state STIRAP pour le cas A. (b) Évolution longitudinale correspondante de la constante de couplage $C(z)$ et du désaccord $\Delta\beta(z)$.

⇨ Cas B :

Dans ce deuxième cas, c'est la constante de coulage $C(z)$ qui précède le désaccord $\Delta\beta(z)$, il correspond au cas intuitif pour le processus du STIRAP standard dans un système à trois niveaux. Concrètement, il suffit d'injecter la lumière de la droite vers la gauche de la structure de Fig. B.6(a) toujours dans le guide 1. Il est à noter qu'un des intérêts du "two-state STIRAP" est que ce transfert s'effectue à la fois pour les cas contre-intuitif (équivalent au cas A), et le cas intuitif (équivalent au cas B), alors que le STIRAP conventionnel ne peut fonctionner que pour le cas contre-intuitif.

En procédant de la même façon que pour le RAP, nous étudions théoriquement la structure de la figure B.6(a), nous obtenons les résultats suivants

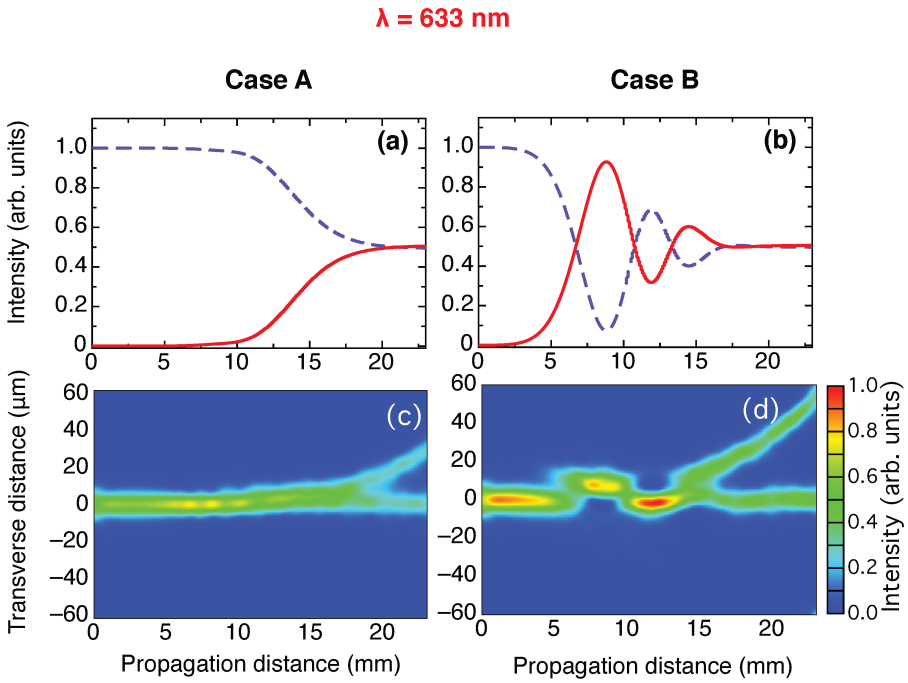

Figure B.7: Simulations numériques de la structure du two-state STIRAP pour une longueur d'onde sonde de $\lambda = 633\,\text{nm}$. Les panels (a) et (c) correspondent au cas A tandis que les panels (b) et (d) correspondent au cas B. (a) et (b) montre l'évolution de l'intensité dans le guide 1 (courbe en traits bleux) et dans le guide 2 (courbe pleine rouge) obtenu par la méthode des modes couplés. (c) et (d) montre l'évolution des intensités dans les guides en utilisant la méthode de BPM. Dans les deux cas une équi-répartition de la lumière est obtenue à la fin de la propagation.

Les résultats de la figure B.7 (a)+(b) sont obtenus en utilisant l'approche des modes couplés et ceux des figures B.7(c) et (d) en utilisant la méthode BPM (Beam Propagation Method)[161, 162] qui simule la propagation d'un faisceau dans une structure d'indice de réfraction donné. Les deux approches donnent des résultats très proches, une équi-répartition de la lumière sur les sorties des guides à la fin de la propagation. Les résultats présentés sont pour une longueur d'onde de 633 nm, des résultats similaires ont été obtenus pour $\lambda = 850\,\text{nm}$. Théoriquement, Le caractère achromatique de la structure optique conçue est vérifié.

Pour vérifier expérimentalement ces prédictions, nous choisissons des profils adéquats de la constante de couplage C et du détuning $\Delta\beta$. Les profils choisis assurent la robustesse de ces paramètres par rapport aux fluctuations dues aux imperfections expérimentales pour les deux longueurs d'onde considérées. La figure B.8 montre les résultats obtenu expérimentalement en sondant la structure du two-state STIRAP en Fig. B.6(a) avec deux longueurs d'onde sondes différentes $\lambda = 633\,\text{nm}$ et $\lambda = 850\,\text{nm}$ pour les cas A et B.

On observe qu'une division de faisceau est obtenue à la sortie des guides et cela confirme le caractère robuste et achromatique de la structure basée sur le processus du two-state STIRAP.

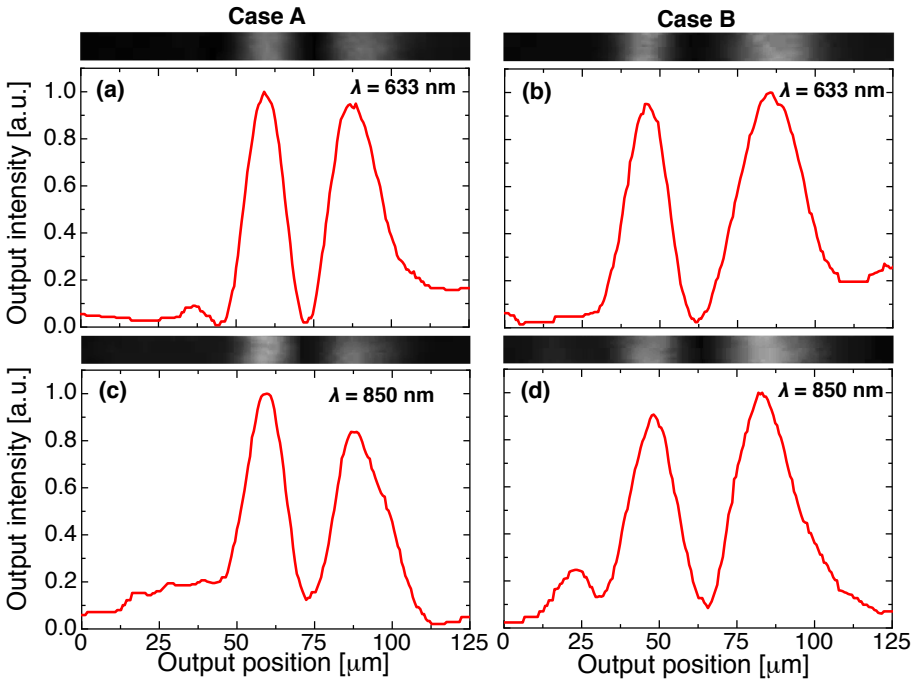

Figure B.8: Profiles expérimentaux de la distribution de l'intensité lumineuse à la sortie des guides pour les deux cas A et B et pour deux longueurs d'onde sondes différentes $\lambda = 633\,\text{nm}$ *et* $\lambda = 850\,\text{nm}$. *Les panels (a) et (c) correspondent au cas A et les panels (b) et (d) au cas B.*

Encore une fois, grâce à la modulation du detuning $\Delta\beta$ assistée par la modulation de la constante de couplage C, l'analogie au two-state STIRAP quantique a pu être démontrée et la structure obtenue fonctionne comme un diviseur de faisceau large bande [157].

B.5 Elimination adiabatique

Le dernier phénomène étudié au cours de cette thèse est la technique d'élimination adiabatique (AE) [31, 32, 33, 34, 35]. Cela consiste a réduire un système atomique à N niveaux d'énergie à un système effectif à deux niveaux d'énergie en "éliminant" les états intermédiaires du fait du fort détuning Δ entre les fréquences des champs laser de couplage et les fréquences de transition. Pour les guides d'onde cela revient à assimiler un système à N guides d'onde couplés à un système effectif à deux guides. Ceci est possible lorsque le désaccord entre les constantes de propagation des guides intermédiaires et celles des guides extérieures est très fort. La figure B.9 montre la structure en question pour un nombre total de guides $N = 3$.

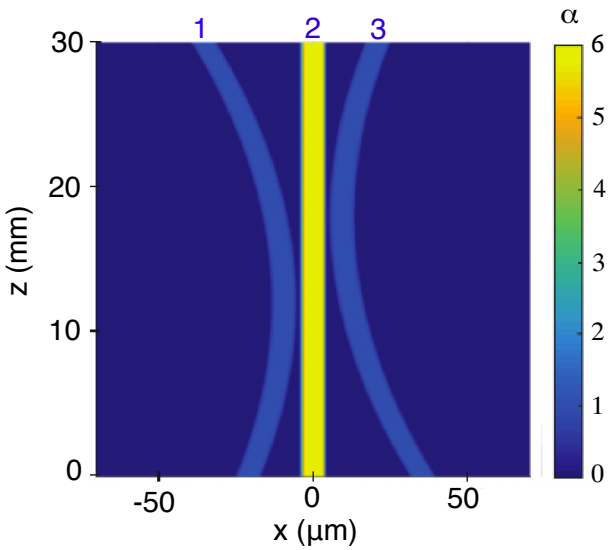

Figure B.9: La structure de guides d'onde considérée pour la mise en oeuvre de l'équivalent optique du processus de l'élimination adiabatique. Le guide central présente un fort détuning de la constante de propagation β par rapport à celles des guides extérieures. L'échelle de couleur présente le contraste d'indice de réfraction normalisé α des guides.

Sur la figure B.9, la courbure des guides extérieurs permettent des couplages C_P entre le guide 1 et le guide 2, C_S entre le guide 2 et le guide 3 variables le long de la propagation tandis que la difference d'indice de réfraction Δn (ou différence d'indice de réfraction normalisée α) entre le guide central et les guides courbés 1 et 3 conduit à un fort désaccord $\Delta\beta$ entre les guides qui ne varie pas le long de la propagation. Quand le désaccord $\Delta\beta$ vis à vis des constantes de couplage C_S et C_P est très grand et donc que :

$$\frac{|\Delta\beta|}{\sqrt{C_P^2(z)+C_S^2(z)}} \gg 1, \tag{B.3}$$

et si aucune lumière n'est initialement injectée dans le guide central, alors la condition (B.3) conduit à une suppression très forte de l'amplitude passant par le guide 2. C'est l'élimination adiabatique. Quand cette condition (B.3) est vérifiée, le système d'équations décrivant l'évolution de la lumière dans la structure de la figure B.9 peut être ramené à un système effectif équivalent à deux guides d'onde dont la dynamique spatiale est décrite par un système à deux équations couplées. Il est similaire à l'équation B.2 pour lequel les nouveaux paramètres C_{eff} et Δ_{eff} sont le couplage effectif et le détuning effectif du système réduit, leurs expressions en fonction de C_S, C_P, et $\Delta\beta$ sont données par

$$\Delta_{eff} = \frac{C_P^2(z) - C_S^2(z)}{\Delta\beta}, \tag{B.4}$$

$$C_{eff} = -\frac{C_P(z)C_S(z)}{\Delta\beta}. \tag{B.5}$$

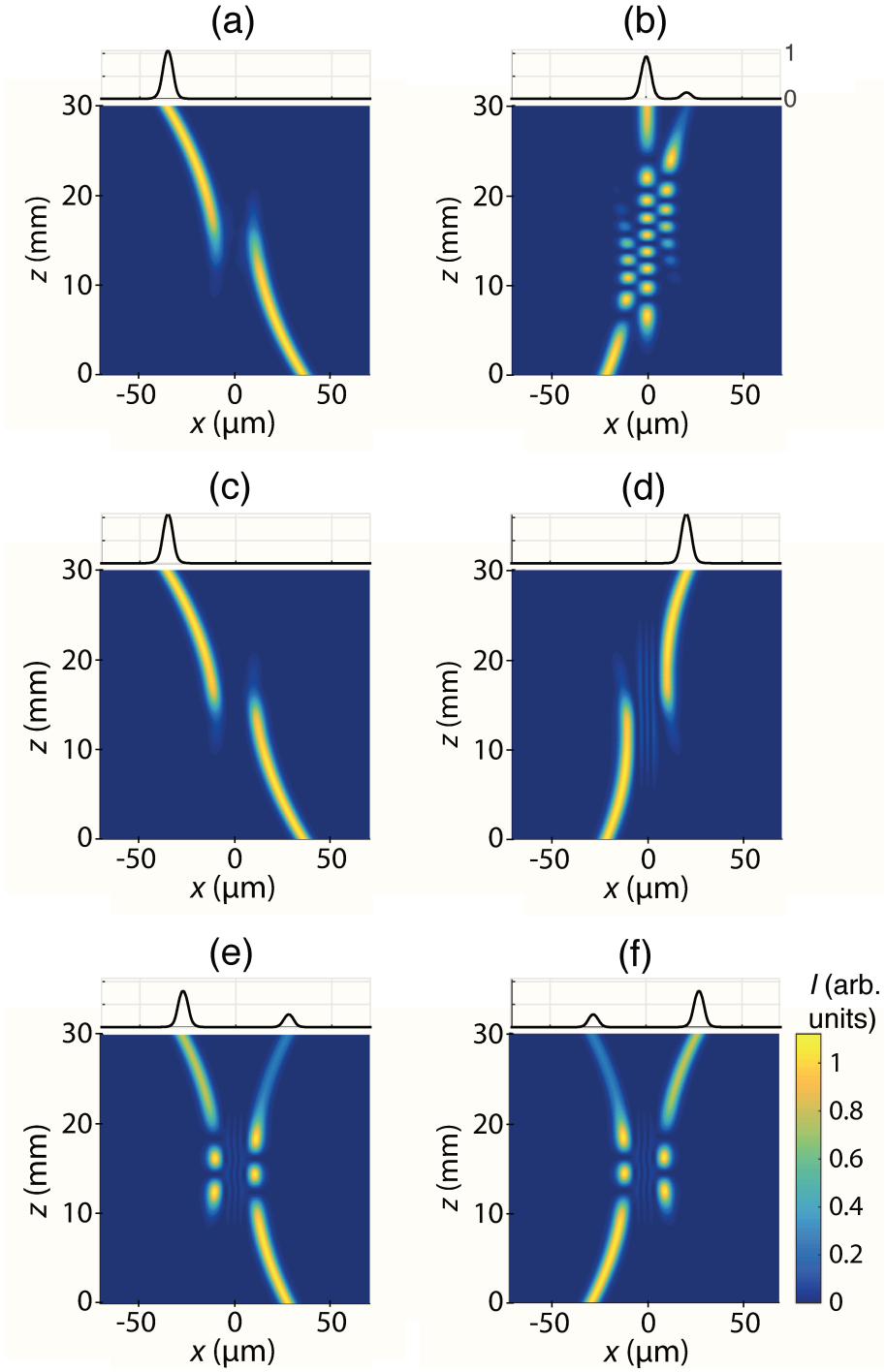

Figure B.10: Propagation de la lumière simulée par la méthode de la BPM pour une longueur d'onde sonde de 1550 nm, *la lumière est injectée en* $z = 0$ *dans le guide de droite (colonne à gauche) et dans le guide de gauche (colonne de droite). (a) et (b) pour une structure de guides permettant le STIRAP conventionnel pour les configurations contre intuitive et intuitive respectivement (pour* $\alpha = 1$*). (c) et (d) pour* $\alpha = 6$ *correspondant à l'élimination adiabatique (structure représentée sur Fig. B.9). un transfert total de lumière vers le guide 3 similaire au RAP est réalisé tandis que pour (e) et (f) représentant une configuration totalement symétrique (*$C_P(z) = C_S(z)$ *et leur maximum est atteint en* $z = L/2$*) ne permet pas un transfert complet et efficace vers le guide 3.*

Nous simulons la structure de la figure B.9 avec la méthode BPM en utilisant un verre de silice pour lequel l'indice de réfraction est de 1.4440 sondé aux longueurs d'onde des télécommunications. Dans cette structure, une onde lumineuse est injectée à l'entrée du guide 1 (ou du guide 3), nous considérons alors deux cas de figures :

⇨ La configuration du STIRAP à trois guides :

La structure correspondante est la même que celle illustrée dans la figure B.9 mais avec un contraste d'indice de réfraction qui est le même pour tous les guides ($\alpha = 1$). Les résultats pour ce cas de figure sont montrés sur les figures B.10(a) pour le cas intuitif (C_P qui arrive avant C_S) (injection dans le guide 3) et (b) contre intuitif (C_S qui arrive avant C_P) (injection dans le guide 1).

Les figures B.10(a+b) montrent l'évolution de la lumière dans une structure permettant l'équivalent optique du STIRAP conventionnel à trois niveaux pour des séquences contre intuitive et intuitive des constantes de couplage C_S et C_P. Un transfert total et efficace du guide 3 (injection de l'onde à l'entrée à droite de la structure en Fig. B.9) vers le guide 1 est observé pour le cas contre intuitif. Dans le cas intuitif, un transfert robuste ne peut avoir lieu et l'énergie oscille entre les guides 1 et 3.

⇨ La configuration de l'élimination adiabatique :

Les figures B.10(c) et (d) illustrent le cas permettant le processus de l'élimination adiabatique du guide 2, pour ce cas la structure utilisée est celle montrée en Fig. B.9 avec $\alpha = 6$ pour le guide central et 1 pour les guides extérieurs. Il est observé que toute la lumière est transférée du guide 3 vers le guide 1 (Fig. B.10(c))(ou guide 1 vers le guide 3 (Fig. B.10(d))) de manière efficace et robuste. On constate par ailleurs, que très peu de lumière transite dans le guide 2, témoignant de "l'élimination du guide 2" même si les constantes de couplage en jeu ne permettent pas un couplage direct des guides 1 et 3. Après "élimination" du guide 2, le système se comporte comme un système à deux guides dont la structure reproduit le processus du RAP pour lequel le désaccord des constantes de propagation des guides passe de valeurs négatives aux valeurs positives tout en passant par zéro au milieu de la propagation, sauf que pour le RAP la modulation de $\Delta\beta$ est nécessaire ce qui n'est pas le cas ici. Par rapport au STIRAP, l'élimination adiabatique permet un transfert quelque soit la séquence des constantes de couplage. Les figures B.9(e) et (f) correspondent au cas où la structure est symétrique ($C_P(z) = C_S(z)$ et leur maximum est atteint en $z = L/2$). Ce contre exemple montre que même si la condition adiabatique soit maintenue, le transfert ne peut avoir lieu puisque $\Delta_{eff} = 0$. Le processus de l'élimination adiabatique à été étendu à une structure comportant 6 de guides avec succès. Les valeurs du contraste d'indice utilisées pour l'élimination adiabatique sont très élevées pour envisager une implémentation expérimentale avec notre technique d'inscription des guides.

La robustesse de la structure basée sur l'élimination adiabatique a également été étudiée et son fonctionnement sur une large bande des longueurs d'ondes autour des longueurs d'onde des télécommunications a été démontré numériquement [167]. La structure manifeste un caractère très achromatique sur une plage de plus de 600 nm.

B.6 Conclusions et perspectives

Dans le cadre de cette thèse, nous avons vu que la propagation d'ondes électromagnétiques dans des guides d'onde optiques présentant une constante de propagation modulée spatialement est analogue à l'évolution des populations dans les systèmes atomiques quantiques avec un couplage évoluant dans le temps.

L'analogie avec le STIRAP à deux états a été exploitée pour démontrer théoriquement et vérifier expérimentalement un diviseur de faisceau achromatique grâce à une modulation longitudinale spécifique de la constante de propagation des guides. En outre, l'analogie optique du processus quantique du RAP a été également étudiée pour un système optique composé de deux guides d'onde couplés dans lesquels un changement de signe dans le détuning a été introduit entre les guides. La structure optique réalise un transfert robuste et complet de la lumière au second guide. Ceci a été implémenté avec succès et utilisé comme coupleur directionnel achromatique. Nous avons utilisé des guides d'ondes optiques photo-induits générés par une technique d'illumination latérale pour la démonstration d'analogies entre la mécanique quantique et l'optique guidée.

La dernière analogie étudiée est liée au phénomène quantique de l'élimination adiabatique qui consiste à éliminer de manière adiabatique la population de le(les) état intermédiaire(s) sous les hypothèses d'un grand désaccord constant entre les états externes et l'état intermédiaire (s). Dans les guides d'onde, ceci conduit à un transfert de lumière complet à partir d'un guide d'onde d'entrée dans lequel la lumière est initialement injectée à un guide d'onde de sortie avec pratiquement aucune lumière dans le(s) guide(s) d'onde intermédiaire(s). Cette dernière étude n'a pas été implémentée expérimentalement car les contrastes d'indices nécessaires sont trop grand pour la plateforme de photo-induction. Par contre cela reste tout à fait réaliste pour d'autres techniques.

En termes de perspectives, plusieurs commentaires peuvent être faits. Tout d'abord, il est utile de remarquer que les systèmes démontrés expérimentalement avec notre technique de photo-inscription prouvent la validité des principes sous-jacents. En principe, toutes ces structures peuvent être réalisées également avec des techniques standard utilisées pour l'optique intégrée, même si pour certaines d'entre elles une solution pour créer une variation contrôlable du contraste d'indice de réfraction nécessiterait des efforts supplémentaires.

Toutes les études menées dans cette thèse ont impliqué une propagation linéaire de la lumière de la sonde guidée dans les structures du guide d'ondes. Cela a été assuré en limitant la puissance du faisceau sonde en dessous de tout phénomène non linéaire.

Dans une prochaine étape, une perspective serait de s'affranchir de cette restriction. Si la lumière sonde guidée peut modifier le contraste d'indice de réfraction qu'elle ressent, la distribution de la lumière en sortie des guides peut être modifiée en fonction de la puissance d'entrée, conduisant à un dispositif de commutation non linéaire. Par exemple, dans le cas d'un transfert de type RAP, on peut imaginer que la structure RAP serait active à faible intensité du faisceau sonde, alors qu'à haute intensité une augmentation du contraste d'indice de réfraction empêcherait le passage par zéro du désaccord $\Delta\beta$, ce qui empêcherait un transfert efficace. Selon le matériau utilisé, la nature de la non-linéarité impliquée pourrait être associée à l'effet photoréfractif, à l'effet Kerr optique, aux effets thermiques ou à d'autres types de non-linéarités. Cette approche sera particulièrement intéressante si l'on considère aussi le cas de la propagation de la lumière à l'intérieur de la structure dans les deux sens, vers l'avant et vers l'arrière. La non-linéarité peut dans ce cas fournir un comportement non réciproque conduisant par exemple à une isolation optique efficace dans un dispositif intégré.

C

Publications and Communications

C.1 Publications in Peer–Reviewed Journals

- H. Oukraou, V. Coda, A. A. Rangelov, and G. Montemezzani , Broadband photonic transport between waveguides by adiabatic elimination. Phys. Rev. A, vol. 97, 023811 (2018)

- H. Oukraou, L. Vittadello, V. Coda, C. Ciret, M. Alonso, A. A. Rangelov, N. V. Vitanov, and G. Montemezzani, Control of adiabatic light transfer in coupled waveguides with longitudinally varying detuning. Phys. Rev. A, vol. 95, 023811 (2017)

C.2 National and International Conferences

- H. Oukraou, V. Coda, and G. Montemezzani, Passage de lumière entre guides d'onde photo induits et analogies avec des systèmes quantiques hors résonance, Workshop Matériaux pour l'Optique & Photonique, Oct 2017, Nancy, France.

- H. Oukraou, L. Vittadello, V. Coda, C. Ciret, M. Alonzo, A. A. Rangelov, N. V. Vitanov, and G. Montemezzani, Quantum-like adiabatic light transfer in photo-induced waveguides with longitudinally varying detuning, Photorefractive photonics 2017 (PR17), Jul 2017, Qingdao, China. Proceedings published in J. Phys.: Conf. Series 867, 012024 (2017).

- G. Montemezzani, V. Coda, H. Oukraou, and A. A. Rangelov, Spatial adiabatic passage of light in waveguide structures. OIST Symposium on Spatial Adiabatic Passage, May 2016, Okinawa, Japon. (invited talk)

- G. Montemezzani, H. Oukraou, C. Ciret, L. Vittadello, V. Coda, and A. A. Rangelov, Light Transfer in Coupled Detuned Photoinduced Waveguides and their Quantum Analogies. Nice Optics, Oct 2016, Nice, France. (invited talk)

- H. Oukraou, V. Coda, and G. Montemezzani, Passage de lumière entre guides d'onde photo induits et analogies avec des systèmes quantiques hors résonance, Journées Nationales de l'Optique Guidée (JNOG), Optique Bordeaux 2016, Jul 2016, Bordeaux, France.

- H. Oukraou, V. Coda, and G. Montemezzani, Guides d'onde photoinduits et analogies avec des systèmes quantiques non résonants, Séminaire École doctorale EMMA, May 2016, Nancy, France.

Bibliography

[1] C. E. Bradley, "Acoustic Bloch wave propagation in a periodic waveguide," Technical report, Texas Univ. at Austin Applied Research Labs (1991) .

[2] A. Larraza and B. Denardo, "An acoustic Casimir effect," Physics Letters A **248,** 151–155 (1998).

[3] D. Dragoman and M. Dragoman, *Quantum-classical analogies* (Springer Science & Business Media, 2013).

[4] S. Longhi, "Quantum-optical analogies using photonic structures," Laser Photon. Rev. **3,** 243–261 (2009).

[5] Y. Aharonov and D. Bohm, "Significance of electromagnetic potentials in the quantum theory," Physical Review **115,** 485 (1959).

[6] A. Tomita and R. Y. Chiao, "Observation of Berry's topological phase by use of an optical fiber," Physical Review Letters **57,** 937 (1986).

[7] M. Berry, "Interpreting the anholonomy of coiled light," Nature **326,** 277 (1987).

[8] M. Onoda, S. Murakami, and N. Nagaosa, "Hall effect of light," Physical Review Letters **93,** 083901 (2004).

[9] O. Hosten and P. Kwiat, "Observation of the spin Hall effect of light via weak measurements," Science **319,** 787–790 (2008).

[10] R. Morandotti, U. Peschel, J. Aitchison, H. Eisenberg, and Y. Silberberg, "Experimental observation of linear and nonlinear optical Bloch oscillations," Physical Review Letters **83,** 4756 (1999).

[11] I. L. Garanovich, S. Longhi, A. A. Sukhorukov, and Y. S. Kivshar, "Light propagation and localization in modulated photonic lattices and waveguides," Physics Reports **518,** 1–79 (2012).

[12] T. Schwartz, G. Bartal, S. Fishman, and M. Segev, "Transport and Anderson localization in disordered two-dimensional photonic lattices," Nature **446,** 52 (2007).

[13] T. Schwartz, S. Fishman, and M. Segev, "Localisation of light in disordered lattices," Electronics Letters **44,** 165–168 (2008).

[14] G. C. des Francs, C. Girard, J.-C. Weeber, C. Chicane, T. David, A. Dereux, and D. Peyrade, "Optical analogy to electronic quantum corrals," Physical Review Letters **86,** 4950 (2001).

[15] K. G. Makris, S. Suntsov, D. N. Christodoulides, G. I. Stegeman, and A. Hache, "Discrete surface solitons," Optics Letters **30,** 2466–2468 (2005).

[16] U. Gaubatz, P. Rudecki, S. Schiemann, and K. Bergmann, "Population transfer between molecular vibrational levels by stimulated Raman scattering with partially overlapping laser fields. A new concept and experimental results," J. Chem. Phys. **92,** 5363–5376 (1990).

[17] N. V. Vitanov, A. A. Rangelov, B. W. Shore, and K. Bergmann, "Stimulated Raman adiabatic passage in physics, chemistry, and beyond," Reviews of Modern Physics **89,** 015006 (2017).

[18] B. W. Shore, "Picturing stimulated Raman adiabatic passage: a STIRAP tutorial," Advances in Optics and Photonics **9,** 563–719 (2017).

[19] E. Paspalakis, "Adiabatic three-waveguide directional coupler," Optics Commun. **258,** 30–34 (2006).

[20] S. Longhi, G. Della Valle, M. Ornigotti, and P. Laporta, "Coherent tunneling by adiabatic passage in an optical waveguide system," Phys. Rev. B **76,** 201101 (2007).

[21] F. Dreisow, A. Szameit, M. Heinrich, S. Nolte, A. Tünnermann, M. Ornigotti, and S. Longhi, "Polychromatic beam splitting by fractional stimulated Raman adiabatic passage," Appl. Phys. Lett. **95,** 261102 (2009).

[22] G. Della Valle, M. Ornigotti, T. Toney Fernandez, P. Laporta, S. Longhi, A. Coppa, and V. Foglietti, "Adiabatic light transfer via dressed states in optical waveguide arrays," Applied Physics Letters **92,** 011106 (2008).

[23] S.-Y. Tseng and M.-C. Wu, "Mode conversion/splitting by optical analogy of multistate stimulated Raman adiabatic passage in multimode waveguides," Journal of Lightwave Technology **28,** 3529–3534 (2010).

[24] C. Ciret, V. Coda, A. A. Rangelov, D. N. Neshev, and G. Montemezzani, "Broadband adiabatic light transfer in optically induced waveguide arrays," Physical Review A **87,** 013806 (2013).

[25] C. Ciret, "Structures de guides d'onde photo-induits et analogies quantiques," Ph.D. thesis, Université de Lorraine, 2013.

[26] C. Ciret, V. Coda, A. A. Rangelov, D. N. Neshev, and G. Montemezzani, "Planar achromatic multiple beam splitter by adiabatic light transfer," Optics letters **37,** 3789–3791 (2012).

[27] C. Ciret, M. Alonzo, V. Coda, A. A. Rangelov, and G. Montemezzani, "Analog to electromagnetically induced transparency and Autler-Townes effect demonstrated with photoinduced coupled waveguides," Physical Review A **88,** 013840 (2013).

[28] N. V. Vitanov and B. V. Shore, "Stimulated Raman adiabatic passage in a two-state system," Phys. Rev. A **73,** 053402 (2006).

[29] L. Yatsenko, N. Vitanov, B. Shore, T. Rickes, and K. Bergmann, "Creation of coherent superpositions using Stark-chirped rapid adiabatic passage," Opt. Commun. **204,** 413 (2002).

[30] N. V. Vitanov, T. Halfmann, B. W. Shore, and K. Bergmann, "Laser-Induced Population Transfer by Adiabatic Passage Techniques," Annu. Rev. Phys. Chem. **52,** 763–809 (2001).

[31] L. A. Lugiato, P. Mandel, and L. Narducci, "Adiabatic elimination in nonlinear dynamical systems," Phys. Rev. A **29,** 1438 (1984).

[32] A. Sinatra, F. Castelli, L. Lugiato, P. Grangier, and J. Poizat, "Effective two-level model versus three-level model," Quantum and Semiclassical Optics: Journal of the European Optical Society Part B **7,** 405 (1995).

[33] M. Fewell, "Adiabatic elimination, the rotating-wave approximation and two-photon transitions," Optics Communications **253,** 125–137 (2005).

[34] E. Brion, L. H. Pedersen, and K. Mølmer, "Adiabatic elimination in a lambda system," Journal of Physics A: Mathematical and Theoretical **40,** 1033 (2007).

[35] B. Shore, "Coherent manipulations of atoms using laser light," Acta Physica Slovaca. Reviews and Tutorials **58,** 243–486 (2008).

[36] P. Dittrich, G. Montemezzani, P. Bernasconi, and P. Günter, "Fast, reconfigurable light-induced waveguides," Optics Letters **24,** 1508–1510 (1999).

[37] M. Gorram, V. Coda, P. Thévenin, and G. Montemezzani, "Bulk channel-type reconfigurable light-induced waveguides recorded by crossed lateral illumination," Applied Physics B: Lasers and Optics **95,** 565–572 (2009).

[38] D. Hondros and P. Debye, "Elektromagnetische wellen an dielektrischen drähten," Annalen der Physik **337,** 465–476 (1910).

[39] H. Zahn, "Über den Nachweis elektromagnetischer Wellen an dielektrischen Drähten," Annalen der Physik **354,** 907–933 (1916).

[40] O. Schriever, "Elektromagnetische Wellen an dielektrischen Drähten," Annalen der Physik **368,** 645–673 (1920).

[41] H. Buchholz, "Die Quasioptik der Ultrakurzwellenweiter," Elektrische Nachrichtentechnik pp. 297–320 (1938).

[42] N. Kapany, "Fiber optics. Principles and applications," New York: Academic Press (1967).

[43] A. Vijayan, M. V. Fuke, R. N. Karekar, and R. C. Aiyer, "Planar Optical Waveguide Evanescent Wave CO_2 Sensor Based on a Clad of Alstonia Scholaris Leaf Extract," IEEE Sensors Journal **9,** 13–19 (2009).

[44] I. Kaminow and J. Carruthers, "Optical waveguiding layers in $LiNbO_3$ and $LiTaO_3$," Applied Physics Letters **22,** 326–328 (1973).

[45] M. D. DeGrandpre, L. W. Burgess, P. L. White, and D. S. Goldman, "Thin film planar waveguide sensor for liquid phase absorbance measurements," Anal. Chem. **62,** 2012–2017 (1990).

[46] K. J. Kuhn and L. W. Burgess, "Chemometric evaluation of the multiple mode response of an ion-diffused planar optical waveguide to liquid-phase analytes," Anal. Chem. **65,** 1390–1398 (1993).

[47] A. W. Snyder, "Coupled-Mode Theory for Optical Fibers," J. Opt. Soc. Am. **62,** 1267–1277 (1972).

[48] D. Marcuse, "Coupled Mode Theory of Round Optical Fibers," Bell System Technical Journal **52,** 817–842 (1973).

[49] A. Yariv, "Coupled-mode theory for guided-wave optics," IEEE Journal of Quantum Electronics **9,** 919–933 (1973).

[50] H. Kogelnik and C. Shank, "Coupled-wave theory of distributed feedback lasers," Journal of Applied Physics **43,** 2327–2335 (1972).

[51] N. Kapany, J. Burke, K. Frame, and R. Wilcox, "Coherent Interactions between Optical Waveguides and Lasers," J. Opt. Soc. Am. **58,** 1176–1183 (1968).

[52] A. Ihaya, H. Furuta, and H. Noda, "Thin-film optical directional coupler," Proceedings of the IEEE **60,** 470–471 (1972).

[53] J. Goell, "Electron-resist fabrication of bends and couplers for integrated optical circuits," Applied Optics **12,** 729–736 (1973).

[54] M. J. Digonnet and H. J. Shaw, "Analysis of a tunable single mode optical fiber coupler," IEEE Transactions on Microwave Theory and Techniques **30,** 592–600 (1982).

[55] K. Kato, "Second-harmonic generation to 2048 Å in β-Ba_2O_4," IEEE Journal of Quantum Electronics **22,** 1013–1014 (1986).

[56] R. Stolen and J. Bjorkholm, "Parametric amplification and frequency conversion in optical fibers," IEEE Journal of Quantum Electronics **18,** 1062–1072 (1982).

[57] D. Kip, M. Soljacic, M. Segev, E. Eugenieva, and D. N. Christodoulides, "Modulation instability and pattern formation in spatially incoherent light beams," Science **290,** 495–498 (2000).

[58] D. Marcuse, "Light transmission optics," (1972).

[59] A. Hardy and W. Streifer, "Coupled mode theory of parallel waveguides," Journal of Lightwave Technology **3,** 1135–1146 (1985).

[60] E. A. J. Marcatili, "Improved coupled-mode equations for dielectric guides," IEEE Journal of Quantum Electronics **22,** 988–993 (1986).

[61] S. Somekh, E. Garmire, A. Yariv, H. Garvin, and R. Hunsperger, "Channel optical waveguide directional couplers," Appl. Phys. Lett. **22,** 46–47 (1973).

[62] D. N. Christodoulides and R. I. Joseph, "Discrete self-focusing in nonlinear arrays of coupled waveguides," Opt. Lett. **13,** 794–796 (1988).

[63] A. Yariv, "Optical Electronics: Saunders College," California Institute of Technology pp. 519–524 (1991).

[64] F. Agullo-Lopez, J. M. Cabrera, and F. Agullo-Rueda, *Electrooptics: Phenomena, Materials and Applications* (Academic Press, 1994), Vol. 1.

[65] S. Wemple and M. DiDomenico Jr, "Oxygen-Octahedra Ferroelectrics. II. Electro-optical and Nonlinear-Optical Device Applications," Journal of Applied Physics **40,** 735–752 (1969).

[66] A. Yariv, "Quantum Electronics,", 1975.

[67] P. Dittrich, G. Montemezzani, P. Bernasconi, and P. Gunter, "Dynamical light induced waveguides by interband photorefraction," OSA Trends in Optics and Photonics **27,** 538–544 (1999).

[68] A. Yariv, "Phase conjugate optics and real-time holography," IEEE Journal of Quantum Electronics **14,** 650–660 (1978).

[69] P. Günter, "Holography, coherent light amplification and optical conjugation with photorefractive materials," Phys. Rep. **93,** 199–299 (1982).

[70] A. Marrakchi, J. Huignard, and P. Günter, "Diffraction efficiency and energy transfer in two-wave mixing experiments with $Bi_{12}SiO_{20}$ crystals," Applied Physics A: Materials Science & Processing **24,** 131–138 (1981).

[71] M. Cronin-Golomb, J. O. White, B. Fischer, and A. Yariv, "Exact solution of a nonlinear model of four-wave mixing and phase conjugation," Optics Letters **7,** 313–315 (1982).

[72] A. E. Chiou and P. Yeh, "Beam cleanup using photorefractive two-wave mixing," Optics Letters **10,** 621–623 (1985).

[73] Y. Tan, F. Chen, X.-L. Wang, L. Wang, V. Shandarov, and D. Kip, "Formation of reconfigurable optical channel waveguides and beam splitters on top of proton-implanted lithium niobate crystals using spatial dark soliton-like structures," Journal of Physics D: Applied Physics **41,** 102001 (2008).

[74] J.-H. Park, J. Kim, and B. Lee, "Three-dimensional optical correlator using a sub-image array," Optics Express **13,** 5116–5126 (2005).

[75] A. Ashkin, G. Boyd, J. i. Dziedzic, R. Smith, A. Ballman, J. Levinstein, and K. Nassau, "Optically-induced refractive index inhomogeneities in $LiNbO_3$ and $LiTaO_3$," Applied Physics Letters **9,** 72–74 (1966).

[76] G. Peterson, A. Ballman, P. Lenzo, and P. Bridenbaugh, "Electro-optic properties of $LiNbO_3$," Applied Physics Letters **5,** 62–64 (1964).

[77] G. Boyd and A. Ashkin, "Theory of Parametric Oscillator Threshold with Single-Mode Optical Masers and Observation of Amplification in $LiNbO_3$," Physical Review **146,** 187 (1966).

[78] F. Chen, T. Hirookau, and M. Kawaharada, "Light Modulation and Beam Deflection with Potassium Tantalate-Niobate Crystals," Journal of Applied Physics **37,** 388–398 (1966).

[79] N. Khukhtarev, "Holographic storage in electro-optic crystals. II. Beam coupling-Light amplification," Ferroelectrics **22,** 961–4 (1979).

[80] F. Chen, J. LaMacchia, and D. Fraser, "Holographic storage in lithium niobate," Applied Physics Letters **13,** 223–225 (1968).

[81] I. Biaggio and P. Günter, "Optical characterization of charge-transport in polar dielectrics by holographic time of flight and space-charge relaxation measurements," Ferroelectrics **223,** 397–404 (1999).

[82] N. Kukhtarev, V. Markov, S. Odulov, M. Soskin, and V. Vinetskii, "Holographic storage in electrooptic crystals. I. Steady state," Ferroelectrics **22,** 949–960 (1978).

[83] M. Gorram, "Génération et étude de guides d'onde dynamiques et reconfigurables induits par illumination latérale," Ph.D. thesis, Université de Metz, 2009.

[84] A. Zozulya and D. Anderson, "Nonstationary self-focusing in photorefractive media," Optics Letters **20,** 837–839 (1995).

[85] A. Okada, "Optical waveguiding properties of sputtered $LiNbO_3$ single crystal thin films on $LiTaO_3$ substrates," Ferroelectrics **14,** 739–742 (1976).

[86] R. Schmidt and I. Kaminow, "Metal-diffused optical waveguides in $LiNbO_3$," Applied Physics Letters **25,** 458–460 (1974).

[87] N. Goto and G. L. Yip, "Characterization of proton-exchange and annealed $LiNbO_3$ waveguides with pyrophosphoric acid," Applied Optics **28,** 60–65 (1989).

[88] J. L. Jackel, C. Rice, and J. Veselka, "Proton exchange for high-index waveguides in $LiNbO_3$," Applied Physics Letters **41,** 607–608 (1982).

[89] F. Laurell, J. Webjorn, G. Arvidsson, and J. Holmberg, "Wet etching of proton-exchanged lithium niobate-a novel processing technique," Journal of Lightwave Technology **10,** 1606–1609 (1992).

[90] H. Ryssel and I. Ruge, "Ion implantation,", 1986.

[91] C. Buchal, "Ion implantation of optical devices," Nuclear Instruments and Methods in Physics Research Section B: Beam Interactions with Materials and Atoms **68,** 355–360 (1992).

[92] K. M. Davis, K. Miura, N. Sugimoto, and K. Hirao, "Writing waveguides in glass with a femtosecond laser," Optics Letters **21,** 1729–1731 (1996).

[93] R. Osellame, G. Cerullo, and R. Ramponi, *Femtosecond laser micromachining: photonic and microfluidic devices in transparent materials* (Springer Science & Business Media, 2012), Vol. 123.

[94] Z. Lu, R. Hiskes, S. DiCarolis, R. Route, R. Feigelson, F. Leplingard, and J. Fouquet, "Epitaxial $LiNbO_3$ thin films on sapphire substrates grown by solid source MOCVD," Journal of Materials Research **9,** 2258–2263 (1994).

[95] Y. Shibata, K. Kaya, K. Akashi, M. Kanai, T. Kawai, and S. Kawai, "Epitaxial growth and surface acoustic wave properties of lithium niobate films grown by pulsed laser deposition," Journal of Applied Physics **77,** 1498–1503 (1995).

[96] S. Lee and R. Feigelson, "Reduced optical losses in MOCVD grown lithium niobate thin films on sapphire by controlling nucleation density," Journal of Crystal Growth **186,** 594–606 (1998).

[97] J.-G. Yoon and K. Kim, "Growth of highly textured $LiNbO_3$ thin film on Si with MgO buffer layer through the sol-gel process," Applied Physics Letters **68,** 2523–2525 (1996).

[98] S. Hirano, T. Yogo, W. Sakamoto, Y. Takeichi, and S. Ono, "Processing of highly oriented $LiNbO_3$ thin films through ametal-organic precursor solution," Journal of the European Ceramic Society **24,** 435–440 (2004).

[99] R. R. Neurgaonkar, "Tungsten bronze family crystals for optical device applications," In *1984 Los Angeles Techincal Symposium*, pp. 97–103 (1984).

[100] P. Lenzo, E. Spencer, and A. Ballman, "Electro-optic coefficients of ferroelectric Stontium Barium Niobate," Applied Physics Letters **11,** 23–24 (1967).

[101] S. Ducharme, J. Feinberg, and R. Neurgaonkar, "Electrooptic and piezoelectric measurements in photorefractive barium titanate and strontium barium niobate," IEEE Journal of Quantum Electronics **23,** 2116–2121 (1987).

[102] T. Volk, T. Woike, U. Doerfler, R. Pankrath, L. Ivleva, and M. Wöhlecke, "Ferroelectric phenomena in holographic properties of strontium-barium niobate crystals doped with rare-earth elements," Ferroelectrics **203,** 457–470 (1997).

[103] P. Jamieson, S. Abrahams, and J. Bernstein, "Ferroelectric tungsten bronze-type crystal structures. I. Barium Strontium niobate $Ba_{0.27}Sr_{0.75}Nb_2O_{5.78}$," Journal of Chemical Physics **48,** 5048–5057 (1968).

[104] T. Chernaya, B. Maksimov, I. Verin, L. Ivleva, and V. Simonov, "Crystal structure of $Ba_{0.39}Sr_{0.61}Nb_2O_6$ single crystals," Crystallography Reports **42,** 375–380 (1997).

[105] M. Ulex, R. Pankrath, and K. Betzler, "Growth of strontium barium niobate: the liquidus–solidus phase diagram," Journal of Crystal Growth **271,** 128–133 (2004).

[106] L. Ivleva, N. Bogodaev, N. Polozkov, and V. Osiko, "Growth of SBN single crystals by Stepanov technique for photorefractive applications," Optical Materials **4,** 168–173 (1995).

[107] L. V. P. R. de Broglie, "Ondes et quanta," CR Acad. Sci. Paris **177,** 507 (1923).

[108] D. Dragoman and M. Dragoman, "Optical analogue structures to mesoscopic devices," Progress in Quantum Electronics **23,** 131–188 (1999).

[109] S. Longhi, "Dynamics of driven two-level systems with permanent dipole moments: an optical realization," Journal of Physics B: Atomic, Molecular and Optical Physics **39,** 1985 (2006).

[110] U. Gaubatz, P. Rudecki, S. Schiemann, and K. Bergmann, "Population transfer between molecular vibrational levels by stimulated Raman scattering with partially overlapping laser fields. A new concept and experimental results," The Journal of Chemical Physics **92,** 5363–5376 (1990).

[111] V. S. Malinovsky and D. J. Tannor, "Simple and robust extension of the stimulated Raman adiabatic passage technique to N-level systems," Physical Review A **56,** 4929 (1997).

[112] S. G. Krivoshlykov, *Quantum-theoretical formalism for inhomogeneous graded-index waveguides* (Vch Pub, 1994).

[113] K. B. Wolf and Kurmyshev, ""Squeezed states"in Helmholtz optics," Physical Review A **47,** 3365 (1993).

[114] A. Messiah, *Quantum mechanics, chapter 2* (North-Holland, Amesterdam, 1962).

[115] B. W. Shore, *The Theory of Coherent Atomic Excitation, volume 1, Simple Atoms and Fields* (1990).

[116] G. Ford and R. O'Connell, "The rotating wave approximation (RWA) of quantum optics: serious defect," Physica A: Statistical Mechanics and its Applications **243,** 377–381 (1997).

[117] K. Bergmann, H. Theuer, and B. Shore, "Coherent population transfer among quantum states of atoms and molecules," Reviews of Modern Physics **70,** 1003 (1998).

[118] R. Unanyan, M. Fleischhauer, B. Shore, and K. Bergmann, "Robust creation and phase-sensitive probing of superposition states via stimulated Raman adiabatic passage (STIRAP) with degenerate dark states," Optics Communications **155,** 144–154 (1998).

[119] F. T. Hioe and J. H. Eberly, "N-level coherence vector and higher conservation laws in quantum optics and quantum mechanics," Physical Review Letters **47,** 838 (1981).

[120] J. Oreg, F. Hioe, and J. Eberly, "Adiabatic following in multilevel systems," Physical Review A **29,** 690 (1984).

[121] G. W. Coulston and K. Bergmann, "Population transfer by stimulated Raman scattering with delayed pulses: analytical results for multilevel systems," Journal of Chemical Physics **96,** 3467–3475 (1992).

[122] B. Shore, J. Martin, M. Fewell, and K. Bergmann, "Coherent population transfer in multilevel systems with magnetic sublevels. I. Numerical studies," Physical Review A **52,** 566 (1995).

[123] V. Romanenko and L. Yatsenko, "Adiabatic population transfer in the three-level Λ-system: two-photon lineshape," Optics Communications **140,** 231–236 (1997).

[124] E. Arimondo and G. Orriols, "Nonabsorbing atomic coherences by coherent two-photon transitions in a three-level optical pumping," Lettere Al Nuovo Cimento (1971–1985) **17,** 333–338 (1976).

[125] B. W. Shore, *Manipulating quantum structures using laser pulses* (Cambridge University Press, 2011).

[126] N. Vitanov, M. Fleischhauer, B. Shore, and K. Bergmann, "Coherent manipulation of atoms and molecules by sequential laser pulses," Advances in Atomic Molecular and Optical Physics **46,** 57–190 (2001).

[127] S. H. Autler and C. H. Townes, "Stark effect in rapidly varying fields," Physical Review **100,** 703 (1955).

[128] M. Fleischhauer, A. Imamoglu, and J. P. Marangos, "Electromagnetically induced transparency: Optics in coherent media," Reviews of Modern Physics **77,** 633 (2005).

[129] S. E. Harris, J. Field, and A. Imamoğlu, "Nonlinear optical processes using electromagnetically induced transparency," Physical Review Letters **64,** 1107 (1990).

[130] J. Kuklinski, U. Gaubatz, F. T. Hioe, and K. Bergmann, "Adiabatic population transfer in a three-level system driven by delayed laser pulses," Physical Review A **40,** 6741 (1989).

[131] M. Crenshaw and C. Bowden, "Quasiadiabatic following approximation for a dense medium of two-level atoms," Physical Review Letters **69,** 3475 (1992).

[132] S. Longhi, "Adiabatic passage of light in coupled optical waveguides," Phys. Rev. E **73,** 026607 (2006).

[133] G. Della Valle, M. Ornigotti, T. Toney Fernandez, P. LaPorta, and S. Longhi, "Adiabatic light transfer via dressed states in optical waveguide arrays," Appl. Phys. Lett. **92,** 011106 (2008).

[134] S.-Y. Tseng and M.-C. Wu, "Mode conversion/splitting by optical analogy of multistate stimulated Raman adiabatic passage in multimode waveguides," J. Lightwave Technol. **28,** 3529–3534 (2010).

[135] A. A. Rangelov and N. V. Vitanov, "Achromatic multiple beam splitting by adiabatic passage in optical waveguides," Phys. Rev. A **85,** 055803 (2012).

[136] C. Ciret, V. Coda, A. A. Rangelov, D. N. Neshev, and G. Montemezzani, "Planar achromatic multiple beam splitter by adiabatic light transfer," Opt. Lett. **37,** 3789–3791 (2012).

[137] W. Huang, A. A. Rangelov, and E. Kyoseva, "Complete achromatic optical switching between two waveguides with a sign flip of the phase mismatch," Phys. Rev. A **90,** 053837 (2014).

[138] A. P. Hope, T. G. Nguyen, A. Mitchell, and A. D. Greentree, "Adiabatic two-photon quantum gate operations using a long-range photonic bus," J. Phys. B: At. Mol. Opt. Phys. **48,** 055503 (2015).

[139] S.-Y. Tseng and M.-C. Wu, "Adiabatic Mode Conversion in Multimode Waveguides Using Computer-Generated Planar Holograms," IEEE Photon. Technol. Lett. **22,** 1211–1213 (2010).

[140] Y. Lahini, F. Pozzi, M. Sorel, R. Morandotti, D. N. Christodoulides, and Y. Silberberg, "Effect of nonlinearity on adiabatic evolution of light," Phys. Rev. Lett. **101,** 193901 (2008).

[141] R. Menchon-Enrich, A. Llobera, J. Vila-Planas, V. J. Cadarso, J. Mompart, and V. Ahufinger, "Light spectral filtering based on spatial adiabatic passage," Light: Sci. Appl. **2,** e90 (2013).

[142] R. Menchon-Enrich, A. Benseny, V. Ahufinger, A. D. Greentree, T. Busch, and J. Mompart, "Spatial adiabatic passage: a review of recent progress," Rep. Prog. Phys. **79,** 074401 (2016).

[143] M. G. F. Wilson and G. A. Teh, "Improved tolerance in optical directional couplers," Electron. Lett. **9,** 453–455 (1973).

[144] R. B. Smith, "Analytic solutions for linearly tapered directional couplers," J. Opt. Soc. Am. **66,** 882–892 (1976).

[145] T. A. Ramadan, R. Scarmozzino, and R. M. Osgood Jr., "Adiabatic couplers: Design rules and optimization," J. Lightwave Technol. **16,** 277–283 (1998).

[146] A. Abragam, *The principles of nuclear magnetism* (Clarendon, Oxford, 1961).

[147] E. B. Treacy, "Adiabatic inversion with light pulses," Phys. Lett. A **27,** 421–422 (1968).

[148] M. M. Loy, "Observation of population inversion by optical adiabatic rapid passage," Phys. Rev. Lett. **32,** 814 (1974).

[149] S. Hamadani, A. Mattick, N. Kurnit, and A. Javan, "Observation of adiabatic rapid passage utilizing narrow infrared saturation resonances," Appl. Phys. Lett. **27,** 21–24 (1975).

[150] S. Avrillier, J.-M. Raimond, C. J. Bordé, D. Bassi, and G. Scoles, "Supersonic beam spectroscopy of low J transitions of the $\nu 3$ band of SF6: Rabi oscillations and adiabatic rapid passage with a CW laser," Optics Communications **39,** 311–315 (1981).

[151] J. Kroon, H. Senhorst, H. Beijerinck, B. Verhaar, and N. Verster, "Rabi oscillations in the optical pumping of a metastable neon beam with a cw dye laser," Physical Review A **31,** 3724 (1985).

[152] L. Allen and J. H. Eberly, *Optical resonance and two-level atoms* (Wiley, New York, 1975), Vol. 28.

[153] C. Liedenbaum, S. Stolte, and J. Reuss, "Inversion produced and reversed by adiabatic passage," Phy. Rep. **178,** 1–24 (1989).

[154] R. Yamazaki, K.-i. Kanda, F. Inoue, K. Toyoda, and S. Urabe, "Robust generation of superposition states," Phys. Rev. A **78,** 023808 (2008).

[155] M. Gorram, V. Coda, P. Thévenin, and G. Montemezzani, "Bulk channel-type reconfigurable light-induced waveguides recorded by crossed lateral illumination," Appl. Phys. B **95,** 565–572 (2009).

[156] C. Ciret, M. Alonzo, V. Coda, A. A. Rangelov, and G. Montemezzani, "Analog to electromagnetically induced transparency and Autler-Townes effect demonstrated with photoinduced coupled waveguides," Phys. Rev. A **88,** 013840 (2013).

[157] H. Oukraou, L. Vittadello, V. Coda, C. Ciret, M. Alonzo, A. A. Rangelov, N. V. Vitanov, and G. Montemezzani, "Control of adiabatic light transfer in coupled waveguides with longitudinally varying detuning," Physical Review A **95,** 023811 (2017).

[158] H. S. Hristova, A. A. Rangelov, G. Montemezzani, and N. V. Vitanov, "Adiabatic three-waveguide coupler," Phys. Rev. A **93,** 033802 (2016).

[159] B. Shore, *The theory of coherent atomic excitation* (John Wiley & Sons, New York, 1990).

[160] R. P. Feynman, F. L. Vernon Jr., and R. W. Hellwarth, "Geometrical Representation of the Schrödinger Equation for Solving Maser Problems," J. Appl. Phys. **28,** 49–52 (1957).

[161] J. Van Roey, J. van der Donk, and P. E. Lagasse, "Beam-propagation method: analysis and assessment," J. Opt. Soc. Am. **71,** 803 (1981).

[162] K. Kawano and T. Kitoh, *Introduction to optical waveguide analysis solving Maxwell's equations and the Schrödinger equation* (John Wiley & Sons, New York, 2001).

[163] S. Longhi, "Photonic transport via chirped adiabatic passage in optical waveguides," Journal of Physics B: Atomic, Molecular and Optical Physics **40,** F189 (2007).

[164] M. Mrejen, H. Suchowski, T. Hatakeyama, Y. Wang, and X. Zhang, "Experimental realization of two decoupled directional couplers in a subwavelength packing by adiabatic elimination," Nano Letters **15,** 7383–7387 (2015).

[165] M. Mrejen, H. Suchowski, T. Hatakeyama, C. Wu, L. Feng, K. O'Brien, Y. Wang, and X. Zhang, "Adiabatic elimination-based coupling control in densely packed subwavelength waveguides," Nature Communications **6,** 7565 (2015).

[166] T. Liu, A. S. Solntsev, A. Boes, T. Nguyen, C. Will, A. Mitchell, D. N. Neshev, and A. A. Sukhorukov, "Experimental demonstration of bidirectional light transfer in adiabatic waveguide structures," Optics Letters **41,** 5278–5281 (2016).

[167] H. Oukraou, V. Coda, A. A. Rangelov, and G. Montemezzani, "Broadband photonic transport between waveguides by adiabatic elimination," Phys. Rev. A **97,** 023811 (2018).

[168] I. Malitson, "Interspecimen comparison of the refractive index of fused silica," Josa **55,** 1205–1209 (1965).

[169] T.-Y. Lin, F.-C. Hsiao, Y.-W. Jhang, C. Hu, and S.-Y. Tseng, "Mode conversion using optical analogy of shortcut to adiabatic passage in engineered multimode waveguides," Optics Express **20,** 24085–24092 (2012).

[170] S.-Y. Tseng and X. Chen, "Engineering of fast mode conversion in multimode waveguides," Optics Letters **37,** 5118–5120 (2012).

[171] N. Vitanov, "Adiabatic population transfer by delayed laser pulses in multistate systems," Physical Review A **58,** 2295 (1998).

[172] N. Vitanov, "Complete population inversion by a phase jump: an exactly soluble model," New Journal of Physics **9,** 58 (2007).

[173] B. Torosov and N. Vitanov, "Coherent control of a quantum transition by a phase jump," Physical Review A **76,** 053404 (2007).

[174] H. S. Hristova, A. A. Rangelov, G. Montemezzani, and N. Vitanov, "Adiabatic frequency conversion with a sign flip in the coupling," Physical Review A **94,** 033849 (2016).

[175] W. Huang, A. A. Rangelov, and E. Kyoseva, "Complete achromatic optical switching between two waveguides with a sign flip of the phase mismatch," Physical Review A **90,** 053837 (2014).

[176] P. Marte, P. Zoller, and J. L. Hall, "Coherent atomic mirrors and beam splitters by adiabatic passage in multilevel systems," Physical Review A **44,** R4118 (1991).

[177] J. Lawall and M. Prentiss, "Demonstration of a novel atomic beam splitter," Physical Review Letters **72,** 993 (1994).

[178] M. Weitz, B. Young, and S. Chu, "Atom manipulation based on delayed laser pulses in three-and four-level systems: light shifts and transfer efficiencies," Physical Review A **50,** 2438 (1994).

[179] F. Dreisow, M. Ornigotti, A. Szameit, M. Heinrich, R. Keil, S. Nolte, A. Tünnermann, and S. Longhi, "Polychromatic beam splitting by fractional stimulated Raman adiabatic passage," Applied Physics Letters **95,** 261102 (2009).